



Institute for Information
and Communication Technologies,
Electronics and Applied Mathematics

Compressive and neural-representation strategies for inverse problems

From interferometric imaging to diffraction
tomography

Olivier Leblanc

Thesis submitted in partial fulfillment
of the requirements for the degree of
the Ph.D. in Engineering Sciences

October 7, 2024

ICTEAM-INMA
Louvain School of Engineering
Université catholique de Louvain
Louvain-la-Neuve
Belgium

Thesis Committee:

Pr. Laurent Jacques (advisor)	UCLouvain
Pr. Christophe Craeye (chair)	UCLouvain
Pr. Christophe De Vleeschouwer	UCLouvain
Pr. François Glineur	UCLouvain
Pr. Yves Wiaux	Heriot-Watt, Edinburgh, UK
Dr. Emmanuel Soubies	IRIT, Toulouse, France

Compressive and neural-representation strategies for inverse problems

From interferometric imaging to diffraction
tomography

by Olivier Leblanc

© Olivier Leblanc 2024
ICTEAM
Université catholique de Louvain
Avenue Georges Lemaitre, 4
1348 Louvain-la-Neuve
Belgium

This work was funded by the F.R.S-FNRS.

“Goals transform a random walk into a chase”

Mihaly Csikszentmihalyi

Abstract

Computational imaging has revolutionized our capabilities to sense the environment, enabling a wide range of applications in domains like medical, biological, or radio-astronomical imaging. This thesis broadens the scope of the computational imaging framework in two main directions.

First, the principle of *compressive imaging*—*i.e.*, capturing the image information with few linear projections data—is applied to two interferometric imaging applications, namely *multicore fiber lensless imaging* and *radio-interferometry*. In both cases, it is shown that compressive imaging is possible with random projections applied at the level of the interfering elements, resulting in a linear sensing model involving *Fourier subsampling* and *rank-one projections*. In addition to the analysis of their computational complexities, the sensing models are accompanied by uniform recovery guarantees highlighting their *sample complexities*—the number of interfering elements and number of measurements required for image recovery. The theoretical sample complexities are confirmed numerically, and also experimentally for multicore fiber imaging.

Second, contributions are brought to the field of *diffraction tomography*, proposing a combination of an *implicit neural representation*—a continuous image representation by a neural network—and a nonlinear (multiple-scattering) sensing model. Significant efforts are made in a review of the different ways to model electromagnetic wave diffraction through inhomogeneous media, leveraging *first-order optimization methods* to solve the subsequent linear system of equations. The reconstruction of the 3-D image through the weights of an implicit neural representation instead of discrete voxels is proposed for this nonlinear sensing model, demonstrating the benefit of (*i*) the nonlinearity over linear approximations of the model, and (*ii*) the continuous representation for handling rotations of the object. The drawbacks of the approach are highlighted and improvements necessary for experimental use are discussed.

Acknowledgments

First and foremost, I would like to express my deepest gratitude to my advisor, Laurent Jacques. I have always been impressed by the *information-to-sentence* ratio of Laurent. Every word he uses to talk is carefully and accurately selected. Just as stunning is his ability to communicate complex mathematical notions on a white board. His clarity of communicating anything is the reason why I initially chose him to be my advisor. Looking backward, the cumulative time we spent at discussing around his white board counts in days, and a vast majority of the content of this thesis is the fruit of these inspiring discussions.

Throughout these four years of supervision, I got to know better an erudit, wise, passionate, humble, but also caring, generous and supportive mentor. He has been encouraging nice personal and scientific news, easing disappointments and annoyances, and even escorting a poor student on crutches (me) all the way to Switzerland by train for a conference. I'm sincerely tempted to transform the quote "don't choose the topic, choose the advisor" by "don't choose the topic, choose Laurent".

I am also very grateful to Yves Wiaux for accepting to be on my thesis jury, for our fruitful and pleasant interactions mostly around radio-interferometry, for letting me present my works to his team, for kindly hosting me for two weeks at *Heriot-Watt University* in Edinburgh (UK) and introducing me to scones there.

Special thanks to Ulugbek Kamilov. Ulugbek's works strongly inspired my contributions in diffraction tomography. I also had the opportunity to visit him and his team for a two-month stay at WashU in Saint-Louis (USA). I'm looking forward to other thought-provoking discussions with Ulugbek in the future.

I thank Hervé Rigneault, who was my very first collaborator in the context of this thesis. Hervé kindly welcomed me at the *Institut Fresnel* at Aix-Marseille Université (France) for one week of optical measurements with a real multicore fiber, which enabled an experimental

★ | Acknowledgments

proof-of-concept of our idea.

I would also like to thank the members of my thesis committee, Christophe De Vleeschouwer, Emrah Bostan and François Glineur, for attending my half-way confirmation defense, and giving me useful feedback and perspectives for the second half part of my PhD project. I additionally thank Christophe Craeye, for presiding my PhD defense, and Emannuel Soubies for being a member of my thesis jury.

I would like to warmly thank the people I had the chance to collaborate with: Matthias Hofer, Siddharth Sivankutty and Hervé Rigneault for the multicore fiber lensless imaging; Yves Wiaux and Taylor Chu for the radio-interferometry; and Ulugbek Kamilov for the diffraction tomography.

I would like to express my gratitude to my office mate Nizar and my PhD brother Rémi who I spent most time with out of the working time. Many thanks also to the many colleagues I've had at the Euler building and who made the workplace so welcoming, especially with its iconic pie breaks. Thanks to my colleagues from ELEN, especially my mates from the electrical engineering master, who discovered with me the different steps of a PhD project, and the other people who shared the supervision of some master courses with me.

I have the incredible chance to have a lot of good friends who supported me during this thesis, and I would also like to thank them all for that. I also thank my parents and my brother for their unconditional support. Finally, I thank Claire for her unwavering patience and mental support during six long weeks of writing rush.

This thesis was funded by the F.R.S.-FNRS, which has my gratitude for giving me "la liberté de chercher". It would also not have been possible without the administrative and technical staff at UCLouvain and the ICTEAM institute in particular.

Finally, I want to highlight the huge supply brought by technical tools developed by many different group of people. I had the opportunity to use the super-computing facilities (*i*) in Belgium made available by the CISM and CECI, (*ii*) in the Computational Imaging Group (CIG) at WashU, and (*iii*) on Cirrus hosted by EPCC at University

Acknowledgments | *

of Edinburgh to conduct highly extensive numerical experimental on GPUs and multi-threaded CPU nodes. I got to use *Visual Studio Code*¹, a free Open-Source software developed by Microsoft and maintained by a community of thousands of people, as my favorite interface for code/paper editing and git managing. My coding speed was also doubled thanks to the AI developer tool *Github Copilot*². I could use (and contribute to some) Python toolboxes like *SPGL1*, *Pyproximal*, *PyUnlockBox* developed by small research teams by the past as well as other bigger scale packages. I acknowledge the use of ChatGPT 4³ for supporting thinking and slightly rephrasing a couple of sentences.

¹<https://code.visualstudio.com>

²<https://github.com/features/copilot>

³Open AI, <https://chatgpt.com>

Contents

Abstract	i
Acknowledgments	iii
Contents	vii
List of Figures	x
List of Tables	xi
1 Introduction	1
1.1 Computational imaging: applications and challenges	2
1.2 Interferometry and Rank-One Projections	6
1.3 Diffraction Tomography	7
1.4 Implicit Neural Representations	8
1.5 Outline and contributions	9
Notations	21
Conventions	23
2 Preliminaries: Flavors of Computational Imaging	25
2.1 Forward Sensing Model	26
2.2 Inverse Problem	35
2.3 Recovery Algorithm	41
2.4 Recovery Guarantees	46
2.5 Complexities	52
2.6 Appendix	55
3 Rank-One Compression of Interferometric Sensing	65
3.1 Introduction	66
3.2 Sensing Model	73
3.3 Recovery Guarantees	85
3.4 Recovery Analysis - Phase Transition Diagrams	94
3.5 Experimental MCFLI	97
3.6 Discussion	103

* | Contents

3.7 Proofs	106
4 Compressive Radio-Interferometry	121
4.1 Introduction	122
4.2 Preliminaries	129
4.3 Acquisition and Sensing Models	134
4.4 Recovery Algorithms	156
4.5 Recovery Guarantees for Batched ROPs	160
4.6 Recovery Analysis	167
4.7 Discussion	176
4.8 Appendix	182
5 Diffraction Through Inhomogeneous Media	197
5.1 Introduction	198
5.2 Lippmann-Schwinger and First-Born	203
5.3 Discrete Model	218
5.4 System Solving	221
5.5 Discussion	233
5.6 Appendix	235
6 Diffraction Tomography with Implicit Neural Representations	247
6.1 Introduction	247
6.2 Preliminaries	254
6.3 Implicit Neural Representations	257
6.4 Sensing Models for ODT and IDT	261
6.5 Recovery Analysis	266
6.6 Discussion	273
6.7 Appendix	277
7 Conclusion	291
7.1 Summary of the Chapters	291
7.2 Future Work and Comments	294
List of symbols and acronyms	297

List of Figures

1.1	Conventional vs computational imaging	3
1.2	Three CI applications in this thesis	10
1.3	Contribution graph of the thesis	13
1.4	Features of Computational Imaging	14
2.1	Example of a CI application	26
2.2	Zoom in on dog image	28
2.3	Wavelet transform of the dog image	29
2.4	Architecture of an autoencoder	31
2.5	Blurred and masked dog images	33
2.6	1-D loss functions	41
2.7	Reconstruction of the dog image	45
2.8	Geometrical intuition of the RIP	51
3.1	Working principle of MCFLI	67
3.2	MCFLI and its link with SROP of the interferometric matrix.	74
3.3	Representation of the MCFLI sensing model	75
3.4	arrangements of the cores and their corresponding Fourier sampling	76
3.5	Illustration of the RS and SI principles.	77
3.6	Phase transition curves	95
3.7	Phase transition diagrams	95
3.8	Phase transition cube	96
3.9	Optical setup	98
3.10	SLM configuration and recorded speckle	98
3.11	Cores activated for the reconstructions	101
3.12	Experimental reconstructions	102
4.1	Direction cosine coordinate system	130
4.2	NUFFT computation	133
4.3	Schematic of the radio-interferometric sensing context . . .	136
4.4	Antenna arrangement of the VLA and its Fourier sampling .	138
4.5	Computations at the acquisition.	142
4.6	Link between beamforming and ROPs	145
4.7	Structure of the modulated ROP operators	153

★ | List of Figures

4.8	Sparse sky and phase transition cube	168
4.9	Phase transition diagrams for modulated ROPs	168
4.10	Success rate vs number of batches	169
4.11	Phase transition diagrams for separated ROPs	171
4.12	3c343 groundtruth and meerkat uv-coverage	173
4.13	SNR and log SNR transition curves using uSARA	173
4.14	Images reconstructed using uSARA	175
5.1	Diffraction through an inhomogeneous medium	198
5.2	Three families of diffraction methods	211
5.3	Diffraction through a slit	212
5.4	Fourier diffraction theorem	214
5.5	Equivalent incident field with passive sources	217
5.6	Stability of the Gradient Descent method	223
5.7	Convergence of toy linear system solving	228
5.8	Convergence of GD and variants for the discrete LS system .	229
6.1	Diffraction tomography with INR	248
6.2	Automatic Differentiation	254
6.3	Positional Encoding	258
6.4	INR architectures	259
6.5	Rotation of the object and missing cone problem	263
6.6	Rotating an object with varying spatial dimensions	264
6.7	Recovery procedure	266
6.8	Memory load on a GPU	267
6.9	First-Born vs Lippmann-Schwinger in ODT	270
6.10	SNR vs illumination angle	272
6.11	SNR vs number of iterations in LS	272
6.12	SGD vs Adam	279
6.13	Error vs number of batches and frequencies	279
6.14	Error vs frequency factor	280
6.15	Error vs number of layers	281
6.16	Reconstruction of a granulocyte phantom	282
7.1	Summary of the contributions	292

List of Tables

1.2	Convention for the algorithms	23
3.1	Complexities in MCFLI	83
4.1	Typical values in RI	150
4.2	Complexities of the acquisition	150
4.3	Complexities of the image reconstruction	152
4.4	Reminder on the costs of modulated ROPs	169
4.5	vector vs matrix forms	186
6.1	Backpropagation example	255
6.2	Parameters of the experiments	269
6.3	Parameters of INRs	278

1

Introduction

IMAGES ARE EVERYWHERE. Imaging is one of the main tools used by humans to record, share, display, and quantify information. More than ever today, we are drowned with dozens of images and videos every day on social media and journals. Watching professional sport, films and series, or online videos is one of the main hobbies. Cameras are placed in the streets, highways, houses, supermarkets and many more for security and statistical analysis. Also for medical diagnosis, radiography, echography, Magnetic Resonance Imaging (MRI) and ultrasound imaging for mammography all produce images that are analyzed either by professionals or even automatically to select the best recovery procedure for each patient. Furthermore, radio-astronomical imaging is key to deepen our understanding of the universe.

However, some imaging modalities cannot directly sense image-like data like a conventional camera. For instance, the target finest angular resolutions in radio-interferometry require to acquire electromagnetic signals at antennas spaced by thousands of kilometers. On the other hand, the indirect nature of MRI data collection, involving frequency and phase encoding, cannot be bypassed to directly sense an image.

In this thesis, we will cover imaging applications whose measurements contain indirect information about the image of interest, and for which an inverse problem must be solved in order to estimate this image. We will present photonic imaging use-cases but the conclusions are not specific, they can be applied to other modalities like electron imaging [Rob+23] and gravitational imaging [Nic95]. Some contributions are the fruit of scientific collaborations, I will use by default the

1 | Introduction

pronoun "We" to mention our shared contributions, and explain some scientific questions that arose from this PhD project.

1.1 Computational imaging: applications and challenges

This section will gradually explain the key concepts of COMPUTATIONAL IMAGING, starting from the basics of conventional cameras, up to the open challenges for the field. This introduction remains mainly textual to take the reader by hand. Though, the key mathematical variables that are the core of any computational imaging application will be gently introduced to build up the intuition.

All imaging is computational nowadays.

The principles of conventional cameras have been inspired by human visual system. In Fig. 1.1.(a), like in the human eye, a transparent curved surface named *lens* maps a specific plane of the field-of-view onto an internal small plane that senses the incoming light. The lens is the key component. Thanks to it, the sensed information generally coined y directly estimates the environment of interest x .

Most of smartphone users may have noticed phones now have multiple cameras. The purpose is not to capture multiple snapshots of the scene. The information of the images obtained via each single camera is combined (through computations) to enhance the resulting image. This is reminiscent of how human eyes work with the brain to combine their information. This is a first example of CI. Slightly less noticeable, a few moments after a photo has been taken, the image is corrected on-the-fly to deblur and improve contrast. The corrections made to our captured images are not random. They are specifically chosen to map the freshly acquired image to a distribution of more *nice-looking* images. These corrections require computations in order to modify each pixel value. Actually, *automatic focusing*—adjusting the focal distance of the camera lens to a target plane to get a sharp image—is another example of CI.

More formally, the term COMPUTATIONAL IMAGING stands for any context where the link between the target image and related measurements differs from identity. As depicted in Fig. 1.1.(b), the measurements y are related to the image x through a *forward operator* A . In most common applications, the imperfection of the sensing device and modeling of A are represented by an additive *noise term* n . The underlying

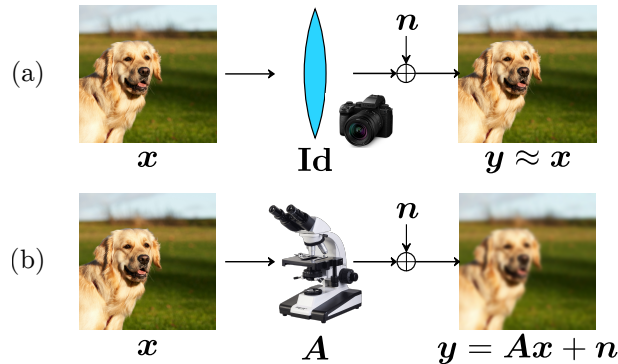


Fig. 1.1 (a) Conventional imaging using a lens. (b) Example of a computational imaging application: deblurring.

mathematical model writes

$$y = Ax + n. \quad (1.1)$$

Obviously, the image of interest is x . But in (1.1), x is no longer directly accessible. The task of computing an *estimate* \tilde{x} of x from the knowledge of y is called an **INVERSE PROBLEM** because (1.1) needs to be inverted in some way.

CI has numerous applications. To cite a few: in *natural imaging*: denoising, motion deblurring, superresolution, inpainting. In *biomedical imaging*: tomography, MRI, endoscopy, microscopy; and *radioastronomical imaging* is another example. The differences between them lie in the forward operator A . The challenges are the following.

Forward model

Each CI modality requires an appropriate model for A . In the majority of currently well-studied cases, a linear model such as (1.1) is sufficient to describe the sensing. This will be our case in Chap. 3-4. In general, however, the relationship between y and x can be nonlinear. Chap. 5-6 will be an example of a nonlinear model. At first glance, a linear forward model seems gentle and easy to analyze. It only involves a linear forward operator A —a *matrix*. But A can take many forms. The problem is that it usually contains *only partial information* about the image of interest x . We call this an *ill-posed* inverse problem; because the inverse of A does not exist.

1 | Introduction

Inverse problem and recovery program

Since A^{-1} does not exist, the image cannot be computed as simply as $\tilde{x} = A^{-1}y$. And even if the inverse does exist, it generally amplifies the noise. The solution to the inverse problem, *i.e.*, the computation of a sound image candidate, is generally obtained by minimising a cost (or loss) function which implies two terms: (*i*) a *data fidelity* term—computing the distance between the acquired measurement and a measurement candidate, and (*ii*) a *regularization* term—forcing the candidate to satisfy some structure known a priori. The choice of the loss function is challenging, as is the scaling factor between data fidelity and regularization.

The practical way to minimise the loss function is the *reconstruction* (or *recovery*) *algorithm*. While algorithms can take many forms, the philosophy is always the same:

1. Start with a first candidate.
2. Compute the error, *i.e.*, the value of the loss function.
3. Update the candidate in a direction that reduces the value of the loss function.
4. Iterate between steps 2. and 3. until a maximum number of iterations is reached or a tolerance criterion is satisfied. Then stop.

There is a large community of researchers in the field of *optimization* who categorize functions to be minimized and provide appropriate algorithms to solve these minimization problems. In this thesis, the results from this community are used as a powerful tool to compute the reconstruction.

Recovery guarantees

In CI applications, the ground truth image is generally unknown. For hobby photography or any situation where only a qualitatively satisfactory reconstruction is required, a nice rendering is sufficient. However, for biomedical diagnosis, chemical analysis, and radio-astronomy, a quantitatively accurate reconstruction is necessary. Obviously, the reconstruction cannot be compared to the ground truth to evaluate its quality. Nevertheless, if the forward operator A preserves a sufficient amount of information of the image of interest, it is possible to show rigorously in some simple cases (for now) that minimizing a distance in the measurement space directly relates to a minimization of a distance

in the image space. These proofs involve demonstrating an isometry property between the two spaces. These works show that the estimation error can be decreased by putting effort into minimizing the data-fidelity term. While a bunch of recovery guarantees have been given mainly for toy inverse problems, it has been numerically and experimentally observed that the reconstructions are also accurate in more realistic cases.

A minimal number of measurements

There are two main reasons to aim for a minimal number of measurements, *a.k.a. sample complexity*.

1. **Reduced memory usage** Some modalities generate a large amount of data on a daily basis. For example, the *Square Kilometer Array* for radio-astronomy will collect about 5 terabits per second of interferometric data [BNB15].
2. **Speed of acquisition** Sometimes multiple snapshots are needed to collect enough information about the image of interest. This is done by tuning the acquisition parameters. This process can be slow, and minimizing the sample complexity can alleviate this bottleneck.

To reduce the memory footprint, post-sensing compression may be sufficient. In other words, the classical acquisition process can be performed, and the eventually huge amount of data can be compressed after acquisition. Unfortunately, this late compression does not speed up the acquisition process. There is a field of research investigating techniques to compress during acquisition. It is called *compressive imaging* (*compressive sensing* in a broader sense) [AH21]. Compressive imaging will be at the core of the contributions of Chap. 3-4

Imaging fast

If real-time sensing is a necessary constraint for the imaging modality, we see three areas that need to be optimized to speed up the sensing: (i) *Hardware optimization*, *i.e.*, designing the most efficient devices to perform the target sensing. These considerations are beyond the scope of this thesis. (ii) *Lower sample complexity*, as discussed in the previous paragraph. (iii) *Fast recovery program*. A good recovery program must not only produce a reliable estimate of the image. It must also produce this estimate within the time constraints. Since reconstruction

1 | Introduction

algorithms are iterative, speed is achieved both by speeding up each iteration and by minimizing the number of iterations.

The application of the forward operator A within each iteration generally appears to be the most costly operation in terms of computational load. The search for an efficient implementation of A is therefore critical. It usually involves algorithmic tricks such as the *Fast Fourier Transform* [CT65], which appears many times in this thesis.

With *convergence rates* provided by the optimization community [Nes18], the reconstruction algorithms are designed with respect to the features of the loss function to be minimized. However, they are data agnostic. To reduce the number of iterations, (deep) *learning techniques*—using data to improve the recovery performance—have raised a lot of interest in the last decade [Luc+18]. Learning techniques are complementary to most of our contributions, but are not really covered in this thesis.

1.2 Interferometry and Rank-One Projections

Interferometry is pivotal in several cutting-edge imaging techniques. In *multicore fiber lensless imaging*, the interference of the light emitted by multiple cores induces an illumination which is a combination of fringes patterns called *speckle*. This interferometric illumination method enables high-resolution visualization [Leb+23]. Similarly, in *atmospheric optical turbulence forecasting*, interferometry helps predicting and mitigating the effects of turbulence on optical systems, thereby increasing the accuracy and reliability of atmospheric observations [Qua+23]. In addition, *radio-interferometry* uses the principles of interferometry to synthesize high-resolution images of astronomical objects by correlating signals received at different telescopes, effectively overcoming the limitations of single-dish telescopes [Wia+09].

Strongly related to the famous *double-slit experiment*, two elements interfering yield a fringe pattern. Interferometric imaging is tantamount to obtain a projection of an image of interest with this fringe, which is a sinewave whose wavelength depends on the distance between these elements. If multiple elements interfere, this results in a linear combination of sinewaves whose wavelengths are inversely proportional to the pairwise distances between the elements. Consequently, interferometric imaging amounts to accessing Fourier samples on the set of differences of the element's positions. This key observation allows for the smart design of antenna or core arrays, optimizing the

spatial configuration to effectively capture the necessary information. By strategically placing antennas or fibers based on the difference-set approach, one can maximize the coverage and resolution of the sampled Fourier space, leading to high-fidelity reconstructions from limited data.

A key aspect of Chap. 3 and 4 is the exploration of the correspondence between computing the square modulus of a sketch of the interferometric measurement vector and *Symmetric Rank-One Projections* (SROPs) of the outer product of this vector—coined *interferometric matrix*—with the same sketching vector. By analyzing the outer product and its projections, we gain insight into the structure of the measurements and develop more robust data reconstruction methods. This correspondence enhances both theoretical understanding and practical applications, improving the efficiency and accuracy of interferometric imaging systems. Leveraging *random* SROPs enables the creation of a *compressive imaging* framework and the design of algorithms that are computationally efficient and capable of handling large data sets.

In summary, Chap. 3-4 aims to bridge the gap between interferometry and rank-one projections, providing a comprehensive framework for understanding and using these concepts in various imaging modalities. Through detailed analysis and practical applications, we aim to advance the state of the art in interferometric imaging.

1.3 Diffraction Tomography

DIFFRACTION TOMOGRAPHY is a sophisticated imaging technique used to reconstruct the internal structure of an object by analyzing how waves, such as X-rays, sound waves, or electromagnetic waves, scatter as they pass through the object. Unlike conventional tomography, which assumes straight-line propagation of waves, diffraction tomography accounts for the wave-like nature of signals, incorporating phenomena such as *diffraction* and *interference*. This method involves collecting data from multiple angles and using mathematical algorithms to solve the inverse problem of reconstructing the object's properties. By exploiting the interactions of waves with the internal features of the object, diffraction tomography is particularly valuable in fields such as *medical imaging*, *material science*, and *nondestructive testing*.

In *medical imaging*, diffraction tomography is particularly useful in

1 | Introduction

optical coherence tomography (OCT) [Hua+91], which allows detailed visualization of biological tissues. This application is critical to the diagnosis of retinal disease and other conditions, providing a *non-invasive* means of obtaining high-resolution images of internal structures. In materials science, diffraction tomography is used to examine the internal structure of composite materials, detecting defects or inhomogeneities at the microscopic level. This ensures the integrity and quality of materials, which is essential for the development and use of advanced composite materials. In addition, diffraction tomography is used in *nondestructive testing* to inspect critical components such as aerospace parts, identifying flaws or damage without causing damage to the objects being analyzed. This capability is essential for maintaining safety and reliability in critical industries where understanding the internal state of a component can prevent catastrophic failure.

These applications highlight the versatility and precision of diffraction tomography in capturing intricate internal details across various domains. The ability to account for wave diffraction and interference allows for more accurate and detailed imaging, surpassing the capabilities of traditional tomographic methods. In Chap. 5-6, we make some contributions to the art of diffraction tomography by combining recently stabilized numerical modeling techniques with a continuous representation of the object to be imaged—an *Implicit Neural Representation*, introduced in Sec. 1.4.

1.4 Implicit Neural Representations

IMPLICIT NEURAL REPRESENTATIONS (INRs), sometimes called “NeRFs” for their historical appearance in view synthesis, are a transformative approach in the realm of data representation, leveraging neural networks to encode continuous spatial data [Mil+20; Sit+20; Yuc+22]. This technique offers a compact and flexible means of representing complex structures, enabling advances in high-resolution image reconstruction, 3-D shape modeling, and efficient signal processing.

Unlike voxel-based techniques, which can be limited by their discrete nature and large memory requirements, INRs allow precise reconstruction of complex structures with significantly fewer parameters. This efficiency enables the capture of fine details and smooth variations within objects, improving the fidelity of reconstructed images. Another notable advantage of INRs is their ability to naturally handle contin-

uous transformations, such as object rotations or spatial derivatives. Consequently, INRs are particularly adept at solving partial differential equations (PDEs), such as the *Helmholtz equation*¹.

Importantly, INRs are not just black-box tools for solving inverse problems; they are sophisticated representations tailored for signal processing. Unlike traditional deep learning approaches that rely on supervised learning with ground-truth input-output pairs—often scarce in emerging applications such as diffraction tomography—INRs can be trained in a *self-supervised* manner.

By leveraging the flexibility and precision of INRs, researchers and practitioners can push the boundaries of what is possible in fields ranging from medical imaging to computational physics, ushering in a new era of high-fidelity data representation and analysis. One contribution of this work, described in Chap. 6, is to exploit the use of an INR for diffraction tomography.

1.5 Outline and contributions

This thesis brings contributions to the field of computational imaging in three different applications depicted in Fig. 1.2. Namely, we propose advances in *MultiCore Fiber Lensless Imaging* in Chap. 3, *Radio-Interferometry* in Chap. 4, and *Diffraction Tomography* in Chap. 5-6. The organization of those contributions into the present manuscript is explained below.

Chapter 1: Introduction.

This chapter is the one the reader is currently looking at. It introduced the context of computational imaging, with an emphasis on three aspects covered in this thesis: *interferometry*, *diffraction tomography*, and *implicit neural representations*.

Chapter 2: Flavors of Computational Imaging.

Chap. 2 provides a more in-depth description of the concepts literally introduced in this chapter. This preliminary section introduces the mathematics of computational imaging.

¹This is not what we do in this thesis.

1 | Introduction

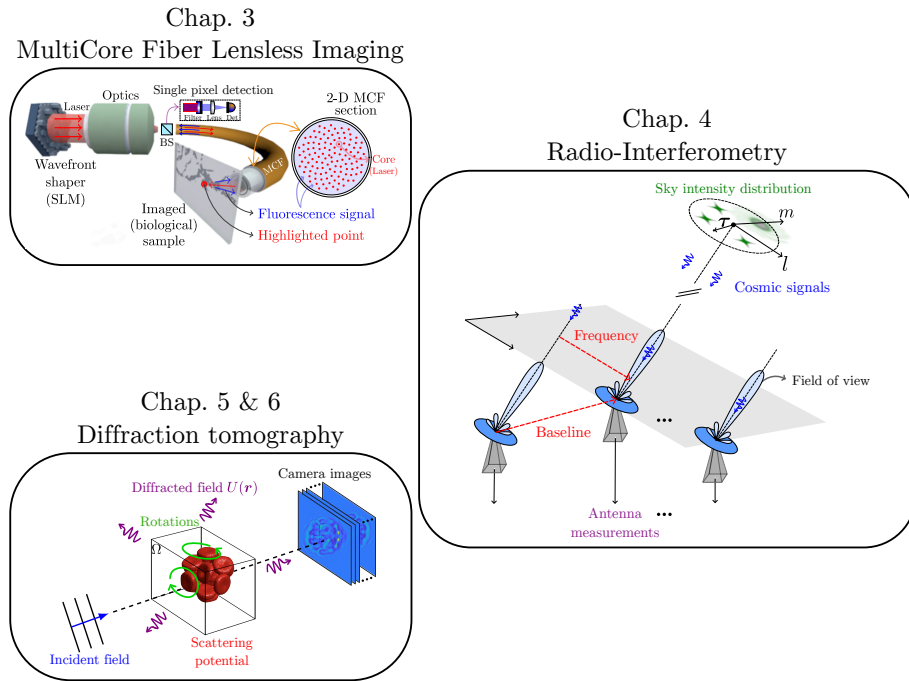


Fig. 1.2 The three computational imaging applications covered in this thesis. Chap. 3 studies the compressive imaging of a 2-D fluorescent biological sample with a *lensless multicore fiber*. Chap. 4 images the light intensity distribution of a small angular portion of the sky by *radio-interferometry*. Chap. 5-6 indirectly observe a 3-D distribution of refractive index by *diffraction tomography*.

It begins by explaining what is *image representation*—*i.e.*, how we can encode the information contained in an image, then how indirect observations of a computational imaging modality can be mathematically linked to that image representation by integrating the physics of acquisition into a *forward operator*. The unwanted random variations that occur in the measurement signal—the *noise*—are briefly described as well.

After formulating the forward sensing model, Chap. 2 explains how to formulate an *inverse problem* to obtain an estimate of the image of interest from indirect and noisy measurements. It is emphasized that solving an inverse problem is tantamount to minimizing a *loss function*, and thus requires the use of *optimization techniques* and *recovery algorithms*.

Next, the two types of *recovery guarantees*—nonuniform and uniform—are presented. And the chapter concludes with a listing of the various *complexities* used to assess the efficiency of a computational imaging modality.

Chapter 3: Rank-One Compression of Interferometric Sensing

There, we provide several contributions to the modeling, understanding, and efficiency of *MultiCore Fiber Lensless Imaging* (MCFLI).

The story begins by leveraging a speckle illumination model to highlight the interferometric nature of the MCF device. A sensing model closer from the physical principle of MCFLI boils down from that observation. It appears that the previously considered illumination modes, but also the arrangement design of the cores, find clear explanations with an interferometric point of view.

Uniform image recovery guarantees are provided based on a couple of realistic assumptions, and are validated by numerical *phase transition diagrams*. The provable theoretical setting is even extended to the recovery of a more realistic image in a *real experimental setup*.

Chapter 4: Compressive Radio-Interferometry.

The contributions of Chap. 3 are transferred and extended to another interferometric imaging modality: *Radio-Interferometry*.

The usual imaging principle, based on the *covariance matrix* of the measurement vector and intrinsically related to a Fourier subsampling of the image of interest, is first properly re-explained. The leap forward of this chapter with respect to the literature is to emphasize that computing a random projection of the measurement vector—*a.k.a. random beamforming*—before computing its covariance, provides a random *rank-one projection* of the covariance matrix. This opens the door to reusing some results of Chap. 3 to do *compressive radio-interferometric imaging*.

The profound novelty of the underlying compression scheme is that it reduces all computational costs: (i) the computation during acquisition, (ii) the number of measurements, and (iii) the computation of the forward imaging model.

Similarly to the previous chapter, *uniform recovery guarantees* are provided and numerically validated with *phase transition diagrams*. Finally, some numerical analysis is proposed in a state-of-the-art realistic simulation environment developed by an internationally renowned research team.

Chapter 5: Diffraction Through Inhomogeneous Media

The explanation of the setting of *Diffraction Tomography* has been divided into two chapters due to the large number of concepts to be cov-

1 | Introduction

ered and the coexistence of two related inverse problems.

Chap. 5 focuses on an accurate discrete model for the diffraction of electromagnetic illumination through an inhomogeneous 3-D refractive index distribution. First, we provide a brief reminder of the simplifying assumptions behind the *Helmholtz equation* and its integral form specifically designed for *inhomogeneous media*—the *Lippmann-Schwinger equation*. This exact nonlinear equation is compared with other popular scattering models which are explained to be approximations. Particular emphasis is made on the linearized model—the *First-Born Approximation*—for its associated *Fourier Diffraction Theorem*, which provides a clear view of the information acquired in a tomographic imaging context.

Next, an accurate and efficient discretization of the *Lippmann-Schwinger model* is provided. The subsequent linear system to be solved is deeply analyzed in the lens of *First-Order Optimization Methods*. It is numerically demonstrated that the ill-conditioning of the linear system is influenced by the *contrast* of the imaged refractive index distribution.

Chapter 6: Diffraction Tomography with Implicit Neural Representations

This chapter builds on the results of Chap. 5 to establish a complete *diffraction tomography* setup.

The first particularity of Chap. 6 is that it considers a continuous representation of the 3-D image by an *implicit neural representation*. This representation brings many benefits to the modality: (i) it provides a reduced parameterization of the image, (ii) it provides easy handling of continuous 3-D rotations of the image, and (iii) it enables the use of an automatic image reconstruction algorithm leveraging *automatic differentiation* and *deep weight backpropagation*.

The second peculiarity is that the sensing models formalized for *optical* and *intensity diffraction tomography* are both *nonlinear sensing models*, letting us dive into the unknown in terms of inverse problem theory. One role of this chapter is to show, by means of numerical simulations, that the nonlinearity of the sensing model improves the image recovery compared to its linear approximation related to the First-Born approximation discussed in the previous section.

Contribution Graph and Features of Computational Imaging

Fig. 1.3 shows a graph of the contributions made in this thesis. The contributions are divided into the aspects already known in the literature and re-explained (in blue), and the novel results (in red). It is shown that this thesis is divided into two main parts:

- Chap. 3-4 covering interferometric imaging and rank-one projections.
- Chap. 5-6 discussing diffraction tomography with implicit neural representations.

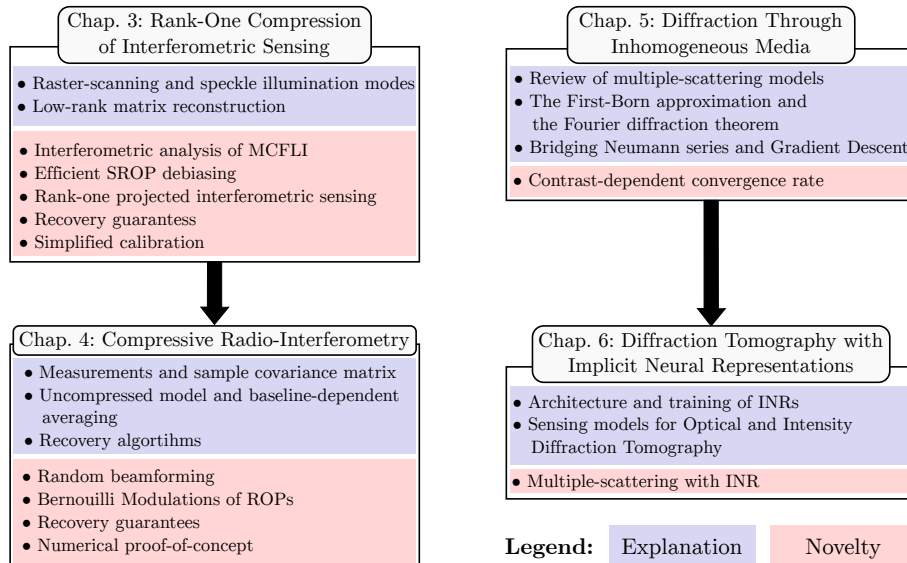


Fig. 1.3 Contribution graph of the thesis. Arrows indicate the prerequisite relations between chapters.

Fig. 1.4 presents 5 features of CI introduced in the preliminary Chap. 2. We report the elements covered in each contributing chapter of this thesis.

List of Publications

Hereafter is the list of scientific publications that have been submitted in the context of this thesis, either peer-reviewed or under review. Several of them inspired significant parts of this manuscript, which are explicitly mentioned at the beginning of the relevant chapters. The publications are grouped according to the part to which they refer and,

1 | Introduction

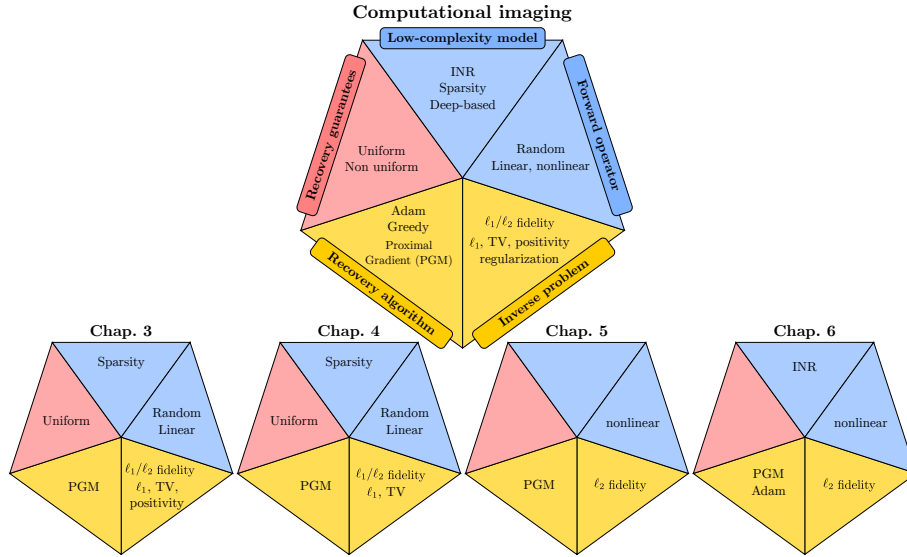


Fig. 1.4 Features of Computational Imaging as described in Chap. 2 and with highlights on the aspects covered in each chapter of this thesis. A *low-complexity model* is a compressed image representation in a transformed domain.

within each part, are listed in order of submission. We also mention the type of publication: journal paper (**J**), conference paper (**C**), poster (**P**), or extended abstract (**A**), *i.e.*, a short version of a conference paper (usually 2 pages).

Related to Chap. 3 - MultiCore Fiber Imaging:

- (**A**) Olivier Leblanc, Matthias Hofer, Siddharth Sivankutty, Hervé Rigneault, and Laurent Jacques, "An Interferometric view of Speckle Imaging", Workshop on Low-Rank Models and Applications at Mons (Belgium), September 2022, cited as [Leb+22].
- (**P**) Olivier Leblanc, Matthias Hofer, Siddharth Sivankutty, Hervé Rigneault, and Laurent Jacques, "An Interferometric view of Speckle Imaging", presented at BASP conference in Villars-sur-Ollon (Switzerland), March 2023.
- (**J**) Olivier Leblanc, Matthias Hofer, Siddharth Sivankutty, Hervé Rigneault, and Laurent Jacques, "Interferometric Lensless Imaging: Rank-one Projections of Image Frequencies with Speckle Illuminations", IEEE Transactions on Computational Imaging (Vol. 10, pp. 208-222), February 2024, cited as [Leb+23].

Related to Chap. 4 - Compressive Radio-Interferometry:

- (J) Olivier Leblanc, Yves Wiaux, and Laurent Jacques, "Compressive radio-interferometric sensing with random beamforming as rank-one signal covariance projections.", **Submitted to IEEE TCI [LWJ24]**.
- (J) Olivier Leblanc, Taylor Chu, Yves Wiaux, and Laurent Jacques, "Compressive radio-interferometric imaging: Rank-One Compression with Bernoulli modulations across time.", **In preparation for Monthly Notices of the Radio-Astronomical Society (MNRAS)..**

Related to Chap. 5-6 - Diffraction Tomography:

- (P) Olivier Leblanc, Laurent Jacques, and Ulugbek Kamilov, "COLSI: Continuous Lippmann-Schwinger Intensity diffraction tomography", presented at the workshops Math-Image in Marseille, September 2023 and DIPopt in Lyon, November 2023.

During this thesis, I also contributed to the following articles in the fields of Computational Imaging and Convex Optimization:

- (A) Siddharth Sivankutty, Stéphanie Guerit, Olivier Leblanc, Matthias Hofer, Géraud Bouwmans, Esben Ravn Andresen, Laurent Jacques, and Hervé Rigneault, "Computational fluorescence imaging with multi-core fiber bundles-Towards high-speed imaging through bare optical fibers", European Conference on Lasers and Electro-Optics at Munich (Germany), June 2023.
- (J) Murielle Kirkove, Yuchen Zhao, Olivier Leblanc, Laurent Jacques, and Marc Georges, "ADMM-inspired image reconstruction for Terahertz off-axis digital holography", Journal of the Optical Society of America A (Vol. 41, Issue 3, pp. A1-A14), December 2023, cited hereafter as [Kir+24].
- (J) Matteo Ravasi, Marcus Valtonen Örnham, Nick Luiken, Olivier Leblanc, and Eneko Uruñuela, "PyProximal - scalable convex optimization in Python", Journal of Open Source Software (Vol. 9, Issue 95, No. 6326), March 2024, cited as [Rav+24].

List of Codes

Related to Chap. 3 - MultiCore Fiber Imaging:

1 | Introduction

- <https://github.com/olivierleblanc/ROPI>.

Related to Chap. 4 - Compressive Radio-Interferometry:

- <https://github.com/olivierleblanc/RAPHA>.
- <https://github.com/olivierleblanc/uSARA>.
- <https://github.com/olivierleblanc/AIRI>.

Related to Chap. 5-6 - Diffraction Tomography:

- <https://github.com/olivierleblanc/cols>

Notations

u	Scalar (lowercase)
$\mathbf{u} = (u_i)_{i=1}^N$	Vector (boldfont lowercase).
\mathbf{U}	Matrix (boldfont uppercase).
$f(\mathbf{u})$	A scalar-to-scalar function is applied componentwise to a vector: $(f(\mathbf{u}))_j = f(u_j)$.
$\gtrsim (\lesssim)$	Proportionally greater (smaller). $a \gtrsim b \Leftrightarrow a > Cb$ for any constant $C > 0$ (and similarly for \lesssim).
$[0, 1)$	Half-open interval including 0 but excluding 1.
$[0, 1]^p$	Unit box of p dimensions. $[0, 1]^p := [0, 1] \times \dots \times [0, 1]$, p times.
$\delta_{k,k'}$	Kronecker delta. $\delta_{k,k'} = \begin{cases} 1, & \text{if } k = k'. \\ 0, & \text{otherwise.} \end{cases}$
\mathbf{e}_i	Standard basis vector. $(\mathbf{e}_i)_j = \begin{cases} 1, & \text{if } j = i \\ 0, & \text{elsewhere.} \end{cases}$
\mathbf{I}	Identity operator or $n \times n$ identity matrix (\mathbf{I}_n when ambiguous).
$\iota_{\mathcal{S}}(x)$	Indicator function. $\iota_{\mathcal{S}}(x) := \begin{cases} 0, & \text{if } x \in \mathcal{S}. \\ +\infty, & \text{otherwise.} \end{cases}$
$\Pi_{\mathcal{S}}(x)$	Projection on the set \mathcal{S} . $\Pi_{\mathcal{S}}(x) := \arg \min_{u \in \mathcal{S}} \ x - u\ _2$.

Complex

\mathbb{R}, \mathbb{C}	Set of all real (resp. complex) numbers.
$i = \sqrt{-1}$	Imaginary number.

1 | Notations

$\Re\{a\}, \Im\{a\}$	Real and imaginary parts of $a \in \mathbb{C}$.
$\bar{\mathbf{u}} = \begin{bmatrix} \mathbf{u}_{\mathcal{R}} \\ \mathbf{u}_{\mathcal{I}} \end{bmatrix}$	Augmented real version $\bar{\mathbf{u}} \in \mathbb{R}^{2n}$ of a complex vector $\mathbf{u} \in \mathbb{C}^n$.

Operations

\mathbf{U}^\top	Transpose.
\mathbf{U}^*	Conjuguate transpose.
\mathbf{U}^\dagger	Pseudo-inverse. For a matrix $\mathbf{U} \in \mathbb{C}^{M \times N}$;
	$\mathbf{U}^\dagger := \begin{cases} (\mathbf{U}^* \mathbf{U})^{-1} \mathbf{U}^*, & \text{if } M < N \\ \mathbf{U}^* (\mathbf{U} \mathbf{U}^*)^{-1}, & \text{otherwise} \end{cases}.$
$\mathbf{u} \cdot \mathbf{v}$	Elementwise product.
$\text{diag}(\mathbf{u})\mathbf{v} = \mathbf{D}_\mathbf{u}\mathbf{v}$	
*	Convolution.
\times	Vector/Cross product.
\circ	Composition of operators.
\otimes	Kronecker product. $\mathbf{U} \otimes \mathbf{V} = \begin{bmatrix} U_{11}\mathbf{V} & \cdots & U_{1n}\mathbf{V} \\ \vdots & \ddots & \vdots \\ U_{m1}\mathbf{V} & \cdots & U_{mn}\mathbf{V} \end{bmatrix}.$
$/k \mod N$	Modulo. $/k \mod N := k \bmod N$
$\lceil \cdot \rceil$	Ceil.
$\det \mathbf{U}$	Determinant of the matrix \mathbf{U} .
$\text{tr } \mathbf{U}$	Trace of the matrix \mathbf{U} . $\text{tr } \mathbf{U} := \sum_i U_{ii}$.
$\text{diag}(\mathbf{U}) \in \mathbb{C}^n$	Extracts the diagonal of \mathbf{U} . $\text{diag}(\mathbf{U})_i = U_{ii}$.
$\text{diag}(\mathbf{u}) = \mathbf{D}_\mathbf{u} \in \mathbb{C}^{n \times n}$	Diagonal matrix s.t. $\text{diag}(\mathbf{u})_{ii} = u_i$.
\mathbf{U}_d	Diagonalized version of \mathbf{U} . $\mathbf{U}_d = \text{diag}(\text{diag } \mathbf{U})$.
\mathbf{U}_h	Hollow version of \mathbf{U} . $\mathbf{U}_h := \mathbf{U} - \mathbf{U}_d$.

$\hat{g}(\chi) = \mathcal{F}(g)[\chi]$	d -dimensional Fourier transform of g evaluated at χ . $\hat{g}(\chi) := \int_{\mathbb{R}^d} g(s) e^{-i2\pi\chi^\top s} ds.$
∂_x	Partial derivative with respect to variable x .
∇	Nabla operator. In 3-D Cartesian coordinates, $\nabla := (\partial_x, \partial_y, \partial_z)$.

Norms

$\ \mathbf{u}\ _p$	p -norm (or ℓ_p -norm) of \mathbf{u} . $\ \mathbf{u}\ _p := (\sum_{n=1}^N u_n ^p)^{1/p}$, for $p \geq 1$. With $\ \mathbf{u}\ := \ \mathbf{u}\ _2$.
$\ \mathbf{u}\ _0$	ℓ_0 -pseudonorm counting the number of nonzero entries of \mathbf{u} . $\ \mathbf{u}\ _0 = \{i : u_i \neq 0\} = \text{supp } \mathbf{u} $.
$\ \mathbf{u}\ _\infty$	Infinite norm. $\ \mathbf{u}\ _\infty = \max_i u_i$.
$\ \mathbf{U}\ _{\text{F}}$	Frobenius norm. $\ \mathbf{U}\ _{\text{F}}^2 := \sum_{j,k} U_{jk} ^2$.
$\ \mathbf{U}\ _*$	Nuclear norm. $\ \mathbf{U}\ _* := \text{tr} \sqrt{\mathbf{U}^* \mathbf{U}}$.
$\ \mathbf{U}\ $	Operator norm. $\ \mathbf{U}\ := \sup \left\{ \frac{\ \mathbf{U}\mathbf{v}\ }{\ \mathbf{v}\ } : \mathbf{v} \in \text{dom } \mathbf{U} \right\}$.
$\ \mathbf{u}\ _{\text{TV}}$	Total Variation norm. In 1-D, $\ \mathbf{u}\ _{\text{TV}} := \sum_{i=1}^{N-1} u_{i+1} - u_i $.
$\ X\ _{\psi_p}$	Sub-exponential ($p = 1$) and sub-Gaussian ($p = 2$) norms of a random variable X . $\ X\ _{\psi_p} := \sup_{q \geq 1} q^{-1/p} (\mathbb{E} X ^q)^{1/q}$.
$\langle \mathbf{u}, \mathbf{v} \rangle$	Scalar product between \mathbf{u} and \mathbf{v} with respect to one of the norms defined above.
$\langle \mathbf{U}, \mathbf{V} \rangle_{\text{F}}$	Frobenius scalar product. $\langle \mathbf{U}, \mathbf{V} \rangle_{\text{F}} = \text{tr } \mathbf{U}^* \mathbf{V}$.

Sets

\emptyset	Empty set.
\mathbb{N}, \mathbb{Z}	Sets of natural numbers and integers, respectively.
$\{s_q\}_{q=1}^Q$	$\{s_q\}_{q=1}^Q := \{s_1, \dots, s_Q\}$.
$ \mathcal{S} $	Cardinality of a finite set \mathcal{S} .

1 | Notations

$\mathcal{A} - \mathcal{B}$	Minkowski difference of two sets \mathcal{A} and \mathcal{B} . $\mathcal{A} - \mathcal{B} = \{a - b : a \in \mathcal{A}, b \in \mathcal{B}\}$.
$\llbracket N \rrbracket$	Indices. $\llbracket N \rrbracket = \{1, \dots, N\}$.
$\llbracket N_1, N_2 \rrbracket$	Indices. $\llbracket N_1, N_2 \rrbracket = \{N_1, N_1 + 1, \dots, N_2\}$ with $N_1 < N_2$.
$A_{\mathcal{S}}$	Restriction of the matrix $A \in \mathbb{C}^{n \times n}$ to the columns indexed in $\mathcal{S} \subset \llbracket n \rrbracket$.
Σ_K	All K -sparse signals. $\Sigma_K := \{\mathbf{u} : \ \mathbf{u}\ _0 \leq K\}$.
\mathcal{H}^Q	Hermitian matrices in $\mathbb{C}^{Q \times Q}$, i.e., square matrices M satisfying $M = M^*$.
$\mathcal{G}_{(N_x, N_y, N_z)}^{(L_x, L_y, L_z)}$	Regular 3-D grid. $\mathcal{G}_{(N_x, N_y, N_z)}^{(L_x, L_y, L_z)} := \{\mathbf{r}_0, \dots, \mathbf{r}_{N-1}\}$ with $\mathbf{r}_n := (\frac{iL_x}{N_x}, \frac{jL_y}{N_y}, \frac{kL_z}{N_z}) - (\frac{L_x}{2}, \frac{L_y}{2}, \frac{L_z}{2})$, where $n := i + jN_x + kN_y^2$, $i \in \llbracket N_x \rrbracket$, $j \in \llbracket N_y \rrbracket$, $k \in \llbracket N_z \rrbracket$. \mathcal{G}_N^L and $\mathcal{G}_{(N_x, N_y)}^{(L_x, L_y)}$ are the analog 1-D and 2-D versions.
$\mathcal{G}_{(N_x, N_y, N_z)}^{(L_x, L_y, L_z)'} \quad '$	Normalized 3-D regular grid $\mathcal{G}_{(N_x, N_y, N_z)}^{(L_x, L_y, L_z)'} \subset [-\frac{1}{2}, \frac{1}{2}]^3$ with resolution (N_x, N_y, N_z) along the (x, y, z) axes respectively. $\mathcal{G}_{(N_x, N_y, N_z)}^{(L_x, L_y, L_z)'} := \{\mathbf{r}'_0, \dots, \mathbf{r}'_{N-1}\}$, with $\mathbf{r}_n := L\mathbf{r}'_n$ using largest spatial dimension $L := \max(L_x, L_y, L_z)$. \mathcal{G}_N^L' and $\mathcal{G}_{(N_x, N_y)}^{(L_x, L_y)'}'$ are the 1-D and 2-D analog versions.

Random distributions

$p(X)$	Probability of the event X .
$p(X Y)$	Probability of the event X knowing that the event Y has occurred.
$X \sim \mathcal{P}$	The random variable or vector X is randomly distributed according to the distribution \mathcal{P} .
$X_i \underset{\text{i.i.d.}}{\sim} \mathcal{P}$	The random variables or vectors $\{X_i\}_{i=1}^N$ are <i>independent and identically distributed</i> according to the distribution \mathcal{P} .
\mathbb{E}_{α}	Expectation with respect to the random vector α .

$\mathcal{U}(\mathcal{A})$	Uniform distribution on a set \mathcal{A} .
$\mathcal{N}(\mu, \Sigma)$	Real multivariate normal distribution with mean μ and covariance matrix Σ (written σ^2 in 1-D).
$\mathcal{CN}(\mu, \Sigma)$	Complex multivariate normal distribution with mean μ and covariance matrix Σ (written σ^2 in 1-D).

Conventions

The “hat” will be reserved for designating the Fourier transform of a signal (e.g., $\hat{f} := \mathcal{F}(f)$) and the “tilda” will be used for an estimate computed as the solution of an inverse problem (e.g., $\tilde{x} = \arg \min_x f(x)$ for a function f to be minimized), or the biased and noisy measurements in Chap. 4. The k -th iterate of the variable x in an optimization algorithm will be denoted $x^{(k)}$.

For the *algorithms*, a *code-like* convention will be used, as shown in Table 1.2.

Table 1.2 Convention for the algorithms

Operation	Notation example
Assignment	$a = 1$
Increment	$b += 1$
Multiplication	$c *= 10$

2

Preliminaries: Flavors of Computational Imaging

This chapter provides a self-contained introduction to the concept of COMPUTATIONAL IMAGING (CI). Throughout the chapter, the different features of CI will be browsed with their mathematical description and some references for the interested reader. Given the vastness of the topic, this presentation will be far from exhaustive; rather, its main goal is to introduce, in a pedagogical manner (assuming little or no prior knowledge), the important concepts and notations that will be relevant throughout this thesis.

In order to provide a clear track for the reader, let us consider the CI example shown in Fig. 2.1. On the left, it reveals a clean $512 \times 512 \times 3$ image of a beautiful dog in a garden. This is the image we would have liked to get directly. Unfortunately, when we took the picture with our smartphone, we accidentally touched the screen and the automatic refocusing system was running. In addition, we are using an old smartphone with a low-quality camera. Because of that, the image captured by the smartphone is the blurred and noisy version shown in Fig. 2.1(right).

This classical context has probably happened to most smartphone owners. One way to mathematically model this blur plus noise in the image is written in (2.1).

2 | Preliminaries: Flavors of Computational Imaging

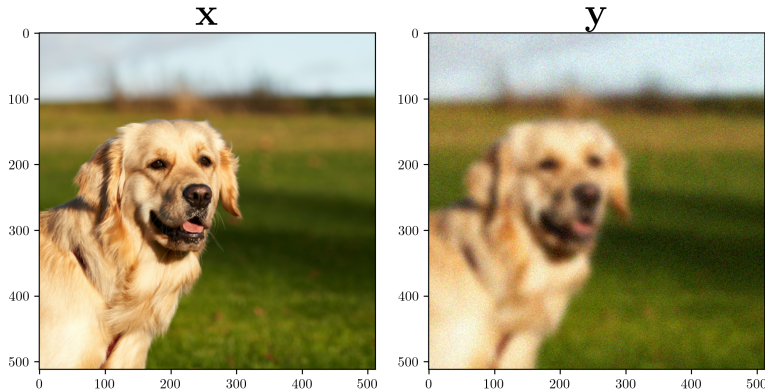


Fig. 2.1 Our CI application example: a blurred and noisy image of a dog. (left) clean $512 \times 512 \times 3$ image of the dog; what we want. (right) Blurred and noisy image of the dog; what has been measured.

Our target CI example.

$$\mathbf{y} = \mathbf{H}\Psi\boldsymbol{\theta} + \mathbf{n}. \quad (2.1)$$

The goal of this chapter is to progressively understand what are the different mathematical variables represented in (2.1), and how it is possible to partially recover the clean image of the dog in Fig. 2.1(left).

2.1 Forward Sensing Model

The *Forward sensing model*, or *forward model* for short, is the core of the CI concept. It is a mathematical representation that describes how an object of interest is transformed into measurement data by an imaging system. The forward model encapsulates the physics and geometry of the imaging system, including the interactions between the imaging medium and the object being imaged.

Mathematically, any forward model can be written in the form

$$\mathbf{y} = \mathcal{P}(\mathcal{A}(\boldsymbol{\theta})) \quad (2.2)$$

where

- $\mathbf{y} \in \mathbb{R}^M$ is the *measurement vector*; containing the measurement data.

- \mathcal{P} is the *noise operator* discussed in Sec. 2.1.3; which incorporates random variability into the measurement vector.
- \mathcal{A} is the *forward operator*, discussed in Sec. 2.1.2; modeling all known physics of the acquisition system.
- $\theta \in \mathbb{R}^K$ are the *image parameters*, discussed in Sec. 2.1.1; encoding all the necessary information to describe the image of interest.

2.1.1 Image Representation

There are many ways to numerically encode and store visual information captured by imaging systems.

Pixel-based Representation

The simplest form of image representation is a grid of pixels, where each pixel value corresponds to the intensity or color at a specific location in the image. In this case, the image writes

$$\mathbf{x} \in \mathbb{R}^N$$

where N is the total number of pixels, and is a *vectorization* of the image, *i.e.*, concatenating all columns of the image into one long vector. This notation is also valid for *videos* (which are just sequences of images in time), *hyperspectral images* (which capture the same scene at different electromagnetic wavelengths), or any combination of space, time, and spectral information.

Fig. 2.2 provides a zoom in the center of the image to highlight its pixelation. For our image of the dog, there are 3 channels for the colors red, green, and blue (RGB), and each channel is 512×512 pixels wide. So the total number of pixels is $N = 786\,432$. $N = 786\,432$ is huge, and this is just for this low-resolution image. A pixel value is generally quantized in the range of 256 values, *i.e.*, $x_i \in \llbracket 256 \rrbracket$ for all pixels $i \in \llbracket N \rrbracket$. If we wanted to store the raw information of the pixels, this single image would require 12.5MB of memory. On a modern smartphone with 128GB of memory, this would only be enough for about 10 000 images (or, equivalently, a single 7min video), neglecting the memory size of applications, etc.

Transform-based Representation

Natural images are not random. There is usually some structure between the pixels, which are not all completely independent of each

2 | Preliminaries: Flavors of Computational Imaging

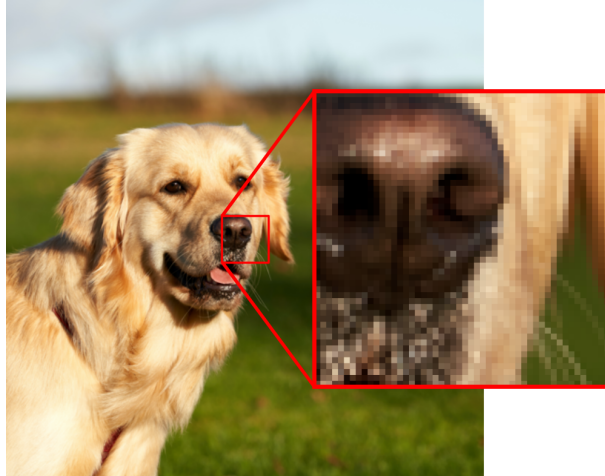


Fig. 2.2 Zoom in on the 50×50 centered square of the dog image.

other. This means that among all possible vectors $x \in \mathbb{R}^N$, natural images are contained in a much smaller domain $\mathcal{S} \subset \mathbb{R}^N$. This observation is the starting point for *image compression* techniques. The idea is always the same: try to find a transformation operator Ψ such that our image x can be represented in this transformed domain as

$$x = \Psi(\theta), \quad (2.3)$$

and there are few nonzero values in the vector of parameters θ . A model like (2.3) is called a *low-complexity model*. There is a mathematical way to count the number of nonzero values in a vector, called the ℓ_0 -pseudonorm¹, it is defined as

$$\|x\|_0 = |\{x_i, \text{ s.t. } x_i \neq 0\}|.$$

An image with nonzero coefficients K , or equivalently *s.t.* $\|x\|_0 \leq K$, is called *K-sparse*. Intuitively, storing only the positions and values of the nonzero coefficients in θ requires less memory than storing all pixel values. This is the foundational idea behind the most popular compression schemes such as *JPEG* [Wal92], *JPEG2000* [TM02], used in all our electronic devices.

The transform operator Ψ can take many forms, depending on what we know about the content of the image. In Fig. 2.3, we provide a simple example of the *second Daubechies wavelet* [Dau92] transform of our

¹This is a pseudonorm because, among the three properties required to be a norm: *non-negativity*, *absolute scalability*, and *triangle inequality*; this norm does not verify the absolute scalability, *i.e.*, $\|\theta u\|_0 = \|u\|_0 \neq \theta \|u\|_0$.

dog image. The image shown is the wavelet coefficients $\theta = \Psi^* x$ where $\Psi : \theta \in \mathbb{R}^N \mapsto x \in \mathbb{R}^N$ is the *Wavelet operator*, whose internal contents need not be explained. Here, Ψ provides a transform that does not change the number of pixels, and it is fully invertible (which is crucial for efficiently reconstructing the image from its wavelet coefficients), *i.e.*, we have access to the *inverse Wavelet operator* $\Psi^{-1} = \Psi^*$ defined so that $\Psi^* \Psi = \mathbf{I}$. In Fig. 2.3, the top left small image of the dog is called *approximation coefficients* and contains a downsampled version of the image. The other sub-images are called *detail coefficients*. They are mostly zero (in black) except for the sharp transitions that outline the dog. For a non-natural image filled with randomly selected pixels, there would not be so many nonzero values in the wavelet-transformed image. If only the nonzero (or negligible) coefficients of θ are stored in memory instead of the pixel values explained above, this example already represents a compression factor of 10. This simple example illustrates how compressible natural images are.

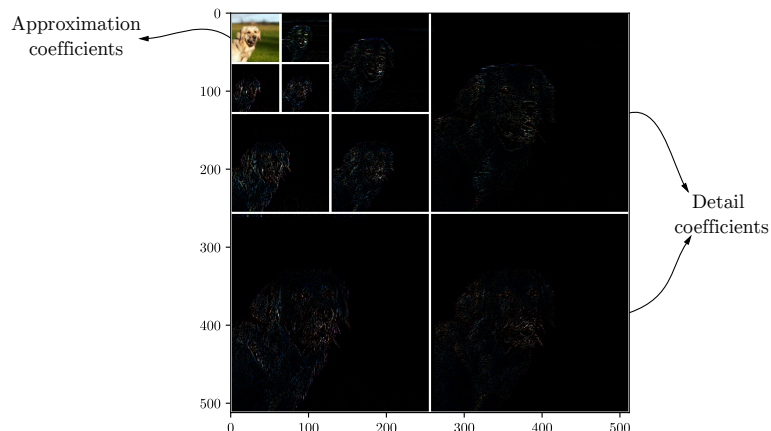


Fig. 2.3 3-level Wavelet transform of our dog image using the DB2 wavelet [Dau92].

Finding an efficient representation of the image is not only interesting for storage. It is also key to image recovery when solving a CI inverse problem. Indeed, finding a good image candidate in a reduced parameter space simplifies the recovery procedure. In that case, it is not strictly necessary to find an invertible sparsity operator, the only requirement is to find a transformation such that there are few nonzero coefficients in the transformed basis. In most work dealing with CI challenges, the sparsity basis remains simple. With the Wavelet (and its cousins), the most popular sparsity bases are

- Identity \mathbf{I} , where the image is directly considered sparse in the

2 | Preliminaries: Flavors of Computational Imaging

spatial domain, *i.e.*, $\|\mathbf{x}\|_0 \leq K$ for a sparsity level K .

- Gradient (or Finite Difference) ∇ , compatible with *piecewise constant images*, *i.e.*, images that have only a few transitions in the pixel representation.
- Fourier \mathbf{F} , assuming the image is exactly represented by a small linear combination of complex exponentials.
- Hadamard \mathbf{H} , similar in concept to the Fourier basis, but using Hadamard matrices instead of sine and cosine functions [Mos19]. Its entries are ± 1 .

Finally, the Singular Value Decomposition (SVD) is also popular to get a sparse representation of a 2-D image which, in matrix form $\mathbf{X} \in \mathbb{R}^{N_x \times N_y}$, can be decomposed into singular values as $\mathbf{X} = \mathbf{U} \text{diag}(\mathbf{s}) \mathbf{V}^*$. If $\|\mathbf{s}\|_0 \leq r$, the 2-D image \mathbf{X} is said to be *low-rank*, with rank- r .

Chap. 3-4 will analyze the reconstruction of sparse and piecewise constant images. With this section, we understood our first two elements in Example (2.1): the discrete image is encoded in a Wavelet sparsity basis as $\mathbf{x} = \Psi \boldsymbol{\theta}$.

Neural Representation

More recently emerged the idea of using deep learning techniques to represent image content.

Discrete: The first architecture that emerged is the *Auto-encoder* [HS06], illustrated in Fig. 2.4, which is a fully-connected neural network architecture whose number of parameters progressively decreases in the first half part called *encoder*, and then increases back up to its original size in the second half part called *decoder*.

The encoder can be mathematically defined as

$$\boldsymbol{\theta} = E(\mathbf{x}) := \mathbf{W}_{L/2} (\sigma_{L-1} \circ \dots \circ \sigma_0)(\mathbf{x}) + \mathbf{b}_{L/2}, \quad (2.4)$$

and the decoder as

$$\tilde{\mathbf{x}} = D(\boldsymbol{\theta}) := \mathbf{W}_L (\sigma_{L-1} \circ \dots \circ \sigma_{L/2-1})(\boldsymbol{\theta}) + \mathbf{b}_L, \quad (2.5)$$

where, for a typical autoencoder with Rectified Linear Unit (ReLU) activations [Vin+10], we have that the hidden features at layer l write

$$\sigma_l(\boldsymbol{\theta}) := \max(\mathbf{0}, \mathbf{W}_l \boldsymbol{\theta} + \mathbf{b}_l),$$

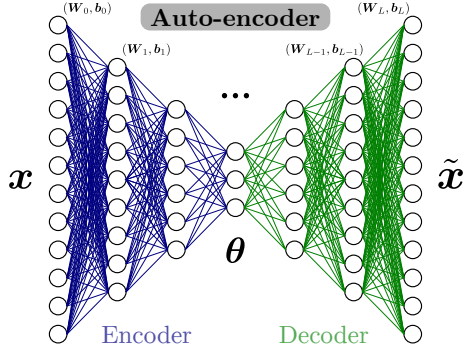


Fig. 2.4 Architecture of an autoencoder. The original image x is input at the first layer, and the encoder compresses its information down to the parameters θ . The decoder tries to invert the effect of the encoder by uncompressing θ up to an output \tilde{x} aimed to resemble x .

for any input vector θ of appropriate size, a weight matrix W_l , and a bias vector b_l . An autoencoder is specifically trained to minimize the error between the input x and the output \tilde{x} images. The parameters of the autoencoder are thus computed to minimize the expected error over natural images as

$$\min_{\{W_l, b_l\}_{l=1}^L} \mathbb{E}_{x \in \mathcal{S}} \|x - \tilde{x}\|_2^2.$$

The compressed image representation is the output of the encoder: θ . There exists tons of other deep architectures with the same goal. To name a few: convolutional and recurrent neural networks, generative adversarial networks [MSS22], and transformers [Vas+17]. These considerations are not covered in this thesis.

Continuous: A common feature of the upper cited deep architectures is that they provide a discrete representation of the image. The only way to numerically encode a continuous representation of an image is to view it as a composition of continuous functions with a known analytical expression. For instance, a continuous image that is sparse in the Fourier domain can be modeled as a finite sum of complex exponentials such as

$$x(r) = \sum_{k=1}^Q \theta_k e^{i2\pi p_k^\top r}, \quad (2.6)$$

where $r \in \mathbb{R}^2$ are the 2-D coordinates in the continuous image space. The *Implicit Neural Representations* (INR) recently emerged [Mil+20] as

2 | Preliminaries: Flavors of Computational Imaging

a nonlinear way to learn a continuous representation of the image, *i.e.*, the image is approximated as $x(r) \approx x_\phi(r)$ where ϕ are the weights of the deep architecture. INR are considered in this thesis. More details can be found in Chap. 6.

2.1.2 Forward Operator

In the general definition of (2.2), the “forward operator” includes everything contained in \mathcal{A} . In a noiseless scenario, it encapsulates the mathematical and physical processes by which an object of interest is transformed into measurable data, *i.e.*, the noiseless data can be written as

$$\bar{y} = \mathcal{A}(\theta). \quad (2.7)$$

The operator $\mathcal{A} : \theta \in \mathbb{R}^K \mapsto \bar{y} \in \mathbb{R}^M$ serves as a comprehensive model that describes how the imaging system interacts with the object, translating its intrinsic properties such as shape, density, or refractive index into observable quantities like intensity or phase. As clear from the notation $\mathcal{A}(\theta)$, the forward operator integrates the *image representation* discussed in Sec. 2.1.1. Even though the image is parameterized by the vector θ , the notations in (2.7) show that this parameterization allows to describe the image continuously, *e.g.*, with a continuous representation such as (2.6). This will be the case for Chap. 3-4, whose sensing models will describe a mapping from the continuous image to a single-pixel measurement (see Sec. 3.2 and 4.3.3).

In the model (2.7), the number of measurements M is typically larger than the number of parameters K to ensure image recovery, but can ultimately be much smaller than the resolution N of a discrete image. When an imaging modality first computes a discrete image $x \in \mathbb{R}^N$ and then its representation in a smaller number of parameters $\theta \in \mathbb{R}^K$ where $K \ll N$, we speak of *image compression*. If the imaging modality is designed to obtain the compressed representation directly, we talk about *compressive imaging* [AH21]. The idea of compressive imaging is at the core of Chap. 3-4, where Chap. 3 imposes a compressive imaging framework due to the physics of acquisition in multi-core fiber lensless imaging, and Chap. 4 proposes a compressive imaging technique to overcome some tremendously large data acquisition and processing in the context of radio-interferometry, and at a small drop in image reconstruction quality.

If the mapping is linear, \mathcal{A} can be written in matrix form $A \in \mathbb{R}^{M \times K}$

s.t.

$$\bar{y} = A\theta. \quad (2.8)$$

Most well-studied CI problems are written as the linear sensor model (2.8). It ranges from basic image restoration tasks like deblurring, super-resolution, and image inpainting [GW07], to a wide variety of tomographic imaging applications, including common types of magnetic resonance imaging [Fes10], X-ray computed tomography [EF02], radar imaging [Bla04], among others [BM13].

Let us return to our example of a dog image x . In Fig. 2.5, we show two examples of a linear forward model A applied to the discrete image x . Fig. 2.5(left) is an example of an *inpainting* problem where the pixels in the center of the image have been lost. Mathematically, the forward model writes as simply as

$$\bar{y} = \mathbf{I}_\Omega x,$$

where \mathbf{I}_Ω subselects the rows of the identity matrix \mathbf{I} into Ω , where Ω is the set of seen pixel positions. Fig. 2.5(center) depicts a blur of the dog image obtained from the discrete convolution²

$$\bar{y} = h * x = Hx, \quad (2.9)$$

where h is the Gaussian kernel shown in Fig. 2.5(right), and H is the circulant matrix that performs the discrete convolution. Eq. (2.9) revealed a second element of the Example 2.1 provided at the beginning of this section: H is the *forward operator* describing a discrete convolution with a Gaussian kernel.

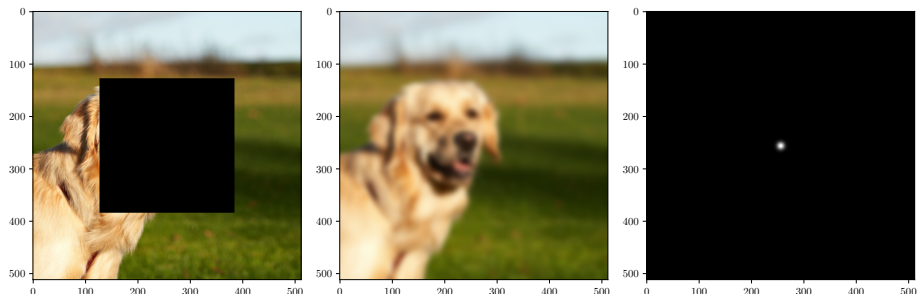


Fig. 2.5 Two transformations of the dog image using a linear forward operator. (left) masking the center of the image. (middle) blurred dog image. (right) Gaussian blur used to obtain (center) from x .

² $\bar{y}_n = \sum_{n'=1}^N h_{n'} x_{n-n'}$, with $n \in \llbracket N \rrbracket$. $n - n'$ is maintained in $\llbracket N \rrbracket$ with a modulo operation.

2 | Preliminaries: Flavors of Computational Imaging

Chap. 3-4 will both study a linear forward model of the form $\bar{y} = Ax$. In particular, the forward operator will be decomposed as

$$A = RGF,$$

where:

- R is a special case of a random projection matrix, which allows for compressive imaging.
- GF provides a *partial Fourier sampling* of the discrete image x . This relates to a rich literature that studies the question of image recovery from GF only [AGH14; AGR19; CRT06]. Worth mentionning, both chapters consider a special case of partial Fourier sampling called *interferometry*, whose most accurate mathematical representation is in a symmetric—or *bilateral*—form (see Sec. 3.2.4 for more details).

Chap. 5-6 examines a more complicated nonlinear forward model, which is difficult to formalize in the notations of this chapter.

2.1.3 Noise

In the general definition of (2.2), “noise” includes everything contained in \mathcal{P} . The noise refers to any unwanted random variation in the measurement data that obscures or distorts the noiseless information \bar{y} . It can be introduced at various stages of image acquisition, processing, and transmission. Noise can originate from several sources, including sensor imperfections, environmental conditions, electronic interference, and quantization errors during analog-to-digital conversion. Since noise is by definition unknown and random, it degrades the quality of image reconstruction. There are many challenges in designing and engineering imaging systems that aim to minimize the noise [GW07].

There are many different types of noise [BJ]. To name a few, there are

- *Additive White Gaussian Noise* (AWGN): the most common type of noise. Its sources can be *thermal noise*, caused by the random motion of electrons in conductors, resulting in a Gaussian distribution of noise.

- *Shot noise* or *Poisson noise*: caused by the discrete nature of electric charge and the random arrival times of carriers (such as electrons or photons) at a junction, or *amplification noise*.
- *Salt and Pepper noise*: characterized as non-physical extreme pixel values and generally caused by digital image transmission errors from defective sensor cells.
- *Quantization noise*: these are rounding errors resulting from analog-to-digital conversions.

In this thesis, we only consider AWGN in Chap. 3-4. The AWGN is easier to analyze theoretically because its statistics does not depend on the signal of interest and is simple with a normal distribution. In the case of AWGN measurements, the measurement vector writes

$$\mathbf{y} = \bar{\mathbf{y}} + \mathbf{n}, \quad (2.10)$$

where \mathbf{n} is the AWGN vector with random distribution

$$\mathbf{n} \underset{\text{i.i.d.}}{\sim} \mathcal{CN}(\mathbf{0}, \sigma^2 \mathbf{I}).$$

Eq. (2.10) ellucidates the last term of the starting Example 2.1 $\mathbf{y} = \mathbf{H}\Psi\theta + \mathbf{n}$. The measured image \mathbf{y} in Fig. 2.1(right) is a noisy version of the blurred image of the dog $\bar{\mathbf{y}} = \mathbf{H}\Psi\theta$ in Fig. 2.5(center).

2.2 Inverse Problem

The *inverse problem* refers to the process of inferring the image parameters from the vector of observations. It consists of finding a way to produce an estimate $\tilde{\theta} \leftarrow \mathbf{y} = \mathcal{P}(\mathcal{A}(\theta))$. The idea is to reconstruct an image from indirect, incomplete, and noisy measurements. This is a fundamental challenge in many areas of science and engineering.

From this section on, if the type of norm is not specified (e.g., $\|x\|$), it means that the discussion is valid for any norm.

2.2.1 Ill-posedness

Inverse problems are typically *ill-posed*, that is, they do not satisfy one or more of the conditions required by the Hadamard definition of well-posed problems [Isa06, Sec. 2.1]: (i) a solution exists, (ii) the solution is unique, and (iii) the solution depends continuously on the data. This leads to challenges such as:

2 | Preliminaries: Flavors of Computational Imaging

- Non-Uniqueness: There may be multiple solutions that satisfy the given observations.
- Instability/Noise Sensitivity: Observations are often contaminated with noise, making the inverse problem more difficult. Small changes in the observations can lead to large changes in the solution.

There are very few theoretical results about the ill-posedness of nonlinear sensing models (except for special cases like *phase retrieval* [CSV13; She+14] or *one-bit compressive sensing* [Jac+13; TJ23]), let us particularize the discussion to linear sensing models with AWGN, as defined in (2.11).

Linear model with AWGN

$$\mathbf{y} = \mathbf{A}\mathbf{x} + \mathbf{n}. \quad (2.11)$$

\mathbf{A} is usually non-invertible because there are less measurements than unknowns. This causes the non-uniqueness of the solutions. For instance, it is clear from Fig. 2.5(left) that the central square of the dog image \mathbf{x} could be replaced by any other set of pixel values and yield the same observed masked image.

From the model (2.11), even in the rare situations where an inverse \mathbf{A}^{-1} of the forward operator exists, applying this inverse directly to the measurement vector yields

$$\tilde{\mathbf{x}} = \mathbf{A}^{-1}\mathbf{y} = \mathbf{x} + \mathbf{A}^{-1}\mathbf{n}, \quad (2.12)$$

where small eigenvalues³ of the forward operator \mathbf{A} imply that $\mathbf{A}^{-1}\mathbf{n}$ explodes the noise and causes huge instabilities in the reconstruction. This explosion also occurs when we consider a generalized inverse (e.g., pseudo inverse) to treat the non-existence and non-uniqueness problems. These issues are compounded by the continuous nature of real-world images, which are thus modeled more faithfully in *infinite-dimensional* function spaces than in any finite-dimensional model [AH16]. The *non-uniqueness* of the solution and the *instabilities*

³The vector \mathbf{v} and the value λ are the eigenvector and associated eigenvalue of a linear operator \mathbf{A} if they satisfy $\mathbf{A}\mathbf{v} = \lambda\mathbf{v}$. In words, the vector \mathbf{v} has its direction unchanged by the linear transformation using \mathbf{A} , and λ informs on the length ratio of \mathbf{v} before and after transformation by \mathbf{A} .

caused by the noise have motivated the inverse problem research community to develop techniques that *regularize* the inverse problem. The concept of regularization is introduced in Sec. 2.2.2.

2.2.2 Loss Function

Solving an inverse problem means minimizing a loss function \mathcal{L} . For the linear sensor model (2.11), the simplest minimization problem writes

$$\tilde{\mathbf{x}} = \arg \min_{\mathbf{u}} \mathcal{L}(\mathbf{y}, \mathbf{u}), \quad \mathcal{L}(\mathbf{y}, \mathbf{u}) := \frac{1}{2} \|\mathbf{y} - A\mathbf{u}\|_2^2. \quad (2.13)$$

The solution of (2.13) if A is full-rank, easily obtained by differentiating \mathcal{L} with respect to \mathbf{u} , is given by

$$\tilde{\mathbf{x}} = (A^* A)^{-1} A^* \mathbf{y}, \quad (2.14)$$

and is known as the *pseudo-inverse* solution. The adjoint operator A^* is formally defined in Def. 2.2.1.

Definition 2.2.1. The adjoint A^* of an operator $\mathcal{A} := \mathbf{u} \in \mathcal{U} \mapsto \mathcal{A}\mathbf{u} \in \mathcal{V}$ for an input domain \mathcal{U} and operator domain \mathcal{V} is defined by the following identity

$$\langle \mathcal{A}\mathbf{u}, \mathbf{v} \rangle_{\mathcal{V}} = \langle \mathbf{u}, \mathcal{A}^* \mathbf{v} \rangle_{\mathcal{U}}, \quad (2.15)$$

for any $\mathbf{v} \in \mathcal{V}$.

If A is not full-rank, the pseudo-inverse is given by

$$\tilde{\mathbf{x}} = A^* (A A^*)^{-1} \mathbf{y} \quad (2.16)$$

which, among the infinite set of solutions in this case, corresponds to the solution of (2.13) of minimal ℓ_2 -norm, *i.e.*,

$$\tilde{\mathbf{x}} = \arg \min_{\mathbf{u}} \|\mathbf{u}\|_2 \text{ s.t. } A\mathbf{u} = \mathbf{y}. \quad (2.17)$$

If A^{-1} exists, the pseudo-inverse solution in (2.14) particularizes to $\tilde{\mathbf{x}} = A^{-1} \mathbf{y}$, thus recovering (2.12). The loss function \mathcal{L} defined in (2.13) is called *data-fidelity* because it computes the squared ℓ_2 distance between the measurement data \mathbf{y} and the candidate measurements $A\mathbf{u}$ obtained from the forward operator model. Depending on the properties of A and on the noise distribution, the data-fidelity can sometimes be defined with other norms, such as the ℓ_1 -norm. The ℓ_1 -norm usually arises in the case of intensity measurements and will be used in particular in Chap. 3-4.

2 | Preliminaries: Flavors of Computational Imaging

Regularization

Due to the ill-posedness of most inverse problems, discussed in Sec. 2.2.1, the loss function is generally modified by adding a *regularization term* $\mathcal{R}(\mathbf{u})$ as written in (2.18).

Regularized loss function

$$\mathcal{L}(\mathbf{y}, \mathbf{u}) := \underbrace{\frac{1}{2} \|\mathbf{y} - \mathbf{A}\mathbf{u}\|^2}_{\text{Data-Fidelity}} + \underbrace{\mathcal{R}(\mathbf{u})}_{\text{Regularization}}. \quad (2.18)$$

Note that the type of norm in the data-fidelity term of (2.18) was intentionally left unspecified in order to remain valid for multiple choices. The goal of the *regularization term* is to promote solutions \mathbf{u} that minimize both the data-fidelity term and the regularization term. The design of the function \mathcal{R} typically requires some *a priori* knowledge of the domain $\mathcal{S} \subset \mathbb{R}^N$ to which the true image \mathbf{x} belongs.

One of the most popular examples of regularization term is $\mathcal{R}(\mathbf{u}) = \|\mathbf{u}\|_0$, which promotes sparse solutions [FSY10], *i.e.*, images \mathbf{u} with only a few nonzero coefficients, as discussed in Sec. 2.1.1. As will become clear in Sec. 2.3, the ℓ_0 -«norm» is generally replaced by convex surrogates such as the ℓ_1 -norm⁴. Sparsity can also be promoted in a transformed domain as $\mathcal{R}(\mathbf{u}) = \|\Psi^*\mathbf{u}\|_0$, where Ψ^* is the adjoint transformation operator (also discussed in Sec. 2.1.1). Other known regularization functions are: the ℓ_2 -norm⁵, which promotes solutions with bounded coefficients and smoother than the ℓ_1 -norm, the *nuclear norm* $\|\cdot\|_*$ promoting low-rank 2-D images, the *Total-Variation* (TV) norm $\|\cdot\|_{\text{TV}}$ promoting piecewise-constant images.

In addition to all declinations of norms, the regularization term can also model a strict *constraint* for the solution to belong to a set. For example, the *non-negativity constraint* is imposed in Chap. 6 with the regularization term

$$\mathcal{R}(\mathbf{u}) = \iota_{\mathbb{R}^+}(\mathbf{u}), \quad (2.19)$$

⁴The *uSARA* algorithm used in Chap. 4 considers another convex surrogate described in (4.47).

⁵The use of the ℓ_2 -norm for regularization is known as *Tikhonov regularization* [Tik43].

where $\iota_{\mathbb{R}^+}(\mathbf{u})$ is the *indicator function* applied componentwise as

$$\iota_{\mathbb{R}^+}(u_i) = \begin{cases} 0, & \text{if } u_i \geq 0, \\ +\infty, & \text{otherwise.} \end{cases} \quad (2.20)$$

Naturally, the considered \mathcal{R} can be any linear combination of the upper mentioned regularization terms.

Remark 2.1. The regularized loss function defined in (2.18) also finds a nice statistical interpretation. Indeed, the minimization estimate can be seen as a Maximum A Posteriori (MAP) estimator, i.e., the estimate is computed as

$$\begin{aligned} \tilde{\mathbf{x}} &= \arg \max_{\mathbf{u}} \log p(\mathbf{u}|\mathbf{y}) \\ &= \arg \min_{\mathbf{u}} -\log p(\mathbf{y}|\mathbf{u}) - \log p(\mathbf{u}) \\ &= \arg \min_{\mathbf{u}} \frac{1}{2} \|\mathbf{y} - \mathbf{A}\mathbf{u}\|^2 + \mathcal{R}(\mathbf{u}). \end{aligned} \quad (2.21)$$

In (2.21), the Bayes law^a was used to jump from the first to the second line. By identification between the second and third lines in (2.21), it is seen that the data-fidelity term can be related to the posterior distribution as

$$p(\mathbf{y}|\mathbf{u}) = e^{-\frac{1}{2}\|\mathbf{y}-\mathbf{A}\mathbf{u}\|^2},$$

and the regularization term can be related to the prior distribution as

$$p(\mathbf{u}) = e^{-\mathcal{R}(\mathbf{u})}.$$

^a $p(\mathbf{x}|\mathbf{y})p(\mathbf{y}) = p(\mathbf{y}|\mathbf{x})p(\mathbf{x})$.

All the minimization problems considered in this thesis are contained within the framework stated in (2.18). Namely, in Chap. 3-4, we analyze for specific forward sensing models the *LASSO* and *Basis Pursuit DeNoise* (BPDN $_{\ell_2}$) programs [VF08] numerically, and the BPDN $_{\ell_1}$ program theoretically.

LASSO

$$\tilde{\mathbf{x}} = \arg \min_{\mathbf{u}} \frac{1}{2} \|\mathbf{y} - \mathbf{A}\mathbf{u}\|_2^2 \text{ s.t. } \|\mathbf{u}\|_1 \leq \tau, \quad (\text{Lasso})$$

for a sparsity parameter $\tau \geq 0$.

2 | Preliminaries: Flavors of Computational Imaging

BPDN $_{\ell_p}$

$$\tilde{\mathbf{x}} = \arg \min_{\mathbf{u}} \|\mathbf{u}\|_1 \text{ s.t. } \|\mathbf{y} - \mathbf{A}\mathbf{u}\|_p^2 \leq \sigma, \quad (\text{BPDN}_{\ell_p})$$

with $p \in \{1, 2\}$ and an additive noise level $\sigma \geq 0$.

The regularization terms associated to (Lasso) and (BPDN $_{\ell_p}$) are respectively $\iota_{\|\cdot\|_1 \leq \tau}$ and $\iota_{\|\mathbf{y} - \mathbf{A}\cdot\|_p^2 \leq \sigma}$.

Optimization Viewpoint

Returning to the definition (2.18) of a regularized loss function, the theoretical characterization of the underlying minimization problem belongs to the field of *First-Order Optimization* [Bec17a]. Depending on the forward sensing model and the regularization term, the loss function \mathcal{L} may or may not be *convex*⁶. In general, \mathcal{R} is a closed proper convex function, but not necessarily *differentiable*, meaning that its gradient does not exist everywhere. We discuss in Sec. 2.3 how to minimize a non-differentiable regularization term. If the loss function is *nonconvex*, this means that \mathcal{L} may have one or more local minima, and optimization algorithms are likely to get stuck in one of these local minima. Chap. 6 studies an inverse problem that is nonconvex. However, a deeper analysis of nonconvex inverse problems is difficult and out of the scope of this thesis.

Fig. 2.6 illustrates 1-D equivalents of common inverse problems. In Fig. 2.6(a), we observe the equivalent of an ℓ_2 (squared value) data-fidelity term, accompanied with the equivalent of an ℓ_1 (absolute value) regularization term. It can be seen that the data-fidelity term $\frac{1}{2}(y - 5u)^2$ is convex and differentiable, but the regularization term $4|x'|$ is convex but non-differentiable at the origin. Fig. 2.6(b) shows the 1-D equivalent of a *phase retrieval* problem, where the observation model is $y = |1.5x|^2 + n$. It can be seen that the measurement in intensity makes the data-fidelity term *nonconvex*, with two local minima. The regularization term makes the total loss function convex, but with global minimum 0, which is proper to the 1-D case.

⁶Simply stated, a *strictly* convex function has at most one global minimizer and no local ones. A sufficient condition for existence is the semi-continuity and coercivity of the function.

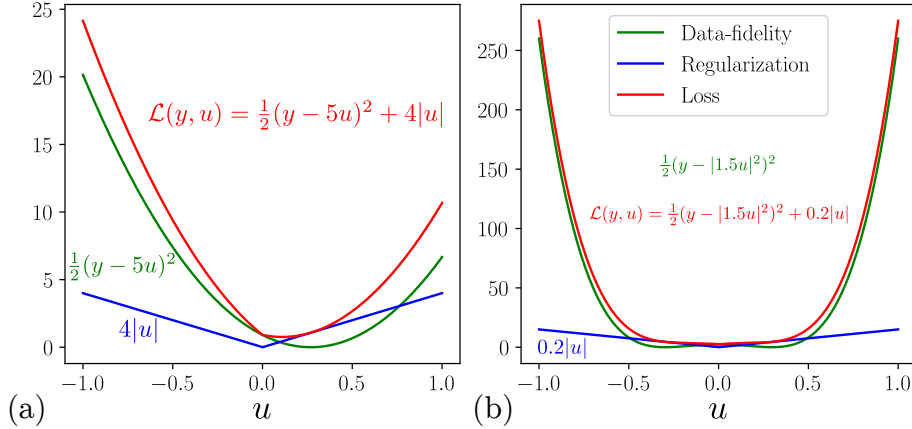


Fig. 2.6 1-D examples of loss functions. (a) A linear sensing model with ℓ_1 -norm penalty. (b) An intensity sensing with ℓ_1 -norm penalty. For both (a-b), the observation y was obtained with the ground truth value $x = 0.3$.

This section has emphasized that solving an inverse problem implies solving a minimization problem, and this requires the use of optimization methods. In Sec. 2.3 we discuss the known algorithms used to solve these minimization problems. We have not discussed the relative weight that must be set between the data-fidelity term and the regularization term. This weight is usually chosen heuristically, based on qualitative metrics, and this is also what is done in this thesis. Still, we propose a heuristic way to iteratively adapt this weighting in Appendix 2.6.1.

2.3 Recovery Algorithm

Choosing the loss function to be minimized in order to solve the inverse problem is not the end of the story. Next, a procedure must be established to effectively compute a minimizer of that loss function. This procedure is called a *recovery algorithm*. Recovery algorithms have been extensively studied in optimization, and new ones are published frequently.

2.3.1 Gradient and Proximal Operator

Naturally, for realistic inverse problems, it is not affordable to evaluate the loss function on a fine grid of search space locations as in Fig. 2.6, first because applying the forward operator generally has a non-negligible computational cost, and second because if one envisioned a grid-search strategy with N points per dimension in a D -

2 | Preliminaries: Flavors of Computational Imaging

dimensional search space, it would require N^D points on which to evaluate the loss function, which is totally unattainable. Instead, all optimization algorithms are built on the same principle; they start with an *initial guess* $\mathbf{x}^{(0)}$, and iteratively update the *candidate minimizer* with a local evaluation of the loss function $\mathcal{L}(\mathbf{y}, \mathbf{x}^{(k)})$ and its derivatives ($\nabla_{\mathbf{u}}\mathcal{L}$, $\nabla_{\mathbf{u}}^2\mathcal{L}, \dots$) evaluated on the current k -th candidate. In this thesis, for the simplicity of the theoretical analysis, we only consider *First-Order Optimization* methods [Bec17a], *i.e.*, methods that require only the evaluation of the loss \mathcal{L} and its gradient $\nabla_{\mathbf{u}}\mathcal{L}$.

An ℓ_2 data-fidelity term of the form $\frac{1}{2}\|\mathbf{y} - \mathcal{A}(\mathbf{u})\|_2^2$ has as a simple gradient $\mathcal{A}^*(\mathcal{A}(\mathbf{u}) - \mathbf{y})$, where \mathcal{A}^* is the adjoint operator (see Def. 2.2.1). However, since some terms in \mathcal{L} may be non-differentiable, this means that their gradient does not exist. The conventional workaround is to use the gradient of a convex surrogate of these non-differentiable functions, called the *proximal operator* (*a.k.a.* prox), defined in Def. 2.3.1.

Definition 2.3.1 (Proximal operator). *The proximal operator of a function $g : \mathbf{u} \in \mathbb{R}^N \mapsto g(\mathbf{u}) \in \mathbb{R}$ is defined as*

$$\text{prox}_g(\mathbf{u}) := \arg \min_{\mathbf{u}'} g(\mathbf{u}') + \frac{1}{2}\|\mathbf{u} - \mathbf{u}'\|_2^2. \quad (\text{prox})$$

It can be shown that the *Moreau envelope* $\min_{\mathbf{u}'} g(\mathbf{u}') + \frac{1}{2}\|\mathbf{u} - \mathbf{u}'\|_2^2$ is a smoothed form of the function g , so it is always convex, and has the same minima. The use of proximal operators in recovery algorithms is a large topic, known in the literature as *proximal algorithms*. [PB14]. In this thesis, we will essentially use two proximal operators: (*i*) the prox of the ℓ_1 -norm, named *Soft-thresholding* and defined in (2.22), and (*ii*) the prox of the indicator function $\iota_{\mathcal{S}}$ for a convex set \mathcal{S} , named *Projection* and defined in (2.24).

Soft-thresholding

$$\text{prox}_{\lambda\|\cdot\|_1}(\mathbf{u}) := \mathcal{T}_\lambda(\mathbf{u}), \quad (2.22)$$

with the soft-thresholding operation applied on each component u_i of \mathbf{u} as

$$\mathcal{T}_\lambda(u_i) = \begin{cases} u_i + \lambda, & \text{if } u_i < -\lambda \\ 0, & \text{if } |u_i| \leq \lambda \\ u_i - \lambda, & \text{if } u_i > \lambda \end{cases}. \quad (2.23)$$

Projection

$$\text{prox}_{\ell_S}(\mathbf{u}) := \Pi_S(\mathbf{u}) := \arg \min_{\mathbf{u}' \in S} \frac{1}{2} \|\mathbf{u} - \mathbf{u}'\|_2. \quad (2.24)$$

The explanations given above are also valid for nonlinear sensing models, where we compute the local gradient of the loss function around the current estimate. The local gradient of a nonlinear sensing model is in particular what is implicitly computed by automatic differentiation in Chap. 6. In Sec. 2.3.2 we review some popular optimization algorithms used in this thesis for image reconstruction.

2.3.2 Popular Algorithms

In order to minimize the regularized loss function (2.18) particularized to an ℓ_2 -norm data-fidelity term, *i.e.*,

$$\mathcal{L}(\mathbf{y}, \mathbf{u}) := \underbrace{\frac{1}{2} \|\mathbf{y} - A\mathbf{u}\|_2^2}_{\ell_2 \text{ Data-Fidelity}} + \underbrace{\mathcal{R}(\mathbf{u})}_{\text{Regularization}}, \quad (2.25)$$

the most popular optimization algorithm is the Proximal Gradient Method (PGM) [Bec17b; PB14; CP11b] (*a.k.a.* Forward-Backward) given in Algo. 2.1.

Algorithm 2.1 Proximal Gradient Method

Require: $\mathbf{y}, A, \mathbf{x}^{(0)}$

- 1: $k = 0$
 - 2: **while** $k < K$ **do**
 - 3: $\mathbf{y}^{(k+1)} = \mathbf{x}^{(k)} - \alpha^{(k)} A^*(A\mathbf{x}^{(k)} - \mathbf{y})$ \triangleright Gradient descent step
 - 4: $\mathbf{x}^{(k+1)} = \text{prox}_{\mathcal{R}}(\mathbf{y}^{(k+1)})$ \triangleright Proximal step
 - 5: $k += 1$
 - 6: $\tilde{\mathbf{x}} = \mathbf{x}^{(K)}$
-

In Algo. 2.1, we voluntarily did not specify the usual stopping criteria used in practice, like absolute or relative tolerances, but only a fixed number of iterations. As its name suggests, the PGM simply alternates between

- a **gradient descent step**: an update in the direction of the negative gradient of the data-fidelity term ℓ_2 , where $\alpha^{(k)}$ is the step-size, which may vary over the iterations. If the stepsize is kept

2 | Preliminaries: Flavors of Computational Imaging

constant, it is known that the condition for convergence is that $\alpha < 2/\|A\|^2$ [PB14]. We derive this condition again (only for the simpler case of gradient descent) in Sec. 5.4.1.

- a **proximal step**: an update applying the proximal operator of the regularization term \mathcal{R} . This term can include a factor λ balancing the two terms.

The PGM simplifies to the classical *Gradient Descent* method when there is no regularization term. An extension called *Generalized Forward-Backward* [RFP13] exists when the regularization term is given as a sum of terms (e.g., $\|\cdot\|_{\text{TV}}$ and $\iota_{\mathbb{R}^+}$). Furthermore, we highlight that the *Lasso* and BPDN_{ℓ_2} minimization problems are both solved by the PGM. Thus, it has been shown [VF08] that there exists a bijection between the two problems for the appropriate pair of parameters (τ, σ) . In Chap. 3-4 we use the *SPGL1*⁷ [VF08] for solving Lasso and BPDN_{ℓ_2} . We stress that *Iterative Shrinkage-Thresholding Algorithm* (ISTA) [DDD04; BT09] is a particular case of the PGM. However, the *Iterative Hard Thresholding* (IHT) [BD08; FS18] solves a nonconvex minimization problem, regardless of its resemblance to the PGM.

Worth mentioning are the *Plug-and-Play* methods [VBW13; KMW18; Ter+23], which consist in replacing the proximal operator in the PGM by a *deep denoiser*. Extensions of the concept of integrating deep architectures into the regularization part of optimization algorithms exist such as *Deep Equilibrium* [BKK19; GOW21]. The *uSARA* and *AIRI* state-of-the-art image recovery algorithms used for radio-interferometry in Chap. 4 are both variants of the PGM, with AIRI being more precisely a Plug-and-Play method.

Coming back to our example of a dog image x , we show in Fig. 2.7(c) the reconstructed image $\tilde{x} = \Psi\tilde{\theta}$ obtained by applying 500 iterations of the PGM to the following minimization problem:

$$\tilde{\theta} = \arg \min_u \frac{1}{2} \|y - H\Psi u\|_2^2 + 5 \cdot 10^{-3} \|u\|_1.$$

It is observed that even with an old image recovery method using a simple wavelet decomposition of the dog image and a few iterations of the PGM, the quality of the reconstructed image improves over the observed blurred and noisy image. Fig. 2.7 concludes our example of dog image recovery started at the beginning of this chapter.

⁷Python toolbox: <https://github.com/drrelyea/spgl1>.

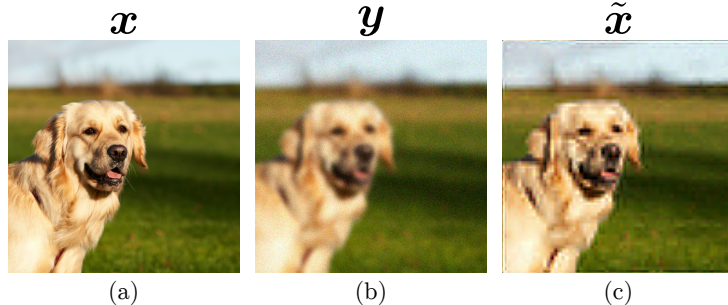


Fig. 2.7 Reconstruction of the dog image applying the PGM with $\mathcal{R}(\mathbf{u}) = \|\Psi^*\mathbf{u}\|_1$.
 (a) Ground truth image x . (b) Observed image y (SNR= 18.6dB). (c) Reconstruction \tilde{x} (SNR= 20.8dB).

In Chap. 4 we use a type of *greedy* algorithm called the *Matching Pursuit* algorithm [MZ93; Hög74]. See Sec. 4.4.1 for more details. There exist other popular proximal algorithms like *Douglas-Rachford* or *Alternating Direction Method of Multipliers* (ADMM) [PB14], unused in this thesis, that use only proximal operators even for the differentiable terms of the loss function. The last two optimization algorithms we mention are the *Stochastic Gradient Descent* (SGD) and *Adam* [KB14] algorithms, which are specifically designed for the optimization of neural network architectures and are used in Chap. 6.

There are tons of other optimization algorithms, and this section was just a brief overview of the ones used in this thesis.

2.3.3 Reconstruction Quality Metrics

For the sake of harmonization, the only quantitative metric used in this thesis to measure the quality of image reconstruction is the *Signal-to-Noise Ratio* (SNR), defined in Def. 2.3.2. We mention the existence of *Mean Square Error*, *Peak Signal-to-Noise Ratio*, *Mean Absolute Error*, and *Structural Similarity Index Metric*, among others [Wan+04].

Definition 2.3.2. *The Signal-to-noise ratio (in dB), which compares the energy contained in a ground truth signal \mathbf{u} to the error $\mathbf{u} - \tilde{\mathbf{u}}$ made by its approximation $\tilde{\mathbf{u}}$, is defined as*

$$\text{SNR}(\mathbf{u}, \tilde{\mathbf{u}}) = 20 \log_{10}(\|\mathbf{u}\|_2 / \|\mathbf{u} - \tilde{\mathbf{u}}\|_2). \quad (2.26)$$

2 | Preliminaries: Flavors of Computational Imaging

2.3.4 Momentum Acceleration

Some iterative algorithms can be accelerated using a certain history of the previous iterates to reach a convergence rate in $\mathcal{O}(1/k^2)$ instead of $\mathcal{O}(1/k)$ without acceleration where k is the number of iterations. An example of accelerating the PGM using momentum is given in Algo. 2.2.

Algorithm 2.2 Accelerated Proximal Gradient Method

Require: $y, A, x^{(0)} = z^{(0)}, t_0 = 1, 0 < \alpha < 1/\|A\|^2$

- 1: $k = 0$
- 2: **while** $k < K$ **do**
- 3: $y^{(k+1)} = z^{(k)} - \alpha A^*(Az^{(k)} - y)$ \triangleright Gradient descent step
- 4: $x^{(k+1)} = \text{prox}_{\mathcal{R}}(y^{(k+1)})$ \triangleright Proximal step
- 5: $t_{k+1} = \frac{1 + \sqrt{1 + 4t_k^2}}{2}$ \triangleright Momentum update
- 6: $z^{(k+1)} = x^{(k+1)} + \left(\frac{t_k - 1}{t_{k+1}}\right)(x^{(k+1)} - x^{(k)})$ \triangleright Apply momentum
- 7: $k += 1$
- 8: $\tilde{x} = x^{(K)}$

The momentum accelerated proximal gradient method is commonly known under the name *FISTA*⁸ [BT09]. This idea of considering a momentum to improve the convergence rate of optimization algorithms is attributed to Nesterov [Nes83]. This momentum acceleration trick is used in Chap. 5-6 for solving a linear system of equations.

Now that we have reviewed all the optimization algorithms used in this thesis, we will jump to what recovery guarantees can be provided for the images reconstructed using these algorithms.

2.4 Recovery Guarantees

In anticipation of the theoretical results of Chap. 3-4, we are interested in reviewing the theoretical image recovery guarantees available in the literature to do *compressive imaging*. A *recovery guarantee* consists in providing an upper bound on the distance between the ground truth image and its reconstruction. In line with the current stabilized theory, the discussion focuses on noisy linear forward models of the form

⁸The *Fast Iterative Shrinkage-Thresholding Algorithm* is strictly speaking only valid for an ℓ_1 regularization term.

$$\mathbf{y} = \mathbf{A}\mathbf{x} + \mathbf{n}^9.$$

The success of image recovery algorithms depends heavily on the loss of information induced by the forward operator \mathbf{A} . If distances in the image \mathbf{x} domain are preserved in the measurement domain of \mathbf{A} , the forward operator is said to be an *isometry* (with respect to a given norm). Formally, an isometric operator satisfies

$$\|\mathbf{A}\mathbf{x}\| = \nu\|\mathbf{x}\|, \quad \forall \mathbf{x} \in \mathbb{R}^N \quad (2.27)$$

where ν is an optional scaling factor. If \mathbf{A} is an isometry, an upper bound $\epsilon := \max_{\tilde{\mathbf{x}}, \mathbf{x}} \|\mathbf{A}\tilde{\mathbf{x}} - \mathbf{A}\mathbf{x}\|$ on the error of a candidate measurement $\mathbf{A}\tilde{\mathbf{x}}$ spontaneously provides an upper bound on the error of the corresponding candidate image as

$$\|\tilde{\mathbf{x}} - \mathbf{x}\| = \frac{1}{\nu} \|\mathbf{A}(\tilde{\mathbf{x}} - \mathbf{x})\| \leq \frac{\epsilon}{\nu}. \quad (2.28)$$

Eq. (2.28) represents a first simple example of an image recovery guarantee for an isometric forward operator and noiseless measurements.

The condition for a matrix \mathbf{A} to be an isometry for all signals of the real space \mathbb{R}^N is generally that this \mathbf{A} must be square, *i.e.*, $\mathbf{A} \in \mathbb{R}^{N \times N}$, and full-rank (an orthogonal matrix is a particular case). The identity \mathbf{I} , Fourier \mathbf{F} , and DB2 Wavelet Ψ matrices are examples of isometric matrices. Strict isometry like (2.27) requires N measurements to ensure image recovery. However, as discussed in Sec. 2.1.1, natural images generally belong to a smaller dimensional domain $\mathcal{S} \subset \mathbb{R}^N$. For example, in Fig. 2.3 we showed visually that the dog image is sparse in the DB2 wavelet basis, *i.e.*, $\mathbf{x} = \Psi\theta$ with $\theta \in \Sigma_K$. Thinking about linear systems that are determined when the number of independent equations equals the number of degrees of freedom, this gives a glimpse that sometimes less than N measurements are needed to recover the fewer $K \ll N$ parameters of a sparse image. This idea is at the core of the *Compressive Sensing* (CS) domain, originally proposed in [Don06]. In a nutshell, CS is a technique that allows the reconstruction of a signal or image from a number of measurements significantly smaller than that traditionally required by the Nyquist-Shannon sampling theorem, *i.e.*, $M \ll N$.

⁹Without loss of generality if the image \mathbf{x} is replaced by the image parameters θ originally given in Sec. 2.1.1.

2 | Preliminaries: Flavors of Computational Imaging

In the aim to provide an isometry between the image domain and the measurement domain for all natural images $x \in \mathcal{S}$, injecting randomness into the measurement process is the only known tool to beat the “square-root bottleneck” [Mix15], i.e., requiring a number of measurements that goes below the square of the sparsity level $M < \mathcal{O}(K^2)$. The recovery guarantees given in Sec. 3.3-4.5 exploit randomness to provide sample complexities $M = \mathcal{O}(K \log(N/K))$. Below we discuss two standard types of recovery guarantees.

2.4.1 Nonuniform Recovery

In the context where A is built randomly, a *nonuniform* guarantee asserts that a single draw of A is sufficient to recover a fixed sparse vector x . Among the technical tools for proving image recovery, let us formally define the *coherence* in Def. 2.4.1.

Definition 2.4.1. Let $A = (a_1, \dots, a_N) \in \mathbb{C}^N$ be an orthogonal matrix, i.e., $A^* A = \mathbf{I}$. The coherence of A is precisely

$$\mu(A) := \max_{i,j \in \llbracket N \rrbracket, i \neq j} \frac{|a_i^* a_j|}{\|a_i\|_2 \|a_j\|_2} \in [N^{-1}, 1]. \quad (2.29)$$

A is perfectly incoherent if $\mu(A) = N^{-1}$.

The coherence $\mu(A)$ measures the maximum correlation between any two columns of A . It is particularly useful for providing image recovery guarantees when a random subsampling of an incoherent orthogonal forward operator is taken (e.g., random Fourier subsampling [CRT06; AGH14]). Let us provide an example of nonuniform recovery with the results of [AH16; CP11a] synthesized in Th. 2.1.

Theorem 2.1 (Exact recovery with subsampled incoherent measurements.). Let $\mathbf{A} \in \mathbb{C}^{N \times N}$ be an orthogonal matrix, and let $\mathbf{A}_\Omega \in \mathbb{C}^{M \times N}$ be a subselection of the rows of \mathbf{A} with the selected subset $\Omega \subseteq [N]$ chosen uniformly at random, then a given sparse image \mathbf{x} , with sparsity level K , and observed through the forward sensing model

$$\mathbf{y} = \mathbf{A}_\Omega \mathbf{x}, \quad (2.30)$$

can be recovered exactly with probability exceeding $1 - \epsilon$, provided that the number of measurements satisfies

$$M \gtrsim \mu(\mathbf{A}) N K (1 + \log(\epsilon^{-1})) \log N. \quad (2.31)$$

What Th. 2.1 shows, is that if the isometric operator \mathbf{A} is *incoherent* ($\mu(\mathbf{A}) = N^{-1}$), like the Fourier matrix \mathbf{F} for instance, then the image can be recovered exactly with a number of measurements M that is proportional to $K \log N$. For a sparse image with sparsity $K \ll N$, this implies $M \ll N$. In other words, the number of measurements can be significantly smaller than the target image resolution, meaning the forward model (2.30) constitutes an example of *compressive imaging*.

Th. 2.1's result has since then been extended to other guarantees that rely on the notions of *sparsity in levels* and *local coherence*. [KW14; Adc+17; AH21]. In a nutshell, these extensions claim that compressive imaging can be achieved even for operators \mathbf{A} that are globally coherent ($\mu(\mathbf{A}) \lesssim 1$) but locally incoherent, provided that the sparsity of the image of interest is distributed with some specific structure over the different levels of its decomposition into a sparsity basis (e.g., wavelets), and the *sampling strategy* is adapted accordingly. This generally implies *variable* or *multilevel sampling strategies*, which are closely related to the Fourier subsampling obtained in Chap. 3-4. While the theoretical results related to local coherence are beyond the scope of this work, we emphasize that they should be used, especially the results in [AH21, Chap. 12-13], to provide more rigorous properties of the Fourier subsampling obtained from interferometric measurements in Chap. 3-4. The shortcut taken in these chapters (for several reasons) was to make the assumption that the Fourier subsampling satisfies the $\text{RIP}_{\ell_2/\ell_2}$.

Nonuniform recovery guarantees prove that image recovery is obtained with *high probability* (w.h.p.) for an *arbitrary* image \mathbf{x} , provided that \mathbf{A} has just been randomly selected [CP11a]. *Uniform* recovery guar-

2 | Preliminaries: Flavors of Computational Imaging

antees claim that if the forward operator A has been randomly sampled and then fixed once and for all, *w.h.p.* image recovery is guaranteed for all sparse signals (in a given basis). Uniform guarantees are more restrictive than nonuniform ones. Even though there exist theoretical results using the coherence, we present in Sec. 2.4.2 another technical tool, named the *Restricted Isometry Property*.

2.4.2 Uniform Recovery

A uniform recovery guarantee asserts that a single draw of the matrix A is (with high probability) sufficient to recover all sparse vectors $\mathbf{x} \in \Sigma_K$. The main tools for proving so-called uniform recovery guarantees are the *coherence* (see Def. 2.4.1), the *robust Null Space Property* (not discussed in this thesis) and the *Restricted Isometry Property* (RIP).

The RIP provides a measure of how well, for all possible K -sparse vectors, the distance between these vectors is preserved when they are mapped to the measurement domain by the matrix A . A formal definition of the RIP is given in Def. 2.4.2.

Definition 2.4.2 (RIP $_{\ell_2/\ell_p}$). *A linear operator A is said to satisfy the (ℓ_2/ℓ_p) restricted isometry property, or RIP $_{\ell_2/\ell_p}(\Sigma_K, \mathbf{m}_K, \mathbf{M}_K)$ with $p \in \{1, 2\}$, if*

$$\mathbf{m}_K \|\mathbf{v}\|^2 \leq \|A\mathbf{v}\|_p^2 \leq \mathbf{M}_K \|\mathbf{v}\|^2, \quad \forall \mathbf{v} \in \Sigma_K. \quad (\text{RIP}_{\ell_2/\ell_p})$$

An abuse of notation will sometimes be used to write $\text{RIP}_{\ell_2/\ell_p}(\Sigma_K, \delta) := \text{RIP}_{\ell_2/\ell_p}(\Sigma_K, 1 - \delta, 1 + \delta)$.

The RIP, unlike coherence, allows to provide *uniform* recovery guarantees (it can be seen in (RIP $_{\ell_2/\ell_p}$) that the isometry is provided $\forall \mathbf{v} \in \Sigma_K$). Note that *Restricted Uniform Boundedness* (RUB) [CZ+15, Def. 2.1] is a relaxation of RIP where the bounds are not necessarily tight. Analogous to local coherence, there is a *RIP in levels* for images *sparse in levels* [BH14; LA19].

The pioneering result of [Don06], which gave birth to the field of *Compressive Sensing*, was to show that all K -sparse vectors $\mathbf{x} \in \Sigma_K \subset \mathbb{R}^N$ sensed by the sensing model $\mathbf{y} = A\mathbf{x} + \mathbf{n}$ for an i.i.d. random Gaussian matrix A could be recovered in a small number of measurements $M \ll N$. The proof essentially relies on proving that A satisfies the $\text{RIP}_{\ell_2/\ell_2}(\Sigma_K, \delta)$ with high probability when the number of measure-

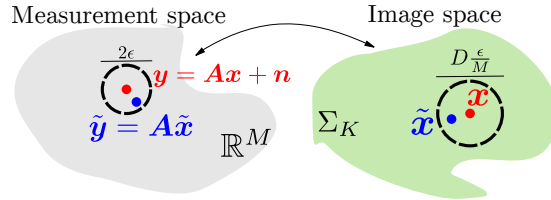


Fig. 2.8 Geometrical intuition of the RIP. The distance between the ground truth \mathbf{y} and the candidate measurements $\tilde{\mathbf{y}}$ is proportional to the distance between the ground truth \mathbf{x} and the candidate sparse images $\tilde{\mathbf{x}}$, where this distance is inversely proportional to the number of measurements M .

ments exceeds a threshold. We formalize this in a simplified formulation in Th. 2.2.

Theorem 2.2 (RIP $_{\ell_2/\ell_2}$ for dense Gaussian sampling). *Let us consider a linear forward operator $\mathbf{A} \in \mathbb{R}^{M \times N}$ filled with i.i.d. random Gaussian entries, i.e., $a_{ij} \stackrel{\text{i.i.d.}}{\sim} \mathcal{N}(0, 1/M)$. For a distortion $\delta > 0$ over the set Σ_K and some constants $C, c > 0$, if*

$$M \geq CK \log(N/K), \quad (2.32)$$

then, with probability exceeding $1 - Ce^{-cM}$, the operator \mathbf{A} respects the RIP $_{\ell_2/\ell_2}(\Sigma_K, \delta)$.

In Th. 2.2, the condition on the number of measurements in order to ensure that \mathbf{A} satisfies the RIP $_{\ell_2/\ell_2}(\Sigma_K, \delta)$ w.h.p. is called the *sample complexity*. It has been shown to be a sharp bound, meaning that it is not possible to go any lower.

One of the contributions of Chap. 3-4 is to prove, by a result analogous to Th. 2.2, that the RIP is satisfied with high probability for a specifically related form of the linear forward operator, thus proposing a compressive imaging modality. More precisely, the forward operator is random with a specific structure, and this is the randomness injected in \mathbf{A} that allows to provide uniform recovery guarantees. The basic principle is to show that the norm of the associated random measurements is a random variable with tail bounds, i.e., concentrated around its expectation. We refer to [Ver10; Tro22] for the main ingredients useful for proving concentration properties. In particular, the fixed and deterministic Fourier sampling imposed by core or antenna positions in Chap. 3-4 is a problem for providing a probabilistic RIP $_{\ell_2/\ell_2}$. This is the origin of the stated Assumptions 3.5-4.5.

2 | Preliminaries: Flavors of Computational Imaging

The final point of discussion is the tractability of all the aspects of inverse problem solving discussed in this chapter. In Sec. 2.5, we discuss three elements involved in the complexity of the image recovery procedure.

2.5 Complexities

There are multiple ways to assess the efficiency of a computational imaging modality. Three aspects related to the computations are listed below.

2.5.1 Sample Complexity

The *sample complexity* measures the size of the measurement vector as a function of the amount of information contained in the image to be recovered.

In uncompressed CI contexts, it is generally possible to design a deterministic scheme that recovers the discrete signal in as many measurements as its intrinsic number of degrees of freedom, *i.e.*, the dimension of the signal ambient space; Prop. 3.1 is an example.

However, we are more interested in compressive imaging schemes where the sample complexity is similar to (2.32), *i.e.*, the number of measurements must satisfy an inequality of the form

$$M \geq CK \log(N/K),$$

but $M \ll N$ for an image resolution N and sparsity level K . We provide three motivations for reducing the sample complexity: (i) accelerated acquisition, (ii) reduced memory cost, (iii) energy efficiency. In Chap. 3-4 we theoretically provide and numerically validate sample complexities similar to (4.54).

2.5.2 Computational Complexity of the Forward Model

The computational cost of applying the forward operator A is critical because it must be computed at least once within each iteration. For example, the Proximal Gradient Method defined in Algo. 2.1 requires one application of A and another of A^* . A naive computation of the matrix product $A\mathbf{u}$ for any vector $\mathbf{u} \in \mathbb{R}^N$ costs $\mathcal{O}(N^2)$ multiplications,

which can be intractable, especially when dealing with 4-D data as in Chap. 6.

Hopefully, there exists many ways to reduce this cost, depending on the structure of the operators involved. First, we will use the *Fast Fourier Transform* (FFT) algorithm [CT65], which computes the Fourier transform F in $\mathcal{O}(N \log N)$ operations, in all three CI contexts covered in this thesis. Second, the *Non Uniform FFT* (NUFFT) GF considered in Chap. 4 computes the Fourier transform of a discrete image at continuous frequencies by applying a sparse interpolation operator G filled with only $50N$ nonzero values. Third, also in Chap. 4, a *Bernoulli* modulation matrix, *i.e.*, a matrix $M \in \{\pm 1\}^{N \times N}$, is used to further reduce the number of measurements. The advantage of Bernoulli modulations is that they only involve sign flipping, which does not require multiplication operations and thus has a negligible impact on the computational load.

2.5.3 Convergence Rate of the Recovery Algorithm

As important as the computational cost of applying the forward model is the number of times it needs to be applied. This is directly related to the number of iterations required by the optimization algorithm used for image recovery (see Sec. 2.3) in order to reach convergence, *a.k.a.* the *convergence rate*.

Among the main recovery algorithms used in this thesis, the Proximal Gradient Method is known to converge at a rate $\mathcal{O}(1/k)$, where k is the number of iterations, using a fixed step size $\alpha \in [0, 2/L]$, where $L = \|A\|^2$ is the Lipschitz constant of $\nabla_x \mathcal{L}$ [PB14]. The accelerated PGM with momentum, described in Algo. 2.2, has a convergence rate $\mathcal{O}(1/k^2)$ and will thus be favored. For strongly convex functions, and in particular quadratic functions like the one studied in Chap. 5, the convergence is linear, *i.e.*, the Gradient Method converges at a rate $\mathcal{O}(c^k)$ for a convergence rate c . The ADAM algorithm, used to optimize the weights of an Implicit Neural Representation in Chap. 6, is suggested to converge to a local minimum at a rate $\mathcal{O}(\log k / \sqrt{k})$ [Déf+20] hence typically requires thousands of iterations to reach convergence.

In summary, the computational efficiency of a CI modality can be evaluated in multiple ways, such as memory, required computational resources, and reconstruction time. These questions are discussed in

2 | Preliminaries: Flavors of Computational Imaging

several parts of this thesis.

2.6 Appendix

2.6.1 Heuristic Adaptative Weighting of the Regularization

The regularization term $\mathcal{R}(\mathbf{u})$, discussed in Sec. 2.2, is generally accompanied by a weighting parameter. For instance,

$$\tilde{\mathbf{x}} = \arg \min_{\mathbf{u}} \frac{1}{2} \|\mathbf{y} - \mathbf{A}\mathbf{u}\|_2^2 + \lambda \|\mathbf{u}\|_1. \quad (2.33)$$

As explicitly written in (2.33), increasing λ increases the weight of the ℓ_1 regularization relative to the data-fidelity term. This parameter can be set to any fixed value. However, a connection with the associated constrained inverse problem can be made as

$$\tilde{\mathbf{x}} = \arg \min_{\mathbf{u}} \|\mathbf{u}\|_1 \text{ s.t. } \|\mathbf{y} - \mathbf{A}\mathbf{u}\|_2 \leq \epsilon,$$

where the fidelity error can be estimated as $\epsilon^k = \|\mathbf{A}\mathbf{u}^{(k)} - \mathbf{y}\|_2$. If $\epsilon^{(k)} > \epsilon$, λ must be decreased, and vice versa. This leads to a simple heuristic adjustment of λ as

$$\lambda^{(k+1)} = \lambda^{(k)} \frac{\epsilon}{\epsilon^{(k)}}. \quad (2.34)$$

A drawback of (2.34) is that it requires an estimate of the energy of the noise $\epsilon = \|\mathbf{n}\|_2$, which is not easy in practice. However, an upper bound on the noise level $\epsilon \leq \epsilon_u$ is sufficient and is directly associated to a target SNR of the reconstruction. One can specify a chosen SNR value for the reconstruction as

$$\text{SNR}(\mathbf{x}, \tilde{\mathbf{x}}) = 20 \log_{10} \left(\frac{\|\mathbf{x}\|_2}{\|\mathbf{x} - \tilde{\mathbf{x}}\|_2} \right) \approx 20 \log_{10} \left(\frac{\|\mathbf{x}\|_2}{\epsilon_u} \right) \quad (2.35)$$

and the $\epsilon^{(k)} = \epsilon_u$ in (2.34) is obtained by inverting (2.35). Naturally, this technique modifies the loss function to be minimized between iterations. We used it for the numerical reconstruction experiments performed to construct the phase transition diagrams in Sec. 3.4 and Sec. 4.6 in order to target an SNR value higher than the success threshold. The Numerical Tours [Pey11] include many numerical tricks like this one.

References

- [Adc+17] B. Adcock et al. “Breaking the coherence barrier: A new theory for compressed sensing”. In: *Forum of Mathematics, Sigma* 5 (2017), e4. DOI: [10.1017/fms.2016.32](https://doi.org/10.1017/fms.2016.32).
- [AGH14] B. Adcock, M. Gataric, and A. Hansen. “On Stable Reconstructions from Nonuniform Fourier Measurements”. In: *SIAM Journal on Imaging Sciences* 7.3 (2014), pp. 1690–1723. DOI: [10.1137/130943431](https://doi.org/10.1137/130943431). eprint: <https://doi.org/10.1137/130943431>.
- [AGR19] B. Adcock, M. Gataric, and J. L. Romero. “Computing reconstructions from nonuniform Fourier samples: Universality of stability barriers and stable sampling rates”. In: *Applied and Computational Harmonic Analysis* 46.2 (2019), pp. 226–249. ISSN: 1063-5203. DOI: <https://doi.org/10.1016/j.acha.2017.05.004>.
- [AH16] B. Adcock and A. C. Hansen. “Generalized sampling and infinite-dimensional compressed sensing”. In: *Foundations of Computational Mathematics* 16 (2016), pp. 1263–1323.
- [AH21] B. Adcock and A. C. Hansen. *Compressive Imaging: Structure, Sampling, Learning*. Cambridge University Press, 2021.
- [BD08] T. Blumensath and M. E. Davies. “Iterative thresholding for sparse approximations”. In: *Journal of Fourier analysis and Applications* 14 (2008), pp. 629–654.
- [Bec17a] A. Beck. *First-Order Methods in Optimization*. Philadelphia, PA, USA: SIAM-Society for Industrial and Applied Mathematics, 2017. ISBN: 1611974984.
- [Bec17b] A. Beck. *First-Order Methods in Optimization*. Philadelphia, PA, USA: SIAM-Society for Industrial and Applied Mathematics, 2017. ISBN: 1611974984.
- [BH14] A. Bastounis and A. C. Hansen. “On the absence of the RIP in real-world applications of compressed sensing and the RIP in levels”. In: *arXiv preprint arXiv:1411.4449* (2014).

2 | References

- [BJ] A. Boyat and B. Joshi. “A review paper: Noise models in digital image processing. arXiv 2015”. In: *arXiv preprint arXiv:1505.03489* ().
- [BKK19] S. Bai, J. Z. Kolter, and V. Koltun. “Deep equilibrium models”. In: *Advances in neural information processing systems* 32 (2019).
- [Bla04] R. E. Blahut. *Theory of Remote Image Formation*. New York, NY, USA: Cambridge University Press, 2004.
- [BM13] H. H. Barrett and K. J. Myers. *Foundations of Image Science*. Hoboken, NJ, USA: John Wiley & Sons, 2013.
- [BNB15] P. Broekema, R. van Nieuwpoort, and H. Bal. “The Square Kilometre Array Science Data Processor. Preliminary compute platform design”. In: *Journal of Instrumentation* 10.07 (July 2015), p. C07004. DOI: [10.1088/1748-0221/10/07/C07004](https://doi.org/10.1088/1748-0221/10/07/C07004).
- [BT09] A. Beck and M. Teboulle. “A Fast Iterative Shrinkage-Thresholding Algorithm for Linear Inverse Problems”. In: *SIAM Journal on Imaging Sciences* 2.1 (2009), pp. 183–202.
- [CP11a] E. J. Candes and Y. Plan. “A probabilistic and RIPless theory of compressed sensing”. In: *IEEE transactions on information theory* 57.11 (2011), pp. 7235–7254.
- [CP11b] P. L. Combettes and J.-C. Pesquet. “Proximal Splitting Methods in Signal Processing”. In: *Fixed-Point Algorithms for Inverse Problems in Science and Engineering*. Ed. by H. H. Bauschke et al. New York, NY: Springer New York, 2011, pp. 185–212. ISBN: 978-1-4419-9569-8. DOI: [10.1007/978-1-4419-9569-8_10](https://doi.org/10.1007/978-1-4419-9569-8_10).
- [CRT06] E. Candes, J. Romberg, and T. Tao. “Robust uncertainty principles: exact signal reconstruction from highly incomplete frequency information”. In: *IEEE Transactions on Information Theory* 52.2 (2006), pp. 489–509. DOI: [10.1109/TIT.2005.862083](https://doi.org/10.1109/TIT.2005.862083).
- [CSV13] E. Candes, T. Strohmer, and V. Voroninski. “PhaseLift: Exact and Stable Signal Recovery from Magnitude Measurements via Convex Programming”. In: *Communications on Pure and Applied Mathematics* 66 (Aug. 2013). DOI: [10.1002/cpa.21432](https://doi.org/10.1002/cpa.21432).

- [CT65] J. W. Cooley and J. W. Tukey. “An algorithm for the machine calculation of complex Fourier series”. In: *Mathematics of Computation* 19 (1965), pp. 297–301.
- [CZ+15] T. T. Cai, A. Zhang, et al. “ROP: Matrix recovery via rank-one projections”. In: *Annals of Statistics* 43.1 (2015), pp. 102–138.
- [Dau92] I. Daubechies. *Ten Lectures on Wavelets*. Vol. 61. Society for Industrial and Applied Mathematics, 1992.
- [DDD04] I. Daubechies, M. Defrise, and C. De Mol. “An iterative thresholding algorithm for linear inverse problems with a sparsity constraint”. In: *Communications on Pure and Applied Mathematics: A Journal Issued by the Courant Institute of Mathematical Sciences* 57.11 (2004), pp. 1413–1457.
- [Déf+20] A. Défossez et al. “A simple convergence proof of adam and adagrad”. In: *arXiv preprint arXiv:2003.02395* (2020).
- [Don06] D. L. Donoho. “Compressed Sensing”. In: *IEEE Transactions on Information Theory* 52.4 (2006), pp. 1289–1306.
- [EF02] I. A. Elbakri and J. A. Fessler. “Statistical image reconstruction for polyenergetic X-ray computed tomography”. In: *IEEE Transactions on Medical Imaging* 21.2 (Feb. 2002), pp. 89–99.
- [Fes10] J. A. Fessler. “Model-based image reconstruction for MRI”. In: *IEEE Signal Processing Magazine* 27.4 (July 2010), pp. 81–89.
- [FS18] S. Foucart and S. Subramanian. “Iterative Hard Thresholding for Low-Rank Recovery from Rank-One Projections”. In: (2018). arXiv: [1810.11749 \[math.NA\]](https://arxiv.org/abs/1810.11749).
- [FSY10] A. C. Fannjiang, T. Strohmer, and P. Yan. “Compressed remote sensing of sparse objects”. In: *SIAM Journal on Imaging Sciences* 3.3 (2010), pp. 595–618.
- [GOW21] D. Gilton, G. Ongie, and R. Willett. “Deep equilibrium architectures for inverse problems in imaging”. In: *IEEE Transactions on Computational Imaging* 7 (2021), pp. 1123–1133.
- [GW07] R. C. Gonzalez and R. E. Woods. *Digital Image Processing*. 3rd. London, U.K.: Pearson, 2007.
- [Hög74] J. A. Högbom. “Aperture Synthesis with a Non-Regular Distribution of Interferometer Baselines”. In: 15 (June 1974), p. 417.

2 | References

- [HS06] G. E. Hinton and R. R. Salakhutdinov. “Reducing the dimensionality of data with neural networks”. In: *science* 313.5786 (2006), pp. 504–507.
- [Hua+91] D. Huang et al. “Optical coherence tomography”. In: *science* 254.5035 (1991), pp. 1178–1181.
- [Isa06] V. Isakov. *Inverse Problems for Partial Differential Equations*. Springer Science & Business Media, 2006.
- [Jac+13] L. Jacques et al. “Robust 1-bit compressive sensing via binary stable embeddings of sparse vectors”. In: *IEEE transactions on information theory* 59.4 (2013), pp. 2082–2102.
- [KB14] D. P. Kingma and J. Ba. “Adam: A method for stochastic optimization”. In: *arXiv preprint arXiv:1412.6980* (2014).
- [Kir+24] M. Kirkove et al. “ADMM-inspired image reconstruction for terahertz off-axis digital holography”. In: *J. Opt. Soc. Am. A* 41.3 (Mar. 2024), A1–A14. DOI: [10.1364/JOSAA.504126](https://doi.org/10.1364/JOSAA.504126).
- [KMW18] U. S. Kamilov, H. Mansour, and B. Wohlberg. “Plug-and-Play FISTA for Solving Nonlinear Imaging Inverse Problems”. In: *IEEE Signal Processing Letters* (2018).
- [KW14] F. Krahmer and R. Ward. “Stable and robust sampling strategies for compressive imaging”. In: *IEEE Transactions on Image Processing* 23.2 (2014), pp. 612–622. ISSN: 10577149. arXiv: [1210.2380](https://arxiv.org/abs/1210.2380).
- [LA19] C. Li and B. Adcock. “Compressed sensing with local structure: uniform recovery guarantees for the sparsity in levels class”. In: *Applied and Computational Harmonic Analysis* 46.3 (2019), pp. 453–477.
- [Leb+22] O. Leblanc et al. “An Interferometric view of Speckle Imaging”. In: (2022).
- [Leb+23] O. Leblanc et al. “Interferometric lensless imaging: rank-one projections of image frequencies with speckle illuminations”. In: (2023). arXiv: [2306.12698 \[eess.IV\]](https://arxiv.org/abs/2306.12698).
- [Luc+18] A. Lucas et al. “Using Deep Neural Networks for Inverse Problems in Imaging: Beyond Analytical Methods”. In: *IEEE Signal Processing Magazine* 35.1 (2018), pp. 20–36. DOI: [10.1109/MSP.2017.2760358](https://doi.org/10.1109/MSP.2017.2760358).

- [LWJ24] O. Leblanc, Y. Wiaux, and L. Jacques. *Compressive radio-interferometric sensing with random beamforming as rank-one signal covariance projections*. 2024. arXiv: [2409.15031 \[eess.IV\]](https://arxiv.org/abs/2409.15031).
- [Mil+20] B. Mildenhall et al. “NeRF: Representing Scenes as Neural Radiance Fields for View Synthesis”. In: (2020). arXiv: [2003.08934 \[cs.CV\]](https://arxiv.org/abs/2003.08934).
- [Mix15] D. G. Mixon. “Explicit matrices with the restricted isometry property: Breaking the square-root bottleneck”. In: *Compressed Sensing and its Applications: MATHEON Workshop 2013*. Springer. 2015, pp. 389–417.
- [Mos19] A. Moshtaghpour. “Computational interferometry for hyperspectral imaging”. PhD thesis. Ph. D. thesis, Université catholique de Louvain, Louvain-la-Neuve, Belgium, 2019.
- [MSS22] D. Mishra, S. K. Singh, and R. K. Singh. “Deep Architectures for Image Compression: A Critical Review”. In: *Signal Processing* 191 (2022), p. 108346. ISSN: 0165-1684. DOI: <https://doi.org/10.1016/j.sigpro.2021.108346>.
- [MZ93] S. G. Mallat and Z. Zhang. “Matching pursuits with time-frequency dictionaries”. In: *IEEE Transactions on Signal Processing* 41.12 (1993), pp. 3397–3415.
- [Nes18] Y. Nesterov. *Lectures on convex optimization*. Second. Louvain-la-Neuve: Springer Publishing Company, Incorporated, 2018. DOI: [10.1007/978-3-319-91578-4](https://doi.org/10.1007/978-3-319-91578-4).
- [Nes83] Y. Nesterov. “A method for solving the convex programming problem with convergence rate $O(1/k^2)$ ”. In: *Dokl akad nauk Sssr*. Vol. 269. 1983, p. 543.
- [Nic95] D. Nicholson. “Inverse problems in gravitational wave astronomy”. In: *Inverse Problems* 11.4 (1995), p. 677.
- [PB14] N. Parikh and S. Boyd. “Proximal Algorithms”. In: *Found. Trends Optim.* 1.3 (Jan. 2014), pp. 127–239. ISSN: 2167-3888. DOI: [10.1561/2400000003](https://doi.org/10.1561/2400000003).
- [Pey11] G. Peyré. “The numerical tours of signal processing—advanced computational signal and image processing”. In: *IEEE Computing in Science and Engineering* 13.4 (2011), pp. 94–97.

2 | References

- [Qua+23] F. Quatresooz et al. “Continuous daytime and nighttime forecast of atmospheric optical turbulence from numerical weather prediction models”. In: *Optics Express* 31.21 (2023), pp. 33850–33872.
- [Rav+24] M. Ravasi et al. “PyProximal - scalable convex optimization in Python”. In: *Journal of Open Source Software* 9.95 (2024), p. 6326. DOI: [10.21105/joss.06326](https://doi.org/10.21105/joss.06326).
- [RFP13] H. Raguet, J. Fadili, and G. Peyré. “A generalized forward-backward splitting”. In: *SIAM Journal on Imaging Sciences* 6.3 (2013), pp. 1199–1226. ISSN: 19364954. DOI: [10.1137/120872802](https://doi.org/10.1137/120872802). arXiv: [1108.4404](https://arxiv.org/abs/1108.4404).
- [Rob+23] A. W. Robinson et al. “Simultaneous high-speed and low-dose 4-D stem using compressive sensing techniques”. In: *arXiv preprint arXiv:2309.14055* (2023).
- [She+14] Y. Shechtman et al. *Phase Retrieval with Application to Optical Imaging*. 2014. arXiv: [1402.7350](https://arxiv.org/abs/1402.7350).
- [Sit+20] V. Sitzmann et al. “Implicit Neural Representations with Periodic Activation Functions”. In: *arXiv*. 2020.
- [Ter+23] M. Terris et al. *Plug-and-play imaging with model uncertainty quantification in radio astronomy*. 2023. arXiv: [2312.07137 \[eess.IV\]](https://arxiv.org/abs/2312.07137).
- [Tik43] A. N. Tikhonov. “On the Stability of Inverse Problems”. In: *Doklady Akademii Nauk SSSR* 39 (1943), pp. 195–198.
- [TJ23] J. Tachella and L. Jacques. “Learning to reconstruct signals from binary measurements”. In: *arXiv preprint arXiv:2303.08691* (2023).
- [TM02] D. S. Taubman and M. W. Marcellin. “JPEG2000: standard for interactive imaging”. In: *Proceedings of the IEEE* 90.8 (2002), pp. 1336–1357.
- [Tro22] J. A. Tropp. *ACM 217: Probability in High Dimensions*. 2022.
- [Vas+17] A. Vaswani et al. “Attention is all you need”. In: *Advances in neural information processing systems* 30 (2017).
- [VBW13] S. V. Venkatakrishnan, C. A. Bouman, and B. Wohlberg. “Plug-and-Play Priors for Model Based Reconstruction”. In: *Proceedings of IEEE Global Conference on Signal and Information Processing (GlobalSIP)*. Austin, TX, USA, Dec. 2013, pp. 945–948. DOI: [10.1109/GlobalSIP.2013.6737048](https://doi.org/10.1109/GlobalSIP.2013.6737048).

- [Ver10] R. Vershynin. “Introduction to the non-asymptotic analysis of random matrices”. In: (2010), pp. 210–268. arXiv: [1011.3027](https://arxiv.org/abs/1011.3027).
- [VF08] D. E. Van Ewout Berg and M. P. Friedlander. “Probing the pareto frontier for basis pursuit solutions”. In: *SIAM Journal on Scientific Computing* 31.2 (2008), pp. 890–912. ISSN: 10648275. DOI: [10.1137/080714488](https://doi.org/10.1137/080714488).
- [Vin+10] P. Vincent et al. “Stacked Denoising Autoencoders: Learning Useful Representations in a Deep Network with a Local Denoising Criterion”. In: *Journal of Machine Learning Research* 11 (2010), pp. 3371–3408.
- [Wal92] G. K. Wallace. “The JPEG still picture compression standard”. In: *IEEE Transactions on Consumer Electronics* 38.1 (1992), pp. xviii–xxxiv.
- [Wan+04] Z. Wang et al. “Image quality assessment: from error visibility to structural similarity”. In: *IEEE transactions on image processing* 13.4 (2004), pp. 600–612.
- [Wia+09] Y. Wiaux et al. “Compressed sensing imaging techniques for radio interferometry”. In: *Monthly Notices of the Royal Astronomical Society* 395.3 (2009), pp. 1733–1742.
- [Yuc+22] G. Yuce et al. “A Structured Dictionary Perspective on Implicit Neural Representations”. In: *Proceedings of the IEEE Computer Society Conference on Computer Vision and Pattern Recognition* 2022-June (2022), pp. 19206–19216. ISSN: 10636919. DOI: [10.1109/CVPR52688.2022.01863](https://doi.org/10.1109/CVPR52688.2022.01863). arXiv: [2112.01917](https://arxiv.org/abs/2112.01917).

3

Rank-One Compression of Interferometric Sensing

HERE we begin our journey into the world of *interferometric sensing* and *Rank-One Projections* (ROP). It will continue in Chap. 4.

Concretely, this chapter studies the problem of recovering an image $f \in \mathbb{R}^N$ from linear combinations of a subset of its Fourier coefficients. More specifically, we are interested in a symmetric sensing model that cascades:

1. **An interferometric matrix:** an *hermitian* matrix $\mathcal{I}[f] \in \mathcal{H}^Q$ of Fourier coefficients of the image (the details of which will be given in Sec. 3.2), with
2. **Symmetric ROPs:** SROP of this matrix with a unique controllable vector $\alpha \in \mathbb{C}^Q$ called *sketching* vector.

In a discretized version, the model boils down to the form

$$y = \alpha^* \mathcal{I}[f] \alpha \quad (3.1)$$

where y is the single measurement. Interestingly, some control on the content of \mathcal{I} will be possible, too.

The main achievements of this chapter are to prove that (*i*) this sensing model actually arises in real applications, (*ii*) the theory of *Compressive Sensing* (CS) can be leveraged to provide formal recovery guarantees when a small¹ number of measurements are taken with the sketch-

¹A number of measurements proportional to the intrinsic complexity of the image to be recovered, which can be much lower than its number of pixels.

3 | Rank-One Compression of Interferometric Sensing

ing vector α being populated with (some given type of) i.i.d. random values, and (iii) it works in practice. This general problem is applied to *MultiCore Fiber Lensless Imaging* (MCFLI), giving a physical sense to the mathematical quantities involved.

These contributions extend earlier results studying the recovery of matrices from ROPs, and others demonstrating the capabilities of MCF imaging in a noncompressive manner.

This chapter mostly coincides with the content of our publication "Interferometric Lensless Imaging: Rank-one Projections of Image Frequencies with Speckle Illuminations" [Leb+23]. However, a discrete form appearing in (ROPI) is new and will be reused in Chap. 4. The code developed in the context of this chapter can be found at <https://github.com/olivierleblanc/ROPI>.

3.1 Introduction

3.1.1 Motivation

The interest in the research questions raised in this chapter is twofold.

Rank-One Projected Interferometric Sensing is Intrinsically Interesting

The model (3.1) itself exhibits nice features to study; the Fourier coefficients of f are encoded in a matrix that is specific to *interferometric sensing* as opposed to general *partial Fourier sampling*. The model is **linear** in the image f and **symmetric**, producing positive (intensity) measurements.

In the application covered in this chapter, the interferometric matrix \mathcal{I} is fixed *once and for all* by design, but its design will be key to good recovery properties.

Since a single measurement from the sensing model (3.1) is insufficient to recover the image, multiple measurements are obtained by tuning the sketching vector α . A simple scheme can recover the interferometric matrix \mathcal{I} exactly from as many well-chosen measurements as there are degrees of freedom in it. Another simple scheme can perform *raster-scanning* (RS), *i.e.*, make the best possible focus on each coefficient of f in as many measurements as the target image resolution. This RS principle will reappear with MCFLI in Sec. 3.2.2. However, **we are interested in studying random projections**, *i.e.*, a scenario where the sensing vector $y = (y_1, \dots, y_M)^\top$ is obtained with, $\forall m \in \llbracket M \rrbracket$,

$y_m = \alpha_m^* \mathcal{I} \alpha_m$, and $(\alpha_m)_q \stackrel{\text{i.i.d.}}{\sim} e^{iU[0,2\pi]}$. While injecting randomness into the α 's might seem strange at first, it has strong connections to the original idea of CS [Don06]. The intuition behind it is that this randomness will result in a set of random linear combinations of the available Fourier samples. In the end, the hope is to recover the image f from only a few of these random projections.

MultiCore Fiber Imaging as a Motivating Application

The interest in the (3.1) model arose from our will to better describe the acquisition in MCFLI. Actually, MCF were already used for telecommunication purposes, attractive for their large capacity transmission [KS09]. Recently, intensive research efforts for Lensless Endoscopy (LE) using multimode [Loc+22; PM16] or MultiCore Fibers (MCF) [Siv+16; And+16; Sun+22] have emerged, paving the way for deep biological tissue [CKH22] and brain imaging. In addition to the biomedical field, MCFLI also has potential applications in *industrial endoscopy* [Liu+22], to inspect hard-to-reach machinery and equipment; and *robotic vision*, where the idea of soft robots [Haw+17] could be pushed down to the microscale.

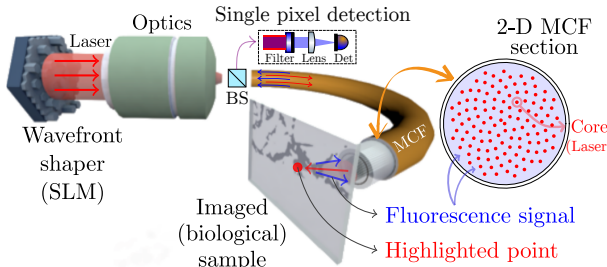


Fig. 3.1 Working principle of MCFLI with cores arranged in Fermat's golden spiral when the SLM is programmed in raster-scanning mode (BS = Beam Splitter).

The principle of MCFLI is illustrated in Fig. 3.1. A laser wavefront is shaped using a *Spatial Light Modulator* (SLM). The SLM allows individual control of the light injected into each of the MCF's cores, which are arranged in *Fermat's golden spiral*. This core arrangement is described in Sec. 3.2. Light injected into the cores propagates from the distal end of the MCF and illuminates an object to be imaged. Fig. 3.1 illustrates a biological sample illuminated in raster-scanning mode. The MCF features a double cladding that collects a fraction of the re-emitted light (either at other wavelengths by fluorescence or by simple reflection) and returns it to a highly sensitive (*single-pixel*) detector. The light integrated by this sensor represents a complete projection of the illumina-

3 | Rank-One Compression of Interferometric Sensing

tion on the object.

The model $y = \alpha^* \mathcal{I}[f] \alpha$ presented in (3.1) will arise naturally from this sensing scheme. The interferometric matrix \mathcal{I} will originate from the interfering light waves emitted by all the cores, the sketching vector α will somehow be related to the way light is injected into the cores to modulate the illumination, and the single measurement will obviously come from the integration of the backscattered light into the single-pixel detector. This anticipated correspondence between the sensing scheme and the mathematical model will be derived in Sec. 3.2.

Even though the mathematical quantities involved in the sensing model can be applied to other modalities, we will stick to the MCF context in this chapter to keep the physical intuition along the derivations.

3.1.2 Related Work

Before detailing the elements of our approach, we find it useful to mention a few related works, showing how they inspired us, and stressing their connections and differences with our contributions.

Sensing Model

Rank-one projected interferometric sensing bears similarities to quadratic measurement models such as *Phase Retrieval* (PR) [Fie82; BCL02] whose sensing is often recast as SROPs of the *lifted* matrix $\mathbf{x}\mathbf{x}^*$ of the (vectorized) image \mathbf{x} . Theoretical guarantees for the recovery of low-complexity matrices (*e.g.*, sparse, circulant, low-rank) from random ROPs have been studied extensively in the last decade [CCG15; CZ+15; SH17]. The symmetric nature of the sensing yields a bias in the mean of the sensing operator. Compensation of this bias is critical for image recovery. A debiasing technique consisting of doubling the number of measurements is proposed in [CCG15]. Our sensing model computes SROPs of an *interferometric* matrix built from spatial frequencies of the image. This has similarities to *random partial Fourier sensing* in compressive sensing (CS) theory [CRT06a; FR17; AGH14]. The nuance with respect to *interferometric sensing* is that with general partial Fourier sampling, the Fourier transform \hat{f} of the image is not necessarily sampled at locations that come from a difference set, so these samples do not always write in a Hermitian matrix. Finally, the nonuniformity of the Fourier sampling comes from the nature of the difference set. The samples tend to be concentrated at lower frequencies, so as *Variable Density Sampling* (VDS) strategies [KW14; PVW11]. However, the results of VDS are out of the scope of this chapter.

MultiCore Fiber Lensless Imaging

In 2008, Duarte *et al.* introduced single-pixel imaging [Dua+08; Tay+22], a subfield of lensless imaging (LI) where each collected observation is equivalent to randomly modulating an image before integrating its intensity. They demonstrated that reliable image estimation is possible at low sampling rates compared to the image resolution by using compressive sensing. More recently, this principle has been integrated into the use of an MCF for both remote illumination and image collection. This technique allows both deep and large FOV imaging [Siv+16; Siv+18a; Gué+22]. Subsequent works have shown that unstructured speckle-based illumination can effectively replace structured or beam-formed illumination [Car+18; Gué+22].

MultiMode Fibers (MMF) [KH66] compete with MCFs in all the cited applications of MCFLI. In fact, both concepts are getting exploited in a hybrid way [Du+22]. Speckle-based imaging is also possible with MMFs, with the interferences occurring between the modes instead of the cores [Bou+23; Loc+23].

In MCFLI, the spatial frequencies in the interferometric matrix correspond to the difference of the MCF core positions. The interferometric view also leads to the fundamental *Abbe diffraction limit* [AB20], determined by the light wavelength, the distance between the diffracting sources and their number. An interferometric sensing arises in radio-interferometric astronomy applications where, as induced by the *van Cittert-Zernike theorem* (see (4.6)), the signal correlation of two antennas gives the Fourier content on a frequency vector (or *visibility*) related to the baseline vector of the antenna pair [Wia+09]. One may recognize in [VWS19, Sec. 4.1.] the RS mode described in Sec. 3.2.2. However, in these works the presence of an interferometric matrix (see *e.g.*, [VWS19, Eq. (15)]) is often implicit, since, in contrast to our scheme, no linear combinations of these visibilities are computed.

The 8-step *phase-shifting interferometry* [CLY04] calibration technique (see Sec. 3.5.2) is used in, *e.g.*, astronomical imaging [Rab+06], and microscopy [Man+22]. The estimated complex wavefields implicitly encode the transmission matrix of the MCF (see [Siv+18b]) and also embed some unpredictable imperfections in the MCF configuration. Compared to previous work [Gué+22], where each speckle generated by a random SLM configuration had to be *a priori* recorded, this calibration is done only once before each acquisition.

3 | Rank-One Compression of Interferometric Sensing

3.1.3 Chapter Contributions

We provide several contributions to the modeling, understanding, and efficiency of MCFLI. The two following paragraphs present contributions to the modeling.

Interferometric analysis of MCFLI: Incorporating the physics of wave propagation, we leverage a speckle illumination model to highlight the interferometric² nature of the MCF device. The resulting approach, which is new compared to [Gué+22], corresponds to applying symmetric rank-one projections, or SROP³, to an interferometric matrix encoding the spectral content of the image. The SROP being controlled by the SLM, we can model the speckles in the sample plane from the random complex amplitude of each core, without assuming Gaussian distributed speckle illuminations [Gué+22].

Efficient SROP debiasing: As explained in [CCG15], SROP sensing must be *debiased* to allow for signal estimation. This is usually done by doubling the number SROP measurements and computing non-adjacent consecutive SROP differences. By considering *sketching* vectors with unit modulus (but random phases), we propose a more efficient debiasing that simply centers the measurements without doubling their number; a definite advantage when recording experimental measurements.

Rank-one projected interferometric sensing: We provide formal recovery guarantees. Following CS theory, we study a novel sensing model, the *rank-one projected interferometric sensing* of a sparse image (see also Fig. 3.3), providing a simplified framework for MCFLI. The theoretical analysis provided in Sec. 3.3 has thus an independent interest, the combination of SROPs with a partial Fourier sampling scheme having not been considered previously in the literature. Specifically, from a set of simplifying assumptions, we show that, with high probability (*w.h.p.*), one can robustly estimate a K -sparse image (in the canonical basis) provided that the number of SROPs M and the number of core pairs $Q(Q - 1)$ are large compared to $\mathcal{O}(K)$ (up to log factors). Our analysis relies on showing that, if the partial Fourier sampling

²“Interferometry is a technique which uses the interference of superimposed waves to extract information” [Wik].

³The ROP terminology was introduced when [CZ+15] extended phase retrieval applications [CCG15; Can11] to the recovery of a low—(but not necessarily one)—rank matrix via rank-one projections.

provided by the cores positions satisfies the classical restricted isometry property, it can be associated with a statistical concentration of the SROP measurements to show that, *w.h.p.*, the sensing operator satisfies (a variant of) that restricted isometry property which enables us to estimate a sparse image with (a variant of) the basis pursuit denoise program. The number of measurements M is thus reduced compared to recovering first the interferometric matrix with $\mathcal{O}(KQ)$ measurements, before estimating the object from this matrix (see Sec. 3.3.1). The overall sample complexity with speckle illumination [Gué+22] is also reduced compared to Raster Scanning (RS) the object with a translating focused (beamformed) spot [Siv+16]. The sample complexities derived theoretically are verified in Sec. 3.4 with extensive Monte Carlo experiments in a numerical setting

Simplified calibration: In Sec. 3.5, we propose a single-step calibration procedure encompassing most sensing imperfections in a real setup, at the exception of intercore interferences. This calibration, which only requires registering the cores locations and imaging depth, enables us to predict speckle illumination from the programmed SLM configuration (reaching 97% of normalized cross-correlation). Compared to [Gué+22] that needed to prerecord the M generated speckle patterns for imaging, we need $\mathcal{O}(Q)$ observations for a Q core MCF to accurately model of these M patterns.

Experimental results made on an actual MCF system demonstrate the effectiveness of this imaging procedure on a benchmark image.

3.1.4 Notations Specific to this Chapter

In this chapter, we are interested in recovering continuous 2-D images. Where x is reserved for the 2-D position in the image plane \mathbb{R}^2 , f will denote the discrete image we seek to recover. The MCFLI application will induce a limited field-of-view, represented by a vignetting function $w(x)$. The *vignetted* image is written as $f^\circ := wf$.

For the guarantees provided in Sec. 3.3, a debiasing procedure will be needed. The main operation associated with this debiasing consists in *centering* the measurements as well as the forward SROP operator. To this aim, we write the *average vector* of a vector $u \in \mathbb{R}^N$:

$$\mathbf{u}^a := \mathbf{1} \frac{1}{N} \sum_{i=1}^N u_i$$

3 | Rank-One Compression of Interferometric Sensing

and the *average matrix* of a set of matrices $\{A_m\}_{m=1}^M$:

$$A^a := \frac{1}{M} \sum_{m=1}^M A_m.$$

For either a vector u or a matrix A (taken from a collection of matrices $\{A_m\}_{m=1}^M$), its *centered* version is obtained by subtracting the *average* from it, *i.e.*,

$$u^c := u - u^a$$

and

$$A^c := A - A^a.$$

3.2 Sensing Model

We develop here the sensing model associated with an MCF lensless imager (MCFLI) under the same speckle imaging conditions as provided in [Gué+22], *i.e.*, interfering coherent light components output by the cores of the MCF with random relative delays. As shown in Fig. 3.2, an MCFLI consists of four main parts: a wavefront shaper (SLM), optics, an MCF, and a single photodetector. The SLM shapes the phase of the light injected into the cores. The optics include mirrors and lenses used to focus the light into the center of each core, thereby preventing multimodal effects.

As explained below, under a common far-field assumption, the MCFLI can be described as a two-component sensing system applying SROP of a specific interferometric matrix. We show how this model subsumes previous descriptions of the MCFLI. For the sake of proof-of-concept experiments, we also highlight that the SROP and interferometric nature of the model hold beyond the far-field assumptions. Finally, this section concludes with two views of the model when the image of interest is discretized—along with their computational complexities. A symmetric discrete model is presented to explain the interferometric matrix.

3.2.1 Rethinking MCFLI with Fourier Optics

An MCF with diameter D contains Q fiber cores with the same diameter $d < D$ (see Fig. 3.2). Our goal is to observe an object (or sample) which, for simplicity, is planar and defined in a plane \mathcal{Z} . This plane is parallel to the plane \mathcal{Z}_0 containing the *distal end* of the MCF, and at distance z from it. For convenience, we assume that the origins of \mathcal{Z}_0 and \mathcal{Z} are aligned, *i.e.*, they only differ by a translation in the plane normal direction. In \mathcal{Z}_0 , the Q cores locations are encoded in the set $\Omega := \{\mathbf{p}_q\}_{q=1}^Q \subset \mathbb{R}^2$.

As illustrated in Fig. 3.2 (and detailed in Sec. 3.5.1 and [Siv+16]), in MCFLI the laser light wavefront entering the MCF is shaped with a spatial light modulator (SLM) so that both the light intensity and phase can be individually adjusted for each core at the MCF distal end. Mathematically, assuming a perfectly calibrated system, this amounts to setting the Q complex amplitudes $\boldsymbol{\alpha} = (\alpha_1, \dots, \alpha_Q)^\top \in \mathbb{C}^Q$, coined *sketching vector*, of the electromagnetic field at each fiber core $q \in \llbracket Q \rrbracket$ located at \mathbf{p}_q .

Under the *far-field approximation*, that is if $z \gg D^2/\lambda$ with λ the laser

3 | Rank-One Compression of Interferometric Sensing

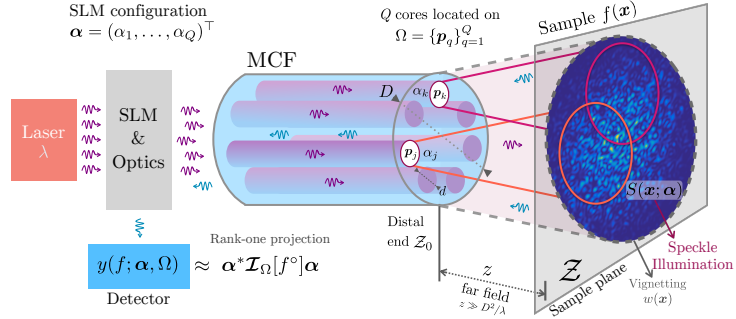


Fig. 3.2 MCFLI and its link with SROP of the interferometric matrix.

wavelength, the illumination intensity $S(x; \alpha)$ produced by the MCF on a point $x \in \mathbb{R}^2$ of the plane \mathcal{Z} reads [Gué+22]

$$S(x; \alpha) \approx w(x) \left| \sum_{q=1}^Q \alpha_q e^{\frac{i2\pi}{\lambda z} \mathbf{p}_q^\top \mathbf{x}} \right|^2, \quad w(x) := \frac{|\hat{E}_0(\frac{x}{\lambda z})|}{(\lambda z)^2}. \quad (3.2)$$

The window $w(x)$, which relates to the output wavefield E_0 of one single core in plane \mathcal{Z}_0 , is a smooth vignetting function defining the imaging field-of-view. Assuming E_0 shaped as a Gaussian kernel of width d , the FOV width scales like $\frac{\lambda z}{d}$.

The sensing model of MCFLI is established by the following key element: in its endoscope configuration, the sample is observed from the light it re-emits (by fluorescence) from its illumination by S , and for each configuration of S a single pixel detector measures the fraction of that light that propagates backward in the MCF (see Fig. 3.1). Therefore, given the sample fluorophore density map $f(x)$, assuming a short time exposure and low intensity illumination, fluorescence theory tells us that the number of collected photons $y \in \mathbb{R}_+$ follows a Poisson distribution $\mathcal{P}(\bar{y})$ with average intensity [Gué+22]

$$\begin{aligned} \bar{y}(f; \alpha, \Omega) &:= c \langle S(\cdot, \alpha), f \rangle = c \int_{\mathbb{R}^2} S(x; \alpha) f(x) dx \\ &= c \sum_{j,k=1}^Q \alpha_j^* \alpha_k \int_{\mathbb{R}^2} e^{\frac{i2\pi}{\lambda z} (\mathbf{p}_k - \mathbf{p}_j)^\top \mathbf{x}} f^o(\mathbf{x}) dx, \end{aligned} \quad (3.3)$$

where $0 < c < 1$ represents the fraction of light collected by the pixel detector, and $f^o := wf$ is the vignetted image, i.e., the restriction of f to the domain of the vignetting w .

Therefore, assuming $c = 1$ for simplicity, if one collects noisy observations $\mathbf{y} = (y_1, \dots, y_M)^\top$, such that $\bar{y}_m = \bar{y}(f; \alpha_m, \Omega)$ with distinct vectors α_m ($m \in [M]$), we can compactly write

$$\bar{y}_m = \alpha_m^* \mathcal{I}_\Omega[f^o] \alpha_m = \langle \alpha_m \alpha_m^*, \mathcal{I}_\Omega[f^o] \rangle_F \quad (3.4)$$

where $\langle \mathbf{A}, \mathbf{B} \rangle_F = \text{tr } \mathbf{A}^* \mathbf{B}$ is the Frobenius scalar product between two matrices \mathbf{A} and \mathbf{B} . This amounts to collecting M sketches of the hermitian *interferometric* matrix $\mathcal{I}_\Omega[f^\circ] \in \mathcal{H}^Q$, with entries defined by

$$(\mathcal{I}_\Omega[g])_{jk} := g\left[\frac{\mathbf{p}_j - \mathbf{p}_k}{\lambda z}\right] = \int_{\mathbb{R}^2} e^{\frac{i2\pi}{\lambda z}(\mathbf{p}_k - \mathbf{p}_j)^\top \mathbf{x}} g(\mathbf{x}) d\mathbf{x}, \quad (3.5)$$

for any function $g : \mathbb{R}^2 \rightarrow \mathbb{R}$. Under a high photon counting regime, and gathering all possible noise sources in a single additive, zero-mean noise \mathbf{n} , the measurement model reads

$$\mathbf{y} = \mathcal{A} \circ \mathcal{I}_\Omega[f^\circ] + \mathbf{n}, \quad (3.6)$$

where the *sketching operator* \mathcal{A} defines M SROP [CCG15; CZ+15] of any Hermitian matrix $\mathbf{H} \in \mathcal{H}^Q$ with

$$\mathcal{A}(\mathbf{H}) := (\langle \boldsymbol{\alpha}_m \boldsymbol{\alpha}_m^*, \mathbf{H} \rangle_F)_{m=1}^M. \quad (3.7)$$

The resulting sensing model is summarized in Fig. 3.3.

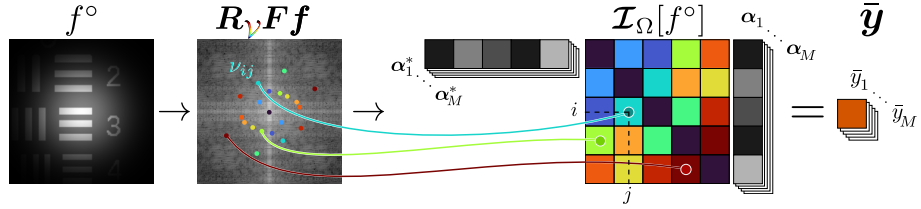


Fig. 3.3 Representation of the sensing model (3.4). The Fourier transform of the vignetted signal $f^\circ := wf$ is first sampled on the frequencies of the difference set $\mathcal{V} := \frac{1}{\lambda z}(\Omega - \Omega)$. This Fourier sampling is illustrated by restricting the FFT F of the discretized vignetted signal f with R_V . Next, these samples are shaped into an (hermitian) interferometric matrix $\mathcal{I}_\Omega[f^\circ] \in \mathcal{H}^Q$. Finally, M SROPs of this matrix are collected from $\bar{\mathbf{y}} = (\bar{y}_m)_{m=1}^M := (\boldsymbol{\alpha}_m^* \mathcal{I}_\Omega[f^\circ] \boldsymbol{\alpha}_m)_{m=1}^M$.

From (3.6), MCFLI corresponds to an *interferometric* system that is linear in f° . Eq. (3.5) and (3.7) show that it is indeed tantamount to first sampling the 2-D Fourier transform of f° over frequencies selected in the difference multiset⁴, or *baselines*,

$$\mathcal{V} := \frac{1}{\lambda z}(\Omega - \Omega) = \{\nu_{jk} := \frac{\mathbf{p}_j - \mathbf{p}_k}{\lambda z}\}_{j,k=1}^Q, \quad (3.8)$$

i.e., $(\mathcal{I}_\Omega[f^\circ])_{jk} = \mathcal{F}[f^\circ](\nu_{jk})$, and next performing M SROP of $\mathcal{I}_\Omega[f^\circ]$ with the rank-one matrices $\boldsymbol{\alpha}_m \boldsymbol{\alpha}_m^*$ as determined by \mathcal{A} .

Interestingly, the model (3.6) shows that we cannot access more information about f° than what is encoded in the frequencies of \mathcal{V} —the *visibilities*. Moreover, this sensing reminds the model of radio-interferometry by aperture synthesis [Wia+09]—each fiber core plays

⁴The elements of a multiset are not necessarily unique.

3 | Rank-One Compression of Interferometric Sensing

somehow the role of a radio telescope and each entry of $(\mathcal{I}_\Omega[f^\circ])_{jk}$ probing the frequency content of f° on the *baseline*⁵ v_{jk} .

Assuming we collect enough M SROP observations, we can potentially estimate the interferometric matrix $\mathcal{I}_\Omega[f^\circ]$, which in turn allows us to estimate f° if \mathcal{V} (with $|\mathcal{V}| \leq Q(Q-1)/2$) is dense enough.

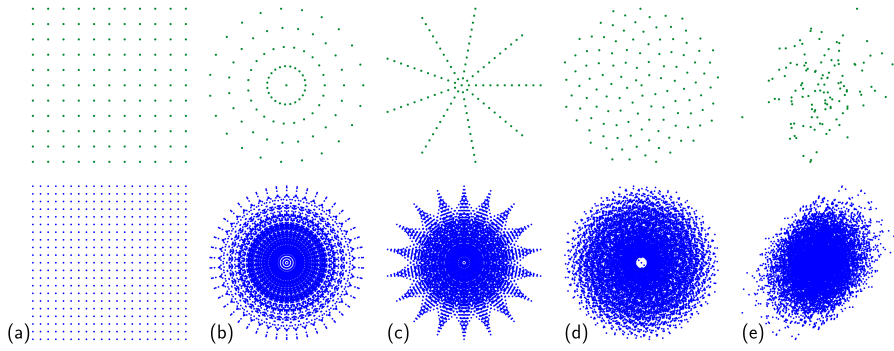


Fig. 3.4 Possible arrangements Ω of the cores (top) and their corresponding Fourier sampling \mathcal{V} (bottom). (a) Regular, (b) Azimuthal, (c) Radial, (d) Fermat’s golden spiral (Our choice in this work), and (e) Random gaussian.

Figure 3.4(top) shows possible designs for the arrangement of the cores, and Fig. 3.4(bottom) shows their corresponding Fourier sampling. The *regular grid* in (a) represents the worst design. Due to their redundancy, a lot of baselines end up at the same Fourier location. The spectral content is also sampled on a regular grid with a small density. The *azimuthal* and *radial* arrangements (in (b) and (c) respectively) improve the sampling. Their drawbacks are: (i) the too small distance between the central cores, (ii) the uneven sampling of the high frequency content, and (iii) the waste of spatial room in the fiber section to place more cores. The inter-core distances must actually be above a threshold value set by the tolerances on the *cross-talk* between the cores [And+13]. Actually, the Fermat’s golden spiral distribution Ω of the cores depicted in Fig. 3.4(d)—initially studied for its beam forming performances in MCFLI by raster scanning [Siv+16] (see below)—displays good properties. For this arrangement, conversely to regular lattice configurations, all (off-diagonal) visibilities are unique, *i.e.*, $|\mathcal{V}| = Q(Q-1)/2$. The *random gaussian* arrangement in Fig. 3.4(e) provides a nice gaussian Fourier sampling, close to the theoretical setting considered in VDS [KW14]. However, it shares the same disadvantages (i) and (iii) as for (b-c) designs.

⁵The word “baseline” being actually borrowed from this context.

3.2.2 Connection to Known MCFLI Modes

The MCFLI model subsumes the Raster Scanning (RS) and the speckle illumination (SI) modes introduced in [Siv+16; Gué+22]. We start this section with a short overview of the two principles, then more mathematically explain them into the MCFLI formalism.

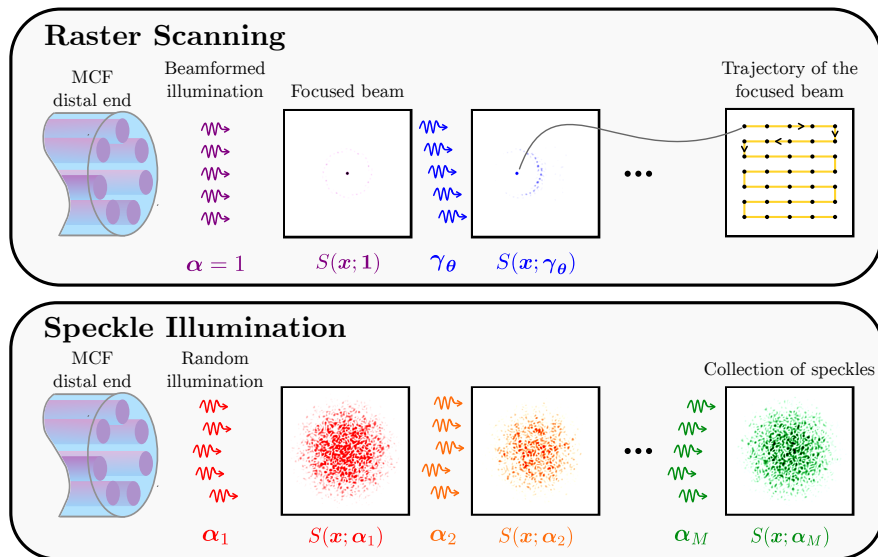


Fig. 3.5 Illustration of the RS and SI principles.

Figure 3.5 depicts the functional principle of the *Raster-Scanning* and *Speckle Illumination* approaches. In RS, in Fig. 3.5(top), a centered focused beam is obtained by setting a flat phase profile at the output of the MCF. This way, the light waves emitted by the cores will interfere constructively at the center of the image plane, and destructively elsewhere. The focused location is shifted by tilting this phase profile. One observes the peripheral illuminated spots, showing the focus is imperfect with a limited number of cores, especially near the edges of the image plane. A blurred image is obtained by raster-scanning the focused location along a trajectory sufficiently dense compared to the target resolution. In SI, in Fig. 3.5(bottom), a collection of speckles are obtained with random realizations of the sketching complex amplitudes α .

Raster scanning mode In the RS mode, the light wavefront is shaped (or *beamformed*) with the SLM to focus the illumination pattern on the sample plane, while galvanometric mirrors translate the focused beam

3 | Rank-One Compression of Interferometric Sensing

by phase shifting, hence ensuring the final imaging of the sample by raster scanning the sample and collecting light at each beamed position. A beamformed illumination is equivalent to set $\alpha = \mathbf{1} = (1, \dots, 1)^\top$ in (3.2).

In this case, the illumination intensity S corresponds to

$$S(\mathbf{x}; \mathbf{1}) \approx w(\mathbf{x}) \left| \sum_{q=1}^Q e^{\frac{i2\pi}{\lambda z} \mathbf{p}_q^\top \mathbf{x}} \right|^2 = w(\mathbf{x}) |\mathcal{F}[\phi_\Omega(\frac{\mathbf{x}}{\lambda z})]|^2, \quad (3.9)$$

where ϕ_Ω is the *array factor* of the core arrangement Ω , with, for any finite set $\mathcal{S} \subset \mathbb{R}^2$, $\phi_{\mathcal{S}}(\mathbf{p}) := \sum_{\mathbf{p}' \in \mathcal{S}} \delta(\mathbf{p} - \mathbf{p}')$. Expanding (3.9), we also note that

$$|\mathcal{F}[\phi_\Omega(\frac{\mathbf{x}}{\lambda z})]|^2 = \mathcal{F}[\phi_V](\mathbf{x}). \quad (3.10)$$

Arranging the core locations as a discretized Fermat's spiral was shown to focus the beam intensity on a narrow spot whose width scales like $\frac{\lambda z}{D}$ [Siv+16]. This is induced by the constructive interferences in (3.9) around $\mathbf{x} \approx \mathbf{0}$ —other locations being associated with almost destructive interferences.

The two galvanometric mirrors adapt the light optical path of the beam according to a tilt vector $\theta \in \mathbb{R}^2$ [Gué+22], *i.e.*, α is set to

$$\gamma_\theta := (\exp(-\frac{i2\pi}{\lambda z} \theta^\top \mathbf{p}_q))_{q=1}^Q \text{ and (3.2) provides}$$

$$S(\mathbf{x}; \gamma_\theta) \approx w(\mathbf{x}) \mathcal{T}_\theta \varphi(\mathbf{x}), \quad \mathcal{T}_\theta \varphi(\mathbf{x}) := \varphi(\mathbf{x} - \theta),$$

i.e., $\varphi := \mathcal{F}[\phi_V](\mathbf{x})$ is translated by θ . We can also write, from the symmetry of φ ,

$$\bar{y}_\theta = \langle S(\cdot, \gamma_\theta), f \rangle = \langle \mathcal{T}_\theta \varphi, f^\circ \rangle = (\varphi * f^\circ)(\theta), \quad (3.11)$$

with $*$ the 2-D convolution. Therefore, by defining a raster scanning path $\Theta \subset \mathbb{R}^2$ for θ sequentially visiting all positions in a given 2-D domain within a certain resolution, we see that by collecting all RS observations we image a blurred version (by φ) of f° over Θ . The RS mode is thus characterized by the sketching vectors $\alpha \in \{\gamma_\theta : \theta \in \Theta\}$.

Moreover, by considering the model (3.4) and the multiset $\mathcal{V}_0 := \{\nu_{jk} : j, k \in \llbracket Q \rrbracket, j \neq k\}$ that removes the Q occurrences of the zero frequency from \mathcal{V} , for $\theta = \mathbf{0}$,

$$\bar{y}_0 = \mathbf{1}^\top \mathcal{I}_\Omega[f^\circ] \mathbf{1} = \sum_{\nu \in \mathcal{V}} \hat{f}^\circ[\nu] = Q \hat{f}^\circ[\mathbf{0}] + \sum_{\nu \in \mathcal{V}_0} \hat{f}^\circ[\nu].$$

This shows that \bar{y}_0 probes the content of f° around the origin if the multiset \mathcal{V}_0 is dense enough over the support of \hat{f}° with distinct frequencies; in this case $y_0 - Q \hat{f}^\circ[\mathbf{0}] = \sum_{\nu \in \mathcal{V}_0} \hat{f}^\circ[\nu] \approx c f^\circ(\mathbf{0})$, for some

$c > 0$. In this context, the narrowness of the focus relates to the density of \mathcal{V}_0 . Moreover, (3.4) and (3.5) provide

$$\bar{y}_\theta = \gamma_\theta^* \mathcal{I}_\Omega[f^\circ] \gamma_\theta = \mathbf{1}^\top \mathcal{I}_\Omega[\mathcal{T}_{-\theta} f^\circ] \mathbf{1}$$

for any tilt θ , meeting the convolution interpretation in (3.11).

Despite its conceptual simplicity, the RS mode has a few drawbacks [Gué+22]: (i) it requires as many illuminations as the target image resolution; (ii) due to limited MCF diameter and the chosen core arrangement, the related convolution kernel φ is actually spatially varying (as seen in Fig. 3.5(top)), which limits the validity of (3.11).

Speckle Illumination mode In the SI mode, the sample f is illuminated with random light patterns called *speckles*. These are generated with random core complex amplitudes α . Conversely to the RS mode, by recording all speckles illuminations at calibration, SI does not require to know the MCF transmission matrix [Siv+18b].

One can interpret SI as a compressive imaging system [CRT06b; CW08; JV10]. By considering that both f and each illumination intensity $S(x; \alpha)$ are discretized and vectorized as $f \in \mathbb{R}^N$ and $s \in \mathbb{R}^N$, respectively, and gathering in a matrix $S := (s_1, \dots, s_M) \in \mathbb{R}^{N \times M}$ the M discretized speckles obtained from the sketching vectors $\{\alpha_m\}_{m=1}^M$, the model (3.6) becomes

$$\bar{y}_m = s_m^\top f, m \in \llbracket M \rrbracket, \text{ or } \bar{y} = S^\top f \in \mathbb{R}_+^M. \quad (3.12)$$

If M is adjusted to the sparsity level of f (with $M < N$), the recovery of f from \bar{y} becomes a classical compressive sensing (CS) problem with the sensing matrix S .

To characterize the properties of the sensing model (3.12) in this CS framework, the authors in [Gué+22] propose to first center (or *debiase*) this model by computing $y^c = y - y^a \mathbf{1}_M$ with the measurement average $y^a := \frac{1}{M} \sum_{j=1}^M y_j$ (we reinterpret this operation in Sec. 3.3.3). This provides, from (3.12), the model

$$y^c = \sqrt{M} \Phi \bar{S} f + n^c, \quad (3.13)$$

with a centered noise $n^c := n - (\frac{1}{M} \sum_{j=1}^M n_j) \mathbf{1}_M$, $\sqrt{M} \Phi := D S^\top \bar{S}^{-1}$ and the debiasing matrix $D := (\mathbf{I}_M - \frac{1}{M} \mathbf{1}_M \mathbf{1}_M^\top)$, $\bar{S} := \text{diag}(\bar{s}) \in \mathbb{R}^{N \times N}$, and $\bar{s} := \mathbb{E}_\alpha s$. The map $\bar{S} f$ relates to the discretization of the vignetted image f° defined above.

The debiasing above allowed the authors of [Gué+22] to hypothesize that Φ satisfies the Restricted Isometry Property (RIP), a crucial

3 | Rank-One Compression of Interferometric Sensing

property in the classical CS problem [CRT06b] ensuring the success of recovery procedures such as the basis pursuit denoise program (see Sec. 3.3). SI both improves the quality of the reconstructed images and reduces the acquisition time compared to RS. However, the RIP of the related sensing matrix which relies on specific random speckle configurations has not been established, keeping the sample complexity unknown for stable and robust image recovery. Moreover, in SI mode, we must prerecord M —object free—illumination speckles to build Φ , before observing the sample in the imaging plane with the same speckles.

3.2.3 Generalized MCFLI Sensing

We can extend the MCFLI model (3.4) beyond the far-field and identical core diameter—but still no crosstalk—assumptions by replacing the interferometric matrix $\mathcal{I}_\Omega[f^\circ]$ with a more general matrix function $\mathcal{I}_\Omega^G[f]$.

Given the wavefield $E_q(\mathbf{x})$ of the q -th core of the MCF in the plane \mathcal{Z} , the illumination reads

$$S(\mathbf{x}; \boldsymbol{\alpha}) := \left| \sum_{q=1}^Q \alpha_q E_q(\mathbf{x}) \right|^2, \quad (3.14)$$

and similar developments to Sec. 3.2 provide

$$\bar{y}_m = \boldsymbol{\alpha}_m^* \mathbf{G}[f] \boldsymbol{\alpha}_m = \langle \boldsymbol{\alpha}_m \boldsymbol{\alpha}_m^*, \mathcal{I}_\Omega^G[f] \rangle_F \quad (3.15)$$

where we defined, for any function $h : \mathbb{R}^2 \rightarrow \mathbb{R}$, the Hermitian matrix $\mathcal{I}_\Omega^G[h] \in \mathcal{H}^Q$ with entries

$$(\mathcal{I}_\Omega^G)_{jk}[h] := \int_{\mathbb{R}^2} E_j^*(\mathbf{x}) E_k(\mathbf{x}) h(\mathbf{x}) d\mathbf{x}. \quad (3.16)$$

By recording a spatial discretization of the fields $\{E_q(\mathbf{x})\}_{q=1}^Q$, we can thus estimate the forward model (3.16)—and thus

$\mathcal{H}[h] := (\boldsymbol{\alpha}_m^* \mathcal{I}_\Omega^G[h] \boldsymbol{\alpha}_m)_{m=1}^M$ —for any function h , as imposed to solve the inverse problem (3.15) with practical algorithms. While slower than the computation of $\mathcal{I}_\Omega[f^\circ]$ (e.g., with a FFT boosting) and its M SROP, estimating \mathcal{H} directly integrates many deviations to the interferometric model, with a calibration limited to the observation of $\mathcal{O}(Q)$ discretized spatial intensities aimed to yield $\{E_q(\mathbf{x})\}_{q=1}^Q$. We detail in Sec. 3.5.2 how to practically achieve this calibration.

3.2.4 ROPI: the Subsequent Discrete Model

In this section, we analyze what happens to the sensing model (3.4) when the vignetted image f° is discretized. The major model change

will occur for the interferometric matrix \mathcal{I}_Ω . The derived *discrete-to-discrete* model, coined *Rank-One Projected Interferometric* (ROPI) imaging, is presented in a general setting, not necessarily considered in the MCFLI framework anymore.

Without loss of generality, the following derivations will be presented for a 1-D analog of (3.5), and $\lambda = z = 1$ to simplify the notation. The image is assumed to have a *bounded field-of-view*, *i.e.*, it is contained in a domain $[0, N\Delta]$ with Δ being the spatial *resolution* of the upcoming discrete image. Additionally, the image is assumed to be *bandlimited*, *i.e.*, $\hat{f}^\circ(k) = 0$ for $|k| > \pi/\Delta$ (we will come back to this assumption in Sec. 3.3.2). The jk -th entry of the *simplified* interferometric matrix writes

$$(\mathcal{I}_\Omega[f^\circ])_{jk} := \int_{\mathbb{R}} f^\circ(x) e^{i2\pi(p_k - p_j)x} dx. \quad (3.17)$$

Consider the spatial discretization III : $f^\circ \in \mathbb{R} \mapsto f \in \mathbb{R}^N$ which yields a *discrete* image as $f := \{f^\circ[n], n \in \llbracket N \rrbracket \subset \mathbb{Z}\}$ with

$$f^\circ[n] = f^\circ(n\Delta) = f^\circ(x) \sum_{n=0}^{N-1} \delta(x - n\Delta). \quad (3.18)$$

Substituting (3.18) into (3.17) gives

$$(\mathcal{I}_\Omega[f])_{jk} := \Delta \sum_{n=0}^{N-1} f^\circ[n] e^{-i2\pi(p_j - p_k)n\Delta}. \quad (3.19)$$

Bilateral form In order to factorize $\mathcal{I}_\Omega[g]$ in a symmetric discrete form, the trick consists in inserting $\sum_{n'=0}^{N-1} \delta_{nn'} = 1$ into (3.19) so as to get

$$(\mathcal{I}_\Omega[f])_{jk} = \Delta \sum_{n,n'=0}^{N-1} e^{-i2\pi p_j n \Delta} f^\circ[n] \delta_{nn'} e^{i2\pi p_k n' \Delta} = \mathbf{e}_{p_j}^* \mathbf{F} \mathbf{D}_f \mathbf{F}^* \mathbf{e}_{p_k} \quad (3.20)$$

with $\mathbf{e}_{p_j} \in \{0, 1\}^N$ the basis vector nonzero at index $p_j N \Delta$, \mathbf{F} the *discrete Fourier transform* (DFT) matrix (here implicitly including the scaling constants $\sqrt{N\Delta}$), and $\mathbf{D}_f = \text{diag}(f)$ the diagonal matrix filled with f . Eq. (3.20) is valid for the particular case when the cores locations are *on-the-grid*—an assumption made in Sec. 3.3.2 with 3.3.

3 | Rank-One Compression of Interferometric Sensing

Remark 3.1. Imposing the cores locations to be on-the-grid is unnecessary to get a symmetric discrete model. In the case of off-grid locations, the selection basis vectors \mathbf{e}_{p_j} will be replaced by interpolation kernels which help approximating the off-the-grid DFT. These kernels, which correspond exactly to the Non-Uniform FFT (NUFFT), will appear in Chap. 4.

At the end, the matrix can be written as

$$\mathcal{I}_\Omega[f] = \begin{bmatrix} \mathbf{e}_{p_1}^\top \\ \vdots \\ \mathbf{e}_{p_Q}^\top \end{bmatrix} \mathbf{F} \mathbf{D}_f \mathbf{F}^* [\mathbf{e}_{p_1} \ \cdots \ \mathbf{e}_{p_Q}] = \mathbf{W} \mathbf{F} \mathbf{D}_f \mathbf{F}^* \mathbf{W}^*. \quad (3.21)$$

Eq. 3.21 also shows that if f is K -sparse, the interferometric matrix $\mathcal{I}_\Omega[f]$ is rank- K . In a discretized version, the noiseless measurement model in (3.4) boils down to the form

$$\bar{y} = \boldsymbol{\alpha}^* \mathbf{W} \mathbf{F} \mathbf{D}_f \mathbf{F}^* \mathbf{W}^* \boldsymbol{\alpha} \quad (\text{ROPI})$$

with y the single measurement, $\boldsymbol{\alpha}$ the controllable *sketching* vector, and $\mathbf{W}^* := [\mathbf{e}_{p_1} \ \cdots \ \mathbf{e}_{p_Q}]$.

In (ROPI), $\mathcal{J} := \mathbf{F} \mathbf{D}_f \mathbf{F}^*$ is by definition a *circulant* matrix with $\mathcal{J}_{kl} = (F^* f)_{(k-l)/N}$ with $(k-l)/N := k - l \bmod N$. In other words, the vector $F^* f$ is repeated in each row of \mathcal{J} with a “one-index” shift between each row. The pure conjuguate symmetry of $\mathcal{I}_\Omega[f]$ (illustrated in Fig. 3.3) now clearly appears from the identity $\mathcal{I}_\Omega[g]^* = (\mathbf{W} \mathbf{F} \mathbf{D}_f \mathbf{F}^* \mathbf{W}^*)^* = \mathbf{W} \mathbf{F} \mathbf{D}_f \mathbf{F}^* \mathbf{W}^* = \mathcal{I}_\Omega[g]$ (valid only for a real image $f \in \mathbb{R}^N$).

Interestingly, the Fourier sampling encoded in \mathbf{W} are only parameterized by the cores locations Ω . This indicates that a denser Fourier sampling would be reachable if the cores could be moved. Unfortunately in MCFLI, Ω is fixed by the design of the cores arrangement. However, this is not true for all applications. This observation will be key for the radio-interferometry context covered in Chap. 4.

Gathering the M measurements in a vector gives the *bilateral* sensing model

$$\bar{y} = \text{diag}(\mathbf{A} \mathbf{W} \mathbf{F} \mathbf{D}_f \mathbf{F}^* \mathbf{W}^* \mathbf{A}^*) \quad (3.22)$$

with $\mathbf{A} := (\boldsymbol{\alpha}_1, \dots, \boldsymbol{\alpha}_M)^*$.

Unilateral form Going back to (3.19), the jk -th entry could have been written as

$$(\mathcal{I}_\Omega[f])_{jk} = \mathbf{e}_{p_j-p_k}^\top \mathbf{F} f.$$

Consequently, a vectorized form of the interferometric matrix is

$$\text{vec}(\mathcal{I}_\Omega[f]) = \mathbf{G}\mathbf{F}\mathbf{f} \quad (3.23)$$

with the *Fourier sampling* matrix $\mathbf{G} := (\mathbf{e}_{p_j} - \mathbf{e}_{p_k}, \forall j, k \in \llbracket Q \rrbracket)^\top$. This yields a *unilateral* sensing model

$$\bar{\mathbf{y}} = \mathbf{R}\mathbf{G}\mathbf{F}\mathbf{f}, \quad (3.24)$$

with each line of the matrix \mathbf{R} computing a single SROP measurement, *i.e.*, $(\mathbf{R}^\top)_m = \text{vec}(\boldsymbol{\alpha}_m \boldsymbol{\alpha}_m^*)^\top, \forall m \in \llbracket M \rrbracket$. The bilateral and unilateral forms of the sensing model are mathematically equivalent. Actually, their equivalence is linked to the observation (3.10) that we made earlier in the continuous domain. In the next section, we compare them in a computational complexity point of view.

3.2.5 Computational Complexity

Table 3.1 reports a comparison of the complexities of the bilateral (3.22), unilateral (3.24), and SI (3.12) sensing models. The SI model will be of particular interest for its use in the experimental reconstructions of Sec. 3.5 from a calibration phase exploiting (3.14) and described in Sec. 3.5.2. It must be noted that the forward model is usually computed hundreds to thousands of times in proximal reconstruction algorithms, so the true cost is more than two orders of magnitude higher the numerical values provided in Table 3.1.

For a fair comparison of the computational costs, we provide an order of magnitude of the quantities involved for the MCFLI application: the image resolution is $N = 10^6$, the number of cores is $Q = 120$, and the number of measurements is $M = 1000$.

Table 3.1 Complexities of the sensing models for MCFLI.

Name	Model	Complexity \mathcal{O}	Value
Bilateral	$\text{diag}(AWFD_f F^* W^* A^*)$	$MN \log N + MQ$	10^{10}
Unilateral	$\mathbf{R}\mathbf{G}\mathbf{F}\mathbf{f}$	$MQ^2 + Q^2N + N \log N$	10^{10}
SI	$S\mathbf{f}$	MN	10^9

For the *bilateral* model, the complexity is computed from right to left with $W^* A^*$ costing only $\mathcal{O}(MQ)$ (since W is just a selection matrix), then M FFTs are taken in $\mathcal{O}(MN \log N)$, applying D_f costs an element-wise product in $\mathcal{O}(N)$, then the symmetrical operations keep the same complexity. The complexity of the *unilateral* model is also computed from right to left.

3 | Rank-One Compression of Interferometric Sensing

In Table 3.1, the *bilateral* model appears to cost $\mathcal{O}(MN \log N) \approx 10^{10}$. For the *unilateral* model, the most costly operation is the computation of the visibilities with G in $\mathcal{O}(Q^2N) \approx 10^{10}$ operations. Omitting the calibration phase, the SI model used for the experimental reconstructions is the fastest.

It is worth mentioning that ROPs of a circulant matrix can be factorized as a projection of the Fourier transform Ff of the image with autocorrelations of the vectors $W^*\alpha$. But this fact does not improve the complexities mentioned above.

3.3 Recovery Guarantees

This section starts with a short analysis of the best sample complexities foreseeable for the recovery of the intermediate interferometric matrix. Then, formal image recovery guarantees are provided up to the use of 6 motivated assumptions for the theoretical setting. The main achievement of this is Prop. 3.2 proving we can compute a *stable and robust* estimate from the sensing setting present in Sec. 3.2. Moreover, the associated sample complexity is optimal.

3.3.1 Interferometric Matrix Reconstruction

It is possible to recover the interferometric matrix \mathcal{I}_Ω from its SROPs y , which allows subsequent image estimation from this matrix. However, as will be shown below in Th. 3.1, this procedure provides a suboptimal sampling complexity compared to the direct sensing approach (combining SROPs and interferometric sensing) proposed in Sec. 3.3.

With Prop. 3.1, we first show that $\mathcal{O}(Q^2)$ deterministic sketching vectors suffice to reconstruct any interferometric matrix \mathcal{I}_Ω in a noiseless scenario—corresponding to its intrinsic complexity. This provides an upper bound on the sampling complexity for further compression measurements of this matrix.

Proposition 3.1. *There exists a set of $M = Q(Q - 1) + 1$ sketching vectors $\{\alpha_m\}_{m=1}^M \in \mathbb{C}^Q$ such that any Hermitian matrix $\mathcal{I} \in \mathcal{H}^Q$ with constant diagonal entries can be reconstructed from the M sketches*

$$y_m = \alpha_m^* \mathcal{I} \alpha_m.$$

Proof. Given the 2-sparse sketching vectors $\alpha_\gamma(q, r) := e_q + \gamma e_r$, with $q, r \in [Q]$, $|\gamma| = 1$ and the s -th canonical vector e_s , we have

$$h_\gamma[q, r] := \alpha_\gamma^*(q, r) \mathcal{I} \alpha_\gamma(q, r) = \mathcal{I}_{q,q} + \mathcal{I}_{r,r} + \gamma \mathcal{I}_{q,r} + \gamma^* \mathcal{I}_{r,q} = \frac{2}{Q} \operatorname{tr} \mathcal{I} + 2\Re\{\gamma \mathcal{I}_{q,r}\}.$$

Therefore,

$$h_1[q, r] + i h_{-i}[q, r] = 2\mathcal{I}_{q,r} + \frac{2}{Q}(1+i) \operatorname{tr} \mathcal{I}. \quad (3.25)$$

From the $Q(Q - 1)$ sketching vectors $\{\alpha_\gamma(q, r) : 1 < q < r \leq Q, \gamma \in \{1, -i\}\} \subset \mathbb{C}^Q$, the value $2\Re\{H\} = H + H^*$ computed from the sum $H = \sum_{1 < q < r \leq Q} (h_1[q, r] + i h_{-i}[q, r])$ respects

$$\Re\{H\} = \sum_{q \neq r} \mathcal{I}_{q,r} + (Q - 1) \operatorname{tr} \mathcal{I} = \mathbf{1}^\top \mathcal{I} \mathbf{1} + (Q - 2) \operatorname{tr} \mathcal{I}.$$

3 | Rank-One Compression of Interferometric Sensing

Using the additional unit sketching vector $\mathbf{1}$ thus recovers $\text{tr } \mathcal{I}$ —and all constant diagonal entries of the Hermitian matrix \mathcal{I} —from $\Re\{H\}$, and (3.25) provides all its off-diagonal entries. Overall \mathcal{I} is thus recovered from $1 + Q(Q - 1)$ measurements. \square

Recovering \mathcal{I}_Ω in less than $\mathcal{O}(Q^2)$ SROP is possible if this matrix, and thus f , respects specific low-complexity models. First, $\mathcal{I}_0 := \mathcal{I}_\Omega[f^\circ]$ is Hermitian. Moreover, if f° is non-negative, this matrix is positive semi-definite since from (3.5), for any $v \in \mathbb{C}^Q$,

$$\begin{aligned} v^* \mathcal{I}_0 v &= \int_{\mathbb{R}^2} f^\circ(x) \sum_{j,k} v_j^* v_k e^{\frac{i2\pi}{\lambda z} (\mathbf{p}_k - \mathbf{p}_j)^\top x} dx \\ &= \int_{\mathbb{R}^2} f^\circ(x) |v^* \rho(x)|^2 dx \geq 0, \end{aligned} \quad (3.26)$$

where $\rho = (\rho_1, \dots, \rho_Q) \in \mathbb{C}^Q$ with $\rho_j(x) := e^{-\frac{i2\pi}{\lambda z} \mathbf{p}_j^\top x}$.

Second, if f° is composed of a few Dirac spikes, *i.e.*, if $f^\circ(x) = \sum_{i=1}^K u_i \delta(x - x_i)$ for K coefficients and locations $\{(u_i, x_i)\}_{i=1}^K$, the interferometric matrix has rank- K since (3.5) reduces to the sum of K rank-one matrices, *i.e.*,

$$\mathcal{I}_\Omega[f^\circ] = \sum_{i=1}^K u_i \rho(x_i) \rho^*(x_i). \quad (3.27)$$

Under this structural assumption, or if \mathcal{I}_0 is well approximated by a rank- K matrix $(\mathcal{I}_0)_K$, we can recover \mathcal{I}_0 with high probability provided the sketching vectors $\{\alpha_m\}_{m=1}^M$, and thus \mathcal{A} , are random, *i.e.*, their entries are i.i.d. from a centered sub-Gaussian⁶ distribution [CCG15, Thm 1].

Theorem 3.1 (From [CCG15]). *With*

$$M \geq M_0 = O(KQ), \quad (3.28)$$

and probability exceeding $1 - \exp(-cM)$, any matrix \mathcal{I}_0 observed through the model $y = \mathcal{A}(\mathcal{I}_0) + \eta$, with bounded noise $\|\eta\|_1 \leq \varepsilon$, can be estimated from

$$\tilde{\mathcal{I}} \in \arg \min_{\mathcal{I}} \|\mathcal{I}\|_* \text{ s.t. } \mathcal{I} \succcurlyeq 0, \|y - \mathcal{A}(\mathcal{I})\|_1 \leq \varepsilon.$$

*This solution is instance optimal, *i.e.*, for some $C, D > 0$,*

$$\|\tilde{\mathcal{I}} - \mathcal{I}_0\|_F \leq C \frac{\|\mathcal{I}_0 - (\mathcal{I}_0)_K\|_*}{\sqrt{K}} + D \frac{\varepsilon}{M}. \quad (3.29)$$

⁶The probability distribution of a random variable X is called sub-Gaussian if there is a positive constant C such that for every $t \geq 0$, $\mathbb{P}[|X| \geq t] \leq 2e^{-t^2/C^2}$.

The sample complexity in (3.28) is, however, not optimal since for a K -sparse f° , \mathcal{I}_0 depends only on $\mathcal{O}(K)$ parameters in (3.27). While [CCG15] provides similar results with reduced sample complexity provided \mathcal{I}_0 is, e.g., sparse or “Toeplitz low-rank”, these models are not applicable here and we show in Sec. 3.3 that a smaller sample complexity is achievable under certain simplifying assumptions.

Image Reconstruction

Let us consider a compressive sensing framework whose objective is to explore the imaging capability of MCFLI, *i.e.*, we study the problem of directly estimating sparse images from their rank-one projected interferometric sensing, as driven by the two sensing components in (3.4). As proved in Sec. 3.3.4, from simplifying assumptions made on both f° and the sensing scenario (see Sec. 3.3.2), this method achieved reduced sample complexities compared to the approach in Sec. 3.3.1, which are also confirmed numerically in Sec. 3.4.

3.3.2 Working Assumptions

We first assume a bounded field of view in MCFLI.

Assumption 3.1 (Bounded FOV). *The support of the vignetting window $w(\mathbf{x})$ in (3.2) is contained in a domain $\mathcal{D} := [-L/2, L/2]^2$ with $L := \frac{c\lambda z}{d}$, for $c > 0$ depending on the (spectrum of the) output wavefield E_0 in (3.2), and $w = 0$ on the frontier of D .*

Therefore, supposing f bounded, we have $\text{supp } f^\circ \subset \mathcal{D}$ and $f^\circ = 0$ over the frontier of D .

We also need to discretize f° by assuming it is bandlimited.

Assumption 3.2 (Bounded and bandlimited image). *The image f is bounded, and f° is bandlimited with bandlimit $\frac{W}{2}$, with $W := \frac{N_1}{L}$ and $N_1 \in \mathbb{N}$, i.e., $\mathcal{F}[f^\circ](\chi) = 0$ for all χ with $\|\chi\|_\infty \geq \frac{W}{2}$.*

As will be clear below, this assumption avoids spectral aliasing during discretization and thus enables the computation of the interferometric matrix $\mathcal{I}_\Omega[f^\circ]$ from the discrete Fourier transform of the following discretization of f° .

From Assumptions 3.1 and 3.2 the function f° can be identified with a vector $\mathbf{f} \in \mathbb{R}^N$ of $N = N_1^2$ components. Up to a pixel rearrangement,

3 | Rank-One Compression of Interferometric Sensing

each component f_j of \mathbf{f} is related to a specific sample of f° taken in the N -point grid.

$$\mathcal{G}_{(N_1, N_1)} := \frac{L}{N_1} \{(s_1, s_2)\}_{s_1, s_2 = -\frac{N_1}{2}}^{\frac{N_1}{2}-1} \subset \mathcal{D}.$$

The Discrete Fourier Transform (DFT) $\hat{\mathbf{f}}$ of \mathbf{f} is then computed from the 2-D DFT matrix $\mathbf{F} \in \mathbb{C}^{N \times N}$, i.e., $\hat{\mathbf{f}} = \mathbf{F}\mathbf{f} \in \mathbb{C}^N$, $\mathbf{F} := \mathbf{F}_1 \otimes \mathbf{F}_1$, with $(\mathbf{F}_1)_{kl} = e^{-\frac{i2\pi}{N_1} kl} / \sqrt{N_1}$, $k, l \in \llbracket N_1 \rrbracket$, and the Kronecker product \otimes . Each component of $\hat{\mathbf{f}}$ is related to a 2-D frequency of

$$\hat{\mathcal{G}}_{(N_1, N_1)} := \frac{W}{N_1} \{(\chi_1, \chi_2)\}_{\chi_1, \chi_2 = -\frac{N_1}{2}}^{\frac{N_1}{2}-1} \subset [-\frac{W}{2}, \frac{W}{2}]^2.$$

We now need to simplify our selection of the visibilities.

Assumption 3.3 (Distinct on-grid non-zero visibilities). *All non-zero visibilities in $\mathcal{V}_0 = \mathcal{V} \setminus \{\mathbf{0}\}$ belong to the regular grid $\hat{\mathcal{G}}_{(N_1, N_1)}$, i.e., $\mathcal{V}_0 \subset \hat{\mathcal{G}}_{(N_1, N_1)}$, and are unique, which means that $|\mathcal{V}_0| = Q(Q-1)$.*

Anticipating over Sec. 3.3.4, assumptions 3.1 and 3.2 show that $\mathcal{I}_\Omega[f^\circ]$ can be computed from $\mathbf{F}\mathbf{f}$; remembering the *unilateral* model (3.23) for the interferometric matrix, $\text{vec}(\mathcal{I}_\Omega[\mathbf{f}]) = \omega \mathbf{G}\mathbf{F}\mathbf{f}$ where $\omega := \frac{L^2}{\sqrt{N}}$ (valid for 2-D signals) can be found from the continuous interpolation formula of the Shannon-Nyquist sampling theorem. Consequently, if f° has zero mean, $(\mathbf{F}\mathbf{f})_0 = 0$ and $\mathbf{G} = \mathbf{R}_{\bar{\mathcal{V}}_0}$, yielding

$$\frac{1}{\omega^2} \|\mathcal{I}_\Omega[f^\circ]\|_{\mathbf{F}}^2 = \frac{1}{\omega^2} \|\text{vec}(\mathcal{I}_\Omega[f^\circ])\|^2 = \|\mathbf{R}_{\bar{\mathcal{V}}_0} \mathbf{F}\mathbf{f}\|^2, \quad (3.30)$$

with $\mathbf{R}_{\mathcal{S}} = \mathbf{I}_{\mathcal{S}}^\top$ the restriction operator defined for any $\mathcal{S} \subset \llbracket N \rrbracket$, and $\bar{\mathcal{V}}_0$ the index set of $\mathbf{F}\mathbf{f}$ related to the off-diagonal entries of $\mathcal{I}_\Omega[f^\circ]$ (with $|\mathcal{V}_0| = |\bar{\mathcal{V}}_0|$ from 3.3). One has $\bar{\mathcal{V}}_0 = \{\bar{l}(j, k) : j, k \in \llbracket Q \rrbracket, j \neq k\} \subset \llbracket N \rrbracket$ with $\bar{l} = l(j, k) \in \llbracket N \rrbracket$ such that $(\mathcal{I}_\Omega[f^\circ])_{j,k} = (\text{vec } \mathcal{I}_\Omega[f^\circ])_{\bar{l}}$.

We need to *regularize* the (ill-posed) MCFLI imaging problem by supposing that \mathbf{f} is *sparse* in the canonical basis.

Assumption 3.4 (Sparse sample image). *The discrete image \mathbf{f} is K -sparse (in the canonical basis): $\mathbf{f} \in \Sigma_K := \{\mathbf{v} : \|\mathbf{v}\|_0 \leq K\}$.*

While the provided guarantees are restrictive, our experiments in Sec. 3.5 show experimentally that other sparsity priors are compatible with our sensing scheme, *e.g.*, the TV norm. A theoretical justification of such possible extensions is challenging with the current literature.

Our theoretical analysis leverages the tools of compressive sensing theory [CRT06a; FR17]. In particular, as stated in the next assumption, we require that the interferometric matrix—actually, its non-diagonal entries encoded in the visibilities of \mathcal{V}_0 —captures enough information about any sparse image f .

Assumption 3.5 (RIP $_{\ell_2/\ell_2}$ for visibility sampling). *Given a sparsity level K , a distortion $\delta > 0$, and provided*

$$|\mathcal{V}_0| = Q(Q-1) \geq \delta^{-2} K \text{plog}(N, K, \delta), \quad (3.31)$$

for some polynomials plog($N, K, 1/\delta$) of $\log N$, $\log K$ and $\log 1/\delta$, the matrix $\Phi := \sqrt{N} \mathbf{R}_{\mathcal{V}_0} \mathbf{F}$ respects the RIP $_{\ell_2/\ell_2}(\Sigma_K, \delta)$, i.e.,

$$(1 - \delta) \|\mathbf{v}\|^2 \leq \frac{1}{|\mathcal{V}_0|} \|\Phi \mathbf{v}\|_2^2 \leq (1 + \delta) \|\mathbf{v}\|^2, \forall \mathbf{v} \in \Sigma_K. \quad (3.32)$$

As will be clear later, combined with (3.30), this assumption ensures that two different sparse images lead to two distinct interferometric matrices, a key element for stably estimating images from our sensing model (see Prop. 3.2).

We now specify the conditions on the distribution of the sketching vectors α .

Assumption 3.6 (Random sketches with unit modules). *The sketching vectors $\{\alpha_m\}_{m=1}^M$ involved in (3.6) have components i.i.d. as the random variable $\alpha \in \mathbb{C}$, with $\mathbb{E}\alpha = 0$ and $|\alpha| = 1$.*

The sketching vectors are thus sub-Gaussian, since the sub-Gaussian norm $\|\alpha_q\|_{\psi_2} = \|\|\alpha_q\|\|_{\psi_2} = 1$ is bounded (see [Ver10, Sec. 5.2.3]). While motivated by the MCFLI application where the SLM mainly acts on the phase of the core complex amplitudes, this assumption enables a *debiasing trick*, described in Sec. 3.3.3, which simplifies the theoretical analysis detailed in Sec. 3.3.4.

Rationale and Limitations of the Assumptions

Here we discuss the rationale and limitations of the assumptions. First, both Assumptions 3.3 and 3.5 are built on the multiset \mathcal{V}_0 (listing all the non-zero visibilities) and not \mathcal{V} . Anticipating over Sec. 3.3.4, this choice is imposed by the SROP measurements; they are strongly biased by the diagonal elements of the projected matrices (see also Lemma 3.1 in Sec. 3.7.1). As a result, we need a *debiased* sensing model (see Sec. 3.3.3)

3 | Rank-One Compression of Interferometric Sensing

removing the diagonal of the interferometric matrix, and hence the zero image frequency.

Second, while we do not prove that the visibility set \mathcal{V}_0 defined by the Fermat's spiral core arrangement Ω in MCFLI verifies Assumption 3.5, we invoke existing results characterizing compressive sensing with partial Fourier sampling—as established for instance in the context of tomographic and radio interferometric applications [CW08; Wia+09]—to prove the existence of a visibility set respecting 3.5. For example, from [FR17, Thm 12.31], if $Q(Q - 1) \geq C\delta^{-2}K\log^4(N)$ (for some constant $C > 0$) and the set of $Q(Q - 1)$ visibilities $\bar{\mathcal{V}}_0$ are picked uniformly at random in $\llbracket N \rrbracket$, then Φ respects the RIP $_{\ell_2/\ell_2}(\Sigma_K, \delta)$ with probability exceeding $1 - N^{-\log^3 N}$.

Third, as stated by Assumption 3.3, our analysis expects that each visibility, except the 0 frequency, is observed only once. However, for large values of Q (and certainly when $Q(Q - 1) > N$), low-frequency visibilities tend to occupy the same points in the gridded frequency domain $\hat{\mathcal{G}}_{(N_1, N_1)}$. For instance, for a 1-D configuration, the pdf of the visibilities would be centered and triangular—with thus increasing multiplicity at low-frequency—if the frequencies were drawn uniformly at random in a given frequency interval.

Relaxing Assumption 3.3 would require adapting our developments in new directions. To account for possible multiplicities in the visibilities, we can indeed introduce a weighting matrix W encoding the number of entries in $\mathcal{I}_\Omega[f^\circ]$ that are related to the same frequency, *i.e.*, using the notations defined above, $W_{qq} := |\{(j, k) : \bar{l}(j, k) = q\}|$, $1 \leq q \leq N$. In that case, (3.30) becomes

$$\frac{1}{\omega^2} \|\mathcal{I}_\Omega[f^\circ]\|_F^2 = \|WR_{\bar{\mathcal{V}}_0}Ff\|^2.$$

However, since our analysis requires that $\|WR_{\bar{\mathcal{V}}_0}Ff\|^2$ is approximately proportional to the norm of $\|f\|^2$ if f is sparse, *i.e.*, the matrix $\Phi' := WR_{\bar{\mathcal{V}}_0}F$ should respect the RIP [CRT06b], we then need to adapt Assumption 3.5 to that matrix. Unfortunately, as soon as $W \neq I$, recovering sparse signals from their random partial Fourier sampling imposes to reweight Φ' to cancel out the impact of W [KW14; Adc+17], both for ensuring the RIP of this matrix and for the stability of the numerical reconstructions. Unfortunately, as we only have access to the SROP of the interferometric matrix, *i.e.*, $\bar{y} = RGFf$, introducing this cancellation in our sensing model is out of the scope of this chapter. It is briefly discussed in the discussion “weighting the visibilities” in Sec. 4.7.

Finally, Assumption 3.4 is restricted to sparse signals in the canonical basis. Generalizing our recovery guarantees developed in Sec. 3.3.4 to general sparsifying bases $\Psi \neq \mathbf{I}$ is challenging and not done in this thesis. Certain bases, such as the Haar wavelet basis Ψ , include the constant vector. Assuming it is in the 1-st column of Ψ , we easily check that the RIP $_{\ell_2/\ell_2}$ in (3.32) can no longer hold for $\Phi = \sqrt{N}R_{\tilde{\mathcal{V}}_0}F\Psi$; since $\tilde{\mathcal{V}}_0$ excludes the DC frequency, taking $v = \lambda e_1 + e_k \in \Sigma_2$ with a sufficiently large value λ breaks (3.32) as $\Phi v = \sqrt{N}R_{\tilde{\mathcal{V}}_0}F\Psi e_k$.

3.3.3 Debiased Sensing Model

As made clear in Sec. 3.3.4, the estimation of f requires a *debiasing* of the MCFLI measurements imposed by the properties of the SROP operator \mathcal{A} in (3.4). This debiasing requirement can be seen as targeting the *isotropy* property of [CP11]. We follow a debiasing inspired by [Gué+22] (and allowed by Assumption 3.6), with a reduced number of measurements compared to the method proposed in [CCG15].

From (3.6), we define the *debiased* measurements

$$y_m^c := y_m - \frac{1}{M} \sum_{j=1}^M y_j = \langle A_m^c, \mathcal{I} \rangle_F + n_m^c,$$

with the centered and the average matrices $A_m^c = \alpha_m \alpha_m^* - A^a$ and $A^a = \frac{1}{M} \sum_{j=1}^M \alpha_j \alpha_j^*$, respectively, $\mathcal{I} := \mathcal{I}_\Omega[f^\circ]$, and noise $n_m^c := n_m - \frac{1}{M} \sum_{j=1}^M n_j$ with $\mathbb{E}|n_m^c|^2 = (1 - \frac{1}{M})\mathbb{E}|n_m|^2$.

Introducing the debiased sensing operator

$$\mathcal{A}^c : \mathcal{J} \in \mathcal{H}^Q \mapsto (\langle A_m^c, \mathcal{J} \rangle)_{m=1}^M \in \mathbb{R}^M, \quad (3.33)$$

which respects $\mathcal{A}^c(\mathcal{J}) = \mathcal{A}^c(\mathcal{J}_h)$ with the *hollow* matrix $\mathcal{J}_h := \mathcal{J} - \mathcal{J}_d$ (*i.e.*, $\text{diag}(\mathcal{J}_h) = \mathbf{0}$) since each A_m^c is hollow from Assumption 3.6, we can compactly write

$$\mathbf{y}^c = (y_1^c, \dots, y_M^c)^\top = \mathcal{A}^c(\mathcal{I}_h) + \mathbf{n}^c. \quad (3.34)$$

The debiasing model thus senses, through \mathcal{I}_h , the off-diagonal elements of $\mathcal{I}_\Omega[f^\circ]$. We will show below that the combination of \mathcal{A}^c with the interferometric sensing respects a variant of the RIP property, thus enabling image reconstruction guarantees.

3.3.4 Stable and Robust Recovery

We show now that we can estimate a sparse image f from its sensing (3.34). From Assumptions 3.1-3.6, it can be recast as

$$\mathbf{y}^c = \mathcal{B}(f) + \mathbf{n}^c, \quad (3.35)$$

3 | Rank-One Compression of Interferometric Sensing

where the sensing operator \mathcal{B} reads

$$\mathcal{B} : \mathbf{v} \in \mathbb{R}^N \mapsto \mathcal{A}^c(\mathcal{I}_\Omega[\mathbf{v}]) \in \mathbb{R}_+^M \quad (3.36)$$

with $\mathcal{I}_\Omega[\mathbf{v}]$ defined in (3.21). We propose to estimate f by solving the basis pursuit denoise program with an ℓ_1 -norm fidelity (or BPDN_{ℓ_1}), *i.e.*,

$$\tilde{f} = \arg \min_{v \in \mathbb{R}^N} \|v\|_1 \text{ s.t. } \|y^c - \mathcal{B}(v)\|_1 \leq \epsilon, \quad (\text{BPDN}_{\ell_1})$$

The specific ℓ_1 -norm fidelity of this program is motivated by the properties of the SROP operator \mathcal{A}^c , and this imposes us to set $\epsilon \geq \|n^c\|_1$ to reach feasibility. We indeed show below that \mathcal{B} , through its dependence on \mathcal{A}^c , respects a variant of the RIP, the $\text{RIP}_{\ell_2/\ell_1}(\Sigma_K, m_K, M_K)$: given a sparsity level K , and two constants $0 < m_K < M_K$, this property imposes

$$m_K \|v\| \leq \frac{1}{M} \|\mathcal{B}(v)\|_1 \leq M_K \|v\|, \quad \forall v \in \Sigma_K. \quad (3.37)$$

Under this condition, the error $\|f - \tilde{f}\|$ is bounded, *i.e.*, instance optimal [FR17]. This is shown in the following proposition (inspired by [CCG15, Lemma 2] and proven in Sec. 3.7.1).

Proposition 3.2 (ℓ_2/ℓ_1 instance optimality of BPDN_{ℓ_1}). *Given K , if there exists an integer $K' > 2K$ such that, for $k \in \{K', K + K'\}$, the operator \mathcal{B} has the $\text{RIP}_{\ell_2/\ell_1}(\Sigma_k, m_k, M_k)$ for constants $0 < m_k < M_k < \infty$, and if*

$$\frac{1}{\sqrt{2}} m_{K+K'} - M_{K'} \frac{\sqrt{K}}{\sqrt{K'}} \geq \gamma > 0, \quad (3.38)$$

then, for all f sensed through $y^c = \mathcal{B}(f) + n^c$ with bounded noise $\|n^c\|_1 \leq \epsilon$, the estimate \tilde{f} provided by BPDN_{ℓ_1} satisfies

$$\|f - \tilde{f}\| \leq C_0 \frac{\|f - f_K\|_1}{\sqrt{K'}} + D_0 \frac{\epsilon}{M}, \quad (3.39)$$

for two values $C_0 = \mathcal{O}(M_{K'}/\gamma)$ and $D_0 = \mathcal{O}(1/\gamma)$.

Notice that (3.38) is satisfied if

$$K' > 8 \left(\frac{M_{K'}}{m_{K+K'}} \right)^2 K, \quad (3.40)$$

in which case $\gamma = \frac{1}{2\sqrt{2}} m_{K+K'}$, and, from Sec. 3.7.1,
 $C_0 = 2(\sqrt{2} + 1)(M_{K'}/m_{K+K'}) + 2$ and $D_0 = 4(\sqrt{2} + 1)/m_{K+K'}$.

Interestingly, if both M and $Q(Q - 1)$ sufficiently exceed K , the operator \mathcal{B} respects the $\text{RIP}_{\ell_2/\ell_1}$ with high probability.

Proposition 3.3 ($\text{RIP}_{\ell_2/\ell_1}$ for \mathcal{B}). Assume that assumptions 3.1-3.6 hold, with 3.5 set to sparsity level $K_0 > 0$ and distortion $\delta = 1/2$ over the set Σ_{K_0} . For some values $C, c > 0$ and $0 < c_\alpha < 1$ only depending on the distribution of α , if

$$M \geq CK_0 \log\left(\frac{12eN}{K_0}\right), \quad Q(Q-1) \geq 4K_0 \text{plog}(N, K_0, \delta), \quad (3.41)$$

then, with probability exceeding $1 - 2 \exp(-cM)$, the operator \mathcal{B} respects the $\text{RIP}_{\ell_2/\ell_1}(\Sigma_{K_0}, \mathbf{m}_{K_0}, \mathbf{M}_{K_0})$ with

$$m_{K_0} > \frac{\omega c_\alpha}{3\sqrt{2}} \frac{\sqrt{|\mathcal{V}_0|}}{\sqrt{N}}, \quad \text{and} \quad M_{K_0} < \frac{8\omega}{3} \frac{\sqrt{|\mathcal{V}_0|}}{\sqrt{N}}. \quad (3.42)$$

In this proposition, proved in Sec. 3.7.2, the constants in (3.42) have not been optimized and may not be tight, e.g., they do not depend on K_0 .

Combining these last two propositions and using the (non-optimal) bounds (3.42) that are independent of K_0 , since $8(\mathbf{M}_{K'}/\mathbf{m}_{K+K'})^2 < \frac{1024}{c_\alpha^2}$, (3.40) holds if $K' > 1024K/c_\alpha^2$. Therefore, provided \mathcal{B} satisfies the

$\text{RIP}_{\ell_2/\ell_1}(\Sigma_{K_0}, \mathbf{m}_{K_0}, \mathbf{M}_{K_0})$ for $K_0 \in \{K', K + K'\}$, the instance optimality (3.39) holds with

$$C_0 < \frac{16(\sqrt{2}+2)}{c_\alpha} = \mathcal{O}(1), \quad D_0 = \mathcal{O}\left(\frac{\sqrt{N}}{\omega\sqrt{|\mathcal{V}_0|}}\right) = \mathcal{O}\left(\frac{N}{L^2Q}\right).$$

While the constraint on K' imposes a high lower bound on M when the sample complexity (3.41) is set to $K_0 = (K + K') > (1024/c_\alpha^2 + 1)K$ —as necessary to reach the RIP *w.h.p.*—the impact of the sparsity error $\|f - f_K\|$ in (3.39) is, however, attenuated by $1/\sqrt{K'} < c_\alpha/(32\sqrt{K})$.

For a fixed FOV L^2 , we also observe a meaningful amplification of the noise error by D_0 when the sampling grid $\mathcal{G}_{(N_1, N_1)}$ is too large compared to Q : if the number of pixels N is too small, 3.2 may not be verified, since the image bandwidth lower bounds N ; if N is too large the noise error in (3.39) is vacuous.

3 | Rank-One Compression of Interferometric Sensing

3.4 Recovery Analysis - Phase Transition Diagrams

We now compare our recovery guarantees with empirical reconstructions obtained on extensive Monte Carlo simulations with S trials and varying parameters K , Q , and M .

To save computations, we adopt a simplified setting where (3.35) is adapted to the sensing of 1-D zero mean sparse vectors in $\mathbb{R}^{N=256}$, without any vignetting, *i.e.*, $f^\circ = f$, and 1-D MCF core locations. At each simulation trial with fixed (K, Q, M) , we verified 3.1–3.4 by picking the 1-D cores locations $\{p_q\}_{q=1}^Q \subset \mathbb{R}$ uniformly at random without replacement in $[-\frac{N}{2}, \frac{N}{2}]$, and M sketching vectors $\{\alpha_m\}_{m=1}^M$ i.i.d. as $\alpha \in \mathbb{C}^Q$ with $\alpha_q \stackrel{\text{i.i.d.}}{\sim} e^{i\mathcal{U}[0, 2\pi)}$, $q \in [Q]$. A zero average vector $f \in \mathbb{R}^{N=256}$ was randomly generated with a K -sparse support picked uniformly at random in $[N]$, its K non-zero components obtained with K i.i.d. Gaussian values $\mathcal{N}(0, 1)$ to which we subtracted their average. Working only on the recovery of zero-average vectors f , no debiasing is needed and the sensing model is matched to the *unilateral* form (3.24) presented in Sec. 3.2.4. We have $\mathcal{B}(f) = RGF_1f$ (with $L = \lambda = z = 1$) using the 1-D DFT matrix F_1 .

To reconstruct f , we solved the (Lasso) program⁷ [VF08] adapted to our problem,

$$\tilde{f} = \arg \min_v \frac{1}{2} \|y^c - \mathcal{B}(v)\|_2^2 \text{ s.t. } \|v\|_1 \leq \tau \quad (3.43)$$

with $\tau = \|f\|_1$ set to the actual ℓ_1 -norm⁸ of the discrete object. Eq. (3.43) is equivalent to BP DN_{ℓ_1} in a noiseless setting (*i.e.*, $\epsilon = 0$) as it implies an equality constraint $y^c = \mathcal{B}(f)$ [FR17, Prop. 3.2]. In the sparse and noiseless sensing scenario set above, we thus expect from (3.39) in Prop. 3.2 that $\tilde{f} = f$ if \mathcal{B} is RIP $_{\ell_2/\ell_1}$, *i.e.*, if both M and $Q(Q-1)$ sufficiently exceeds K from Prop. 3.3.

In Fig. 3.6–3.8, the success rates—*i.e.*, the percentage of trials where the reconstruction SNR exceeded 40dB—were computed for S set to 80 and 100 trials per value of $(K, |\mathcal{V}|, M)$, respectively, and for a range of $(K, |\mathcal{V}|, M)$ specified in the axes. Since 3.3 was partially verified, we tested these rates in function of the **averaged** value of $|\mathcal{V}| \leq Q(Q-1)$ (which had a std $\leq 0.08N$) over the S trials instead of $Q(Q-1)$. In Fig. 3.6, which displays several transition curves of the success rate vs.

⁷We used SPGL1 [VF08] (Python module: <https://github.com/drrelyea/spgl1>).

⁸While this information is unavailable in practice, an appropriate value of the threshold τ can generally be estimated from the structure of the expected image, or heuristically by performing multiple reconstructions with different values.

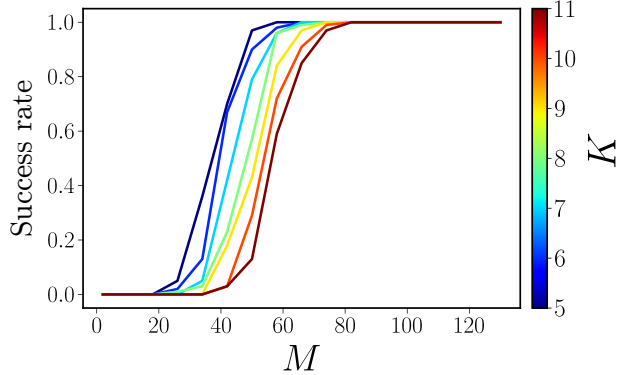


Fig. 3.6 Phase transition curves obtained with fixed $|\mathcal{V}| = 240$, ensuring widespread Fourier sampling. The success rate is computed from $S = 100$ trials. The transition abscissa shifts to the right for an increasing number K of spikes in f , indicating more SROP are necessary to reconstruct the interferometric matrix.

M for different values of K at $|\mathcal{V}| = 240$, the failure-success transition is shifted towards an increasing number of SROPs as K increases.

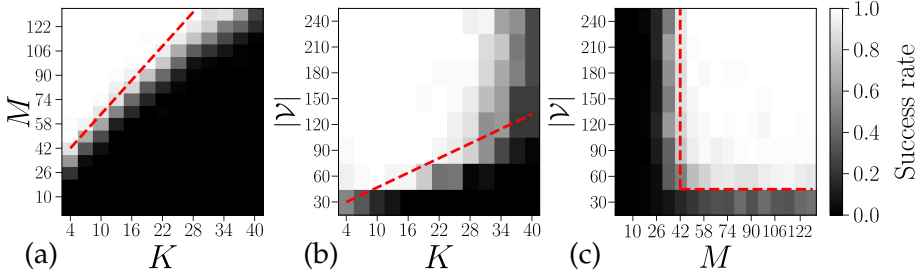


Fig. 3.7 Phase transition diagrams showing M SROP of a $Q \times Q$ interferometric matrix for a K -sparse object f (with $|\mathcal{V}| = 240$ in (a), $M = 122$ in (b), and $K = 4$ in (c)). One considers a uniformly random 1-D core arrangement and SROP using circularly-symmetric unit-norm random $\{\alpha_m\}_{m=1}^M$. Each pixel is constructed with $S = 80$ reconstruction trials solving (3.43) where we consider success if $\text{SNR} \geq 40\text{dB}$. The probability of success ranges from black (0%) to white (100%). Dashed red lines link the transition frontiers to the samples complexities provided in Sec. 3.3.2 and Sec. 3.3.4. In (b), the line coincides only with low values of \mathcal{V} due to multiplicity effects.

We observe in Fig. 3.7(a) that high reconstruction success is reached as soon as $M \geq CK$, with $C \simeq 11$, in accordance with (3.41) in Prop. 3.3 (up to log factors). Fig. 3.7(b) highlights that the Fourier sampling $|\mathcal{V}|$ (and thus Q) must increase with K . At small value of Q , we reach high reconstruction success if $|\mathcal{V}| \approx Q(Q-1) \geq C'K$, with $C' \simeq 10$, in agreement with (3.41) (up to log factors). However, as Q rises that linear trend is biased since the multiplicities in \mathcal{V} increases, *i.e.*, $Q(Q-1) - |\mathcal{V}| \geq 0$ increases. As expected from (3.41), the transition diagram in Fig. 3.7(c) shows that at a fixed $K = 4$, both M and

3 | Rank-One Compression of Interferometric Sensing

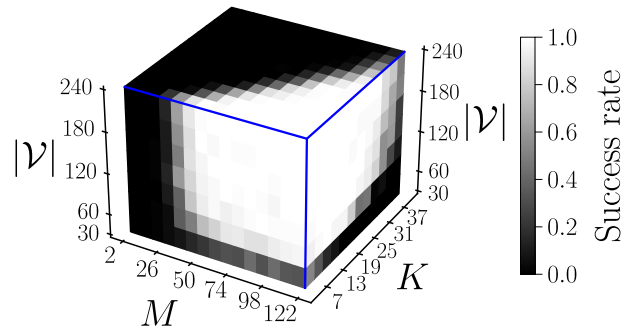


Fig. 3.8 Phase transition cube. The diagrams of Fig. 3.7 in a 3-D projection to better get the interdependence between the quantities (K , $|\mathcal{V}|$, M).

$|\mathcal{V}|$ must reach a threshold value to trigger high reconstruction success. The maps of Fig. 3.7 are replaced in a transition cube in Fig. 3.8 to give another insight into the sampling conditions for recovery.

3.5 Experimental MCFLI

This section stands out as it is the only part of the thesis where real experiments were conducted, providing a convincing demonstration that the theory can be applied in practice. In contrast, the results presented in the other parts on radio-interferometry and diffraction tomography are exclusively derived from numerical simulations. There are several reasons for this: real experiments require expensive equipment (such as optical tables, lasers, and other optical devices), ample space, a controlled environment, and a high level of experimental expertise, which is often hard to acquire. For the MCFLI experiments, I was fortunate to collaborate with a team of experts who possess extensive experimental experience.

We have tested our approach on a proof-of-concept imaging system set in a transmission mode so as to limit both light power loss and Poisson noise [Siv+18a] in the measurements. We describe below the key aspects of this setup, its specific *SLM-to-speckle* calibration, before providing examples of reconstructed images and studying the influence of the number of cores, and speckle illuminations on the quality of the reconstruction.

3.5.1 Setup

In the setup explained in Fig. 3.9, a continuous wave laser operating at $\lambda = 1053\text{nm}$, (YLM-1, IPG Photonics) is expanded and impinges upon a Spatial Light Modulator (SLM X10468-07, Hamamatsu) used to code the incident wavefront to the MCF. The MCF is made of $Q = 120$ cores arranged in Fermat's golden spiral (as shown in Fig. 3.1), each exhibiting a single mode at the laser wavelength [Gué+22]. Because of fabrication defects, a maximum of only 110 cores will be simultaneously used. The MCF exhibits an inter-core coupling term of less than 20 dB [Siv+18a]. Unlike multimode fibers with stronger core coupling, the focused or speckle patterns generated by an MCF are resilient to thermal and mechanical external perturbations.

The SLM consists of a 800×600 grid of liquid-crystal phase modulators that control the phase of reflected light. As shown in Fig. 3.10(a), by mapping specific pixel groups (segments) on the SLM to individual cores of the fiber, an orthogonal basis of input modes is created to modulate the light entering each core. After calibrating the SLM's phase response, any phase pattern in the range of $[0-2\pi]$ can be conveniently represented as an 8-bit grayscale image. The phase pattern

3 | Rank-One Compression of Interferometric Sensing

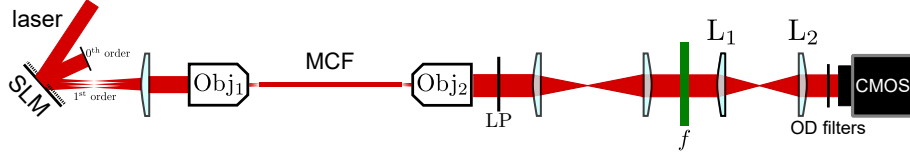


Fig. 3.9 Schematic of the optical setup. Cutoff $\lambda_c = 600\text{nm}$, SLM=Spatial Light Modulator, MCF=Multi-Core Fiber, LP=Linear Polarizer, f =object to be imaged, OD=Optical Density (neutral density filters).

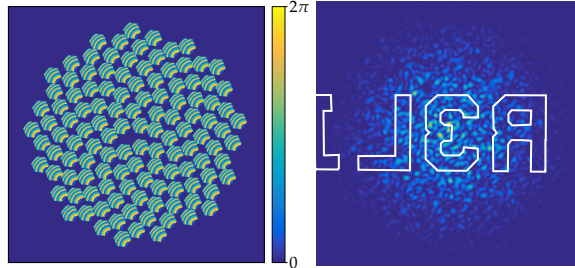


Fig. 3.10 (a) SLM configuration (800×600 pixels) with lenslet hexagonal arrays dedicated to each core. Blaze gratings applied to each microlens deflect the rays toward the proximal end of the MCF, while the 0^{th} beam is reflected out of the optical path. (b) Speckle generated from $\alpha = (e^{i\theta_q})_{q=1}^Q$ with $\theta_q \sim \mathcal{U}[0, 2\pi]$. The part of the speckle that reaches the camera is inside the white contours representing the examined object f .

on each segment q comprises three terms: (i) a blazed grating ensures to shift the modulated light to the first-order of the SLM, preventing unmodulated light from entering the fibers, (ii) a convex lens and a series of telescopes produce a focused spot array aligned with the fiber cores, achieving single-modal behavior with a demagnification factor of 64; and (iii) a constant phase-offset for each segment which controls the relative phases between the segments.

The light coming from the SLM is focused into the MCF proximal end by Obj₁ ($20\times/0.75$ Numerical Aperture (NA), Nikon), then re-expanded on the distal end side with Obj₂ ($20\times/0.45$ NA, Olympus). The dependence to fiber bending is avoided by placing the MCF straight. Under these conditions, the *transmission matrix*⁹ of the MCF remains constant and a single calibration phase is sufficient. However, it is possible to greatly attenuate the MCF sensitivity to external perturbation such as mechanical bending by twisting the MCF along the fiber during its manufacture [Tsv+19]. To ensure the validity of the scalar model described in Sec. 3.2, a *linear polarizer* is placed after the

⁹A matrix mapping the electric fields in the cores at the proximal end to the electric fields in the cores at the distal end of the MCF [Siv+18b].

fiber end to eliminate any polarization effects. To satisfy the *far-field* approximation (a key assumption for (3.2)), the object is positioned at the front-focal plane of a lens while the fiber's distal end is placed at the back-focal plane of the same lens [Goo05]. In our setup, the fiber is positioned at the focal plane of Objective lens (Obj_2), and lenses L_1 and L_2 (75 and 100mm, respectively) are used to re-image the conjugate focal plane to a more accessible location on the optical bench. The object can be positioned within $\pm 3.5\text{mm}$ tolerance, easily achieved with standard positioning equipment.

The conjugate focal plane is re-imaged onto a 1920×1200 CMOS camera (BFLY-U3-23S6M-C, FLIR) which aids in the calibration and positioning of the system described in Sec. 3.5.2. The same CMOS camera is also used for emulating single-pixel detection by summing up the pixels of the image. Each measurement has an integration time of 19.2ms, and Optical Density (OD) filters are applied to match the light intensity to the dynamic range of the camera for improved accuracy. Working in transmission mode, we image a negative 1951 USAF test target mask, contoured in Fig. 3.10(b). The sample image f is therefore binary.

3.5.2 Calibration and Generalized Sensing Model

Our MCFLI setup contains optical system imperfections that are difficult to model. For instance, regarding the hypotheses stated in Sec. 3.2, (i) the interferometric matrix should be estimated on a set of continuous, off-grid, visibilities, (ii) the imaging depth z is a priori unknown and the fiber core diameters are not constant, and (iii) the linear polarizer (see Sec. 3.5.1) induces spatially variable, but deterministic, attenuation of the sketching vector component.

Rather than correcting all these deviations one by one, we adopt the generalized MCFLI sensing introduced in Sec. 3.2.3 in (3.15). This requires us to properly calibrate the system and to determine for each core $q \in \llbracket Q \rrbracket$ the complex wavefields E_q in the object plane \mathcal{Z} from intensity-only measurements. We thus follow a standard 8-step phase-shifting interferometry technique [CLY04]. We first fix a reference core, arbitrarily indexed at $q = 0$, and we program the SLM to activate only that core and another core q , for $1 \leq q < Q$. We then record in the CMOS camera the 8 fringe patterns $I_{q0}(\mathbf{x}; \phi_k) := S(\mathbf{x}; e_0 + e_q e^{i\phi_k})$ (with the speckle definition from (3.14)) induced by the light interference for 8 different phase steps $\phi_k = \frac{2\pi k}{8}$ ($k \in \llbracket 8 \rrbracket$) of the reference core, as well as the intensity $I_{00}(\mathbf{x}; 0) = r_0^2(\mathbf{x})$ obtained from activating only the reference core. Mathematically, given the polar representation

3 | Rank-One Compression of Interferometric Sensing

$E_q(\mathbf{x}) := r_q(\mathbf{x})e^{i\varphi_q(\mathbf{x})}$ of each complex wavefields,

$$\begin{aligned} I_{q0}(\mathbf{x}; \phi_k) &= |r_0(\mathbf{x})e^{i\varphi_0(\mathbf{x})+\phi_k} + r_q(\mathbf{x})e^{i\varphi_q(\mathbf{x})}|^2 \\ &= I_q^s(\mathbf{x}) + I_q^i(\mathbf{x}) \cos(\varphi_{q0}(\mathbf{x}) + \phi_k), \end{aligned}$$

where $I_q^s := r_0^2 + r_q^2$, $I_q^i := 2r_0r_q$ and $\varphi_{q0} := \varphi_q - \varphi_0$. We can then recover $r_q(\mathbf{x})$ and $\varphi_{q0}(\mathbf{x})$ in each \mathbf{x} by first applying a 8-length DFT on $I_{q0}(\mathbf{x}; \phi_k)$ along the phase steps, and next dividing the last (7-th) DFT coefficient $4I_q^i(\mathbf{x})e^{i\varphi_{q0}(\mathbf{x})}$ by $8r_0(\mathbf{x}) = 8\sqrt{I_{00}(\mathbf{x})}$, which gives

$$\tilde{E}_q(\mathbf{x}) = r_q(\mathbf{x})e^{i(\varphi_q(\mathbf{x}) - \varphi_0(\mathbf{x}))} = E_q(\mathbf{x})e^{-i\varphi_0(\mathbf{x})}. \quad (3.44)$$

From the fields estimated in (3.44) for all $q \in \llbracket Q \rrbracket$, we can reproduce any speckle $S(\mathbf{x}; \alpha)$ generated from a sketching vector $\alpha \in \mathbb{C}^Q$ using (3.14) since this equation is independent of $e^{-i\varphi_0(\mathbf{x})}$.

While the model (3.15) extends beyond the far-field assumption—it only relies on accurate estimation of the wavefields—the optical constraints followed in Sec. 3.5.1 to reach the far-field model are necessary. They allow these fields not to strongly deviate from pure complex exponentials, which preserves the validity of the FOV and sampling assumptions 3.1 and 3.2 in the sensing model.

In particular, applying the debiasing procedure explained in Sec. 3.3.3, we get the debiased observation model

$$\mathbf{y}^c = \mathcal{B}(f) + \mathbf{n}^c, \quad (3.45)$$

where $\mathcal{B}(f)$ is now associated with the generalized interferometric matrix \mathcal{I}_Ω^G defined in (3.16). In other words, we abuse the notations of (3.35) and consider a sensing operator $\mathcal{B} : h \mapsto \mathcal{B}(h) := \mathcal{A}^c(\mathcal{I}_\Omega^G[h])$ applied to a non-vignetted continuous image h . Regarding the computation of \mathcal{B} , we leverage the calibration to compute an estimate $\tilde{\mathcal{B}}(h) := \mathcal{A}^c(\tilde{\mathcal{I}}_\Omega^G[h])$ from a sampling $\mathbf{h} \in \mathbb{R}^N$ of h , assuming that the proximity to the far-field assumption ensures that $\mathcal{B}(h) \approx \tilde{\mathcal{B}}(h)$. For each measurement $m \in \llbracket M \rrbracket$, we in fact compute $z_m = \langle \tilde{S}(\cdot; \alpha_m), \mathbf{h} \rangle$, with $\tilde{S}(\cdot; \alpha_m)$ computed from the estimated fields in (3.44), before debiasing all the measurements from (3.3.3), i.e., $(\tilde{\mathcal{B}}(\mathbf{h}))_m = z_m^c$. Therefore, the matrix $\tilde{\mathcal{I}}_\Omega^G$ is never explicitly estimated.

3.5.3 Results

We now present examples of reconstructed sample images obtained with the considered optical setup described in Sec. 3.5.1, and the calibration and the sensing model from Sec. 3.5.2.

For these experiments, our reconstruction scheme differs from the one followed in Sec. 3.3. First, as explained in Sec. 3.5.2, the sensing model considers a sampling of the un-vignetted sample image f , with a sensing operator computed in the pixel domain. Second, instead of the ℓ_1 -prior, we decided to estimate this image by promoting a small Total Variation (TV) norm, as it is better adapted to the cartoon-shape model of the USAF targets. This deviation from the theoretical setting described in Sec. 3.3 aims to provide insight into whether the proposed SROP model and its associated single calibration can also reconstruct images more realistically than sparse images. Third, the non-smooth data-fidelity term of BPDN_{ℓ_1} is replaced by a smooth quadratic ℓ_2 -norm to facilitate the iterative computation of the associated convex optimization. Thus, we solve the following optimization scheme:

$$\tilde{f} = \arg \min_f \frac{1}{2M} \|y^c - \tilde{\mathcal{B}}(f)\|_2^2 + \rho \|f\|_{\text{TV}} \text{ s.t. } f \geq 0, \quad (3.46)$$

with ρ empirically set to $2 \cdot 10^6$. Since vignetting limits the image quality at the boundary of the FOV, we decided to measure the quality of the estimated images with the SNR achieved between the vignetted ground truth $wf := w \cdot f$ and the vignetted reconstruction $w\tilde{f} := w \cdot \tilde{f}$, i.e., $\text{SNR}(f, \tilde{f}) = 20 \log_{10}(\|wf\|_2 / \|wf - w\tilde{f}\|_2)$ with the estimated vignetting $w := Q^{-1} \sum_{q=1}^Q |\tilde{E}_q|^2$.

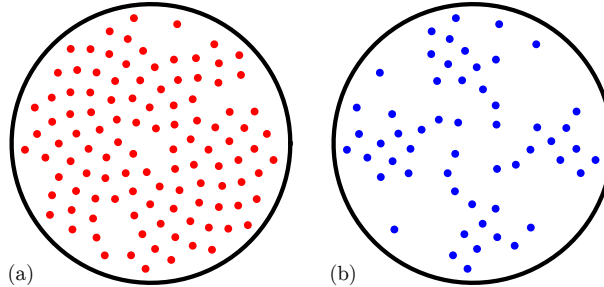


Fig. 3.11 Cores activated for the reconstructions shown in Fig. 3.12. (a) $Q = 110$ (b) $Q = 55$.

Experimental reconstruction analyses are provided in Fig. 3.12 for images of $N = 256 \times 256$ pixels. In accordance with 3.6, the phase of the Q components of the sketching vectors were uniformly drawn i.i.d. in $[0, 2\pi)$ with the 8-bit resolution allowed by the SLM. This configuration maximizes the intensity of light injected in the cores. We tested two values for Q , $Q = 110$, when all the MCF cores are used, and $Q = 55$, by downsampling the Fermat's spiral by a factor 2, as depicted in Fig. 3.11. In Fig. 3.12(a), we tested the quality of the recon-

3 | Rank-One Compression of Interferometric Sensing

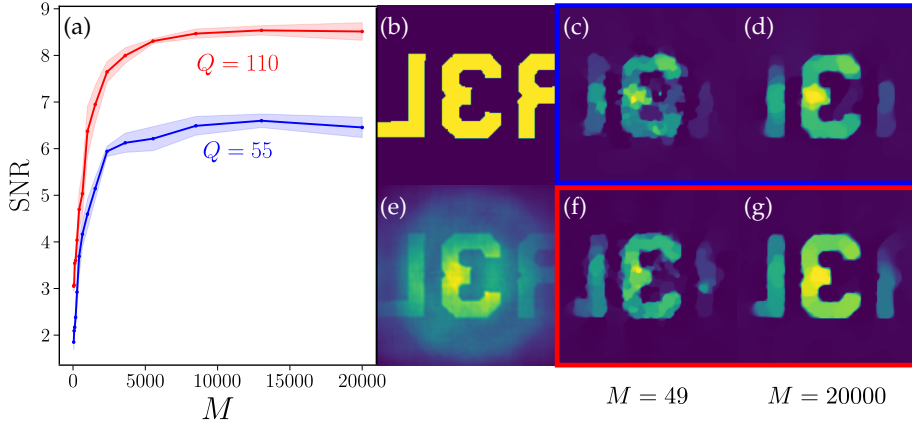


Fig. 3.12 Experimental reconstruction on images with $N = 256 \times 256$ pixels. (a) $\text{SNR}(\tilde{w}\tilde{f}, w\tilde{f})$ vs. number of observations M for $Q = 55$ (blue) and $Q = 110$ (red) cores. Solid lines represent the average, and light areas show $\pm 1\sigma$ positions from 5 trials. (b) Ground truth f obtained by illuminating the USAF target with white light passing through the MCF (c-d) Reconstruction using $M = \{49, 2 \cdot 10^4\}$ with $Q = 55$ cores (e) Rec. in RS mode (see Sec. 3.2.2) (f-g) Same as (c-d) with $Q = 110$ cores. (b-g) are zoomed-in versions of the camera plane seen in Fig. 3.10(b).

struction for $M \in [49, 20\,000]$ in comparison with an imperfect “ground truth”(GT) f estimated by white light illumination through the MCF, shown in Fig. 3.12(b). Transitions similar to those in Fig. 3.6 occur for a small number of observations and a plateau is reached around $M = 5000$, representing a compression factor of $M/N = 7.6\%$. The highest SNR reached with $Q = 110$ cores is better than with $Q = 55$ cores, as higher image frequencies are captured with the denser core configuration. This effect can also be viewed in Fig. 3.12(c-d,f-g).

In Fig. 3.12(e), we show the *backprojection* of the interferometric matrix, *i.e.*, $f_{\text{BP}} = \mathcal{I}_{\Omega}^{G*}(\mathcal{I}_{\Omega}^G[f])$. The reconstruction SNR is 1.38dB. In a nutshell, f_{BP} is obtained by computing the inverse Fourier transform of the partial Fourier sampling encoded in \mathcal{I}_{Ω}^G . This corresponds to the best reconstruction achievable in RS mode modeled in Sec. 3.2.2 without an *a posteriori* deconvolution step, *i.e.*, without regularization. Compared to the reconstruction obtained in Fig. 3.12(e) with the RS mode, the TV norm penalty reduces the blur of the reconstructed object. The low SNR values attained in Fig. 3.12 are due to the comparison of the reconstructed images with the imperfect “ground truth” f which is also an estimation of the true sample f .

3.6 Discussion

What has been done

In this chapter, we extended the modeling of MCFLI with speckle illumination by including the physics of light propagation. This new model highlights that the sensing of a 2-D refractive index map of interest is limited both by the number M of applied illuminations and the number Q (and arrangement) of cores at the distal end of the MCF. We provided recovery guarantees and observed the derived sample complexities in both numerical and experimental conditions.

In the Next Chapter

Here, two quantities were involved in the sample complexity of the sensing model, namely Q and M . In MCFLI, the Fourier subsampling operator W is fixed once and for all by design. In Chap. 4, the sensing will benefit from a time-varying W , hence allowing for a denser Fourier coverage. In the discussion of Chap. 4, we also briefly discuss clever ways to do joint calibration and imaging [Dab+21]; an idea which is also applicable to MCFLI and was unknown to the contributors at the time these contributions were made.

Limits and Open Questions

Guarantees Future research could extend our recovery guarantees in Sec. 3.3 to general sparsifying bases $\Psi \neq \mathbf{I}$. This would require particularizing our proofs to sparse signals with zero mean, *i.e.*, belonging to $\Sigma_K^0 := \{v \in \Sigma_K : \sum_j (\Psi v)_j = 0\}$.

As announced in Sec. 3.3, a limitation of our approach lies in the distinct visibilities Assumption 3.3. By construction, the density of the visibilities—as achieved by a difference set—cannot be uniform. As shown in Fig. 3.4, this is also true for the golden Fermat’s spiral arrangement. Therefore, when Q grows on a fixed frequency resolution, close visibilities are hardly distinguishable. A more promising sensing model could integrate a variable density sampling (VDS) of the image spectral domain [PVW11; Adc+17]. At the same time, this could also allow for more general sparsifying basis by accounting for their variable local coherence with the Fourier basis. However, combining this aspect within the ROP model is an open question.

3 | Rank-One Compression of Interferometric Sensing

Experiments In a first step, a truly single-pixel sensing reconstruction may be demonstrated. This requires an optical setup designed for swapping the camera used for the calibration detailed in Sec. 3.5.2 and a photo-detector, which was not the case for our experiments.

The MCF used in this work is made with straight cores, indicating that a fiber bending modifies its transmission matrix. This explains why, in our experiments, the MCF was fixed straight on the optical bench. We look forward to experimental reconstructions using a twisted MCF whose transmission matrix has been shown to be robust to fiber bending [Tsv+19].

Future works on MCFLI also include experimental proof of concept under reflective/endoscopic conditions. This endoscopic imaging is more challenging because the factor $0 < c < 1$, which gives the fraction of light collected by the single-pixel detector, can be very small. In low-light conditions, other types of noise tamper the measurements—*e.g.*, *Poisson noise* [SGR23]—thus making the inverse problem more challenging.

Extensions The proposed sensing model is a scalar model—it does not include any polarization effect. Besides this brought us to place a linear polarizer in our setup (see Fig. 3.9). An extension of the model to *vector diffraction theory* would allow taking the polarization effect into account.

Also, assuming that we only image a far-field 2-D plane perpendicular to the MCF axis is incorrect. In practice, the light emitted by the MCF propagates into a 3-D volume, and consequently interacts with the entire volume. While temporal focusing is a good candidate to get closer to this 2-D assumption, an interesting track is to explore the capabilities of imaging 3-D maps with generalized ROP models.

Coming back to the current rivalry between MCFs and MMFs, a model explaining the speckles produced by MMFs in the same fashion as done for the MCFs would allow to study a sensing model very similar to MCFLI (we would undoubtably call it “MMFLI”). In this case, a symmetric model includes an Hermitian *modal matrix* whose coefficients relate to the pairs of modes (instead of cores), and a *sketching* vector that also directly controls each mode. The subtle difference in MMFLI is that this anticipated model would not be interferometric.

Thus, it would include an intermediate forward operator other than the Fourier transform F to explain the modal matrix. An open question is the form and possible ways to accelerate the computation of this operator. However, a second quantity; the number of modes Q —analogous to the number of cores in MCFLI—would determine the sample complexity of this compressive imaging model.

Broader framework The MCFLI model highlighted a sensing conditioned by a two-component sample complexity. An interesting review in the CI community would present all the compressive imaging modalities—interferometric or not—that present this *two-or-more-component* sampling in a discrete-to-discrete sensing model.

3 | Rank-One Compression of Interferometric Sensing

3.7 Proofs

3.7.1 Proof of Prop. 3.2

The proof of this proposition is inspired by that of [CCG15, Lemma 2], itself inspired by [Can08]. This lemma was developed in the context of sparse matrix recovery from SROP measurements using a variant of BPDN regularized by the trace of the matrix estimate. While certain elements of our proof are similar to the one of that lemma, its adaptation to the context of sparse signal recovery from BPDN_{ℓ_1} (with a ℓ_1 fidelity) is not direct, which justifies the following compact derivations.

Let us first write $\tilde{f} = f + h$ with the true image f , and some residual $h \in \mathbb{R}^N$. We define the support $T_0 = \text{supp } f_K$ containing the indices of the K strongest entries of f . Next, recursively for $1 \leq i \leq \lceil (N - K)/K' \rceil$, we define the supports $T_i := \text{supp } (\mathbf{h}_{T_0^c})_{K'}$ of length at most K' containing the indices of the K' strongest entries of $\mathbf{h}_{T_0^c}$, with $T_{:i} := \bigcup_{j=0}^{i-1} T_j$, and $T_{:i}^c = [N] \setminus T_{:i}$.

We first observe that, by construction, for all $j \in T_{i+1}$ with $i \geq 1$, $|h_j| \leq \frac{1}{K'} \sum_{l \in T_i} |h_l| = \frac{1}{K'} \|\mathbf{h}_{T_i}\|_1$ so that $\|\mathbf{h}_{T_{i+1}}\|^2 \leq \frac{1}{K'} \|\mathbf{h}_{T_i}\|_1^2$. This shows that

$$\sum_{i \geq 2} \|\mathbf{h}_{T_i}\|_2 \leq \frac{1}{\sqrt{K'}} \sum_{i \geq 1} \|\mathbf{h}_{T_i}\|_1 = \frac{1}{\sqrt{K'}} \|\mathbf{h}_{T_0^c}\|_1. \quad (3.47)$$

By optimality of \tilde{f} in BPDN_{ℓ_1} and using twice the triangular inequality, we have

$$\begin{aligned} \|f\|_1 &\geq \|\tilde{f}\|_1 = \|f + h\|_1 \geq \|f_{T_0} + h\|_1 - \|f_{T_0^c}\|_1 \\ &\geq \|f_{T_0}\|_1 + \|\mathbf{h}_{T_0^c}\|_1 - \|\mathbf{h}_{T_0}\|_1 - \|f_{T_0^c}\|_1, \end{aligned}$$

so that

$$\|\mathbf{h}_{T_0^c}\|_1 \leq 2\|f_{T_0^c}\|_1 + \|\mathbf{h}_{T_0}\|_1 \leq 2\|f_{T_0^c}\|_1 + \sqrt{K} \|\mathbf{h}_{T_0}\|. \quad (3.48)$$

Therefore, combining (3.47) and (3.48) we get

$$\sum_{i \geq 2} \|\mathbf{h}_{T_i}\|_2 \leq 2 \frac{\|f_{T_0^c}\|_1}{\sqrt{K'}} + \frac{\sqrt{K}}{\sqrt{K'}} \|\mathbf{h}_{T_0}\|_2. \quad (3.49)$$

By linearity of \mathcal{B} and since both f and \tilde{f} are feasible vectors of the BPDN_{ℓ_1} constraint, we note that since $h = f - \tilde{f}$

$$\|\mathcal{B}(h)\|_1 \leq \|\mathcal{B}(f) - \mathbf{y}^c\|_1 + \|\mathcal{B}(\tilde{f}) - \mathbf{y}^c\|_1 \leq 2\epsilon.$$

Therefore, if \mathcal{B} has the RIP $_{\ell_2/\ell_1}(\Sigma_k, \mathbf{m}_k, \mathbf{M}_k)$ for $k \in \{K', K + K'\}$, we can develop the following inequalities

$$\begin{aligned} \frac{2\epsilon}{M} &\geq \frac{1}{M} \|\mathcal{B}(\mathbf{h})\|_1 \geq \frac{1}{M} \|\mathcal{B}(\mathbf{h}_{T_{1:}})\|_1 - \frac{1}{M} \|\mathcal{B}(\mathbf{h}_{T_{1:}^c})\|_1 \\ &\geq \mathbf{m}_{K+K'} \|\mathbf{h}_{T_{1:}}\|_2 - \frac{1}{M} \sum_{i \geq 2} \|\mathcal{B}(\mathbf{h}_{T_i})\|_1 \\ &\geq \frac{1}{\sqrt{2}} \mathbf{m}_{K+K'} (\|\mathbf{h}_{T_0}\|_2 + \|\mathbf{h}_{T_1}\|_2) - \frac{1}{M} \sum_{i \geq 2} \|\mathcal{B}(\mathbf{h}_{T_i})\|_1 \\ &\geq \frac{1}{\sqrt{2}} \mathbf{m}_{K+K'} (\|\mathbf{h}_{T_0}\|_2 + \|\mathbf{h}_{T_1}\|_2) - \mathbf{M}_{K'} \sum_{i \geq 2} \|\mathbf{h}_{T_i}\|_2 \\ &\geq \frac{1}{\sqrt{2}} \mathbf{m}_{K+K'} (\|\mathbf{h}_{T_0}\|_2 + \|\mathbf{h}_{T_1}\|_2) - \mathbf{M}_{K'} \frac{2\|f_{T_0^c}\|_1 + \sqrt{K'} \|\mathbf{h}_{T_0}\|_2}{\sqrt{K'}}, \end{aligned}$$

where we used several times the triangular inequality, the fact that $|T_i| = K'$ for $i \geq 1$, and (3.49) in the last inequality. The passage from the second to the third line is due to $\|\mathbf{h}_{T_{1:}}\|^2 = \|\mathbf{h}_{T_0}\|^2 + \|\mathbf{h}_{T_1}\|^2 \geq (\|\mathbf{h}_{T_0}\| + \|\mathbf{h}_{T_1}\|)^2/2$.

Therefore, rearranging the terms, and since $\|f_{T_0^c}\|_1 = \|f - f_K\|_1$, we get

$$\begin{aligned} \frac{2\epsilon}{M} + 2\mathbf{M}_{K'} \frac{\|f - f_K\|_1}{\sqrt{K'}} &\geq \left(\frac{1}{\sqrt{2}} \mathbf{m}_{K+K'} - \mathbf{M}_{K'} \frac{\sqrt{K}}{\sqrt{K'}} \right) \|\mathbf{h}_{T_0}\| + \frac{\mathbf{m}_{K+K'}}{\sqrt{2}} \|\mathbf{h}_{T_1}\| \\ &\geq \left(\frac{1}{\sqrt{2}} \mathbf{m}_{K+K'} - \mathbf{M}_{K'} \frac{\sqrt{K}}{\sqrt{K'}} \right) (\|\mathbf{h}_{T_0}\| + \|\mathbf{h}_{T_1}\|). \end{aligned} \tag{3.50}$$

Finally, if $\frac{1}{\sqrt{2}} \mathbf{m}_{K+K'} - \mathbf{M}_{K'} \frac{\sqrt{K}}{\sqrt{K'}} \geq \gamma > 0$ and $K' > 2K$, then

$$\begin{aligned} \|f - \tilde{f}\| &= \|\mathbf{h}\| \leq \|\mathbf{h}_{T_0}\| + \|\mathbf{h}_{T_1}\| + \sum_{i \geq 2} \|\mathbf{h}_{T_i}\| \\ &\stackrel{(3.49)}{\leq} \|\mathbf{h}_{T_0}\| + \|\mathbf{h}_{T_1}\| + 2 \frac{\|f_{T_0^c}\|_1}{\sqrt{K'}} + \frac{\sqrt{K}}{\sqrt{K'}} \|\mathbf{h}_{T_0}\| \\ &\leq \frac{\sqrt{2}+1}{\sqrt{2}} (\|\mathbf{h}_{T_0}\| + \|\mathbf{h}_{T_1}\|) + 2 \frac{\|f_{T_0^c}\|_1}{\sqrt{K'}} \\ &\stackrel{(3.50)}{\leq} \frac{2+\sqrt{2}}{\gamma} \left(\frac{\epsilon}{M} + \mathbf{M}_{K'} \frac{\|f - f_K\|_1}{\sqrt{K'}} \right) + 2 \frac{\|f_{T_0^c}\|_1}{\sqrt{K'}}. \end{aligned}$$

This thus proves the instance optimality (3.39) by taking

$$C_0 = \frac{2+\sqrt{2}}{\gamma} \mathbf{M}_{K'} + 2, \text{ and } D_0 = \frac{2+\sqrt{2}}{\gamma}.$$

3.7.2 Proof of Prop. 3.3

The proof of Prop. 3.2 below shows that the intermediate (debiased) SROP operator \mathcal{A}^c does not have to satisfy a RIP on its own, which

3 | Rank-One Compression of Interferometric Sensing

would have been required if it was used to recover a sparse Fourier sampling vector provided by $\mathbf{R}_{\bar{\mathcal{V}}_0} F f$. In this proof, we associate the RIP $_{\ell_2/\ell_2}$ assumed to be satisfied by the Fourier sampling (see Assumption 3.5) with a concentration of the debiased SROP measurements in their ℓ_1 -norm to provide a RIP $_{\ell_2/\ell_1}$ on the composed forward operator. This procedure can be seen as a *RIP preservation*.

We will need the following lemmata to prove Prop. 3.3. We first need to prove that $\|\mathcal{A}^c(\mathcal{I})\|_1$, with \mathcal{A}^c defined in (3.33) concentrates around its mean. This slightly extends [CCG15, Prop. 1] where the authors rather proved that the *debiased* operator \mathcal{A}' —such that, for any matrix \mathcal{I} and an even number of measurements $M = 2M'$, $\mathcal{A}'(\mathcal{I})_i := \mathcal{A}(\mathcal{I})_{2i+1} - \mathcal{A}(\mathcal{I})_{2i}$ for $i \in \llbracket M' \rrbracket$ —respects the RIP $_{\ell_2/\ell_1}$. This debiasing is introduced to ensure that $\mathbb{E}\mathcal{A}'(\mathcal{I}) = \mathbf{0}$. We show that this is also true for \mathcal{A}^c .

We first show some useful facts about \mathcal{A} and \mathcal{A}^c .

Lemma 3.1 (Mean and anisotropy of the SROP operator). *Given an Hermitian matrix $\mathcal{I} \in \mathcal{H}^Q$, a zero-mean complex random variable α with $\mathbb{E}\alpha^2 = 0$, and bounded second and fourth moments $\mathbb{E}|\alpha|^2 = \mu_2$, and $\mathbb{E}|\alpha|^4 = \mu_4$, and a set of random vectors $\{\boldsymbol{\alpha}_m\}_{m=1}^M \subset \mathbb{C}^M$ with components i.i.d. as $\alpha_{mq} \sim \alpha$ (for $m \in \llbracket M \rrbracket$, $q \in \llbracket Q \rrbracket$), the SROP operator \mathcal{A} associated with $\{\boldsymbol{\alpha}_m\}_{m=1}^M$ is such that*

$$\mathbb{E}\mathcal{A}_m(\mathcal{I}) = \mathbb{E}\langle \boldsymbol{\alpha}_m \boldsymbol{\alpha}_m^*, \mathcal{I} \rangle = \mu_2 \operatorname{tr} \mathcal{I}, \quad \forall m \in \llbracket M \rrbracket \quad (3.51)$$

$$\frac{1}{M}\mathbb{E}\mathcal{A}^*\mathcal{A}(\mathcal{I}) = \mu_2^2 \mathcal{I} + (\mu_4 - 2\mu_2^2) \mathcal{I}_d + \mu_2^2 (\operatorname{tr} \mathcal{I}) \mathbf{I}, \quad (3.52)$$

where the operator \mathcal{A}^* is the adjoint (see def. 2.2.1) of \mathcal{A} with

$$\mathcal{A}^* : z \in \mathbb{R}^M \mapsto \mathcal{A}^*(z) := \sum_{m=1}^M z_m \boldsymbol{\alpha}_m \boldsymbol{\alpha}_m^* \in \mathcal{H}^Q,$$

and the matrix $\mathcal{I}_d := \operatorname{diag}(\operatorname{diag}(\mathcal{I}))$ zeroes all but the diagonal entries of \mathcal{I} . Therefore, if $\mathcal{I}, \mathcal{J} \in \mathcal{H}^Q$ with \mathcal{I} hollow, then

$$\mathbb{E}\mathcal{A}^c(\mathcal{J}) = \mathbf{0}, \quad \mathbb{E}\mathcal{A}(\mathcal{I}) = \mathbf{0}, \quad \text{and} \quad \frac{1}{M}\mathbb{E}\mathcal{A}^*\mathcal{A}(\mathcal{I}) = \mu_2^2 \mathcal{I}.$$

Proof. Eq. (3.51) is an immediate consequence of $\mathbb{E}\boldsymbol{\alpha}_m \boldsymbol{\alpha}_m^* = \mu_2 \mathbf{I}$. Regarding (3.52), we first note that $\mathbb{E}\mathcal{A}^*\mathcal{A}\mathcal{I} = \mathbb{E}\sum_{m=1}^M (\boldsymbol{\alpha}_m^* \mathcal{I} \boldsymbol{\alpha}_m) \boldsymbol{\alpha}_m \boldsymbol{\alpha}_m^* = M\mathbb{E}(\boldsymbol{\alpha}^* \mathcal{I} \boldsymbol{\alpha}) \boldsymbol{\alpha} \boldsymbol{\alpha}^*$, and for $q, r \in \llbracket Q \rrbracket$, $[\mathbb{E}(\boldsymbol{\alpha}^* \mathcal{I} \boldsymbol{\alpha}) \boldsymbol{\alpha} \boldsymbol{\alpha}^*]_{qr} = \sum_{j,k=1}^Q \mathcal{I}_{j,k} \mathbb{E}(\boldsymbol{\alpha}_j^* \boldsymbol{\alpha}_k \boldsymbol{\alpha}_q \boldsymbol{\alpha}_r^*)$.

If $q = r$, then $\mathbb{E}(\boldsymbol{\alpha}_j^* \boldsymbol{\alpha}_k \boldsymbol{\alpha}_q \boldsymbol{\alpha}_r^*) = \mathbb{E}(\boldsymbol{\alpha}_j^* \boldsymbol{\alpha}_k |\boldsymbol{\alpha}_q|^2)$ is zero if $j \neq k$, μ_2^2 if

$j = k \neq q$, and μ_4 if $j = k = q$. Therefore,

$$\begin{aligned} [\mathbb{E}(\alpha^* \mathcal{I} \alpha) \alpha \alpha^*]_{qq} &= \sum_{j=1}^Q \mathcal{I}_{j,j} \mathbb{E}(|\alpha_j|^2 |\alpha_q|^2) \\ &= \mu_2^2 \text{tr}(\mathcal{I}) + (\mu_4 - \mu_2^2) \mathcal{I}_{qq}. \end{aligned}$$

If $q \neq r$, then $\mathbb{E}(\alpha_j^* \alpha_k \alpha_q \alpha_r^*)$ is non-zero only if $j = q$ and $k = r$ (since $\mathbb{E}\alpha^2 = 0$ and $\mathbb{E}|\alpha|^2 = \mu_2$), in which case it is equal to μ_2^2 . Consequently, $[\mathbb{E}(\alpha^* \mathcal{I} \alpha) \alpha \alpha^*]_{qr} = \mu_2^2 \mathcal{I}_{q,r}$. Gathering these identities, we finally find (3.52). \square

The next lemma (adapted from [CCG15, App. A]) relates the expectation of $\|\mathcal{A}(\mathcal{I})\|_1$ to the Frobenius norm of hollow matrices \mathcal{I} ; a useful fact for studying below the concentration of $\|\mathcal{A}(\mathcal{I})\|_1$.

Lemma 3.2 (Controlling the expected SROP ℓ_1 -norm). *In the context of Lemma 3.1, if the random variable α has unit second moment ($\mu_2 = 1$) and bounded sub-Gaussian norm $\|\alpha\|_{\psi_2} \leq \kappa$ (with $\kappa \geq 1$), then, for any hollow matrix $\mathcal{I} \in \mathcal{H}^Q$, the random variable $\xi := \alpha^* \mathcal{I} \alpha$ is sub-exponential with norm $\|\xi\|_{\psi_1} \leq \kappa^2$, and there exists a value $0 < c_\alpha < 1$, only depending on the distribution of α , such that*

$$c_\alpha \|\mathcal{I}\|_{\text{F}} \leq \frac{1}{M} \mathbb{E} \|\mathcal{A}(\mathcal{I})\|_1 = \mathbb{E} |\xi| \leq \|\mathcal{I}\|_{\text{F}}. \quad (3.53)$$

Proof. The proof is an easy adaptation of [CCG15, App. A] to the random variable $\xi = \langle \alpha \alpha^*, \mathcal{I} \rangle_{\text{F}} = \alpha^* \mathcal{I} \alpha$, for \mathcal{I} hollow. The constant c_1 (Eq. 50) in that work is here set to 1 since $(\mathbb{E}|\alpha^* \mathcal{I} \alpha|)^2 \leq \mathbb{E}|\alpha^* \mathcal{I} \alpha|^2 = \frac{1}{M} \mathbb{E} \|\mathcal{A}(\mathcal{I})\|_2^2 = \|\mathcal{I}\|_{\text{F}}^2$. \square

The following lemma leverages the result above to characterize the concentration of $\frac{1}{M} \|\mathcal{A}(\mathcal{I})\|_1$.

Lemma 3.3 (Concentration of SROP in the ℓ_1 -norm). *In the context of Lemmata 3.1 and 3.2, given a hollow matrix $\mathcal{I} \in \mathcal{H}^Q$, there exists a value $0 < c_\alpha < 1$, only depending on the distribution of α , such that, for $t \geq 0$, with a failure probability smaller than $2 \exp(-cM \min(t^2, t))$,*

$$(c_\alpha - 2t\kappa^2) \|\mathcal{I}\|_{\text{F}} \leq \frac{1}{M} \|\mathcal{A}(\mathcal{I})\|_1 \leq (1 + 2t\kappa^2) \|\mathcal{I}\|_{\text{F}}. \quad (3.54)$$

Proof. We can assume $\|\mathcal{I}\|_{\text{F}} = 1$ by homogeneity of (3.54). Defining the random variables $\xi_m := \alpha_m^* \mathcal{I} \alpha_m$ and $\tilde{\xi}_m := |\xi_m| - \mathbb{E}|\xi_m|$ for $m \in \llbracket M \rrbracket$, Lemma 3.2 shows that each ξ_m is sub-exponential with $\|\xi_m\|_{\psi_1} \leq$

3 | Rank-One Compression of Interferometric Sensing

κ^2 . Moreover, using the triangular inequality and $\mathbb{E}|\xi_m| \leq \|\xi_m\|_{\psi_1}$ (from [Ver10, Def. 5.13]), we get $\|\tilde{\xi}_m\|_{\psi_1} \leq \|\xi_m\|_{\psi_1} + \mathbb{E}|\xi_m| \leq 2\kappa^2$, showing the sub-exponentiality of each $\tilde{\xi}_m$ for $m \in \llbracket M \rrbracket$.

Therefore, given $t \geq 0$, using [Ver10, Cor. 5.17], we get, with a failure probability lower than $2 \exp(-cM \min(\frac{t^2}{4\kappa^4}, \frac{t}{2\kappa^2}))$,

$$-t \leq \frac{1}{M} \sum_{m=1}^M \tilde{\xi}_m = \frac{1}{M} \|\mathcal{A}(\mathcal{I})\|_1 - \frac{1}{M} \mathbb{E}\|\mathcal{A}(\mathcal{I})\|_1 \leq t$$

for some $c > 0$. The result follows by applying (3.53) to the lower and upper bounds $\frac{1}{M} \mathbb{E}\|\mathcal{A}(\mathcal{I})\|_1$, followed by a rescaling in t . \square

Despite the non-independence of the centered matrices A_m^c defining the components of \mathcal{A}^c , we can show the concentration of $\mathcal{A}^c(\mathcal{J})$ in the ℓ_1 -norm by noting that, if Assumption 3.6 holds, $\mathcal{A}_m^c(\mathcal{J}) = \mathcal{A}_m^c(\mathcal{J}_h) = \mathcal{A}_m(\mathcal{J}_h) - \langle A^a, \mathcal{J}_h \rangle$, applying Lemma 3.3 to the ℓ_1 -norm of the first term, and noting the second concentrates around 0.

Lemma 3.4 (Concentration of centered SROP in the ℓ_1 -norm). *In the context of Lemmata 3.1 and 3.2 and supposing Assumption 3.6 holds, given a matrix $\mathcal{J} \in \mathcal{H}^Q$ and $\mathcal{J}_h = \mathcal{J} - \mathcal{J}_d$, there exists a value $0 < c_\alpha < 1$, only depending on the distribution of α , such that, for $t \geq 0$, with a failure probability smaller than $2 \exp(-cM \min(t^2, t))$,*

$$(c_\alpha - 3t\kappa^2) \|\mathcal{J}_h\|_F \leq \frac{1}{M} \|\mathcal{A}^c(\mathcal{J})\|_1 \leq (1 + 3t\kappa^2) \|\mathcal{J}_h\|_F. \quad (3.55)$$

Proof. Given $\mathcal{J} \in \mathcal{H}^Q$ and its hollow part $\mathcal{J}_h = \mathcal{J} - \mathcal{J}_d$, the operator \mathcal{A}^c is defined componentwise by $\mathcal{A}_m^c(\mathcal{J}) = \mathcal{A}_m(\mathcal{J}) - \langle A^a, \mathcal{J} \rangle = \langle \alpha_m \alpha_m^* - A^a, \mathcal{J} \rangle$, with $A^a = \frac{1}{M} \sum_{j=1}^M \alpha_j \alpha_j^*$. Moreover, from Assumption 3.6, $\mathcal{A}_m^c(\mathcal{J}) = \mathcal{A}_m^c(\mathcal{J}_h)$ since both matrices $\alpha_m \alpha_m^*$ and A^a have unit diagonal entries. Therefore, by triangular inequality

$$\left| \frac{1}{M} \|\mathcal{A}^c(\mathcal{J})\|_1 - \frac{1}{M} \|\mathcal{A}(\mathcal{J}_h)\|_1 \right| \leq |\langle A^a, \mathcal{J}_h \rangle|. \quad (3.56)$$

Given the i.i.d. random variables $\xi_j = \alpha_j^* \mathcal{J}_h \alpha_j$, we get $\langle A^a, \mathcal{J}_h \rangle = \frac{1}{M} \sum_{j=1}^M \xi_j$, with $\mathbb{E}\xi_j = 0$ from the hollowness of \mathcal{J}_h . According to Lemma 3.2, each ξ_j is sub-exponential with $\|\xi_j\|_{\psi_1} \leq \kappa^2$. Therefore, using again [Ver10, Cor. 5.17], we have, with a failure probability lower than $2 \exp(-cM \min(\frac{t^2}{4\kappa^4}, \frac{t}{2\kappa^2}))$,

$$-t \leq \langle \frac{1}{M} \sum_{j=1}^M \alpha_j \alpha_j^*, \mathcal{J}_h \rangle \leq t,$$

for some $c > 0$. The result follows from a union bound on the failure of this event and the event (3.54) in Lemma 3.3, both inequalities and (3.56) justifying (3.55). \square

As a simple corollary of the previous lemma, we can now establish the concentration of $\mathcal{B}(f) := \omega \mathcal{A}^c(\mathcal{T}(Ff)) \in \mathbb{R}_+^M$ in the ℓ_1 -norm for an arbitrary K -sparse vector $f \in \Sigma_K$.

Corollary 3.1 (Concentration of \mathcal{B} in the ℓ_1 -norm). *In the context of Lemma 3.4, suppose that 3.1–3.6 are respected, with 3.5 set with sparsity level $K_0 > 0$ and distortion $\delta = 1/2$. Given $f \in \Sigma_{K_0}$, and the operator \mathcal{B} defined in (3.36) from the M SROP measurements and the $|\mathcal{V}_0| = Q(Q-1)$ non-zero visibilities with*

$$Q(Q-1) \geq 4K_0 \text{plog}(N, K_0, \delta),$$

we have, with a failure probability smaller than $2 \exp(-c'M)$ (for some $c' > 0$ depending only on the distribution of α),

$$\frac{\omega c_\alpha}{2\sqrt{2}} \frac{\sqrt{|\mathcal{V}_0|}}{\sqrt{N}} \|f\|_2 \leq \frac{1}{M} \|\mathcal{B}(f)\|_1 \leq 2\omega \frac{\sqrt{|\mathcal{V}_0|}}{\sqrt{N}} \|f\|_2.$$

Proof. Given $f \in \Sigma_{K_0}$ and $\mathcal{J} = \mathcal{T}(Ff) \in \mathcal{H}^Q$, let us assume that (3.55) holds on this matrix with $t = c_\alpha/(6\kappa^2) < 1/6$, an event with probability of failure smaller than $2 \exp(-c'M)$ with $c' > 0$ depending only on c_α and κ , i.e., on the distribution of α . We first note that $\|\mathcal{J}_h\|_F = \|R_{\bar{\mathcal{V}}_0} Ff\|$ from (3.30). Second,

$$\frac{1}{2} \|f\|^2 \leq \frac{N}{|\mathcal{V}_0|} \|R_{\bar{\mathcal{V}}_0} Ff\|^2 \leq \frac{3}{2} \|f\|_2^2. \quad (3.57)$$

since from Assumption 3.5 the matrix $\Phi := \sqrt{N} R_{\bar{\mathcal{V}}_0} F$ respects the $\text{RIP}_{\ell_2/\ell_2}(\Sigma_{K_0}, \delta = 1/2)$ as soon as $|\mathcal{V}_0| = Q(Q-1) \geq 4K_0 \text{plog}(N, K_0, \delta)$. Therefore, since $\mathcal{B}(f) = \omega \mathcal{A}^c(\mathcal{J}) = \omega \mathcal{A}^c(\mathcal{J}_h)$, combining (3.55) and (3.57) gives

$$\frac{1}{M} \|\mathcal{B}(f)\|_1 \geq (c_\alpha - 3t\kappa^2) \omega \|\mathcal{J}_h\|_F = \frac{1}{2} c_\alpha \omega \|R_{\bar{\mathcal{V}}_0} Ff\| \geq \frac{\omega c_\alpha}{2\sqrt{2}} \frac{\sqrt{|\mathcal{V}_0|}}{\sqrt{N}} \|f\|.$$

Similarly, using $\sqrt{\frac{3}{2}}(1 + 3t\kappa^2) < (\frac{3}{2})^{3/2} < 2$, we get

$$\frac{1}{M} \|\mathcal{B}(f)\|_1 \leq \sqrt{\frac{3}{2}}(1 + 3t\kappa^2) \omega \frac{\sqrt{|\mathcal{V}_0|}}{\sqrt{N}} \|f\| < 2\omega \frac{\sqrt{|\mathcal{V}_0|}}{\sqrt{N}} \|f\|.$$

\square

3 | Rank-One Compression of Interferometric Sensing

We are now ready to prove Prop. 3.3. We will follow the standard proof strategy developed in [Bar+08]. By homogeneity of the RIP $_{\ell_2/\ell_1}$ in (3.37), we restrict the proof to unit vectors f of Σ_{K_0} , i.e., $f \in \Sigma_{K_0}^* := \Sigma_{K_0} \cap \mathbb{S}_2^{N-1}$.

Given a radius $0 < \lambda < 1$, let $\mathcal{G}_\lambda \subset \Sigma_{K_0}^*$ be a λ covering of $\Sigma_{K_0}^*$, i.e., for all $f \in \Sigma_{K_0}^*$, there exists a $f' \in \mathcal{G}_\lambda$, with $\text{supp } f' = \text{supp } f$, such that $\|f - f'\| \leq \lambda$. Such a covering exists and its cardinality is smaller than $\binom{N}{K_0}(1 + \frac{2}{\lambda})^{K_0} \leq (\frac{3eN}{K_0\lambda})^{K_0}$ [Bar+08].

Invoking Cor. 3.1, we can apply the union bound to all points of the covering so that

$$\forall f' \in \mathcal{G}_\lambda, \frac{\omega c_\alpha}{2\sqrt{2}} \frac{\sqrt{|\mathcal{V}_0|}}{\sqrt{N}} \leq \frac{1}{M} \|\mathcal{B}(f')\|_1 \leq 2\omega \frac{\sqrt{|\mathcal{V}_0|}}{\sqrt{N}}, \quad (3.58)$$

holds with failure probability smaller than

$$2(\frac{3eN}{K_0\lambda})^{K_0} \exp(-c'M) \leq 2 \exp(K_0 \ln(\frac{3eN}{K_0\lambda}) - c'M).$$

Therefore, there exists a constant $C > 0$ such that, if $M \geq CK_0 \ln(\frac{3eN}{K_0\lambda})$, then (3.58) holds with probability exceeding $1 - 2 \exp(-cM)$, for some $c > 0$.

Let us assume that this event holds. Then, for any $f \in \Sigma_{K_0}$,

$$\begin{aligned} \frac{1}{M} \|\mathcal{B}(f)\|_1 &\leq \frac{1}{M} \|\mathcal{B}(f')\|_1 + \frac{1}{M} \|\mathcal{B}(f - f')\|_1 \\ &\leq 2\omega \frac{\sqrt{|\mathcal{V}_0|}}{\sqrt{N}} + \frac{1}{M} \|\mathcal{B}(\frac{f-f'}{\|f-f'\|})\|_1 \|f - f'\| \\ &\leq 2\omega \frac{\sqrt{|\mathcal{V}_0|}}{\sqrt{N}} + \frac{1}{M} \|\mathcal{B}(r)\|_1 \lambda, \end{aligned}$$

with the unit vector $r := \frac{f-f'}{\|f-f'\|}$. However, this vector r is itself K_0 -sparse since f and f' share the same support. Therefore, applying recursively the same argument on the last term above, and using the fact that $\|\mathcal{B}(w)\|_1$ is bounded for any unit vector w , we get $\frac{1}{M} \|\mathcal{B}(r)\|_1 \lambda \leq 2\omega \frac{\sqrt{|\mathcal{V}_0|}}{\sqrt{N}} \sum_{j \geq 1} \lambda^j = 2 \frac{\lambda}{1-\lambda} \omega \frac{\sqrt{|\mathcal{V}_0|}}{\sqrt{N}}$.

Consequently, since we also have

$$\begin{aligned} \frac{1}{M} \|\mathcal{B}(f)\|_1 &\geq \frac{1}{M} \|\mathcal{B}(f')\|_1 - \frac{1}{M} \|\mathcal{B}(f - f')\|_1 \\ &\geq \frac{\omega c_\alpha}{2\sqrt{2}} \frac{\sqrt{|\mathcal{V}_0|}}{\sqrt{N}} - \frac{1}{M} \|\mathcal{B}(r)\|_1 \lambda, \end{aligned}$$

we conclude that

$$\frac{\omega c_\alpha}{2\sqrt{2}} \left(\frac{1-2\lambda}{1-\lambda} \right) \frac{\sqrt{|\mathcal{V}_0|}}{\sqrt{N}} \leq \frac{1}{M} \|\mathcal{B}(f)\|_1 \leq 2\omega \frac{1}{1-\lambda} \frac{\sqrt{|\mathcal{V}_0|}}{\sqrt{N}},$$

Picking $\lambda = 1/4$ finally shows that, under the conditions described above, \mathcal{B} respects the $\text{RIP}_{\ell_2/\ell_1}(\Sigma_{K_0}, m_{K_0}, M_{K_0})$ with $m_{K_0} > \frac{\omega c_\alpha}{3\sqrt{2}} \frac{\sqrt{|\mathcal{V}_0|}}{\sqrt{N}}$, and $M_{K_0} < \frac{8\omega}{3} \frac{\sqrt{|\mathcal{V}_0|}}{\sqrt{N}}$.

References

- [AB20] L. V. Amitonova and J. F. de Boer. “Endo-microscopy beyond the Abbe and Nyquist limits”. In: *Light, Science & Applications* 9 (2020).
- [Adc+17] B. Adcock et al. “Breaking the coherence barrier: A new theory for compressed sensing”. In: *Forum of Mathematics, Sigma* 5 (2017), e4. DOI: [10.1017/fms.2016.32](https://doi.org/10.1017/fms.2016.32).
- [AGH14] B. Adcock, M. Gataric, and A. Hansen. “On Stable Reconstructions from Nonuniform Fourier Measurements”. In: *SIAM Journal on Imaging Sciences* 7.3 (2014), pp. 1690–1723. DOI: [10.1137/130943431](https://doi.org/10.1137/130943431). eprint: <https://doi.org/10.1137/130943431>.
- [And+13] E. R. Andresen et al. “Two-photon lensless endoscope”. In: *Opt. Express* 21.18 (Sept. 2013), pp. 20713–20721. DOI: [10.1364/OE.21.020713](https://doi.org/10.1364/OE.21.020713).
- [And+16] E. R. Andresen et al. “Ultrathin endoscopes based on multicore fibers and adaptive optics: status and perspectives”. In: *Journal of Biomedical Optics* 21.12 (2016), p. 121506. DOI: [10.1117/1.JBO.21.12.121506](https://doi.org/10.1117/1.JBO.21.12.121506).
- [Bar+08] R. Baraniuk et al. “A simple proof of the restricted isometry property for random matrices”. In: *Constructive Approximation* 28.3 (2008), pp. 253–263. ISSN: 01764276. DOI: [10.1007/s00365-007-9003-x](https://doi.org/10.1007/s00365-007-9003-x).
- [BCL02] H. H. Bauschke, P. L. Combettes, and D. R. Luke. “Phase retrieval, error reduction algorithm, and Fienup variants: a view from convex optimization”. In: *J. Opt. Soc. Am. A* 19.7 (July 2002), pp. 1334–1345. DOI: [10.1364/JOSAA.19.001334](https://doi.org/10.1364/JOSAA.19.001334).
- [Bou+23] D. Bouchet et al. “Speckle-correlation imaging through a kaleidoscopic multimode fiber”. In: *Proceedings of the National Academy of Sciences* 120.26 (2023), e2221407120. DOI: [10.1073/pnas.2221407120](https://doi.org/10.1073/pnas.2221407120). eprint: <https://www.pnas.org/doi/pdf/10.1073/pnas.2221407120>.

3 | References

- [Can08] E. J. Candes. “The restricted isometry property and its implications for compressed sensing”. In: *Comptes rendus mathematique* 346.9-10 (2008), pp. 589–592.
- [Can11] E. J. Cand. “PhaseLift : Exact and Stable Signal Recovery from Magnitude Measurements via Convex Programming”. In: (2011). arXiv: [arXiv:1109.4499v1](https://arxiv.org/abs/1109.4499v1).
- [Car+18] A. M. Caravaca-Aguirre et al. “Hybrid photoacoustic/fluorescence microendoscopy through a multimode fiber using speckle illumination”. In: (2018), pp. 1–10. arXiv: [1812.11206](https://arxiv.org/abs/1812.11206).
- [CCG15] Y. Chen, Y. Chi, and A. J. Goldsmith. “Exact and stable covariance estimation from quadratic sampling via convex programming”. In: *IEEE Transactions on Information Theory* 61.7 (2015), pp. 4034–4059.
- [CKH22] W. Choi, M. Kang, and J. e. a. Hong. “Flexible-type ultra-thin holographic endoscope for microscopic imaging of unstained biological tissues”. In: *Nature Communications* 4469.13 (2022). DOI: [10.1038/s41467-022-32114-5](https://doi.org/10.1038/s41467-022-32114-5).
- [CLY04] L. Cai, Q. Liu, and X. Yang. “Simultaneous digital correction of amplitude and phase errors of retrieved wave-front in phase-shifting interferometry with arbitrary phase shift errors”. In: *Optics Communications* 233.1 (2004), pp. 21–26. ISSN: 0030-4018. DOI: <https://doi.org/10.1016/j.optcom.2004.01.033>.
- [CP11] E. J. Candes and Y. Plan. “A probabilistic and RIPless theory of compressed sensing”. In: *IEEE transactions on information theory* 57.11 (2011), pp. 7235–7254.
- [CRT06a] E. J. Candès, J. K. Romberg, and T. Tao. “Robust uncertainty principles: Exact signal reconstruction from highly incomplete frequency information”. In: *IEEE Transactions on Information Theory* 52.2 (2006), pp. 489–509.
- [CRT06b] E. J. Candès, J. K. Romberg, and T. Tao. “Stable signal recovery from incomplete and inaccurate measurements”. In: *Communications on Pure and Applied Mathematics* LIX (2006), pp. 1207–1223.
- [CW08] E. J. Candès and M. Wakin. “An Introduction To Compressive Sampling”. In: *IEEE Signal Processing Magazine* 25.2 (2008), pp. 21–30. ISSN: 1053-5888. arXiv: [arXiv : 1307.1360v1](https://arxiv.org/abs/1307.1360v1).

- [CZ+15] T. T. Cai, A. Zhang, et al. “ROP: Matrix recovery via rank-one projections”. In: *Annals of Statistics* 43.1 (2015), pp. 102–138.
- [Dab+21] A. Dabbech et al. “Cygnus A jointly calibrated and imaged via non-convex optimization from VLA data”. In: *Monthly Notices of the Royal Astronomical Society* 506.4 (2021), pp. 4855–4876. ISSN: 13652966. DOI: [10.1093/mnras/stab1903](https://doi.org/10.1093/mnras/stab1903). arXiv: [2102.00065](https://arxiv.org/abs/2102.00065).
- [Don06] D. L. Donoho. “Compressed Sensing”. In: *IEEE Transactions on Information Theory* 52.4 (2006), pp. 1289–1306.
- [Du+22] Y. Du et al. “Hybrid multimode - multicore fibre based holographic endoscope for deep-tissue neurophotonics”. In: *Light: Advanced Manufacturing* 3.LAM2021080029 (2022), p. 408. ISSN: 2689-9620. DOI: [10.37188/lam.2022.029](https://doi.org/10.37188/lam.2022.029).
- [Dua+08] M. F. Duarte et al. “Single-Pixel Imaging via Compressive Sampling”. In: *IEEE Signal Processing Magazine* 25.2 (2008), pp. 83–91. ISSN: 1053-5888. DOI: [10.1109/MSP.2007.914730](https://doi.org/10.1109/MSP.2007.914730). arXiv: [1203.3815](https://arxiv.org/abs/1203.3815).
- [Fie82] J. R. Fienup. “Phase retrieval algorithms: a comparison”. In: *Appl. Opt.* 21.15 (Aug. 1982), pp. 2758–2769. DOI: [10.1364/AO.21.002758](https://doi.org/10.1364/AO.21.002758).
- [FR17] S. Foucart and H. Rauhut. “A mathematical introduction to compressive sensing”. In: *Bull. Am. Math* 54.2017 (2017), pp. 151–165.
- [Goo05] J. W. Goodman. *Introduction to Fourier optics*. Roberts and Company Publishers, 2005.
- [Gué+22] S. Guérit et al. “Compressive imaging through optical fiber with partial speckle scanning”. In: *SIAM Journal on Imaging Sciences* 15.2 (2022), pp. 387–423.
- [Haw+17] E. W. Hawkes et al. “A soft robot that navigates its environment through growth”. In: *Science Robotics* 2.8 (2017), eaan3028. DOI: [10.1126/scirobotics.aan3028](https://doi.org/10.1126/scirobotics.aan3028). eprint: <https://www.science.org/doi/pdf/10.1126/scirobotics.aan3028>.
- [JV10] L. Jacques and P. Vandergheynst. “Compressed Sensing: “When sparsity meets sampling””. In: *Optical and Digital Image Processing - Fundamentals and Applications*. Wiley-Blackwell, 2010, pp. 1–30.

3 | References

- [KH66] C. K. Kao and G. A. Hockham. “Dielectric-Fiber Surface Waveguides for Optical Frequencies”. In: *Proceedings of the IEE - Part B: Electronic and Communication Engineering* 113.7 (1966), pp. 1151–1158.
- [KS09] M. Koshiba and K. Saitoh. “Multicore Fibers for Large Capacity Transmission”. In: *IEICE Electronics Express* 6.2 (2009), pp. 98–103.
- [KW14] F. Krahmer and R. Ward. “Stable and robust sampling strategies for compressive imaging”. In: *IEEE Transactions on Image Processing* 23.2 (2014), pp. 612–622. ISSN: 10577149. arXiv: [1210.2380](https://arxiv.org/abs/1210.2380).
- [Leb+23] O. Leblanc et al. “Interferometric lensless imaging: rank-one projections of image frequencies with speckle illuminations”. In: (2023). arXiv: [2306.12698 \[eess.IV\]](https://arxiv.org/abs/2306.12698).
- [Liu+22] C. Liu et al. “Real scene acquisition and holographic near-eye display system based on a zoom industrial endoscope”. In: *Opt. Express* 30.18 (Aug. 2022), pp. 33170–33181. DOI: [10.1364/OE.468267](https://doi.org/10.1364/OE.468267).
- [Loc+22] B. Lochocki et al. “Epi-fluorescence imaging of the human brain through a multimode fiber”. In: *APL Photonics* 7 (2022). DOI: [10.1063/5.0080672](https://doi.org/10.1063/5.0080672).
- [Loc+23] B. Lochocki et al. “Swept-source multimode fiber imaging”. In: *Scientific Reports* 13 (May 2023). DOI: [10.1038/s41598-023-34062-6](https://doi.org/10.1038/s41598-023-34062-6).
- [Man+22] P. Mann et al. “White light phase shifting interferometric microscopy with whole slide imaging for quantitative analysis of biological samples”. In: *Journal of Biophotonics* 15 (Apr. 2022). DOI: [10.1002/jbio.202100386](https://doi.org/10.1002/jbio.202100386).
- [PM16] D. Psaltis and C. Moser. “Imaging with Multimode Fibers”. In: *Optics and Photonics News* 27.1 (2016), pp. 24–31. DOI: [10.1117/3.853722.ch14](https://doi.org/10.1117/3.853722.ch14).
- [PVW11] G. Puy, P. Vandergheynst, and Y. Wiaux. “On variable density compressive sampling”. In: *IEEE Signal Processing Letters* 18.10 (2011), pp. 595–598. ISSN: 10709908. DOI: [10.1109/LSP.2011.2163712](https://doi.org/10.1109/LSP.2011.2163712). arXiv: [1109.6202](https://arxiv.org/abs/1109.6202).
- [Rab+06] Rabien, S. et al. “Atmospheric turbulence compensation with laser phase shifting interferometry”. In: *A&A* 450.1 (2006), pp. 415–425. DOI: [10.1051/0004-6361:20054143](https://doi.org/10.1051/0004-6361:20054143).

- [SGR23] C. Scotté, F. Galland, and H. Rigneault. "Photon-noise: is a single-pixel camera better than point scanning? A signal-to-noise ratio analysis for Hadamard and Cosine positive modulation". In: *Journal of Physics: Photonics* 5.3 (June 2023), p. 035003. DOI: [10.1088/2515-7647/acc70b](https://doi.org/10.1088/2515-7647/acc70b).
- [SH17] M. Soltani and C. Hegde. "Improved Algorithms for Matrix Recovery from Rank-One Projections". In: (2017), pp. 1–19. arXiv: [1705.07469](https://arxiv.org/abs/1705.07469).
- [Siv+16] S. Sivankutty et al. "Extended field-of-view in a lensless endoscope using an aperiodic multicore fiber". In: *Optics Letters* 41.15 (2016), p. 3531. ISSN: 0146-9592. DOI: [10.1364/ol.41.003531](https://doi.org/10.1364/ol.41.003531). arXiv: [1606.08169](https://arxiv.org/abs/1606.08169).
- [Siv+18a] S. Sivankutty et al. "Nonlinear imaging through a Fermat's golden spiral multicore fiber". In: *Optics Letters* 43.15 (2018), p. 3638. ISSN: 0146-9592. DOI: [10.1364/ol.43.003638](https://doi.org/10.1364/ol.43.003638). arXiv: [1806.01451](https://arxiv.org/abs/1806.01451).
- [Siv+18b] S. Sivankutty et al. "Single-shot noninterferometric measurement of the phase transmission matrix in multicore fibers". In: *Opt. Lett.* 43.18 (Sept. 2018), pp. 4493–4496. DOI: [10.1364/OL.43.004493](https://doi.org/10.1364/OL.43.004493).
- [Sun+22] J. Sun et al. "Quantitative phase imaging through an ultra-thin lensless fiber endoscope". In: *Light: Science and Applications* 11.1 (2022). ISSN: 20477538. DOI: [10.1038/s41377-022-00898-2](https://doi.org/10.1038/s41377-022-00898-2). arXiv: [2112.12055](https://arxiv.org/abs/2112.12055).
- [Tay+22] M. Taylor et al. "Experimental Setup for Single-Pixel Imaging of Turbulent Wavefronts and Speckle-Based Phase Retrieval". In: *2022 IEEE International Conference on Space Optical Systems and Applications (ICSOS)*. 2022, pp. 78–84. DOI: [10.1109/ICSOS53063.2022.9749732](https://doi.org/10.1109/ICSOS53063.2022.9749732).
- [Tsv+19] V. Tsvirkun et al. "Flexible lensless endoscope with a conformationally invariant multi-core fiber". In: *Optica* 6.9 (2019). ISSN: 23318422. DOI: [10.1364/optica.6.001185](https://doi.org/10.1364/optica.6.001185). arXiv: [1905.09643](https://arxiv.org/abs/1905.09643).
- [Ver10] R. Vershynin. "Introduction to the non-asymptotic analysis of random matrices". In: (2010), pp. 210–268. arXiv: [1011.3027](https://arxiv.org/abs/1011.3027).

3 | References

- [VF08] D. E. Van Ewout Berg and M. P. Friedlander. “Probing the pareto frontier for basis pursuit solutions”. In: *SIAM Journal on Scientific Computing* 31.2 (2008), pp. 890–912. ISSN: 10648275. DOI: [10.1137/080714488](https://doi.org/10.1137/080714488).
- [VWS19] A.-J. van der Veen, S. J. Wijnholds, and A. M. Sardarabadi. “Signal processing for radio astronomy”. In: *Handbook of Signal Processing Systems* (2019), pp. 311–360.
- [Wia+09] Y. Wiaux et al. “Compressed sensing imaging techniques for radio interferometry”. In: *Monthly Notices of the Royal Astronomical Society* 395.3 (2009), pp. 1733–1742.
- [Wik] Wikipedia. *Interferometry*.

4

Compressive Radio-Interferometry

OUR journey into the world of *interferometric sensing* and *Rank-One Projections* (ROP), started in Chap. 3, continues, and ends with this chapter.

In a nutshell, we build upon the discoveries made in the sensing model associated to *MultiCore Fiber Lensless Imaging*, and extend them to another interferometric imaging modality: *Radio-Interferometry* (RI).

As in Chap. 3, this chapter studies the problem of recovering an image $\sigma \in \mathbb{R}^N$ from linear combinations of a subset of its Fourier coefficients. However, multiple interferometric matrices $\{\mathcal{I}_b[\sigma]\}_{b=1}^B$ will now be accessed, with the index b associated to a short-time interval (or *batch*), thus offering a denser Fourier sampling and a flexible way to associate them. At each batch b , the compression of the interferometric matrix $\mathcal{I}_b[\sigma]$ will rely upon rank-one projections (ROP) of the form

$$y_b = \alpha_b^* \mathcal{I}_b[\sigma] \beta_b, \quad (4.1)$$

which ressembles the model (3.1) introduced in Chap. 3, except for the index b representing time and the use of another sketching vector β_b on the right. Another compression, namely *Bernoulli modulations*, will be considered for the time dimension b . The final compressed measurements will write in the form

$$z_m = \sum_{b=1}^B \epsilon_{mb} \tilde{\epsilon}_{mb} y_b \quad (4.2)$$

with ± 1 modulations $\epsilon_b, \tilde{\epsilon}_b$.

In summary, the studied sensing model will here cascade:

4 | Compressive Radio-Interferometry

1. **An interferometric matrix:** an *hermitian* matrix $\mathcal{I}_b[\sigma] \in \mathcal{H}^Q$ of Fourier coefficients of the image, with
2. **Rank-One Projections:** ROP of this matrix with two controllable *sketching* vectors $\alpha_b, \beta_b \in \mathbb{C}^Q$.
3. **Bernoulli modulations:** ± 1 modulations of the ROP measurements along the b -axis.

The main achievements of this chapter are to prove that (*i*) this sensing model boils down directly from compressing the vector of measurements at the level of the antennas, (*ii*) the huge compression ratio for the measurements comes at a limited price of increased computational complexity and decreased reconstruction performances when Bernoulli modulations are applied, (*iii*) formal recovery guarantees can be provided, and (*iv*) it works using state-of-the-art reconstructions algorithms in a realistic numerical setting.

This chapter mostly coincides with the content of our publications:

- (J) Olivier Leblanc, Yves Wiaux, and Laurent Jacques, "Compressive radio-interferometric sensing with random beamforming as rank-one signal covariance projections.", **Submitted to IEEE TCI [LWJ24]**.
- (J) Olivier Leblanc, Taylor Chu, Yves Wiaux, and Laurent Jacques, "Compressive radio-interferometric imaging: Rank-One Compression with Bernoulli modulations accross time.", **In preparation for Monthly Notices of the Radio-Astronomical Society (MNRAS)..**

The codes developed in the context of this chapter can be found at <https://github.com/olivierleblanc/RAPHA>, and in the forks of the *uS-ARA* and *AIRI* projects accessible at <https://github.com/olivierleblanc/uSARA> and <https://github.com/olivierleblanc/AIRI>.

4.1 Introduction

4.1.1 Motivation

The inspirations for the contributions proposed to the field of RI imaging are divided in two aspects.

Addressing a Scalability Challenge

While contributing to MCFLI, we rapidly noticed the similarities with radio-interferometric imaging where an interferometric matrix natu-

rally arises from the partial Fourier sampling at a difference set of antenna positions. In radio-interferometry, a tremendous amount of data is processed and collected every day. This includes the Fourier samples contained in all the covariance matrices, which are consecutive in time due to the rotation of the Earth. For the low-frequency array (LOFAR), this represents **around 5 petabytes (5 10^{15} bytes) of data per year** [Haa13].

Compression is therefore becoming increasingly essential for reducing data size and ensuring the scalability of RI, particularly with **upcoming arrays like the Square Kilometer Array [Bra+19], which will involve thousands of antennas**. The issue faced by *post-sensing* compression techniques is that they require computing the signal covariance matrix to compress it afterward, hence temporarily storing the uncompressed data. Furthermore, the compression mechanism often impedes the forward model calculation, repeatedly called in iterative reconstruction algorithms.

With the “Rank-One Projection” view developed in Chap. 3, we believed there was some room for improvement in understanding the close relationship between antenna-level acquisition and stored interferometric data. The idea was to see how far ROP compression could be applied to RI to save several orders of magnitude of data, while preserving nearly all of the information contained in this compressed data.

Paving the Way for Advanced Interferometric Sensing

It was clear from MFCLI that sensing the object of interest with many different receiver arrangements was key to providing a denser Fourier sampling of the image. In MCFLI, the relative position between the cores was difficult to adjust. Only axial rotation of the MCF was possible. In RI, the varying Fourier sampling comes for free with the rotation of the Earth. Chap 3 showed how to make efficient SROPs of an interferometric matrix, but not how to combine the projections made on several interferometric matrices, each associated with a different visibility set. This RI context was a good opportunity to (i) highlight a link between all interferometric imaging modalities, (ii) study what are smart¹ ways to make these ROP combinations, and (iii) test the idea of random ROP compression in advanced image recovery programs.

¹In the sense of low computational cost and information preservation.

4 | Compressive Radio-Interferometry

4.1.2 Differences Compared to Chapter 3

In this chapter, we exploit the similarities between radio-interferometric imaging and MCFLI. However, there are many subtle differences between the two modalities that we will mention here.

In RI, antennas receive cosmic signals—or radiation from cosmic radio sources. “Such signals are generated by natural processes and almost universally take the form of Gaussian random noise” [TMS17]. This is due to the incoherence of the sources, and the Van Cittert-Zernike theorem that we access partial Fourier information. The target image here is a statistical quantity, namely the *sky intensity distribution*, which influences the variability of the cosmic signals coming from different directions. This will motivate a clear separation between the acquisition and the image reconstruction.

The underlying Fourier transform partially accessed is obtained in *direction cosine* coordinates, *i.e.*, the array of antenna images the sky in a narrow set of directions, rather than in a plane perpendicular to the pointing direction as in MCFLI. The visibilities are thus now normalized by the wavelength λ , rather than by λz .

The frequencies are no longer assumed to be *on-grid* as in the simplification made for MCFLI. The *NonUniform Fast Fourier Transform* will be used to interpolate the on-grid frequencies obtained from an FFT to continuous frequencies corresponding to the baseline positions.

The origin of the noise in the visibilities in RI differs from MCFLI. In MCFLI, thermal additive noise is directly impinging the single photodetector measurements. In RI, the correlations computed to get the visibilities transform the thermal noise at the receivers into the covariance matrix of the noise, seen as a deterministic bias. The additive Gaussian noise terms are rather a combination of statistical noise due to the estimation of the covariance matrix and all other unknown imperfections to the system, going from time variation of the sky intensity to quantum noise [TMS17] and passing through quantization noise.

4.1.3 Related Work

We mention works that address some of the latest challenges in the context of radio-interferometric imaging. They are divided into those contributing to the sensing model, and the others proposing efficient and accurate image reconstruction algorithms.

Sensing Model

The reader is invited to start by reading the works related to the interferometric sensing model of MCFLI in Sec. 3.1.2 as most of them are still relevant in this chapter.

An important element of this chapter is to review the way visibility measurements can be obtained from the radio-interferometric sensing modality. The emphasis made on the random nature of the cosmic signals coming from the sky and incorporated into the antenna measurements has been strongly inspired by [VWS18]. Radio-interferometric sensing yields a partial Fourier sampling at locations obtained from all antenna position differences, also named *baselines*; [Boo02] studied optimized array designs. The visibilities are related to continuously located baselines (pairwise differences of antenna positions). The forward model considered for RI imaging generally uses the *NonUniform Fast Fourier Transform* (NUFFT) to compute the Fourier transform of the image at off-grid frequencies. In this work, we use the standard Min-Max interpolation with Kaiser-Bessel kernels [FS03]. We will consider both a small field of view and an array of antennas close to each other compared to their distance to the cosmic source in the pointing direction. The invalidity of this assumption can be addressed with a spread spectrum model, *i.e.*, by considering the partial Fourier transform of the image with a linear chirp modulation [CGB08; Wia+09a].

There exist several compression techniques in the literature, either *post-sensing compression*² or *compressive sensing*, that have a connection with our method.

Among the post-sensing compression techniques for RI, compressing the observation vector that collects all the visibilities by multiplication with a Gaussian random matrix (with much fewer rows than columns) was discussed in [Vij+17] and was shown to significantly increase the computational cost of the forward model. [Vij+17] proposed an efficient Fourier reduction model approximating the optimal (in the least-squares sense) dimensionality reduction that projects the data with the adjoint of \mathbf{U} where \mathbf{U} contains the left singular vectors of the SVD of the visibility operator $\Phi := \mathbf{U}\Sigma\mathbf{V}^*$. On another hand, *baseline-dependent averaging* [WWS18; Ate+18] offers an effective reduction in data volume by averaging consecutive visibilities corresponding to short baselines, *i.e.*, those with nearly constant frequency locations.

²A post-sensing compression technique necessitates computing the uncompressed data before applying compression.

4 | Compressive Radio-Interferometry

Finally, as most of the reconstruction algorithms involve the matrix-to-vector multiplication with the matrices Φ and $\Phi^*\Phi$, storing the *dirty map*—that is the mere application of the adjoint sensing operation to the observed visibilities—instead of the visibility vector was considered as a practical compression technique [Vij+17]. It can even be computed *on-the-fly* during the acquisition [Thy+17; Kri+23].

Our scheme is a *compressive sensing* technique relying on *random beamforming*, which had already been highlighted in [Öça+15]. Our decomposition of the beamforming capabilities into direction-dependent gains per antenna, then direction-agnostic gains per antenna for the projection of the measurement vector, corresponds to the random beamforming strategy R3 described in [Öça+15]. The novelty in this chapter is the emphasis on the theory of ROP, allowing us to derive the sample complexity in a simplified case. In the last decade, different works have provided matrix recovery guarantees via ROPs. In particular, [CZ+15] derived sample complexities for the recovery of low-rank matrices, showing that a matrix of rank $r \ll Q$ could be recovered from a number $n \gtrsim rQ^2$ of random ROPs, and [CCG15] studied the reconstruction of a signal covariance matrix from symmetric ROP when the matrix satisfies one structural assumption among low-rankness, Toeplitz, sparsity, and joint sparsity and rank-one. Furthermore, we tackled the challenge regarding time-dependence by proposing *Bernoulli modulations* of the different rank-one projected vectors. Using Bernoulli modulations for compressive imaging purposes is not new, and was considered, for instance, in coded aperture [FC78; Wag+08], lensless imaging, and in binary mask schemes [Kol+15]. It is used for computer vision and robotics but also astronomical and medical imaging applications.

Recovery Algorithms

Although this thesis does not contribute to the large literature of inverse problem solving, and more precisely those focused on RI imaging, several of them are used in the reconstruction analyses provided at the end of this chapter. We distinguish two types of reconstruction algorithms: (i) those that reconstruct images σ sparse in some orthogonal basis Ψ s.t. $\Psi^*\Psi = \mathbf{I}$, i.e., $\sigma = \Psi^*\alpha$ with the sparse vector of coefficients $\alpha \in \Sigma_K$. They are well suited for images of the sky composed of multiple point sources such as stars. (ii) Those that reconstruct even more realistic RI images $\sigma \in \mathcal{S} \subset \mathbb{R}^N$ for some domain \mathcal{S} of possible RI images in \mathbb{R}^N . In addition to point sources, the sky can also contain clouds

of cosmic particles, as is the case with galaxy formation.

Among the algorithms designed for images sparse in an orthogonal basis, CLEAN [Hög74] is one of the oldest techniques. It consists in first acquiring a dirty map of the sky by raster-scanning a focus into a specific direction, and then recover each spot of the image iteratively using a *Matching Pursuit* algorithm [MZ93].

More complicated RI images are obtained from a more complicated prior knowledge on their possible intrinsic content. SARA [CMW12], and its *unconstrained* variant uSARA [RW20; Ter+22], integrate an *average sparsity* prior by composing an overcomplete dictionary made of eight Daubechies wavelets and the Dirac basis. The “data-fidelity plus prior” function minimized for the image reconstruction is then solved with a re-weighted³ Proximal Gradient Method (PGM). In the same fashion, AIRI [Ter+22], and its constrained variant cAIRI [Ter+23], propose a Plug-and-Play approach by replacing the proximal operator in the PGM by a deep denoiser specifically trained to remove additive Gaussian noise in RI images. It was shown that the inserted denoiser can be seen as the proximal operator of an implicit regularization function. The overall resulting PnP algorithm converges to a solution of the set S of plausible RI images that has been implicitly learned by the denoiser. Finally, R2D2 [A+23] is a data-driven approach relying on the alternation between Deep Neural Networks (DNNs) and data-consistency updates. The reconstruction is computed as a series of residual images estimated as the outputs of DNNs, each taking the residual dirty image of the previous iteration as an input. The approach can be interpreted as a learned version of CLEAN. CLEAN, uSARA, AIRI and R2D2 are scalable to very high dimensional visibility data thanks to their parallelizability.

BlueBild [Tol+23; HS19] has recently received attention for its interpretable energy level decomposition—practical for dealing with the high dynamic range of RI imaging. The solution computed by BlueBild is a least-square solution assuming a sparse image. The reconstructed image is a sparse combination of array PSF, but there is no explicit regularization in the inverse problem solving. Moreover, a generalized eigenvalue decomposition must be considered to represent the image in an orthogonal basis.

Finally, we find it worth mentioning that weighting the visibilities generally improves the quality of the reconstruction [Pra+18].

³Addressing the nonconvexity of the underlying minimization problem.

4 | Compressive Radio-Interferometry

4.1.4 Chapter Contributions

We provide several contributions to the modeling, understanding, and efficiency of RI when combined with random beamforming.

Random beamforming Random beamforming of antenna signals before computing their correlation is shown to be equivalent to applying random ROPs of the initial signal covariance matrix. Replacing the Q^2 coefficients of this matrix with a small—but sufficient—number N_p of these projections for each STI represents a compression technique that can be applied on-the-fly during the acquisition of the antenna measurements.

Modulations of ROPs The ROP vectors corresponding to consecutive STI intervals, or *batches*, are further compressed by progressively aggregating them by applying random Bernoulli modulations; this allows keeping a fixed final data size $N_p N_m$ for N_p ROP per batch and N_m modulations, reducing the number $N_p B$ of ROP elements.

Recovery guarantees Formal recovery guarantees are provided in Sec. 4.5 for a sensing scheme—simpler to analyze theoretically—that simply sums the ROP vectors of different batches, namely *batched ROP*. Nonetheless, batched and modulated ROPs are shown to both find an interpretation of ROPs applied to a total covariance matrix gathering all matrices coming from different batches in blocks along its diagonal. Guarantees adapted to modulated ROPs are expected to exist but not proven here. From a set of simplifying assumptions, we show that one can with high probability (*w.h.p.*) robustly estimate a K -sparse image provided that the number of ROPs N_p and the Fourier coverage with $Q(Q - 1)B$ visibilities guided by both the number of antennas Q and the number of batches B are large compared to $\mathcal{O}(K)$ (up to logarithmic factors). Our analysis relies on showing that, *w.h.p.*, the sensing operator ***RGF*** satisfies the ℓ_2/ℓ_1 restricted isometry property which enables us to estimate a sparse image with the **BP DN _{ℓ_1}** program. This theoretical analysis is accompanied by phase transition diagrams obtained from extensive Monte Carlo numerical experiments using the modulated ROP model.

Numerical proof-of-concept: The imaging capabilities of the approach are demonstrated in a realistic simulation setting. The ROP and

modulations operators are plugged into actively maintained numerical projects considering *uv*-coverages of the existing antenna array MeerKAT [Asa+21] and applying the state-of-the-art reconstruction algorithm uSARA [RW20; Ter+22]. The provided analyzes demonstrate that the information contained in the visibilities can be compressed with the modulated ROP scheme, reaching compression factors of 1% for an equivalent quality of reconstruction of a realistic groundtruth image than with the classical scheme.

4.1.5 Notations Specific to this Chapter

This chapter involves statistical quantities which were absent in Chap. 3. The notation $X_i \stackrel{\text{i.i.d.}}{\sim} \mathcal{P}$ indicates that the random variables $\{X_i\}_{i=1}^N$ are *independent and identically distributed* according to the distribution \mathcal{P} . The uniform distribution on a set \mathcal{A} is denoted by $\mathcal{U}(\mathcal{A})$. The expectation with respect to the random vector α is written \mathbb{E}_α .

4.2 Preliminaries

Before delving into the core of this chapter, we anticipate on some subtle aspects of the discussion by detailing the mathematics of three concepts; namely the *direction cosines*, *Van Cittert-Zernike theorem*, and *Non-Uniform FFT*.

Reminder on Direction Cosines

The radio-astronomical imaging differs from MCFLI in its extremely large distances that separate the signal sources from the receivers. In *Radio-Interferometry* (RI), the distance to the signal sources is not as important as the specific region of the sky being observed. This is why we use another coordinate system than in Chap. 3, namely the *direction cosine* coordinate system. With direction cosines, only the direction matters. If $\mathbf{u} := ue_u + ve_v + we_w \in \mathbb{R}^3$ is the blue Euclidean vector represented in Fig. 4.1, its coordinates in direction cosines are $\mathbf{l} := (l, m, n)$ with

$$\begin{aligned} l &= \cos \theta_u = \frac{\mathbf{u} \cdot \mathbf{e}_u}{\|\mathbf{u}\|_2} \\ m &= \cos \theta_v = \frac{\mathbf{u} \cdot \mathbf{e}_v}{\|\mathbf{u}\|_2} \\ n &= \cos \theta_w = \frac{\mathbf{u} \cdot \mathbf{e}_w}{\|\mathbf{u}\|_2}. \end{aligned} \tag{4.3}$$

4 | Compressive Radio-Interferometry

It is clear from (4.3) that $l^2 + m^2 + n^2 = 1$. We will thus replace n to write $\mathbf{l} := (l, m, \sqrt{1 - l^2 - m^2})$. A vector in direction cosine coordinates is always unitary. In this chapter, the coordinate system will be chosen such that e_w is parallel to the line-of-sight.

The antennas will be assumed to be in a plane normal to e_w . This way, for the considered very large distance, the third component $n \approx 1$, and we will continue this chapter with 2-D only coordinates $\mathbf{l} := (l, m)$.

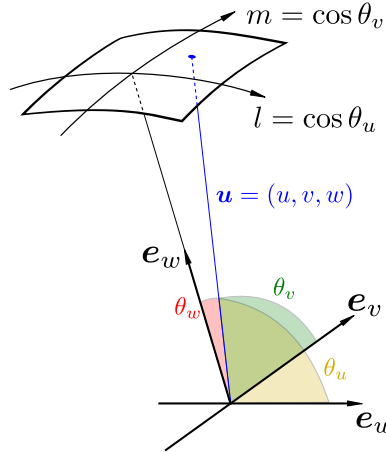


Fig. 4.1 The direction cosine coordinate system. An orthonormal basis (e_u, e_v, e_w) has by definition a third component e_w pointing in the direction of the coordinates $(l, m) = (0, 0)$. An arbitrary direction with coordinates $\mathbf{u} = ue_u + ve_v + we_w$ has direction cosine coordinates $(l, m) = (\frac{u}{\|\mathbf{u}\|_2}, \frac{v}{\|\mathbf{u}\|_2})$.

The Van Cittert-Zernike Theorem

We want to get an image of the intensity distribution $\sigma^2(\mathbf{l})$ from *incoherent* cosmic signals generated by a Gaussian *stochastic process*. The cosmic signal s at direction $\mathbf{l} := (l, m)$ and time instant t follows

$$s(\mathbf{l}, t) \sim \mathcal{N}(0, \sigma^2(\mathbf{l})). \quad (4.4)$$

The electric fields measured at two point P_1 and P_2 are written $E_1(\mathbf{l}, t)$ and $E_2(\mathbf{l}, t)$, respectively. We write \mathbf{u} their distance (in units of the wavelength) along the XY axes. The cross-correlation between the signals received at these two points writes (in the *wide sense stationary* case) as $\mathbb{E}[E_1(\mathbf{l}, t)E_2^*(\mathbf{l}, t - \tau)]$. The *mutual coherence* function is obtained by integrating this cross-correlation over the entire source as

$$\Gamma(\mathbf{u}, \tau) := \int_{\mathbb{R}^2} \mathbb{E}[E_1(\mathbf{l}, t)E_2^*(\mathbf{l}, t - \tau)] d\mathbf{l}.$$

First, we replace—with an *ergodicity* argument—the statistical expectation \mathbb{E} by a time average as

$$\Gamma(\mathbf{u}, \tau) := \int_{\mathbb{R}^2} \lim_{T \rightarrow \infty} \frac{1}{T} \int_0^T E_1(\mathbf{l}, t) E_2^*(\mathbf{l}, t - \tau) dt d\mathbf{l}. \quad (4.5)$$

By the means of radio-telescope measurements, we will be able to implicitly obtain this mutual coherence function. Due to the incoherence of the sources, we are particularly interested in $\Gamma(\mathbf{u}, 0)$. In our context, the difference in arrival time between the two receiving points is negligible compared to the total travel time, which means that the signals received at the same time at these two points are mutually coherent, despite the incoherence of the emitting source. This result is known as the *Van Cittert-Zernike* (VCZ) theorem [Van34; Zer38].

Theorem 4.1 (Van Cittert-Zernike). *Consider two very distant parallel planes, both perpendicular to the line of sight; if $\Gamma(\mathbf{u}, \tau)$ is the mutual coherence function between two points in the observation plane as defined in (4.5), then*

$$\Gamma(\mathbf{u}, 0) = \int_{\mathbb{R}^2} \sigma^2(\mathbf{l}) e^{-i2\pi \mathbf{u}^\top \mathbf{l}} d\mathbf{l}, \quad (4.6)$$

where $\mathbf{l} := (l, m)$ are the direction cosines of a point on a distant source in the source plane, $\mathbf{u} := (u, v)$ are respectively the x -distance and the y -distance between the two observation points on the observation plane in unit of wavelength and $\sigma^2(\mathbf{l}) := \mathbb{E}[|s(\mathbf{l}, t)|^2]$ is the intensity of the source.

In the case where either the pairwise distances between the antennas are not negligible compared to the distance to the cosmic source in the pointing direction or the sky is observed with a large field-of-view, the measured visibilities are essentially identified with a noisy and incomplete Fourier coverage of the product of the planar signals with a linear chirp modulation [Wia+09a]. This modifies (4.6) as

$$\Gamma(\mathbf{u}, 0) = \int_{\mathbb{R}^2} \sigma^2(\mathbf{l}) e^{i\pi w(\mathbf{u}) \|\mathbf{l}\|_2^2} e^{-i2\pi \mathbf{u}^\top \mathbf{l}} d\mathbf{l},$$

for a chirp rate $w(\mathbf{u})$. Interestingly, this chirp modulation provides access to higher spatial frequencies—improving the quality of image reconstructions [Wia+09a].

4 | Compressive Radio-Interferometry

Non-Uniform Fast Fourier Transform

In this chapter, the *continuous visibilities*—the value of the image spectrum at continuous frequency locations—will be obtained from the *Non-Uniform Fast Fourier Transform* (NUFFT). This compares to Chap. 3 where the frequency locations were assumed to be *on-grid* hence the FFT was sufficient to compute the visibilities. Denoting (in the 1-D case for simplicity) $\hat{\sigma}^2(\omega)$ the Fourier transform of the intensity distribution $\sigma^2(l)$ at the continuous frequency ω , this value is *linearly interpolated* from the FFT $F\sigma$ of the discrete image σ using the MIN-MAX interpolation technique of [FS03] as

$$\hat{\sigma}^2(\omega) = \sum_{j=1}^J (F\sigma)_{/k(\omega)+j/_N} g_j^*(\omega), \quad (4.7)$$

where

- J is the *number of nearest neighbours* to ω ,
- $k(\omega)$ is the *integer offset*—centering around the closest on-grid frequency of the FFT $F\sigma$, and
- $g(\omega) \in \mathbb{C}^N$ is the *linear interpolation kernel*.
- $/k(\omega) + j/_N = k(\omega) + j \bmod N$ is a modulo operation.

Consequently, the (noiseless) *continuous visibility vector* $\bar{c} \in \mathbb{R}^{Q^2B}$ containing off-the-grid Fourier samples of the image will be obtained in (4.16) as $\bar{c} = GF\sigma$ where the combined operator GF represents the NUFFT, with $G \in \mathbb{C}^{Q^2B \times N}$ the *linear interpolation operator*. Here, Q , B , and N are the number of antennas, batches, and pixels detailed later. As clear from (4.7), and illustrated in Fig. 4.2, G is sparse with only J nonzero values per row. This will be important for the computation of the complexities of the models in Sec. 4.3.4.

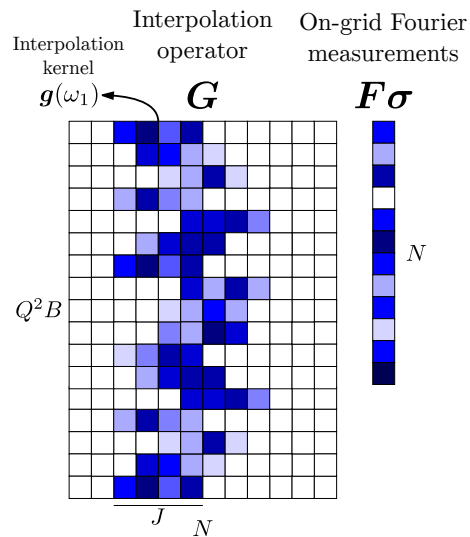


Fig. 4.2 Illustration of the NUFFT computations. The FFT $F\sigma \in \mathbb{C}^N$ is linearly interpolated with the operator $G \in \mathbb{C}^{Q^2B \times N}$ of sparsity Q^2BJ , using only J neighbors to interpolate the FFT coefficients to a continuous frequency. G is the concatenation of the interpolation kernels $\{g(\omega_i)\}_{i=1}^{Q^2B}$.

4 | Compressive Radio-Interferometry

4.3 Acquisition and Sensing Models

Here, we present three models compatible with radio interferometry. The first is the *classical scheme* computing frequency samples of the images, or *visibilities*, from the signal covariance matrix. Then follow *random Gaussian compression* and *baseline-dependent averaging*; two post-sensing compression techniques acting on the visibilities. Finally, we propose a new compressive sensing scheme, coined *modulated ROP*, occurring at the antenna level and circumventing the limitations raised in the other models.

4.3.1 Classical Acquisition: From the Antenna Signals to the Visibilities

This section provides a recapitulation of the classical sensing scheme. The radio-interferometric measurements and the link of their covariance matrix to the visibilities are derived. Then we show how the visibilities are usually accumulated over B batches in order to obtain a sufficiently dense Fourier sampling of the image of interest.

Let us consider a context of radio-astronomical imaging, as depicted in Fig. 4.3, with Q antennas⁴ receiving complex Gaussian cosmic signals $s(l, t) \stackrel{\text{i.i.d.}}{\sim} \mathcal{CN}(0, \sigma^2(l))$ from the sky with power flux density distribution $\sigma^2(l)$ [W/m²]—the image of interest. We write $l = (l, m)$ the direction cosines of the portion of the sky looked from the array formed by the antennas. More precisely, a *direction cosine* coordinate system fixed with its origin at the center of the Earth is chosen such that the center of the field to be imaged is denoted by the unit vector $s_0 = (l, m, n) = (0, 0, 1)$. The other directions in the region of interest are denoted by $s = s_0 + \tau$ with $\tau = (l, m, \sqrt{1 - l^2 - m^2})$. The region of interest will be considered sufficiently small to approximate it as a plane⁵, or equivalently $\sqrt{1 - l^2 - m^2} \approx 1$. The set $\Omega(t) := \{p_q^\perp(t)\}_{q=1}^Q \subset \mathbb{R}^2$ denotes the projection onto the plane perpendicular to s_0 of the instantaneous position of the Q antennas—moving in time due to the rotation of the Earth. Our reasoning is inspired by the framework of [VWS18] with the following adaptations:

⁴We will write “antennas” as a generic term to designate telescope dishes, single antennas or beamformed subarrays.

⁵The invalidity of this assumption can be addressed with a spread spectrum model, *i.e.*, by considering the partial Fourier transform of the image with a linear chirp modulation [CGB08; Wia+09b; Dab+21a].

- G1. We assume a monochromatic signal with a single wavelength λ and associated frequency $f = \frac{c}{\lambda}$ with the speed of light c . The separation into frequency subbands can be done efficiently with filter banks [VWS18].
- G2. We consider the signals at instantaneous time t and thus report their sampling to later.
- G3. We deal with a continuous intensity distribution $\sigma^2(\mathbf{l})$ rather than a finite number of signal sources. On the time scale of the acquisition, the intensity distribution is stationary.
- G4. We give the explicit expression of the phase factors $a_q(\mathbf{l}, t) = e^{\frac{i2\pi}{\lambda} \mathbf{p}_q^\perp(t)^\top \mathbf{l}}$ that inform on the position-dependent geometric delays.
- G5. We consider the same direction-dependent gain $g(\mathbf{l})$ for all antennas.

Note that G1. is in practice partially satisfied as we sample then break the received signal into S subbands with frequency f_s for $s \in \llbracket S \rrbracket$ to get $\mathbf{x}(n, s)$ where the index n is associated to the time [VWS18]. The response of the receiving system, with eventual filtering and conversion to baseband, is not explained in this thesis but more information about it can be found in [TMS17, Chap. 6].

Up to a compensation for the arrival time difference between individual antennas, we can always assume that all antennas lie in a plane perpendicular to the pointing direction \mathbf{s}_0 . Under the stated conditions, [VWS18, Eq. (9)] which describes the temporal signal received by antenna $q \in \llbracket Q \rrbracket$ can be modified as $x_q(t) = \bar{x}_q(t) + n_q(t)$ with the noiseless measurements⁶

$$\bar{x}_q(t) = \int_{\mathbb{R}^2} g(\mathbf{l}) s(\mathbf{l}, t) e^{\frac{i2\pi}{\lambda} \mathbf{p}_q^\perp(t)^\top \mathbf{l}} d\mathbf{l}, \quad (4.8)$$

where $s(\mathbf{l}, t) \underset{\text{i.i.d.}}{\sim} \mathcal{CN}(0, \sigma^2(\mathbf{l}))$ and $\mathbf{n}(t) := (n_q(t))_{q=1}^Q \sim \mathcal{CN}(\mathbf{0}, \Sigma_n)$ are complex zero mean white Gaussian random processes with the assumption [VWS18]

$$\mathbb{E}[s(\mathbf{l}, t)s^*(\mathbf{l}', t)] = \sigma^2(\mathbf{l})\delta(\mathbf{l} - \mathbf{l}'). \quad (4.9)$$

We can stack the Q received signals into an instantaneous measurement vector $\mathbf{x}(t) = (x_1(t), \dots, x_Q(t))$, with the (Hermitian) covariance

⁶The integration over \mathbb{R}^2 is possible, despite $\mathbf{l} \in [0, 1]^2$, because the gains g will be zero outside $[0, 1]^2$.

4 | Compressive Radio-Interferometry

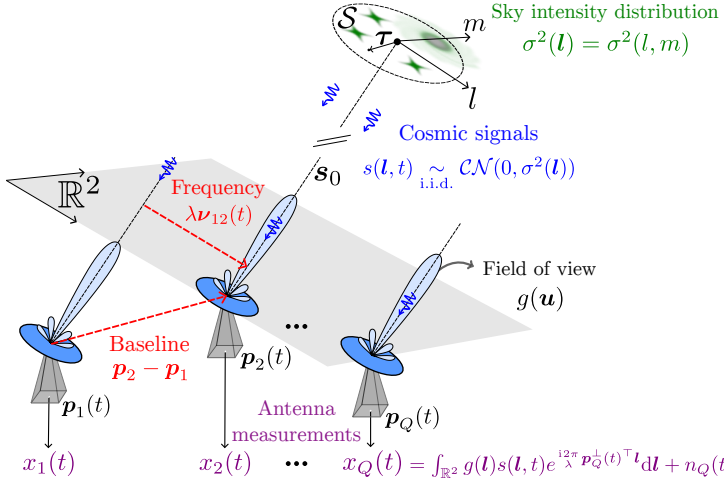


Fig. 4.3 Schematic of the radio-interferometric sensing context. Far-away cosmic signals following a Gaussian random process, *i.e.*, $s(l, t) \sim_{\text{i.i.d.}} \mathcal{CN}(0, \sigma^2(l))$ with an intensity distribution $\sigma^2(l)$, are received by Q antennas. The antennas, positionned in $\Omega(t) := \{p_q^\perp(t)\}_{q=1}^Q$, have the same direction-dependent gain $g(l, t)$ focusing a specific region S of the sky. Each antenna $q \in \llbracket Q \rrbracket$ integrates—with its own geometric delay $p_q^\perp(t)^\top l$ the cosmic signals from all direction into a noisy measurement $x_q(t) = \int_{\mathbb{R}^2} g(l) s(l, t) e^{\frac{i 2 \pi}{\lambda} p_q^\perp(t)^\top l} dl + n_q(t)$.

matrix as $\mathbf{C}(t) := \mathbb{E}_s \mathbb{E}_n [x(t) x^*(t)] \in \mathcal{H}^Q$. Leveraging the *Van Cittert-Zernike* theorem [Van34; Zer38] and assuming that the same realization of the cosmic signals $s(l, t)$ is received simultaneously at time t for all antennas, the covariance matrix can be recast as

$$\mathbf{C}(t) = \mathcal{I}_{\Omega(t)}[\sigma^\circ] + \Sigma_n. \quad (4.10)$$

In (4.10), $\Sigma_n := \mathbb{E}_n [n(t) n^*(t)]$ is the noise covariance and

$$(\mathcal{I}_{\Omega(t)}[\sigma^\circ])_{jk} := \int_{\mathbb{R}^2} \sigma^\circ(l) e^{\frac{-i 2 \pi}{\lambda} (p_k^\perp(t) - p_j^\perp(t))^\top l} dl \quad (4.11)$$

is the jk -th entry of the *interferometric matrix* of the map σ° —analogous to [LWJ24]—where $\sigma^\circ(l) := g^2(l) \sigma^2(l)$ is the *vignetted map*. Overall, (4.10) and (4.11) show that RI corresponds to an interferometric system that is *affine* in σ° . It is tantamount to sampling the 2-D Fourier transform of σ° over frequencies selected in the difference multiset,

$$\mathcal{V}(t) := \frac{1}{\lambda} (\Omega(t) - \Omega(t)) = \{\nu_{jk}(t) := \frac{p_j^\perp(t) - p_k^\perp(t)}{\lambda}\}_{j,k=1}^Q, \quad (4.12)$$

i.e., $(\mathcal{I}_{\Omega}[\sigma^\circ](t))_{jk} = \mathcal{F}[\sigma^\circ](\nu_{kj}(t))$, then adding the covariance matrix of the noise Σ_n .

Remark 4.1. It is impossible in practice to set the gains $g(l) = 1$, i.e., to observe the whole sky with direction-independent gains. Like in (3.4) in Chap. 3, the image of interest is vigneted, i.e., its field-of-view is restricted. The nuance is that, unlike the vignetting imposed by the effective width of the cores for MCFLI, the vignetting in RI is designed by beamforming each antenna, either with the geometry of the dish, by combining the signals received in a subarray of antennas, or a combination of both.

Remark 4.2. The assumption of identical antenna gains in G5 removes the calibration aspects from the discussion in this chapter. We will return to this question in the final discussion in Sec. 4.7.

In practice, the measurement vector $\mathbf{x}(t)$ must be time sampled as $\mathbf{x}[i] = \mathbf{x}(iT)$ with sampling period T and i an integer to perform digital computations. Due to the rotation of the Earth, the time samples $\mathbf{x}[i]$ are separated into B Short-Time Integration (STI) intervals, or *batches*, indexed by b and of duration IT with I samples per STI. All these samples can be stacked into a *signal set* \mathcal{X} as

$$\mathcal{X} := \bigcup_{b \in \llbracket B \rrbracket} \mathcal{X}_b, \quad \mathcal{X}_b := \{\mathbf{x}_b[i], i \in \llbracket I \rrbracket\}, \quad (4.13)$$

where $\mathbf{x}_b[i] := \mathbf{x}[(b-1)I + i]$. With a typical sampling rate of 1GHz, and an STI interval IT of 15s, $I \approx 15 \cdot 10^9$ samples are enough to accurately approximate the covariance matrix with a *sample covariance*. The batch duration is sufficiently short to assume that the set of antenna positions for batch b remains nearly stationary within the time interval $\mathcal{T}_b := [bIT, (b+1)IT]$, i.e., $\Omega_b := \{\mathbf{p}_q^\perp(t)\}_{q=1, t \in \mathcal{T}_b}^Q \approx \{\mathbf{p}_{bq}^\perp\}_{q=1}^Q$. An example of realistic antenna arrangements $\{\Omega_b\}_{b=1}^B$ and corresponding visibility sets $\{\mathcal{V}_b\}_{b=1}^B$ for $\mathcal{V}_b := \Omega_b - \Omega_b$ is given in Fig. 4.4.

From the definition of $\mathbf{x}_b[i]$ in (4.13), the *sample covariance matrix* of batch b is defined as

$$\begin{aligned} \tilde{\mathbf{C}}_b(\mathcal{X}_b) &:= \frac{1}{I} \sum_{i=1}^I \mathbf{x}_b[i] \mathbf{x}_b^*[i] \\ &= \mathbb{E}_{s,n} [\mathbf{x}_b[i] \mathbf{x}_b[i]^*] + \left(\frac{1}{I} \sum_{i=1}^I \mathbf{x}_b[i] \mathbf{x}_b[i]^* - \mathbb{E}_{s,n} [\mathbf{x}_b[i] \mathbf{x}_b[i]^*] \right) \\ &= \mathbf{C}_b + \mathbf{N}_b(\mathcal{X}_b) \stackrel{(4.11)}{=} \mathbf{I}_{\Omega_b}[\sigma^{\circ}] + \Sigma_n + \mathbf{N}_b(\mathcal{X}_b), \end{aligned} \quad (4.14)$$

4 | Compressive Radio-Interferometry

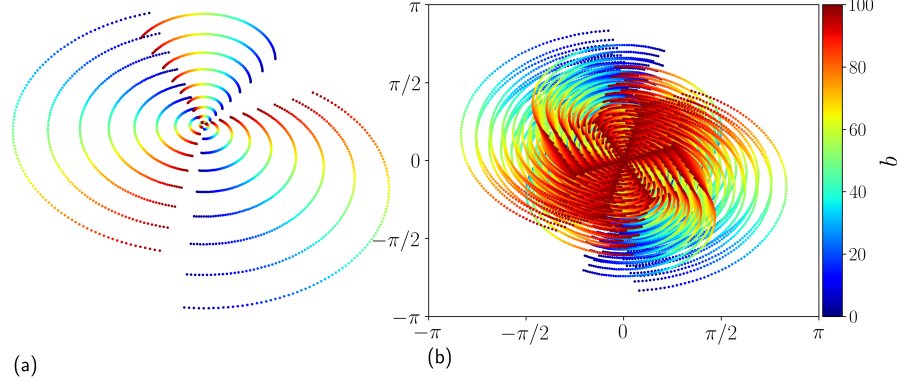


Fig. 4.4 (a) Arrangement $\{\Omega_b\}_{b=1}^{100}$ of the antennas of the *Very Large Array* (VLA) [Tho+80] for a total observation time of five hours. (b) the visibility set $\{\mathcal{V}_b\}_{b=1}^{100}$ corresponding to (a). The colors vary from blue for $b = 1$ to red for $b = 100$.

for any $i \in \llbracket I \rrbracket$, $\mathcal{I}_{\Omega_b}[\sigma^\circ] := \mathcal{I}_{\Omega(t=(b-1/2)IT)}[\sigma^\circ]$, and where we defined the *statistical noise* as

$$N_b(\mathcal{X}_b) := \tilde{\mathbf{C}}_b(\mathcal{X}_b) - \mathbf{C}_b = \frac{1}{I} \sum_{i=1}^I (\mathbf{x}_b[i] \mathbf{x}_b^*[i] - \mathbf{C}_b).$$

Separating the expectation term from the statistical noise is not a new idea [VWS18, Eq. (29)]. We are interested in studying the concentration of $\tilde{\mathbf{C}}_b(\mathcal{X}_b)$ around its expectation \mathbf{C}_b to quantify the amount of statistical noise. To this end, we will use the complex version⁷ of [Ver12, Corollary 5.50]

Corollary 4.1 (Covariance estimation for complex sub-Gaussian distributions). *Consider a sub-Gaussian distribution in \mathbb{C}^Q with covariance matrix \mathbf{C}_b , and let $\eta \in (0, 1)$, $t \geq 1$. Define the sample covariance matrix $\tilde{\mathbf{C}}_b(\mathcal{X}_b) := \frac{1}{I} \sum_{i=1}^I \mathbf{x}_b[i] \mathbf{x}_b^*[i]$ with independent realizations $\{\mathbf{x}_b[i]\}_{i=1}^I$ of this distribution. Then with probability at least $1 - 2e^{-t^2 Q}$ one has*

$$\text{If } I \geq C(t/\eta)^2 Q \text{ then } \|N_b\| = \|\tilde{\mathbf{C}}_b(\mathcal{X}_b) - \mathbf{C}_b\| \leq \eta \|\mathbf{C}_b\|.$$

Here $C = C_K$ depends only on the sub-Gaussian norm $K = \|\mathbf{x}\|_{\psi_2}$.

⁷[Ver12, Corollary 5.50] is easily extended to the complex case from a separation into real and imaginary parts.

Cor. 4.1 shows that the statistical noise can be decreased to any arbitrarily small value $\eta \|C_b\|$ as long as a sufficient number I of samples is used and as long as one can suppose each $x_b[m]$ having the same covariance, which is in concurrence with large values of I . From a linearity argument, and remembering that the cosmic signals follow an i.i.d. complex Gaussian process $s(\mathbf{l}, t) \stackrel{\text{i.i.d.}}{\sim} \mathcal{CN}(0, \sigma^2(\mathbf{l}))$, the antenna signals vector $\mathbf{x}(t)$ can be shown to also follow a Gaussian distribution [Oks13]. The vector $\mathbf{x}(t)$ has zero mean and covariance $C(t)$ as derived in (4.10). The zero mean is verified with

$$\mathbb{E}_s [x_q(t)] = \int_{\mathbb{R}^2} \mathbb{E}_s [s(\mathbf{l}, t)] e^{\frac{12\pi}{\lambda} \mathbf{p}_q^\perp(t)^\top \mathbf{l}} d\mathbf{l} = 0, \quad \forall q \in \llbracket Q \rrbracket.$$

The complex Gaussian random vector $\mathbf{x}(t)$ is thus also sub-Gaussian with $\|\mathbf{x}(t)\|_{\psi_2} \leq C \sqrt{\lambda_{\max}(C(t))}$ for a constant $C > 0$. Indeed,

$$\begin{aligned} \|\mathbf{x}(t)\|_{\psi_2} &:= \sup_{v \in \mathcal{S}^{Q-1}} \|\langle \mathbf{x}(t), v \rangle\|_{\psi_2} \\ &\leq \sup_{v \in \mathcal{S}^{Q-1}} C \mathbb{E}[\langle \mathbf{x}(t), v \rangle^2] \\ &= \sup_{v \in \mathcal{S}^{Q-1}} C v^* \mathbb{E}[\mathbf{x}(t) \mathbf{x}^*(t)] v \\ &= \sup_{v \in \mathcal{S}^{Q-1}} C v^* C(t) v = C \sqrt{\lambda_{\max}(C(t))} \end{aligned}$$

where \mathcal{S}^{Q-1} is the unit sphere of dimension $Q - 1$ and we used [Ver12, Ex. 5.8] between the first and second line. In the following sections, we will assume that I is always chosen accordingly to target a given statistical noise constant η .

Re-using the *boundedness* and *bandlimitedness* assumptions 3.1 and 3.2 given in Sec. 3.3, σ° can be represented by a vectorized image $\sigma \in \mathbb{R}^N$ of N pixels in the FOV. Compared to Chap. 3 (see Sec. 3.2.4), the antenna locations are now allowed to be *off-the-grid*. While the interferometric matrix at batch b , \mathcal{I}_{Ω_b} , can be modeled in matrix form as shown in Appendix 4.8.3, the discrete representation of σ° yields a vector formulation

$$\bar{v}_b := \text{vec}(\mathcal{I}_{\Omega_b}[\sigma]) = G_b F \sigma \tag{4.15}$$

where $G_b \in \mathbb{C}^{Q^2 \times N}$ is a convolutional interpolation operator that interpolates the *on-grid* frequencies obtained from the FFT $F\sigma$ in the continuous Fourier plane at frequencies corresponding to the difference

4 | Compressive Radio-Interferometry

set $\mathcal{V}_b := \mathcal{V}(t = (b - 1/2)IT)$ defined in (4.12). This procedure is known as *Non-Uniform Fast Fourier Transform* (NUFFT). We practically use the MIN-MAX interpolation technique [FS03]. Finally, as depicted in Fig. 4.5(a), all the visibilities accumulated with the B batches are combined as

$$\bar{\mathbf{v}} = \begin{bmatrix} \bar{v}_1 \\ \vdots \\ \bar{v}_B \end{bmatrix} = \begin{bmatrix} \mathbf{G}_1 \\ \vdots \\ \mathbf{G}_B \end{bmatrix} \mathbf{F}\sigma = \mathbf{G}\mathbf{F}\sigma. \quad (4.16)$$

Note that (4.16) compares to the standard RI forward model [Pra+18] with less details about the NUFFT compensation terms. Indeed, they write $\bar{\mathbf{v}} = \Phi\sigma$ with

$$\Phi = WGFZDB \quad (4.17)$$

where $\mathbf{B} \in \mathbb{C}^{N \times N}$ (already included into σ in our model (4.16)) applies the direction-dependent gain function $g(\mathbf{l})$ to the discrete image, $\mathbf{D} \in \mathbb{C}^{N \times N}$ is a gridding correction operator that scales the image to correct for the interpolation convolution kernel \mathbf{G} , $\mathbf{Z} \in \mathbb{C}^{\alpha^2 N \times N}$ is a zero-padding operator that provides oversampling by factor α in each dimension of the Fourier domain, $\mathbf{F} \in \mathbb{C}^{\alpha^2 N \times \alpha^2 N}$ is the DFT operator, $\mathbf{G} \in \mathbb{C}^{Q^2 B \times \alpha^2 N}$ is the interpolation operator playing the same role as in (4.16), and $\mathbf{W} \in \mathbb{C}^{Q^2 B \times Q^2 B}$ weights the visibilities according to their density. For the sake of notational simplicity, we will use the simplified model (4.16) by keeping in mind that the realistic model (4.17) is used in practice.

We emphasize the difference between the *acquisition operator*

$$\begin{aligned} \mathcal{X} \mapsto \Psi(\mathcal{X}) &:= (\Psi_1(\mathcal{X}_1)^\top, \dots, \Psi_B(\mathcal{X}_B)^\top)^\top \in \mathbb{C}^{Q^2 B}, \\ \text{with } \Psi_b(\mathcal{X}_b) &:= \text{vec}(\mathbf{C}_b(\mathcal{X}_b) - \boldsymbol{\Sigma}_{\mathbf{n}}) \in \mathbb{C}^{Q^2}, \end{aligned} \quad (4.18)$$

that computes the visibility vector $\mathbf{v} = \Psi(\mathcal{X})$ from the antenna signals \mathcal{X} , and the *imaging operator*

$$\sigma' \in \mathbb{R}^N \mapsto \Phi(\sigma') := \mathbf{G}\mathbf{F}\sigma' \quad (4.19)$$

that computes a candidate visibility vector $\bar{\mathbf{v}}' = \Phi(\sigma')$ from a candidate image σ' . These operators are identical up to the statistical noise defined in (4.14), which means that

$$\mathbb{E}_{\mathcal{X}} \Psi(\mathcal{X}) = \Phi(\sigma). \quad (4.20)$$

Historically, the goal of radio-interferometric imaging has been to compute a good estimate $\tilde{\sigma}$ fitting the visibility data \mathbf{v} yielded from

$\Psi(\mathcal{X}(\sigma))$. Among the latest state-of-the-art reconstruction algorithms, both SARA [CMW12] and AIRI [Ter+22] algorithms aim to provide an estimate $\tilde{\sigma} \approx \sigma$ by solving

$$\tilde{\sigma} = \arg \min_{\sigma' \in \mathbb{R}^N} \frac{1}{2} \|v - GF\sigma'\|_2^2 + \lambda r(\sigma')$$

where the term $r(\sigma')$ is a specific *regularization*. Unfortunately, the total number of visibilities⁸ $\frac{1}{2}Q(Q-1)B$ can become too large for arrays containing thousands of antennas and aggregating measurements over thousands of batches. The following sections describe ways to reduce this number of measurements.

⁸Half of the Hermitian matrix $\mathcal{I}_{\Omega_b}[\sigma]$ as well as its diagonal, containing the DC component, are usually removed from the measurements to avoid redundancy.

4 | Compressive Radio-Interferometry

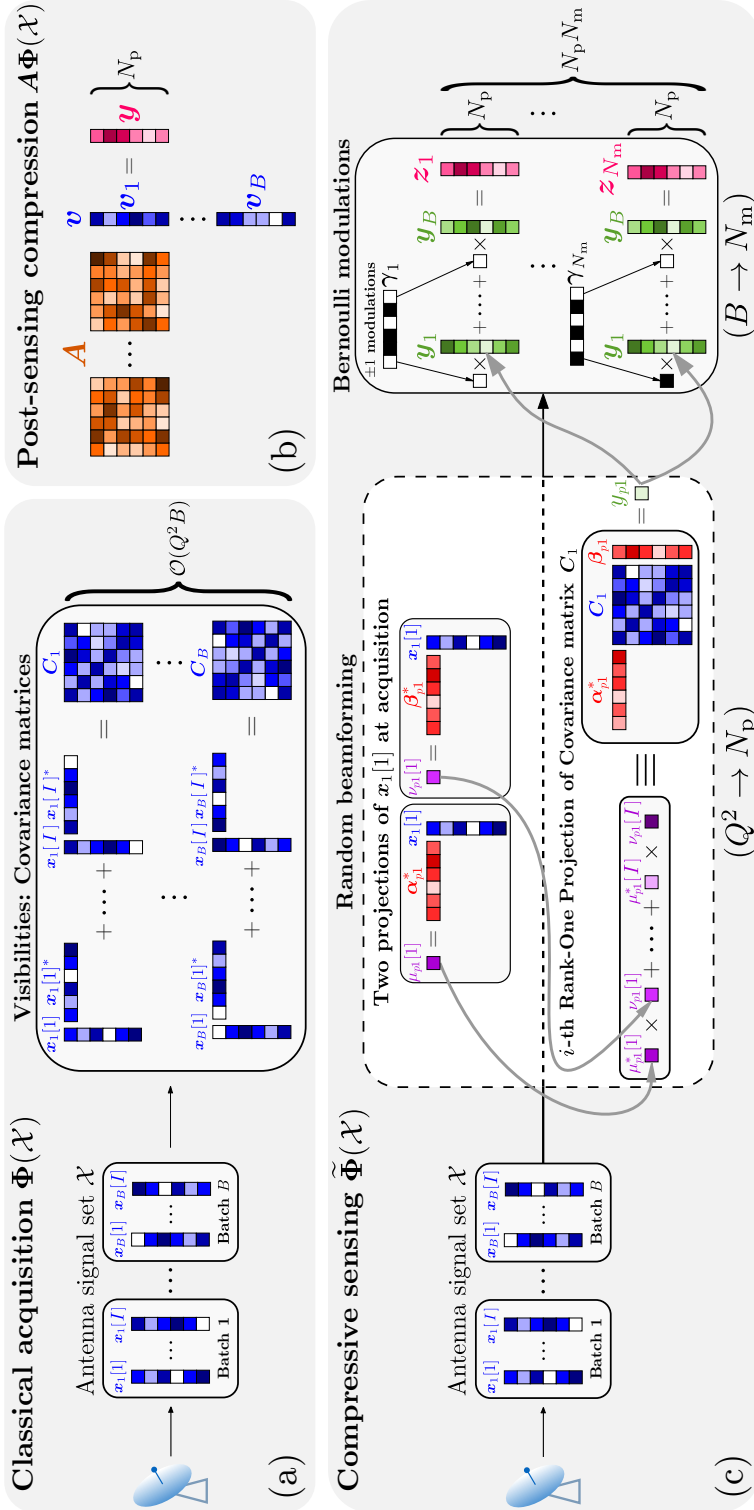


Fig. 4.5 Computations at the acquisition: from the antenna signals \mathcal{X} to the (compressed) visibilities. We consider the noiseless case ($\Sigma_n = 0$) to simplify the illustration. (a) **Classical scheme.** For each batch b , the sample covariance matrix is computed as $\tilde{C}_b = \frac{1}{I} \sum_{i=1}^I x_b[i] x_b[i]^*$. The covariance matrices include all visibilities. (b) **Post-sensing compression.** The (vectorized) visibilities are compressed using an i.i.d. random Gaussian matrix as $y = Av$. (c) **Compressive sensing.** For each batch b , N_p ROPs of the covariance matrix are obtained as $y_{pb} = \frac{1}{I} \sum_{i=1}^I \alpha_{pb}^* x_b[i]^* \beta_{pb}$ $\forall p \in [N_p]$. The $\{y_b\}_{b=1}^B$ ROP vectors are next *modulated* with Bernoulli modulation vectors $\{\gamma_m\}_{m=1}^{N_m}$ and $\gamma_{mb} \sim \mathcal{U}\{-1, 1\}$ as $z_m := \sum_{b=1}^B \gamma_m y_b$ i.i.d. The ± 1 values in the modulation vectors are represented by black and white cells.

4.3.2 Post-Sensing Compression

Several post-sensing compression techniques have been considered in the past.

Random Gaussian compression For instance, as depicted in Fig. 4.5(b), one can reduce the dimension (and thus the memory footprint) of both operators Ψ and Φ with N_p random Gaussian projections and compute, at the acquisition and at the reconstruction,

$$\mathbf{y} = \mathbf{A}\Psi(\mathcal{X}), \text{ and} \quad (4.21)$$

$$\bar{\mathbf{y}} = \mathbf{A}\Phi(\sigma) = \mathbf{AGF}\sigma, \quad (4.22)$$

respectively, with $\mathbf{y}, \bar{\mathbf{y}} \in \mathbb{C}^{N_p}$ and $\mathbf{A} \in \mathbb{C}^{N_p \times Q^2B}$ with $A_{jk} \stackrel{\text{i.i.d.}}{\sim} \mathcal{N}(0, 1/N_p)$ [Wia+09b]. It appears clearly in (4.21) that the compression is applied after the acquisition of the visibilities, justifying the “post-sensing” terminology. Unfortunately, \mathbf{A} is dense and makes its application untractable with $\mathcal{O}(N_p Q^2 B)$ operations.

Baseline-dependent averaging Another possibility named *Baseline-dependent averaging* [WWS18] consists in averaging the visibilities associated to low-frequency content over consecutive batches. This yields a reduced number of measurements, scaling as $\mathcal{O}(Q^2 B')$, with an equivalent number of batches $B' \ll B$. Applying the *averaging operator* $\mathbf{S} \in \{0, 1\}^{Q^2 B' \times Q^2 B}$ provides

$$\mathbf{y} = \mathbf{S}\Psi(\mathcal{X}), \text{ and} \quad (4.23)$$

$$\bar{\mathbf{y}} = \mathbf{S}\Phi(\sigma) = \mathbf{G}'\mathbf{F}\sigma \quad (4.24)$$

where $\mathbf{G}' \in \mathbb{C}^{Q^2 B' \times N}$ is the *averaged* version of \mathbf{G} . Baseline-dependent averaging is cheap and can provide more than 80% of compression [WWS18]. However, the resulting projection does not leverage the low-complexity representation of the image σ .

4.3.3 Compressive Sensing Scheme: Random Beamforming and Bernoulli Modulations

This section develops a two-layer compressive sensing model relying on (i) random beamforming for compressing the information stored in the interferometric matrix of each batch, and (ii) Bernoulli modulations followed by time integration to further compress the data stream along

4 | Compressive Radio-Interferometry

the time domain. The so-called *modulated ROPs* are presented as a good candidate for reduced memory storage and cheap acquisition.

The *separated ROP* model that includes only the first compression layer and the *batched ROP* model that compress along the time domain by integrating the separated ROPs without modulations are presented along the way. The bottlenecks of the *separated ROP* and *batched ROP* approaches are explained in Sec. 4.5.3 and Sec. 4.3.4, respectively.

The following mathematical derivations focus on the noiseless measurements, and the impact of noise is discussed at the end of this section.

First layer: random beamforming In RI, *beamforming* is a signal processing technique that has been used to enhance the sensitivity and resolution of radio telescopes by combining signals from multiple antennas [VWS18]. Mathematically, given a sketching vector α and the signals defined in (4.8), beamforming can be modeled as a projection (or *sketch*) of the measurements vector as

$$\begin{aligned}\mu(t) := \alpha^* \mathbf{x}(t) &= \int_{\mathbb{R}^2} g(\mathbf{l}) s(\mathbf{l}, t) \sum_{q=1}^Q \alpha_q^* e^{\frac{i 2 \pi}{\lambda} \mathbf{p}_q^\perp(t)^\top \mathbf{l}} d\mathbf{l} \\ &= \int_{\mathbb{R}^2} g_\alpha(\mathbf{l}) s(\mathbf{l}, t) d\mathbf{l}\end{aligned}\quad (4.25)$$

for an equivalent direction-dependent gain $g_\alpha(\mathbf{l}) := g(\mathbf{l}) \sum_{q=1}^Q \alpha_q^* e^{\frac{i 2 \pi}{\lambda} \mathbf{p}_q^\perp(t)^\top \mathbf{l}}$. By adjusting the phase and amplitude of the signals from the Q antennas using the sketching vector α , beamforming allows the array to focus on a specific direction in the sky by narrowing $g_\alpha(\mathbf{l})$ compared to $g(\mathbf{l})$.

As depicted in Fig. 4.6, let us consider two sketches $\mu(t)$ and $\nu(t)$ of the measurement vector computed from (4.25) with the sketching vectors $\alpha := (\alpha_1, \dots, \alpha_Q)$ and $\beta := (\beta_1, \dots, \beta_Q)$, and more specifically their sampling $\mu_b[i]$ and $\nu_b[i]$ obtained in the same way as how $x_b[i]$ was obtained in (4.13). Aggregating their product in time gives

$$\begin{aligned}y_b &= \frac{1}{I} \sum_{i=1}^I \mu_b[i] \nu_b^*[i] \\ &= \frac{1}{I} \sum_{i=1}^I \alpha^* \mathbf{x}_b[i] \mathbf{x}_b^*[i] \beta = \alpha^* \tilde{\mathbf{C}}_b \beta.\end{aligned}\quad (4.26)$$

In (4.26), it appears that $\alpha^* \tilde{\mathbf{C}}_b \beta := \langle \alpha \beta^*, \tilde{\mathbf{C}}_b \rangle_F$ is a *rank-one projection* (ROP) of the sample covariance matrix because it amounts to projecting \mathbf{C}_b with the rank-one matrix $\alpha \beta^*$ [CZ+15; CCG15]. Eq. (4.26) showcases that the acquisition process has changed compared to Sec. 4.3.1. These random beamforming computations are illustrated in the center box in Fig. 4.5(c). We will define a new acquisition operator after introducing *layer 2*.

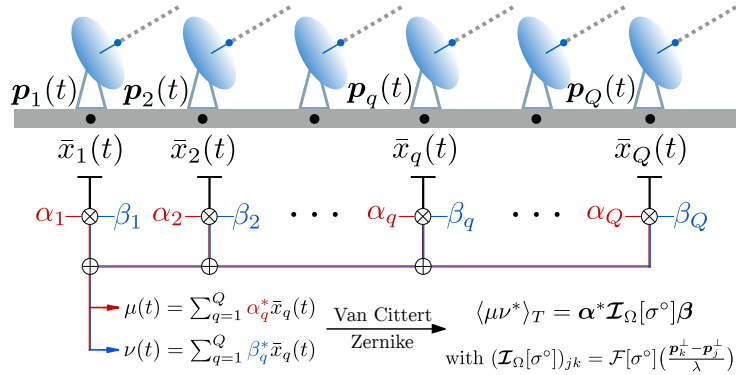


Fig. 4.6 Projections of the (noiseless) measurement vector $\bar{x}(t)$ with the sketching vectors α and β . By leveraging the Van Cittert-Zernike theorem, integrating the product of the projections $\mu(t)$ and $\nu(t)$ over time yields a ROP of the interferometric matrix of the vigneted image $\mathcal{I}_{\Omega}[\sigma^\circ]$.

Inserting the definition of the sample covariance matrix (4.14) into (4.26) yields

$$y_b = \alpha^* \tilde{C}_b \beta = \alpha^* \mathcal{I}_{\Omega_b}[\sigma^\circ] \beta + \alpha^* \Sigma_n \beta + \alpha^* N_b \beta. \quad (4.27)$$

Three terms appear in (4.27). First, the signal of interest, the ROP $\alpha^* \mathcal{I}_{\Omega_b}[\sigma^\circ] \beta$ of the interferometric matrix (as detailed in App. 4.8.1, this is analogous to [LWJ24, Eq. (3)] in MCFLI). Second, the quantity $\alpha^* \Sigma_n \beta$ is a *fixed* bias term due to noise in the antenna measurements. This bias is expected to be compensated, at least partially, by the knowledge of the sketching vectors $\{\alpha, \beta\}$ and a good estimate of the noise covariance matrix Σ_n . Finally, $\alpha^* N_b \beta$ is a ROP of the statistical noise, expected to be controlled by the number of samples I . App. 4.8.2 provides more details about beamforming. It makes the link between focused beamforming and the raster-scanning approach described in Sec. 3.2.2, and presents the *adaptive beamforming* technique.

We are going to show that one can devise a specific sensing scheme of the antenna signals that avoids storing individually the B sample covariance matrices $\{\tilde{C}_b\}_{b=1}^B$ as done classically in (4.27). This is possible while still ensuring an accurate estimation of the image of interest. This sensing first records $N_p \ll Q^2$ different random ROPs of each \tilde{C}_b , or, equivalently, N_p evaluations of y_b in (4.26) from different $\mu_b[i]$ and $\nu_b[i]$, associated with random vectors α and β . Following [LWJ24], we consider N_p i.i.d. random *sketching* vectors $\alpha_{pb}, \beta_{pb} \sim_{\text{i.i.d.}} \rho$, $p \in \llbracket N_p \rrbracket$, for some random vector $\rho \in \mathbb{C}^Q$ with $\rho_q \stackrel{\text{i.i.d.}}{\sim} \exp(i\mathcal{U}[0, 2\pi])$, $q \in \llbracket Q \rrbracket$. While random Gaussian vectors α and β were another appropriate

4 | Compressive Radio-Interferometry

choice (the only condition is sub-Gaussianity), unitary vectors are more practical for implementation on real antennas, especially in analog operations, as they only require tuning the phase by beamforming techniques.

Separated ROP

We focus here on the forward imaging model. The N_p ROPs are gathered in the measurement vector $\bar{\mathbf{y}}_b := (\bar{\mathbf{y}}_{pb})_{p=1}^{N_p} \in \mathbb{C}^{N_p}$, with $\bar{\mathbf{y}}_{pb} = \boldsymbol{\alpha}_{pb}^* \mathcal{I}_{\Omega_b}[\sigma] \boldsymbol{\beta}_{pb}$. Moreover, following the methodology of Sec. 4.3.1, we can write

$$\bar{\mathbf{y}}_b = \mathbf{R}_b \mathbf{G}_b \mathbf{F} \boldsymbol{\sigma}, \quad (4.28)$$

where each row of the matrix \mathbf{R}_b computes a single ROP measurement, *i.e.*, $(\mathbf{R}_b^\top)_p = \text{vec}(\boldsymbol{\alpha}_{pb} \boldsymbol{\beta}_{pb}^*)^\top$, for all $p \in [N_p]$. The B ROPed batches can then be concatenated as

$$\bar{\mathbf{y}} = \begin{bmatrix} \bar{\mathbf{y}}_1 \\ \vdots \\ \bar{\mathbf{y}}_B \end{bmatrix} = \begin{bmatrix} \mathbf{R}_1 & & & \mathbf{G}_1 \\ & \ddots & & \vdots \\ & & \mathbf{R}_B & \mathbf{G}_B \end{bmatrix} \mathbf{F} \boldsymbol{\sigma} = \mathbf{D} \mathbf{G} \mathbf{F} \boldsymbol{\sigma}, \quad (4.29)$$

with $\bar{\mathbf{y}} \in \mathbb{C}^{N_p B}$. The imaging model (4.29), simply consists of adding the *separated ROP* operator \mathbf{D} to the conventional model (4.16) sensing the visibilities.

We show in App. 4.8.4 how it is also possible to write the measurement vector with the *matrix form* of the forward imaging model, similarly to (ROPI), and conclude that its associated computational complexity is higher than the equivalent vector form.

Layer 2: Bernoulli modulations

Batched ROP

Unfortunately, in (4.29), the number of measurements $N_p B$ still depends on the (fixed) number of batches B . Furthermore, as the name implies, the separated ROPs approach does not mix the visibilities of different batches. The forward operator in (4.29) contains a *non-dense* ROP operator \mathbf{D} —which is actually block-diagonal. This makes it more difficult to analyze in the same theoretical framework as in Sec. 3.3. There exists work on providing the RIP for dense i.i.d. random block-diagonal matrices [Eft+15], but it does not apply to the ROP matrices $\{\mathbf{R}_b\}_{b=1}^B$ which are not i.i.d.

The *Batched ROP* approach, consists in compressing along the time domain by *batching* the measurement vectors obtained for each batch together as $\bar{\mathbf{y}} = \sum_{b=1}^B \bar{\mathbf{y}}_b \in \mathbb{C}^{N_p}$. This is equivalent to writing

$$\bar{\mathbf{y}} = [\mathbf{R}_1 \quad \dots \quad \mathbf{R}_B] \begin{bmatrix} \mathbf{G}_1 \\ \vdots \\ \mathbf{G}_B \end{bmatrix} \mathbf{F}\sigma = \mathbf{R}\mathbf{G}\mathbf{F}\sigma = \mathbf{R}\Phi\sigma, \quad (4.30)$$

with $\mathbf{R} \in \mathbb{C}^{N_p \times Q^2 B}$. As clear from (4.30), the ROP operator \mathbf{R} is now dense, and a RIP of the total forward operator $\mathbf{R}\Phi$ can be provided (see Sec. 4.5).

Remark 4.3. *The batched ROP approach also finds a nice interpretation in terms of ROPs of a total interferometric matrix, defined as*

$$\mathcal{I} := \begin{bmatrix} \mathcal{I}_{\Omega_1} & & \\ & \ddots & \\ & & \mathcal{I}_{\Omega_B} \end{bmatrix}. \quad (4.31)$$

The p-th measurement writes

$$\bar{\mathbf{y}}_p = \boldsymbol{\alpha}_p^* \mathcal{I} \boldsymbol{\beta}_p = \begin{bmatrix} \boldsymbol{\alpha}_{p1}^* & \dots & \boldsymbol{\alpha}_{pB}^* \end{bmatrix} \begin{bmatrix} \mathcal{I}_{\Omega_1} & & \\ & \ddots & \\ & & \mathcal{I}_{\Omega_B} \end{bmatrix} \begin{bmatrix} \boldsymbol{\beta}_{p1} \\ \vdots \\ \boldsymbol{\beta}_{pB} \end{bmatrix} = \sum_{b=1}^B \boldsymbol{\alpha}_{pb}^* \mathcal{I}_{\Omega_b} \boldsymbol{\beta}_{pb}. \quad (4.32)$$

And the final ROP vector writes as $\bar{\mathbf{y}} = (\bar{\mathbf{y}}_p)_{p=1}^{N_p} := \mathcal{A}(\mathcal{I})$ where the sketching operator \mathcal{A} defines I ROP [CCG15; CZ+15] of any Hermitian matrix $\mathbf{H} \in \mathcal{H}^Q$ with

$$\mathcal{A}(\mathbf{H}) := (\langle \boldsymbol{\alpha}_p \boldsymbol{\beta}_p^*, \mathbf{H} \rangle_F)_{p=1}^{N_p}. \quad (4.33)$$

The name given to this approach appears even more clearly in (4.32); each ROP measurement is given as a ROP of the total interferometric matrix—summing all the batches together. This viewpoint in (4.32) will be useful for the guarantees given in Sec. 4.5.

Modulated ROP

Despite being accompanied by recovery guarantees, the *batched ROP* model suffers from a severe increase of the computational cost of the forward model, as will be discussed in Sec. 4.3.4. Following an approach whose feasibility will be discussed momentarily, we thus apply

4 | Compressive Radio-Interferometry

N_m Bernoulli modulations of the ROP vectors before aggregating them, *i.e.*, we compute

$$\bar{z}_m = \sum_{b=1}^B \gamma_{mb} \bar{y}_b \quad (4.34)$$

with the *modulation vectors* $\gamma_m \stackrel{\text{i.i.d.}}{\sim} \gamma$, $m \in \llbracket N_m \rrbracket$, and $\gamma_b \stackrel{\text{i.i.d.}}{\sim} \mathcal{U}\{\pm 1\}$, $b \in \llbracket B \rrbracket$.

From the separated ROP model (4.29), this can also be viewed as

$$\bar{z}_m = [\gamma_{m1} \mathbf{I} \quad \dots \quad \gamma_{mB} \mathbf{I}] \bar{y} = (\gamma_m^\top \otimes \mathbf{I}) \bar{y}$$

with $\mathbf{I} \in \mathbb{R}^{N_p \times N_p}$ and the Kronecker product \otimes . Moreover, the N_m modulations can be concatenated as

$$\bar{z} = \begin{bmatrix} \bar{z}_1 \\ \vdots \\ \bar{z}_{N_m} \end{bmatrix} = (\boldsymbol{\Gamma}^\top \otimes \mathbf{I}) \bar{y} = \mathbf{M} \bar{y},$$

with $\boldsymbol{\Gamma} := [\gamma_1, \dots, \gamma_{N_m}] \in \{\pm 1\}^{B \times N_m}$, $\mathbf{M} := \boldsymbol{\Gamma}^\top \otimes \mathbf{I} \in \{\pm 1\}^{N_p N_m \times N_p B}$, and $\bar{z} \in \mathbb{C}^{N_p N_m}$. The resulting imaging model writes

$$\bar{z} = \tilde{\Phi}(\sigma) := \mathbf{M} \mathbf{D} \mathbf{G} \mathbf{F} \sigma \quad (4.35)$$

which turns in to simply apply the *modulation operator* $\mathbf{M} \in \{\pm 1, 0\}^{N_p N_m \times N_p B}$ to the separated ROP model in (4.29).

On the acquisition side, this defines the *compressive sensing operator*

$$\mathcal{X} \in \mathbb{C}^Q \mapsto z = (z_1^\top, \dots, z_{N_m}^\top)^\top := \tilde{\Psi}(\mathcal{X}) \in \mathbb{C}^{N_p N_m}, \quad (4.36)$$

with

$$z_{mp} := \sum_{b=1}^B \gamma_{mb} \boldsymbol{\alpha}_{pb}^* (\tilde{\mathbf{C}}_b(\mathcal{X}_b) - \boldsymbol{\Sigma}_n) \boldsymbol{\beta}_{pb}^*, \quad p \in \llbracket N_p \rrbracket, \quad m \in \llbracket N_m \rrbracket. \quad (4.37)$$

As illustrated in Fig. 4.5(c), this also means that, in the noiseless case ($\boldsymbol{\Sigma}_n = \mathbf{0}$) or up to a debiasing step removing the contribution of the noise covariance,

$$z_{mp} := \sum_{b=1}^B \gamma_{mb} y_{pb}, \quad \text{with } y_{pb} = \frac{1}{I} \sum_{i=1}^I \mu_{pb}[i] \nu_{pb}^*[i] \quad (4.38)$$

which involves the computation of antenna signal sketches $\mu_{pb}[i] := \boldsymbol{\alpha}_{pb}^* \mathbf{x}_b[i]$ and $\nu_{pb}[i] := \boldsymbol{\beta}_{pb}^* \mathbf{x}_b[i]$.

Remark 4.4. Like the batched ROPs, the modulated ROPs approach also finds a nice interpretation in terms of ROPs of the total interferometric matrix \mathcal{I} . Introducing the modulation vectors $\epsilon_m, \tilde{\epsilon}_m \in \{\pm 1\}^B$ with $\epsilon_{mb} \stackrel{\text{i.i.d.}}{\sim} \mathcal{U}\{-1, 1\}$, $\forall m \in \llbracket N_m \rrbracket$, and the diagonal matrices $D_{\epsilon_m}, D_{\tilde{\epsilon}_m} \in \{\pm 1, 0\}^{QB \times QB}$ with

$$D_{\epsilon_m} := \text{diag}(\epsilon_m) \otimes \mathbf{I}_Q, \quad (4.39)$$

and equivalently for $D_{\tilde{\epsilon}_m}$, the (p, m) -th measurement writes

$$\begin{aligned} \bar{z}_{mp} &= (D_{\epsilon_m} \alpha_p)^* \mathcal{I} (D_{\tilde{\epsilon}_m} \beta_p) \\ &= \begin{bmatrix} \epsilon_{m1} \alpha_{p1}^* & \dots & \epsilon_{mB} \alpha_{pB}^* \end{bmatrix} \begin{bmatrix} \mathcal{I}_{\Omega_1} & & \\ & \ddots & \\ & & \mathcal{I}_{\Omega_B} \end{bmatrix} \begin{bmatrix} \tilde{\epsilon}_{m1} \beta_{p1} \\ \vdots \\ \tilde{\epsilon}_{mB} \beta_{pB} \end{bmatrix} \\ &= \sum_{b=1}^B \epsilon_{mb} \tilde{\epsilon}_{mb} \alpha_{pb}^* \mathcal{I}_{\Omega_b} \beta_{pb} = \sum_{b=1}^B \epsilon_{mb} \tilde{\epsilon}_{mb} \bar{y}_{pb} = \sum_{b=1}^B \gamma_{mb} \bar{y}_{pb}. \end{aligned} \quad (4.40)$$

With $\gamma_{mb} := \epsilon_{mb} \tilde{\epsilon}_{mb}$, we recover in (4.40) the modulation principle introduced in (4.34).

For the computational complexity of the forward imaging model, critical in all image reconstruction algorithms, the discussion about the structural differences between the operator MD composing the ROP and Bernoulli modulations, and the operators A for the Gaussian compression and G' for the baseline-dependent averaging, is given in Sec. 4.3.4.

4.3.4 Complexities

This section compares the complexities of the models presented in Sec. 4.3.1-4.3.3. It starts with the analysis of the acquisition process given in Table 4.2 and the complexities involved in the image reconstruction process are provided in Table 4.3.

The complexities are accompanied by a numerical value using Table 4.1 as reference. We distinguish the number of projections N_p applied in the *batched ROP* approach from the number of projections *per batch* N_{pb} applied in the *separated* and *modulated ROP* approaches because the sample complexities required for image recovery are differ-

4 | Compressive Radio-Interferometry

ent. The provided numerical values are not self-explanatory for the actual complexities occurring in real arrays of antennas. First, there are indeed arrays coming up with thousands of antennas. Second, the total number of batches associated to 24h of acquisition depends on the duration of a batch. And finally, the cosmic signals are separated into many frequency subbands whose number is a multiplication factor for the computational complexity. Consequently, the differences in order of magnitude of the different models are more important than their absolute values.

Table 4.1 Typical values in RI. A number of batches $B = 1000$ approximately corresponds, for batches of 15s, to a total acquisition of four hours.

Symbol	Value	Number of
N	10^6	Image pixels
Q	10^2	Antennas
B	10^3	Batches
N_p	10^3	Projections
N_{pb}	50	Projections per batch
N_m	10^2	Modulations
J	50	Neighbours for interpolation with G
$B' \ll B$	10^2	Equivalent batches
$N'_b \lesssim JQ^2$	10^3	Pixels activated by visibilities in b
$N' \lesssim QJ^2B$	10^4	Pixels activated by all visibilities

Acquisition

Table 4.2 Computational cost of the acquisition and sample complexities in \mathcal{O} . The green and red cell colors indicate low and high complexity, respectively.

Name	Model	Cost per batch		Max size	
Classical acquisition	Ψ	Q^2	10^4	Q^2B	10^7
Post-sensing compression	$A\Psi$	$N_p Q^2$	10^7	Q^2	10^4
Compressive sensing	$\tilde{\Psi}$	$N_{pb} Q$	$5 \cdot 10^3$	$N_{pb} N_m$	$5 \cdot 10^3$

The computational cost during the acquisition is as important as controlling the memory usage. Table 4.2 compares the computational cost and maximal data size of the classical, post-sensing compression and compressive sensing schemes.

To compute the visibilities, the outer product of each antenna signal vector is taken, each costing $\mathcal{O}(Q^2) = 10^4$ operations. In the *dense Gaussian compression* approach, the visibilities must first be computed and then projected by a large matrix, costing $\mathcal{O}(N_p Q^2) = 10^7$. This

need to compute the visibilities and then project them with long vectors strongly increases the cost at acquisition. It shows why no dense matrix compression was considered earlier and more complex dimensionality reduction techniques were required [Vij+17].

All ROP approaches require N_{pb} (or N_p) projections per measurement vector, costing $\mathcal{O}(N_{pb}Q) = 5 \cdot 10^3$ (resp. $\mathcal{O}(N_pQ) = 10^5$). It is seen that the cost of the modulated ROP sensing approach becomes smaller than the classical sensing scheme if $N_{pb} < Q$.

The key observation in Fig. 4.5(c) is that the number of measurements never exceeds $N_{pb}N_m$ during the acquisition because the ROP and modulations can be computed and aggregated on the fly. As shown in the numerical experiments in Sec. 4.6, $N_{pb}N_m$ can be much smaller than the Q^2B visibilities of the classical scheme while still ensuring accurate image estimations.

The random Gaussian post-sensing compression must compute an intermediate number Q^2 of visibilities during each batch. More particularly, computing N_p projections of each visibility matrix costs $\mathcal{O}(N_pQ^2)$ operations per batch.

In the compressive sensing scheme, we do not account for the number $\mathcal{O}(N_{pb}B)$ of sketching elements needed for the random beamforming because these values can be selected and stored with less precision than the final data.

Image reconstruction

In Table 3.1, the provided complexities were slightly misleading because the fact that only some pixels are hit by the visibilities was not taken into account. In this section, a better evaluation of the complexities is given by exploiting the sparsity of the interpolation matrix G .

Table 4.3 provides an ordered comparison of the models presented in this section.

Memory storage As will be clear in Sec. 4.6, the number of random projections needed for reliable image reconstruction is typically $N_p = 10^3$. In Table 4.3, one observes that storing all the visibilities \bar{v} is expensive; with $Q^2B = 10^7$ values to store. Averaging the visibilities, as explained in Sec. 4.3.2, reduces the storage to $Q^2B' = 10^6$. The number of stored visibilities for separated ROPs is $N_{pb}B = 5 \cdot 10^4$ and for modulated ROPs is $N_{pb}N_m = 5 \cdot 10^3$.

4 | Compressive Radio-Interferometry

Table 4.3 Complexities of the forward imaging models for CRI in \mathcal{O} . The green, orange, and red cell colors indicate low, medium, and high complexity, respectively. The $*$ denotes precomputed versions.

Model	Name	Acquisition per sample		Forward model		Memory	
		$N \log N$	$2 \cdot 10^7$	$+ \quad +$	$Q^2 B$	$5 \cdot 10^8$	$Q^2 B$
Φ	Classical	Q^2	10^4		JQ^2B		10^7
$SP\Phi$	Averaging	Q^2	10^4		JQ^2B'	$5 \cdot 10^7$	$Q^2 B'$
$A\Phi$	Gaussian	$N_p Q^2$	10^7		$N_p Q^2 B$	10^{10}	N_p
$D\Phi$	Separated	$N_{pb} Q$	$5 \cdot 10^3$		$N_{pb} Q^2 B$	$5 \cdot 10^8$	$N_{pb} B$
$R\Phi$	Batched	$N_p Q$	10^5		$*N_{pb} BN'_b$	$5 \cdot 10^7$	
$MD\Phi$	Modulated	$N_{pb} Q$	$5 \cdot 10^3$		$N_p Q^2 B$	10^{10}	N_p
					$N_{pb} B(Q^2 + N_m)$	$5 \cdot 10^8$	$N_{pb} N_m$
					$*N_{pb} N_m N'_b$	$5 \cdot 10^6$	$5 \cdot 10^3$

Cost of the forward model With the consecutive application of A , G , and F in (4.22), the computational cost is $\mathcal{O}(N \log N + JQ^2B + N_p Q^2B) \approx 10^{10}$.

The cost of applying consecutively $D\Phi$ for the *separated ROPs* approach is $\mathcal{O}(N \log N + JQ^2B + N_{pb} Q^2B) \approx \mathcal{O}(N_{pb} Q^2B) \approx 5 \cdot 10^8$. As already explained in Table 4.5, the cost of the forward model by precomputing $\{A_b G_b\}_{b=1}^B$ is $\mathcal{O}(N_{pb} BN'_b + N \log N) \approx 5 \cdot 10^7$. The precomputation costs $\mathcal{O}(N_{pb} BJQ^2) \approx 10^{10}$. As the precomputation step is unique and the recovery algorithms presented in Sec. 4.4 require thousands of iterations to converge, this precomputation cost is generally acceptable.

For the *batched ROPs* approach, applying consecutively F , G , and R costs $\mathcal{O}(N \log N + JQ^2B + N_p Q^2B) \approx 10^{10}$ operations. This is exactly the same cost as for the *dense Gaussian* compression. If RG is precomputed, the precomputation costs $\mathcal{O}(N_p JQ^2B) \approx 10^{10}$ and the forward model costs $\mathcal{O}(N_p N' + N \log N) \approx 5 \cdot 10^7$.

For the *modulated ROPs* approach, whose forward imaging operators are illustrated in Fig. 4.7, applying M to the separated ROPs only adds the negligible $\mathcal{O}(N_m N_{pb} B) = 5 \cdot 10^6$ operations to the complexity of the (precomputed or not) separated ROPs. The effective cost of the modulations is negligible compared to all other operations because the ± 1 values only imply flipping signs of the values processed in RAM. Still, the cost of applying the operators $MDGF$ sequentially is dominated by the cost of D , *i.e.*, $\mathcal{O}(N_{pb} BQ^2) = 5 \cdot 10^8$. In order to never need to compute either all the visibilities or the projections per batch, the whole operator MDG can be precomputed in

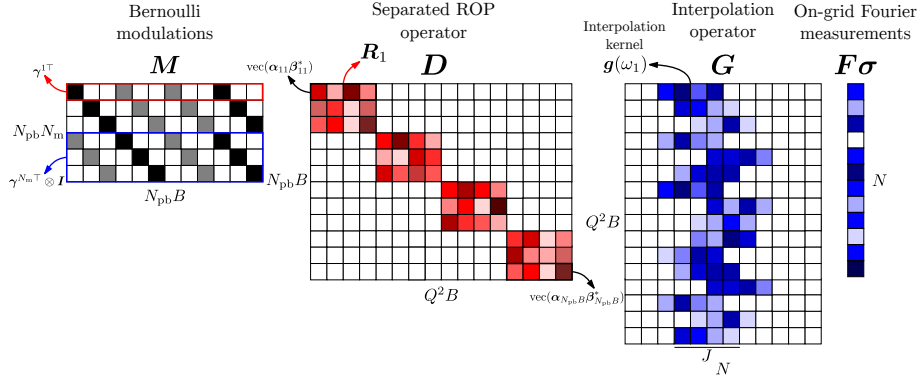


Fig. 4.7 Structure of the modulated ROP operators. As already illustrated in Fig. 4.2, the Q^2B visibilities are obtained by interpolating with G , and at a cost $\mathcal{O}(JQ^2B)$, between the on-grid frequencies computed from an FFT of the image $F\sigma$ costing $\mathcal{O}(N \log N)$ operations. The separated ROP operator D requires $\mathcal{O}(N_{pb}Q^2B)$ operations and consists of a block-diagonal matrix, where each row of each block is the vectorization of a rank-one matrix. The modulated ROP are finally obtained by applying the Bernoulli modulation operator M at a negligible cost $\mathcal{O}(N_m N_{pb} B)$.

$\mathcal{O}(N_m N_{pb} B + N_{pb} B J Q^2) \approx 10^{10}$ operations. After this precomputation, the forward model has the overall lowest cost of $\mathcal{O}(5 \cdot 10^6)$.

The *baseline-dependent averaging* has a computational cost of $\mathcal{O}(JQ^2B') \approx 5 \cdot 10^7$ with the costless precomputation of G' .

In conclusion, the *modulated ROPs* approach gets the best of all complexities, with a small acquisition cost, forward model, a compression of the measurements, and sum of the projections along the batches to come close to the recovery guarantees provided in Sec. 4.5.

4.3.5 Noise Sources

In this section, we bring back the noise terms forsaken since Sec. 4.3.1 and derive the effect of noise added to the separated ROPs on their Bernoulli modulations.

To be realistic, it is unclear at which stage of the forward model an additive noise needs to be inserted. The position (in the sensing model) of the dominant thermal noise heavily depends on the practical implementation of the acquisition process. From [TMS17], it seems reasonable to consider an additive Gaussian noise on the separated ROP measurements. However, it is still possible to consider an additive noise on the visibilities, and to infer the noise resulting on the separated ROPs, but this is fastidious. In the following, we directly start from a noise

4 | Compressive Radio-Interferometry

model on the separated ROPs.

As a reminder, in the Sec. 4.3.3 which describes the noise in each ROP measurement when *random beamforming* is applied to the antennas, we ended up with two major noise terms in (4.27) rewritten here

$$\tilde{y}_b = \alpha^* \mathcal{I}_{\Omega_b}[\sigma^\circ] \beta + b_b + \xi_b :$$

(i) a bias $b_b := \alpha^* \Sigma_n \beta$ with the covariance of the noise Σ_n , (ii) a statistical noise term $\xi_b := \alpha^* N_b \beta$. Interestingly, the covariance of the thermal noise on the antennas Σ_n is generally orders of magnitude higher than the visibilities coming from sometimes very weak cosmic sources and contained in $\mathcal{I}_{\Omega_b}[\sigma^\circ]$ [VWS18]. Depending on the spatial arrangement and proximity of the antennas as well as their physical connections, the covariance of the noise Σ_n can sometimes be well approximated as a diagonal matrix. In any case, the bias b_b must be systematically subtracted by using a good estimate of Σ_n [TMS17].

The statistical noise, studied in Sec. 4.3.1, is in practice very mitigated because the sampling rate is on the order of 1GHz, and a typical STI interval is 15s. This makes a sample covariance computed using $M \approx 15 \cdot 10^9$ samples. The unstopping rotation of the Earth also induces noise in the measurements, as we had to assume a fixed position for the antennas within each batch in Sec. 4.3.1. The frequencies associated to each batch are not exactly punctual but rather a blurred version of curved paths into the Fourier plane. There are obviously many other noise sources such as quantum, quantization, and correlator⁹ noise for instance.

In the following, we make an abuse of notation to rewrite ξ_b as the *additive noise term* encompassing both the part of the bias b_b remaining from an imperfect compensation and all the other upper cited noise sources. The *compensated* version y_b of separated ROP measurements in (4.28) can thus be written as

$$y_b = R_b G_b F \sigma + \xi_b \quad (4.41)$$

with $\xi_b \underset{\text{i.i.d.}}{\sim} \mathcal{CN}(\mathbf{0}, \Xi_b)$ for a noise covariance Ξ_b at batch b . Recalling the definition in (4.34) of the modulated ROPs $z_m := \sum_{b=1}^B \gamma_{mb} y_b$, the noisy model arises as

$$z = M D G F \sigma + \zeta \quad (4.42)$$

⁹Older radio-interferometers used to compute analog correlations, inducing correlator noise [TMS17].

with the *modulated noise*

$$\zeta := \begin{bmatrix} \zeta_1 \\ \vdots \\ \zeta_{N_m} \end{bmatrix}$$

and $\zeta_m := \sum_{b=1}^B \gamma_{mb} \xi_b \stackrel{\text{i.i.d.}}{\sim} \mathcal{CN}(\mathbf{0}, \sum_{b=1}^B \Xi_b)$, $\forall m \in \llbracket N_m \rrbracket$ conditionally to the knowledge of the modulations $\{\gamma_{mb}\}_{b=1, m=1}^{B, N_m}$. One easily verifies that

$$\zeta \sim \mathcal{CN} \left(\mathbf{0}, \begin{bmatrix} \sum_{b=1}^B \Xi_b & \sum_{b=1}^B \gamma_{1b} \gamma_{2b} \Xi_b & \cdots & \sum_{b=1}^B \gamma_{1b} \gamma_{N_m, b} \Xi_b \\ \sum_{b=1}^B \gamma_{2b} \gamma_{1b} \Xi_b & \sum_{b=1}^B \Xi_b & \cdots & \\ \vdots & \vdots & \ddots & \\ \sum_{b=1}^B \gamma_{N_m, b} \gamma_{1b} \Xi_b & & & \sum_{b=1}^B \Xi_b \end{bmatrix} \right).$$

By remembering $\gamma_{mb} \stackrel{\text{i.i.d.}}{\sim} \mathcal{U}\{-1, 1\}$, one has $\mathbb{E}_\gamma [\sum_{b=1}^B \gamma_{mb} \gamma_{m', b} \Xi_b] = 0$. Hence, defining $\Xi := \sum_{b=1}^B \Xi_b$, the noise distribution is well approximated as

$$\zeta \sim \mathcal{CN}(\mathbf{0}, I_{N_m} \otimes \Xi). \quad (4.43)$$

where

$$I_{N_m} \otimes \Xi = \begin{bmatrix} \Xi & & & \\ & \ddots & & \\ & & \underset{N_m \text{ times}}{\Xi} & \\ & & & \Xi \end{bmatrix}.$$

Eq. (4.43) shows that the noise ζ added into the modulated ROP measurements z can be approximated as a centered complex Gaussian noise with a block-diagonal covariance matrix $I_{N_m} \otimes \Xi$. In this approximation, valid for a big number of batches B , the $\{\zeta_m\}_{m=1}^{N_m}$ are mutually independent.

As a concluding remark of this section, the good news is that the additive noise ζ in the modulated ROP model (4.42) remains a centered Gaussian noise. Furthermore, if the covariance matrix Ξ_b of the noise added to the separated ROP measurements is diagonal, so is the covariance of ζ .

4 | Compressive Radio-Interferometry

4.4 Recovery Algorithms

In this section, we present the image recovery algorithms used in the *recovery analysis* given in Sec. 4.6. As motivated in Sec. 4.3.3, we analyze these algorithms applied to the *modulated ROP* scheme with sensing model

$$z = MDGF\sigma + \zeta = A_m\sigma + \zeta, \quad (4.44)$$

where σ is the image of interest, ζ is the additive noise on the modulated ROPs explained in Sec. 4.3.5, F , G , D and M are respectively the DFT, visibility, separated ROP, and modulation operators.

The simplest algorithm—namely CLEAN—suitable for sparse images is presented first. The BPDN program is briefly recalled. Then, we explain USARA; a *state-of-the-art* algorithm based on a *proximal gradient* approach.

4.4.1 The Good Old CLEAN

For half a century, *beamforming* techniques have been used to focus the received cosmic signal in a specific direction l^* in the sky S and to reconstruct the image of the sky from successive translations of that focus. As explained in Sec. 4.3.3 with the correspondence between beamforming and raster-scanning, it is possible to construct a *blurry* version of the image of interest—often called *dirty image* $\sigma_{\text{dirty}}^2(l)$ —using a beamforming technique.

Mathematically, constructing a *dirty image* from any sensing model $y = \Phi x$ consists in computing a raw estimate as $x_{\text{dirty}} = \Phi^* y$ or $x_{\text{dirty}} = \Phi^\dagger y$. The beamforming technique explained above is equivalent to compute the dirty image as $\sigma_{\text{dirty}} = F^* G^* G F \sigma$. With our scheme, a dirty image can be computed as

$$\sigma_{\text{dirty}} = A_m^* z. \quad (4.45)$$

Naturally, the dirty image in (4.45) is of lower quality than what could have been obtained by beamforming. Still, we can apply a simple recovery algorithm to it. We can associate a dirty image $\sigma_{\text{dirty}}^2(l)$ with the discrete σ_{dirty} , which will be used for CLEAN.

The standard algorithm CLEAN¹⁰ [Hög74] is based on the assumption that the sky is mostly empty, and consists of a set of discrete point sources of size K . The sky can thus be written as $\sigma^2(l) =$

¹⁰It has been shown that CLEAN is equivalent to *Matching Pursuit* [MZ93].

$\sum_{k=1}^K \sigma_k^2 \delta(\mathbf{l} - \mathbf{l}_k)$. The ponctual sources are estimated one-by-one iteratively from the brightest to the darkest via a sequential *Least Squares fitting* method. CLEAN uses the *dirty image* $\sigma_{\text{dirty}}^2(\mathbf{l})$ and the *dirty beam* (which is a synonym for PSF) $\phi_{\Omega}(\mathbf{l}) = \sum_{q=1}^Q e^{\frac{i2\pi}{\lambda} \mathbf{l}^\top \mathbf{p}_{bq}^\perp}$ for the reconstruction. The simplest form of the algorithm is reminded in Algo. 4.1.

Algorithm 4.1 CLEAN

Require: $\sigma_{\text{dirty}}^2(\mathbf{l})$ and $\phi_{\Omega}(\mathbf{l})$

- 1: $q = 1$
 - 2: **while** $q < K$ **do**
 - 3: $q += 1$
 - 4: $\mathbf{l}_q = \arg \max_{\mathbf{l}} \sigma_{\text{dirty}}^2(\mathbf{l})$ $\triangleright q\text{-th brightest source position}$
 - 5: $\tilde{\sigma}_q^2 = \sigma_{\text{dirty}}^2(\mathbf{l}_q) / \phi_{\Omega}(\mathbf{0})$ $\triangleright \text{source intensity}$
 - 6: $\sigma_{\text{dirty}}^2(\mathbf{l}) -= \tilde{\sigma}_q^2 \phi_{\Omega}(\mathbf{l} - \mathbf{l}_q), \forall \mathbf{l} \in \mathcal{S}$ $\triangleright \text{dirty image cleaning}$
- return** $\tilde{\sigma}^2(\mathbf{l}) = \sigma_{\text{dirty}}^2(\mathbf{l}) + \sum_{k=1}^K \tilde{\sigma}_k^2 \delta(\mathbf{l} - \mathbf{l}_k), \forall \mathbf{l} \in \mathcal{S}$.
-

There exists improvements to Algo 4.1. For instance, in lines 6 and 7, a scaling parameter can be introduced to account for the off-grid location of the sources—gridded in a discrete image. Also, the $\delta(\mathbf{l})$ function in line 7 can be replaced by a *synthetic beam* $\phi(\mathbf{l})$ (generally shaped as a Gaussian) in order to mask the otherwise high artificial resolution of the image. Current imaging systems rather iteratively clean the *covariance matrix* instead, being represented as a sum of K rank-one matrices, as shown in Sec. 3.3.1 [VWS18, Sec. 4.2].

4.4.2 BPDN

For the phase transition diagrams presented in Sec. 4.6.1, the basis pursuit denoising (BPDN) program explained in (BPDN $_{\ell_p}$) and, for this inverse problem application, written as

$$\tilde{\sigma} = \arg \min_{\sigma} \|\sigma\|_1 \text{ s.t. } \|z - A_m \sigma\|_2^2 \leq \epsilon$$

for a given noise level ϵ is solved using the *Proximal Gradient Method* presented in Prelim. 2.3.

4.4.3 uSARA

The *unconstrained Sparsity Averaging Reweighted Analysis* (uSARA) [RW20; Ter+22] is a sophisticated version of the *Proximal Gradient* method (see Algo 2.1). It recently demonstrated state-of-the-art reconstruction

4 | Compressive Radio-Interferometry

results on the uncompressed visibilities model explained in Sec. 4.3.1. Applied to our modulated ROP sensing model in (4.44), the minimization problem associated with uSARA writes

$$\tilde{\sigma} = \arg \min_{\sigma \in \mathbb{R}^N} \frac{1}{2} \|A_m \sigma - z\|_2^2 + \lambda \mathcal{R}(\sigma), \quad (4.46)$$

for a *regularization parameter* $\lambda > 0$, and prior model

$$\mathcal{R}(\sigma) := \rho \sum_{j=1}^{9N} \log (\rho^{-1} |(\Psi^* \sigma)_j| + 1) + \iota_{\mathbb{R}_+^N}(\sigma) \quad (4.47)$$

where $\rho > 0$ and the $+1$ are used to avoid reaching zero values in the argument of the logarithmic terms. The “average sparsity” prior in (4.47) consists of a positivity constraint and a log-sum prior¹¹ promoting average sparsity in an over-complete Wavelet dictionary $\Psi \in \mathbb{R}^{N \times 9N}$. More specifically, the dictionary Ψ is the concatenation of the first eight Daubechies wavelets [Dau92] and the Dirac basis I_N .

The nonconvexity of the minimization task in (4.46) is addressed by a reweighting procedure, where a sequence of convex surrogate minimization problems are solved iteratively, each involving a weighted- ℓ_1 prior g given by

$$g(\sigma, W) := \|W \Psi^* \sigma\|_1 + \iota_{\mathbb{R}_+^N}(\sigma), \quad (4.48)$$

where $W \in \mathbb{R}^{9N \times 9N}$ is a diagonal weighting matrix that needs to be updated after each resolution of the surrogate problem.

The resulting reconstruction algorithm used for uSARA is a *three-level* iterative scheme summarized in Algos 4.2-4.3. This seemingly computationally intensive algorithm has been shown to require only a fixed number K of proximal steps in the second for loop [RW21], and a small number of iterations in Algo 4.3 when using an appropriate initialization strategy for the dual variable $v^{(0)}$. The variables $\xi_1 > 0$, $\xi_2 > 0$ are relative variation convergence criteria, $L := \|A_m^* A_m\|$ is the *Lipschitz constant*, and $0 < \gamma < 2/L$ is the *stepsize*. The inequality condition on the stepsize is explained in Sec. 5.4.

¹¹A non-convex approximation of the ℓ_0 -norm.

Algorithm 4.2 Re-weighted PGM for uSARA

Require: $0 < \gamma < 2/L, \lambda > 0, \rho > 0, \tilde{\sigma}^{(0)} \in \mathbb{R}^N, \xi_1 > 0$

- 1: Set $\mathbf{W}^{(0)} = \mathbf{I}$
- 2: **repeat**
- 3: **for** $i = 0, 1, \dots$ **do**
- 4: $\sigma^{(0)} = \tilde{\sigma}^{(i)}$
- 5: **for** $k = 0, \dots, K$ **do**
- 6: $\sigma^{(k+1)} = \text{prox}_{\gamma\lambda g(\cdot, \mathbf{W}^{(0)})}(\sigma^{(k)} - \gamma \mathbf{A}_m^* (\mathbf{A}_m \sigma^{(k)} - \mathbf{z}))$ \triangleright FB
step
- 7: $\tilde{\sigma}^{(i+1)} = \sigma^{(K)}$
- 8: $\mathbf{W}^{(i+1)} = \text{diag}\left(\rho / \left(\rho + \Psi^* \tilde{\sigma}^{(i+1)}\right)\right)$ \triangleright Reweighting
- 9: $\sigma^{(i+1)} = \tilde{\sigma}^{(i+1)}$
- 10: **until** $\|\sigma^{(i+1)} - \sigma^{(i)}\|_2 / \|\sigma^{(i+1)}\|_2 < \xi_1$
- 11: **return** $\sigma^{(i+1)}$

Algorithm 4.3 Dual Forward-Backward for computing $\text{prox}_{\gamma\lambda g(\cdot, \mathbf{W})}(\mathbf{z})$ in Algorithm 4.2

Require: $\gamma > 0, \lambda > 0, \mathbf{W}, \mathbf{z} \in \mathbb{R}^N, \mathbf{v}^{(0)} \in \text{Span}(\Psi^*), \xi_2 > 0$

- 1: **repeat**
- 2: **for** $l = 0, 1, \dots$ **do**
- 3: $\sigma^{(l+1)} = \Pi_{\mathbb{R}_+^N}(\mathbf{z} - \Psi \mathbf{v}^{(l)})$ \triangleright Projection on real positive orthant
- 4: $\mathbf{v}^{(l+1)} = \left(\mathbf{I} - \text{prox}_{\gamma\lambda \|\mathbf{W}\cdot\|_1}(\mathbf{v}^{(l)} + \Psi^* \sigma^{(l+1)})\right) \mathbf{v}^{(l)} + \Psi^* \sigma^{(l+1)}$ \triangleright Soft-thresholding
- 5: **until** $\|\sigma^{(l+1)} - \sigma^{(l)}\|_2 / \|\sigma^{(l+1)}\|_2 < \xi_2$
- 6: **return** $\sigma^{(l+1)}$

4 | Compressive Radio-Interferometry

4.5 Recovery Guarantees for Batched ROPs

In this section, recovery guarantees are given for the *batched ROPs* model. Next, two arguments are given why it is unlikely for $\mathbf{D}\Phi$ to satisfy a RIP in the *separated ROPs* approach. The section concludes with an incomplete proof that motivates the likely provable success of modulated ROPs.

The noisy measurements \mathbf{y} are assumed to follow the *batched ROPs* model

$$\mathbf{y} = \mathbf{R}\Phi\sigma + \xi \quad (4.49)$$

for an additive noise ξ and after a debiasing step removing the measurement noise bias \mathbf{b} (see (4.27)). Because of the multiplicity Q of the DC component in the sensing operator Φ , only its *centered version* Φ_0 —removing the Q DC samples—can satisfy a $\text{RIP}_{\ell_2/\ell_2}$, as stated in Assumption 4.5. While SROP measurements can be debiased following the procedure of Sec. 3.3.3, the DC component $\hat{\sigma}_0 = (\mathbf{F}\sigma)_0$ can be easily estimated from the autocorrelation of the measurements at a single antenna. From this, the contribution of the DC component at each batch b can be subtracted from the measurements as

$$\mathbf{y}_b^c := \mathbf{y}_b - \hat{\sigma}_0 \mathbf{R}_b \mathbf{G}_b \mathbf{e}_1. \quad (4.50)$$

With this DC compensation, a *centered* version of the *batched ROPs* model (4.49) is considered as

$$\mathbf{y}^c = \mathbf{R}\Phi_0\sigma + \xi^c \quad (4.51)$$

We propose to estimate σ by solving the *Basis Pursuit DeNoise* program with an ℓ_1 -norm fidelity (or BPDN_{ℓ_1}), *i.e.*,

$$\tilde{\sigma} = \arg \min_{\sigma \in \mathbb{R}^N} \|\sigma\|_1 \text{ s.t. } \|\mathbf{y}^c - \mathbf{R}\Phi_0\sigma\|_1 \leq \epsilon, \quad (\text{BPDN}_{\ell_1})$$

The specific ℓ_1 -norm fidelity of this program is motivated by the properties of the ROP operator \mathbf{R} , and this imposes us to set $\epsilon \geq \|\xi^c\|_1$ to achieve feasibility.

We are interested in extending the guarantees given in Chap. 3 to prove both ℓ_2/ℓ_1 instance optimality of BPDN_{ℓ_1} and the $\text{RIP}_{\ell_2/\ell_1}$ for the operator $\mathbf{R}\Phi_0$ in (4.51). We indeed show below that $\mathbf{R}\Phi_0$, through its dependence on \mathbf{R} , respects the $\text{RIP}_{\ell_2/\ell_1}(\Sigma_K, \mathbf{m}_K, \mathbf{M}_K)$.

4.5.1 Instance Optimality of the BPDN_{ℓ_1} Program

Let us start by showing that if the $\text{RIP}_{\ell_2/\ell_1}$ holds for $\mathbf{R}\Phi_0$, then (BPDN_{ℓ_1}) is instance optimal.

Proposition 4.1 (ℓ_2/ℓ_1 instance optimality of BPDN_{ℓ_1}). *Given K , if there exists an integer $K' > 2K$ such that, for $k \in \{K', K + K'\}$, the operator $\mathbf{R}\Phi_0$ has the $\text{RIP}_{\ell_2/\ell_1}(\Sigma_k, \mathbf{m}_k, \mathbf{M}_k)$ for constants $0 < \mathbf{m}_k < \mathbf{M}_k < \infty$, and if*

$$\frac{1}{\sqrt{2}}\mathbf{m}_{K+K'} - \mathbf{M}_{K'} \frac{\sqrt{K}}{\sqrt{K'}} \geq \gamma > 0, \quad (4.52)$$

then, for all σ sensed through $\mathbf{y}^c = \mathbf{R}\Phi_0\sigma + \boldsymbol{\xi}^c$ with bounded noise $\|\boldsymbol{\xi}^c\|_1 \leq \epsilon$, the estimate $\tilde{\sigma}$ provided by BPDN_{ℓ_1} satisfies

$$\|\sigma - \tilde{\sigma}\|_2 \leq C_0 \frac{\|\sigma - \sigma_K^2\|_1}{\sqrt{K'}} + D_0 \frac{\epsilon}{N_p}, \quad (4.53)$$

for two values $C_0 = \mathcal{O}(\mathbf{M}_{K'}/\gamma)$ and $D_0 = \mathcal{O}(1/\gamma)$.

Proof. The proof follows exactly the proof given in Sec. 3.7.1. □

4 | Compressive Radio-Interferometry

Remark 4.5. As for classical additive white Gaussian noise, the statistical noise component of the centered noise ξ^c remains upper bounded with high probability. Indeed, with the total statistical noise matrix

$$\mathbf{N} := \begin{bmatrix} \mathbf{N}_1 & & \\ & \ddots & \\ & & \mathbf{N}_B \end{bmatrix},$$

its hollow version $\mathbf{N}_h := \mathbf{N} - \mathbf{N}_d$ and \mathbf{A} defined in (4.33), one can write

$$\begin{aligned} \|\frac{1}{N_p} \mathbf{A}(\mathbf{N}_h)\|_1 &\stackrel{\text{Lem. 4.2}}{\leq} c_2 \|\mathbf{N}_h\|_{\text{F}} \\ &= c_2 \sqrt{\sum_{b=1}^B \|(\mathbf{N}_b)_h\|_{\text{F}}^2} \leq c_2 \sqrt{Q} \sqrt{\sum_{b=1}^B \|(\mathbf{N}_b)_h\|^2} \\ &\stackrel{\text{Corr. 4.1}}{\leq} c_2 \eta \sqrt{Q} \sqrt{\sum_{b=1}^B \|(\mathbf{R}_b)_h\|^2} \\ &\leq c_2 \eta \sqrt{Q} \|\mathbf{R}_h\|_{\text{F}} := \epsilon \end{aligned}$$

which holds with probability $\geq (1 - \exp(-c_3 N_p))(1 - 2 \exp(-\frac{\eta^2 M}{C Q}))$ when setting $M = C(t/\eta)^2 Q$ in Cor. 4.1.

4.5.2 RIP _{ℓ_2/ℓ_1} for $\mathbf{R}\Phi_0$

The ingredients to prove the RIP _{ℓ_2/ℓ_1} for $\mathbf{R}\Phi_0$ will be essentially the same as in Sec. 3.3. The main difference compared to Chap. 3 here is that the Fourier sampling is now allowed to be *off-grid*, and is obtained through the B interferometric matrices $\{\mathcal{I}_{\Omega_b}\}_{b=1}^B$. To account for this, we consider adaptations of Assumptions 3.3 and 3.5 that write as

Assumption 4.3 (Distinct non-zero visibilities). Defining the total visibility set $\mathcal{V}_0 = \bigcup_{b=1}^B \mathcal{V}_b \setminus \{\mathbf{0}\}$ for the visibilities $\mathcal{V}_b := \left\{ \frac{\mathbf{p}_{bj}^\perp - \mathbf{p}_{bk}^\perp}{\lambda} \right\}_{j,k=1}^Q$ defined in Sec. 4.3, we assume that all non-zero visibilities in \mathcal{V}_0 are unique, which means that $|\mathcal{V}_0| = \sum_{b=1}^B |\mathcal{V}_b| = Q(Q-1)B$.

and

Assumption 4.5 (RIP $_{\ell_2/\ell_2}$ for visibility sampling). *Given a sparsity level K , a distortion $\delta > 0$, and provided*

$$|\mathcal{V}_0| = Q(Q-1)B \geq \delta^{-2}K \text{plog}(N, K, \delta), \quad (4.54)$$

for some polynomials plog($N, K, 1/\delta$) of $\log N$, $\log K$ and $\log 1/\delta$, the matrix $\Phi_0 = G_0 F$ defined in (4.16)^a respects the RIP $_{\ell_2/\ell_2}(\Sigma_K, \delta)$, i.e.,

$$(1-\delta)\|\mathbf{v}\|^2 \leq \frac{N}{|\mathcal{V}_0|} \|\Phi_0 \mathbf{v}\|_2^2 \leq (1+\delta)\|\mathbf{v}\|^2, \quad \forall \mathbf{v} \in \Sigma_K.$$

^aThe index 0 indicates that the DC component is excluded from the Fourier sampling. Only the frequencies at \mathcal{V}_0 are computed.

A significant gain in these adaptations is the new Fourier coverage that is denser than in the context of Chap. 3 because we consider B different sets $\{\Omega_b\}_{b=1}^B$ of antenna positions. Now, in Assumption 4.5, this is the total number of visibilities $Q(Q-1)B$ that must scale linearly with the image sparsity K . This condition is less demanding than it the one in Assumption 3.5.

The following proposition provides a RIP $_{\ell_2/\ell_1}$ for *asymmetric* ROPs using the property of *concentration of ROPs in the ℓ_1 -norm* from [CCG15, Prop. 1]. Because the ROPs are asymmetric here, compared to Chap. 3, the bounds of the RIP will be tighter than in Prop. 3.3. The proof is reported at the end of this chapter in Sec. 4.8.5.

Proposition 4.2 (RIP $_{\ell_2/\ell_1}$ for $R\Phi_0$ using asymmetric ROP). *Assume that assumptions [3.1, 3.2, 4.3, 3.4, 4.5, 3.6] hold, with 4.5 set to sparsity level $K_0 > 0$ and distortion δ over the set Σ_{K_0} . For some values $C, c > 0$, if*

$$N_p \geq CK_0 \ln\left(\frac{12eN}{K_0}\right), \quad Q(Q-1)B \geq 4K_0 \text{plog}(N, K_0, \delta), \quad (4.55)$$

then, with probability exceeding $1 - \exp(-cN_p)$, the operator $R\Phi_0$ respects the RIP $_{\ell_2/\ell_1}(\Sigma_{K_0}, m_{K_0}, M_{K_0})$ with

$$m_{K_0} > \frac{2}{3}\omega c_1 \sqrt{1-\delta} \frac{\sqrt{|\mathcal{V}_0|}}{\sqrt{N}}, \quad \text{and} \quad M_{K_0} < \frac{4}{3}\omega c_2 \sqrt{1+\delta} \frac{\sqrt{|\mathcal{V}_0|}}{\sqrt{N}}, \quad (4.56)$$

where the constants c_1 and c_2 depend only on the sub-Gaussian norm of the random sketching vectors $\{\alpha_p\}_{p=1}^{N_p}$ and $\{\beta_p\}_{p=1}^{N_p}$ hidden in R (see (4.30)).

4 | Compressive Radio-Interferometry

4.5.3 Doubts for Separated ROPs

Here we provide two arguments explaining why the *separated ROP* operator $D\Phi$ probably do not have the $\text{RIP}_{\ell_2/\ell_1}$.

Intuitive argument As stated in Assumption 4.5, the $\text{RIP}_{\ell_2/\ell_2}$ is assumed for the total (nonzero) visibility sampling G_0F , and not for the individual samplings $\{G_{b0}F\}_{b=1}^B$. In the *separated ROPs* approach, as is clear from (4.29), the *centered* forward model writes

$$\bar{\mathbf{y}}^c = \begin{bmatrix} \mathbf{R}_1 G_{10} \\ \vdots \\ \mathbf{R}_B G_{B0} \end{bmatrix} F\sigma.$$

Statistical argument Because the separated ROP measurements \bar{y}_b follow a different statistical distribution depending on the interferometric matrix \mathcal{I}_{Ω_b} that they sketch, it is not possible to control the ROP ℓ_1 -norm as in Lem. 3.3. To demonstrate this, we will show by using [Ver12, Prop. 5.16] and [CZ+15, Lem. 7.2] that the ℓ_1 -norm of the measurement $\frac{1}{N_p B} \|\bar{\mathbf{y}}\|_1$ does not concentrate nicely around the Frobenius norm of the total interferometric matrix $\|\mathcal{I}\|_{\text{F}}$.

The *subexponential* norm of each \bar{y}_{pb} writes

$$\begin{aligned} \|\bar{y}_{pb}\|_{\psi_1} &= \| |\langle \boldsymbol{\alpha}_{pb} \boldsymbol{\beta}_{pb}^*, \mathcal{I}_{\Omega_b} \rangle| \|_{\psi_1} \\ &= \sup_{q \geq 1} \frac{1}{q} (\mathbb{E} [|\langle \boldsymbol{\alpha}_{pb} \boldsymbol{\beta}_{pb}^*, \mathcal{I}_{\Omega_b} \rangle|^q])^{1/q} \\ &\leq K \|\mathcal{I}_{\Omega_b}\|_{\text{F}} \end{aligned} \quad (4.57)$$

with $K := \|\boldsymbol{\alpha}\|_{\psi_2}$ and where the last inequality comes from [CZ+15, Proof Lem. 7.1.]. Let us define the random variable

$$Z := \|\bar{\mathbf{y}}\|_1 - \mathbb{E} \|\bar{\mathbf{y}}\|_1 = \sum_{b=1}^B \sum_{p=1}^{N_p} (|\bar{y}_{pb}| - \mathbb{E} |\bar{y}_{pb}|).$$

Z is composed of $B N_p$ independent centered random variables, with $\|\bar{y}_b^i\|_{\psi_1} \leq K \|\mathcal{I}_{\Omega_b}\|_{\text{F}}$, as shown in (4.57). The result [Ver12, Prop. 5.16] provides a concentration of a sum of independent centered subexponential random variables. Applied to our problem, it writes

$$\mathbb{P} [|Z| > t] \leq 2 \exp \left(-c \min \left(\frac{t^2}{K^2 \max_b \|\mathcal{I}_{\Omega_b}\|_{\text{F}}^2}, \frac{t}{K \max_b \|\mathcal{I}_{\Omega_b}\|_{\text{F}}} \right) \right). \quad (4.58)$$

Hence,

$$\mathbb{P} \left[\frac{1}{N_p B} |Z| > Kt \max_b \|\mathcal{I}_{\Omega_b}\|_F \right] \leq 2 \exp(-c N_p B \min(t^2, t)). \quad (4.59)$$

Using [CZ+15, Lem. 7.2], one has

$$\frac{1}{3} \|\mathcal{I}_{\Omega_b}\|_F \leq \frac{1}{N_p} \mathbb{E} \|\bar{\mathbf{y}}_b\|_1 \leq \|\mathcal{I}_{\Omega_b}\|_F.$$

Combining this with (4.59) gives

$$\begin{aligned} \mathbb{P} \left[\frac{1}{3B} \sum_{b=1}^B \|\mathcal{I}_{\Omega_b}\|_F - Kt \max_b \|\mathcal{I}_{\Omega_b}\|_F \leq \frac{1}{N_p B} \|\bar{\mathbf{y}}\|_1 \leq Kt \max_b \|\mathcal{I}_{\Omega_b}\|_F + \frac{1}{B} \sum_{b=1}^B \|\mathcal{I}_{\Omega_b}\|_F \right] \\ \geq 1 - 2 \exp(-c N_p B \min(t^2, t)). \end{aligned} \quad (4.60)$$

It appears in (4.60) that a concentration of $\frac{1}{N_p B} \|\bar{\mathbf{y}}\|_1$ around $\|\mathcal{I}\|_F$ is unreachable, and (4.60) can thus not be easily combined with the RIP $_{\ell_2/\ell_2}$ in Assumption 4.5 of the Fourier sampling. Indeed, the inequalities that could be used to replace these norms by $\|\mathcal{I}\|_F$ are

$$\begin{aligned} \max_b \|\mathcal{I}_{\Omega_b}\|_F &\leq \|\mathcal{I}\|_F \\ \sum_{b=1}^B \|\mathcal{I}_{\Omega_b}\|_F &\geq \|\mathcal{I}\|_F \\ \sum_{b=1}^B \|\mathcal{I}_{\Omega_b}\|_F &\leq B \|\mathcal{I}\|_F, \end{aligned}$$

and it is not possible to provide tight bounds from it by this way.

4.5.4 Hope for Modulated ROPs

The *modulated ROP* sensing model in (4.35) is hard to analyze theoretically. It requires to study the concentration property of the combined modulations and ROPs, *i.e.*, the combined operator MD . This analysis is out of the scope of this thesis. However, thanks to the ROP interpretation highlighted in (4.40), we claim this scheme mimicks the *batched ROP* scheme sufficiently closely to envision recovery guarantees to be proven later.

It is worth mentionning that, similarly to Lem. 3.2, it is possible to control the expected ℓ_1 -norm of the modulated ROPs. We formalize this in Lem. 4.1.

4 | Compressive Radio-Interferometry

Lemma 4.1 (Controlling the expected modulated ROP ℓ_1 -norm). *If the random vectors α, β are filled with i.i.d. random variables with a unit second moment ($\mu_2 = 1$) and bounded sub-Gaussian norm $\|\alpha_p\|_{\psi_2}, \|\beta_p\|_{\psi_2} \leq \kappa$ (with $\kappa \geq 1$) $\forall p \in [\![N_p]\!]$, then, for any hollow matrix $\mathcal{I} \in \mathcal{H}^{QB}$, the random variable $\xi := \epsilon \tilde{\epsilon} \alpha^* \mathcal{I} \beta$ (with $\epsilon, \tilde{\epsilon} \sim \mathcal{U}\{\pm 1\}$) is sub-exponential with norm $\|\xi\|_{\psi_1} \leq \kappa^2$, and there exists a value $0 < c_{\alpha, \beta} < 1$, only depending on the distribution of the α_i 's and β_i 's, such that*

$$c_{\alpha, \beta} \|\mathcal{I}\|_F \leq \frac{1}{N_{pb} N_m} \mathbb{E} \|\mathcal{A}_m(\mathcal{I})\|_1 = \mathbb{E} |\xi| \leq \|\mathcal{I}\|_F, \quad (4.61)$$

where we defined the modulated ROP operator $\mathcal{A}_m : H \in \mathcal{H}^{QB} \mapsto \mathcal{A}_m(H) = (\langle (D_{\epsilon_m} \alpha_p)(D_{\tilde{\epsilon}_m} \beta_p)^*, H \rangle)_{p=1, m=1}^{N_{pb}, N_m} \in \mathbb{C}^{N_{pb} N_m}$ with the modulations contained in D_{ϵ_m} and $D_{\tilde{\epsilon}_m}$ defined in (4.39).

Proof. After observing that

$$\mathbb{E}_{\epsilon, \tilde{\epsilon}, \alpha, \beta} |\xi| = \mathbb{E}_{\alpha, \beta} |\alpha^* \mathcal{I} \beta|$$

because flipping the sign of α (resp. β) with ϵ (resp. $\tilde{\epsilon}$) has no effect on the expectation, one can directly invoke [CZ+15, Lem. 7.2]. \square

4.6 Recovery Analysis

4.6.1 Phase Transition Diagrams

We provide empirical reconstructions obtained from extensive Monte Carlo simulations with S trials on the reconstruction of sparse images $\sigma \in \Sigma_K$ with $N = 100 \times 100$ pixels from the (noiseless) *modulated ROP* observation model $\bar{z} = \mathbf{MDGF}\sigma$ derived in Sec. 4.3.3. The *Basis Pursuit DeNoise* recovery program is used to compute the estimate $\tilde{\sigma}$ as

$$\tilde{\sigma} = \arg \min_{\sigma} \|\sigma\|_1 \text{ s.t. } \|\bar{z} - \mathbf{MDGF}\sigma\|_2 \leq 10^{-2}. \quad (4.62)$$

Remark 4.6. Using SPGL1^a, (4.62) is solved in its equivalent unconstrained formulation [VF08] using the proximal gradient (a.k.a. forward-backward) algorithm [Bec17; PB14]. While the constrain is imposed in the ℓ_2 -norm hence deviates from the theoretical setting established in Sec. 4.4 that uses the ℓ_1 -norm, it avoids solving an internal minimization problem for computing the proximal operator of that constrain. Despite these differences, we provide similar conclusions than in Sec. 4.4 for the sample complexity, as shown below.

^a(Python module: <https://github.com/drrelyea/spgl1>).

We consider the reconstruction of a non-vignetted 2-D image, *i.e.*, $\sigma^\circ = \sigma$. A vectorized image $\sigma \in \mathbb{R}^N$ was generated with a K -sparse support picked uniformly at random in $\llbracket N \rrbracket$, its K non-zero components being all set to 1. An example of a sparse sky¹² image with $K = 25$ is shown in Fig. 4.8(a). The partial Fourier sampling induced by the NUFFT operator GF is fixed by a realistic uv -coverage of the VLA [Tho+80] with $Q = 27$ antennas and $B = 100$ batches corresponding to a total integration time of 5 hours. At each simulation trial, we used $N_{pb}B$ sketching vectors $\alpha_{pb}, \beta_{pb} \in \mathbb{C}^Q$, $\forall p \in \llbracket N_{pb} \rrbracket$, i.i.d. with $(\alpha_{pb})_q \underset{\text{i.i.d.}}{\sim} e^{i\mathcal{U}[0, 2\pi]}$, $q \in \llbracket Q \rrbracket$, and similarly for β_{pb} . The Bernoulli modulation vectors $\{\gamma_m\}_{m=1}^{N_m}$ were randomly picked as $\gamma_m \underset{\text{i.i.d.}}{\sim} \mathcal{U}\{\pm 1\}$.

In Fig. 4.8-4.9, the success rates—*i.e.*, the percentage of trials where the reconstruction SNR exceeded 40dB—were computed for $S = 80$ trials per value of (K, N_{pb}, N_m) , and for a range of (K, N_{pb}, N_m) specified in the axes. The transition cube in Fig. 4.8(b) is shown in addition to

¹²The shown image has been slightly blurred with a Gaussian kernel to enhance visual appeal.

4 | Compressive Radio-Interferometry

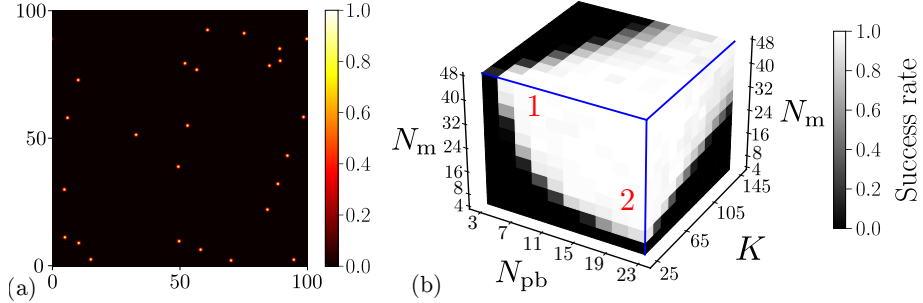


Fig. 4.8 (a) Example of a randomly generated K -sparse sky with $K = 25$. (b) Phase transition cube. The diagrams of Fig. 4.9 in a 3-D projection to better see the interdependence between the quantities (K, N_m, N_{pb}) . For a fixed number of measurements $N_{pb} \times N_m$, the zone 1—with smaller N_{pb} —has a lower computational cost than zone 2.

the maps of Fig. 4.9 as it provides a better insight of the dependence between the variables (K, N_{pb}, N_m) than the maps alone.

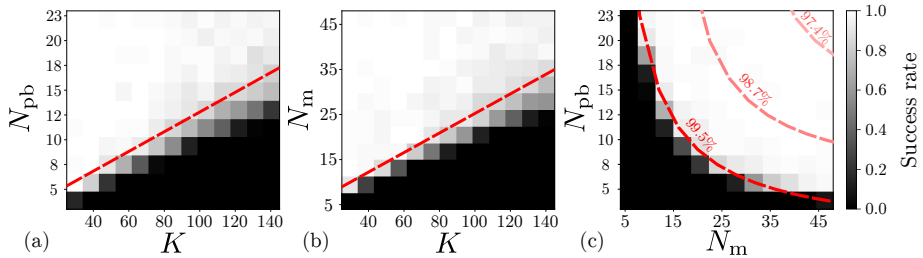


Fig. 4.9 Phase transition diagrams showing $N_{pb} \times N_m$ modulated ROPs of $B = 100$ different 27×27 interferometric matrices for a K -sparse image σ (with $N_m = 50$ in (a), $N_{pb} = 25$ in (b), and $K = 25$ in (c)). One considers the uv -coverage shown in Fig. 4.4, ROP using circularly-symmetric unit-norm random α_{pb} , β_{pb} , and Bernoulli modulation vectors $\gamma_{mb} \stackrel{\text{i.i.d.}}{\sim} \{\pm 1\}$, $\forall b \in [B]$, $p \in [N_{pb}]$, $m \in [N_m]$. Each pixel is constructed with $S = 80$ reconstruction trials solving (4.62) where we consider success if $\text{SNR} \geq 40\text{dB}$. The probability of success ranges from black (0%) to white (100%). Dashed red lines highlight the transition frontiers.

We observe in Fig. 4.9(a-b) that high reconstruction success is reached as soon as $N_{pb}N_m \geq CK$, with $C \simeq 5$. This is closely related to the sample complexity obtained for the batched ROP scheme in Prop. 4.2, where $N_p \geq C'K$ were needed (up to log factors). Here, the transitions diagrams seem to indicate that N_{pb} and N_m play the same role in the sample complexity, with only the product $N_{pb}N_m$ mattering. This is also confirmed in Fig. 4.9(c) were the transition frontier in red describes an hyperbola at (N_{pb}, N_m) coordinates satisfying $N_{pb}N_m \approx 150$. A comparison between the sample complexity $N_{pb}N_m$ needed for the modulated ROPs and $N_p \lesssim N_{pb}N_m$ needed for

the batched ROPs would have been compelling, but the batched ROP model is impossible to compute because of the cost $N_p Q^2 B$ of computing the forward model as given in Table 4.3.

Reminding the different complexity costs of the *modulated ROP* scheme in Table 4.4, it appears that favoring more modulations N_m than ROPs N_{pb} for a fixed budget $N_{pb}N_m = \text{cst}$ reduces the acquisition cost $N_{pb}Q$ as well as the weight of the computational cost $N_{pb}BQ^2$ of the ROPs which have a more significant impact than the sign-flipping modulations. The conclusion is that the upper-left side (zone 1) of the (N_{pb}, N_m) slices in the success region of the transition cube in Fig. 4.8 offers a reduced acquisition cost and forward modeling computational complexity while ensuring image recovery.

Table 4.4 Reminder on the costs of modulated ROPs at different stages: during the acquisition, for the forward model computation, and the memory storage.

Acquisition	Forward model	Memory
$N_{pb}Q$	$N_{pb}B(Q^2 + N_m)$	$N_{pb}N_m$

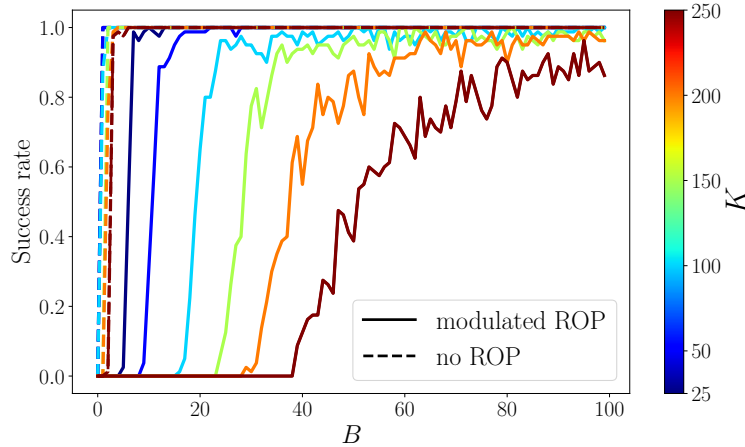


Fig. 4.10 Phase transition curve showing $N_{pb}N_m = 25 \times 50$ modulated ROPs of B different 27×27 interferometric matrices for a K -sparse image σ , and K varying into $\{25, 50, 100, 150, 200, 250\}$. One considers the uv -coverage shown in Fig. 4.4 with a number of batches B ranging from 1 to 100 and corresponding to a proportional integration time. The ROPs are obtained using circularly-symmetric unit-norm random $\alpha_{pb}, \beta_{pb}, \forall b \in \llbracket B \rrbracket, p \in \llbracket N_{pb} \rrbracket$, and the modulations using Bernoulli random $\gamma_m, \forall m \in \llbracket N_m \rrbracket$. Each pixel is constructed with $S = 80$ reconstruction trials solving (4.62) where we consider success if $\text{SNR} \geq 25\text{dB}$.

In Fig. 4.10, which displays several transition curves of the success rate vs. B for different values K with $(N_{pb}, N_m) = (25, 50)$, the failure-success transition is shifted towards an increasing number of batches as

4 | Compressive Radio-Interferometry

K increases, and the transition abscissa are equispaced for equispaced sparsity values K . This is in accordance with the sample complexity condition $Q(Q - 1)B \geq \delta^{-2}K \log(N, K, \delta)$ set in the RIP $_{\ell_2/\ell_2}$ Assumption 4.5 for the visibility sampling. It also shows that it is not possible to recover the image from a single batch ($B = 1$), because the associated Fourier sampling is not dense enough to obtain the RIP $_{\ell_2/\ell_2}$. Interestingly, the number of measurements related to each curve in Fig. 4.10 remains unchanged, and equal to $N_{pb}N_m = 1250$ compared to $Q^2B = 72900$ in the worst case; representing a compression factor of 98%. For the highest sparsity levels ($K \in \{200, 250\}$), the condition $N_pN_m > CK$ observed in Fig. 4.9 is not consistently satisfied for $(N_p, N_m) = (25, 50)$, as suggested from an extrapolation of the transition curve in Fig. 4.9(b). This likely accounts for the increasing variability observed in the curves for higher values of K .

The success rate is also shown for the uncompressed scheme in dashed lines. The sparse image is recovered with a minimal number of batches $B < 5$, also shifted towards the right for increasing sparsity values K . This confirms that the total number of measurements needed for image recovery is around 1250, and that more visibility measurements contain redundant information about the image of interest. Obviously, the information contained in the modulated ROP measurements $\bar{z} = MDGF\sigma$ was already included in the visibilities $GF\sigma$, so MD can only yield additional information loss about σ . The difference is that the number of antennas Q and batches B are usually imposed by the acquisition setting, while the number of ROP and modulations is free and controllable.

Despite the arguments against the separated ROP model regarding the theoretical guarantees in Sec. 4.5, Fig. 4.11 shows that satisfying reconstruction performances can be attained in a noiseless setting with this scheme. In fact, with a number of measurements $N_{pb}B$ (to be compared with $N_{pb}N_m$), the transition frontiers—with the same dashed red lines than in Fig. 4.9—seem to indicate that the number of batches B plays a role similar to the number of modulations N_m for the modulated ROP scheme. However, the modulated ROP remain more advantageous because (i) B is generally imposed by the acquisition context, while tuning N_m is much more flexible. It is easier to construct a sufficient number $N_{pb}N_m$ of modulated ROP measurements for a target reconstruction SNR than $N_{pb}B$ separated ROP measurements. (ii) As explained above, the computational complexity can be significantly re-

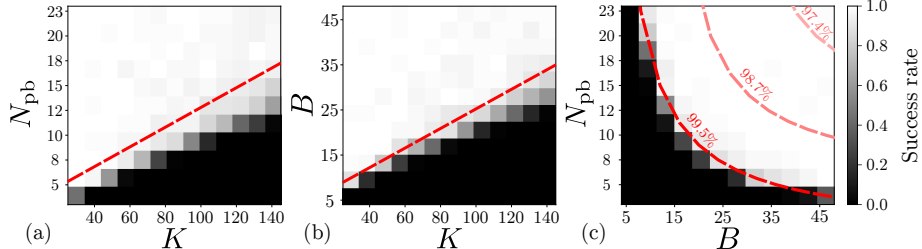


Fig. 4.11 Phase transition diagrams showing $N_{pb}B$ separated ROPs B different 27×27 interferometric matrices for a K -sparse image σ (with $B = 50$ in (a), $N_{pb} = 25$ in (b), and $K = 25$ in (c)). One considers a fraction $B/100$ of the uv -coverage shown in Fig. 4.4 and ROP using circularly-symmetric unit-norm random $\alpha_{pb}, \beta_{pb}, \forall b \in [B], p \in [N_{pb}]$. Each pixel is constructed with $S = 80$ reconstruction trials solving (4.62) where we consider success if $\text{SNR} \geq 40\text{dB}$. The probability of success ranges from black (0%) to white (100%). The dashed red lines, highlighting the transition frontiers, are exactly the same as in Fig. 4.9. The level curves with compression factors (97.4%, 98.7%, 99.5%) are given in (c).

duced by decreasing N_{pb} and increasing N_m in compensation¹³, which is not possible with separated ROPs. (iii) In a scenario where $N_{pb}B$ is highly sufficient for image reconstruction, the modulated ROP represent an additional compression operation if $N_m < B$ with enough measurements $N_{pb}N_m$. (iv) The theoretical arguments provided in Sec. 4.5.

4.6.2 Realistic Reconstructions

In this section, we present reconstruction analyses conducted in a super realistic numerical setting. These analyses could not have been possible without a fruitful collaboration with a research group at the cutting edge of our current understanding of RI imaging—the BASP laboratory¹⁴ at Herriot-Watt University in Edinburgh—who granted me access to their latest reconstructions algorithms presented in Sec. 4.4, to uv -coverages associated with many real antenna arrays such as the VLA [Tho+80], MeerKAT [Asa+21], ASKAP [McC+20], and LOFAR [Haa13], and also to *Cirrus*, a UK National Tier-2 HPC Service at EPCC funded by the University of Edinburgh and EPSRC (EP/P020267/1).

Numerical setting

The results that will follow are non exhaustive but still deliver some key messages that validate the benefit of the compressive imaging approach described in this chapter. Similarly to Sec. 4.6.1, we numerically

¹³As long as N_m remains negligible compared to 2^B .

¹⁴<https://basp.site.hw.ac.uk>

4 | Compressive Radio-Interferometry

study the reconstruction of a groundtruth image observed by the intermediate of the forward imaging operators. In this section:

- We use uSARA to reconstruct the image from the classical (4.16) and modulated ROP (4.35) forward imaging models. The parameters of uSARA (see Algo. 4.2) are set to different values depending on the experiment. We do not provide details about these parameters in this section.
- We apply a *uniform weighting* (see [Bri95]) of the visibilities to improve the reconstruction quality. A comparison of different weighting schemes is expected for the paper in preparation for MNRAS. As explained in Sec. 4.7, it is still possible to apply a visibility weighting in the modulated ROP sensing scheme at an increased acquisition cost.
- We do not provide the reconstruction times, intrinsically related to the computational complexities given in Table 4.3, because the analyzes have been obtained with a naive composition of the operators $MDGF$ involved in the forward imaging model (4.35).
- We do not display the dirty images σ_{dirty} and residual images $r = \sigma_{\text{dirty}} - \Re\{\Phi^*\Phi\}\tilde{\sigma}$, that are the mere application of the adjoint operator to the final measurements and the difference between the dirty image and the estimate of the image projected with the adjoint-forward imaging operators, respectively, because we compare the use of the compressive scheme to the classical scheme rather than study the image reconstruction algorithm and its fine-tuning.

Our test image, depicted in Fig. 4.12(a) is the 3c353 galaxy resized to $N = 256 \times 256$ pixels. It has a peak value equal to 1 and dynamic range of 7546.2. Fig. 4.12(b) shows a *uv*-coverage associated to the MeerKAT array. In the following analyzes, the total observation time $IB = 8\text{h}10\text{m}$ will remain constant, yielding similar Fourier coverages, and three integration times $I \in \{800, 80, 80\}$ s will be considered.

Results

Fig. 4.13 provides curves depicting the SNR (defined in Def. 2.3.2) and log SNR of the image estimate using uSARA. The log SNR [Ter+22] that compares the groundtruth image to the estimation error in logarithmic scale is defined in Def. 4.6.1.

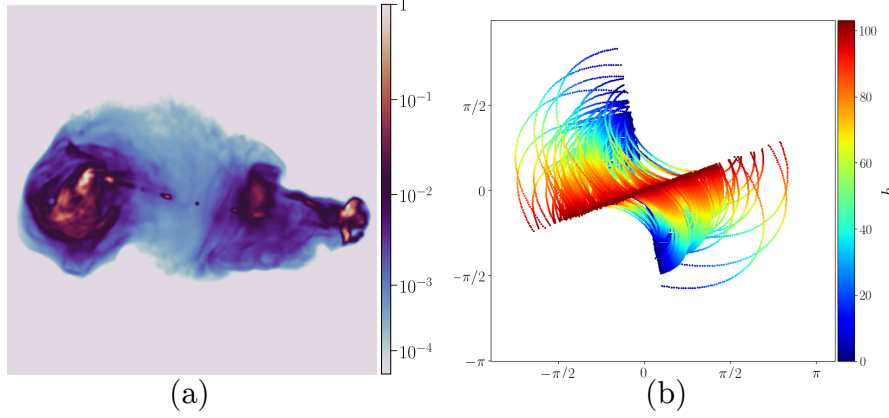


Fig. 4.12 (a) The 3c353 galaxy groundtruth image with $N = 256^2$ pixels and shown in logarithmic scale. (b) The uv -coverage of the MeerKAT [Asa+21] array, shown with $B = 103$.

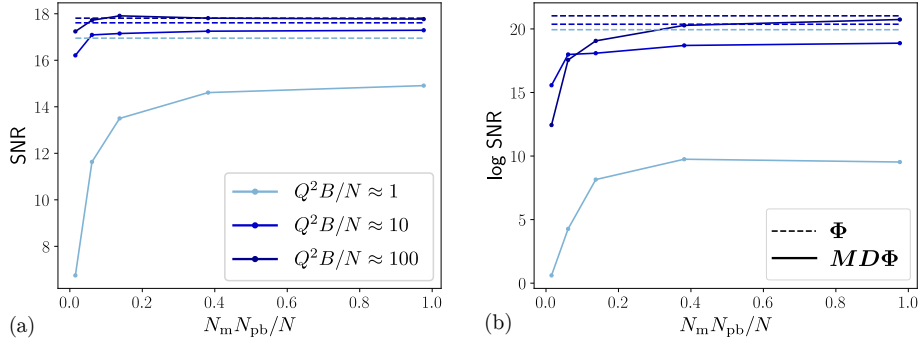


Fig. 4.13 Transition curves using uSARA. (a) SNR, and (b) log SNR in function of the number $N_{\text{pb}} \times N_{\text{m}}$ of modulated ROPs for three different number of batches: $B \in \{37, 368, 3680\}$ corresponding to $Q^2B/N \approx 1, 10, 100$, respectively. The five pairs in this experiment are $(N_{\text{pb}}, N_{\text{m}}) \in \{(10, 100), (20, 200), (30, 300), (50, 500), (80, 800)\}$. The dashed lines represent an upper bound associated to the reconstruction in the classical scheme.

Definition 4.6.1. *The log Signal-to-noise ratio (in dB), which compares a ground truth signal \mathbf{u} to the error $\mathbf{u} - \tilde{\mathbf{u}}$ made by its approximation $\tilde{\mathbf{u}}$ in logarithmic scale, is defined as*

$$\log \text{SNR}(\mathbf{u}, \tilde{\mathbf{u}}) = \text{SNR}(\text{rlog}(\mathbf{u}), \text{rlog}(\tilde{\mathbf{u}})) \quad (4.63)$$

where the rlog function converts an image to the logarithmic scale as

$$\text{rlog}(\mathbf{u}) := \frac{\max(\mathbf{u})}{\log_{10}(d)} \log_{10} \left(\frac{d}{\max(\mathbf{u})} \mathbf{u} + 1 \right) \quad (4.64)$$

where d is the dynamic range.

4 | Compressive Radio-Interferometry

In Fig. 4.13, the three shades of blue correspond to a number of visibilities $Q(Q - 1)/2$ (shown Q^2B in the legend for simplicity) approximately equal to 1, 10, and 100 times the image size N from light to dark blue.

The dashed lines show the reconstruction quality with the classical imaging scheme, *i.e.*, with only the forward operator $\Phi = GF$ involved. The quality of the reconstruction is improved for a higher number of visibilities.

For the image reconstruction experiments with the modulated ROP model and plotted in solid line, the number $N_m N_{pb}$ of modulated ROPs is set within the range $[0, N]$ where it is cheaper to store the modulated ROPs rather than the dirty image, which is sufficient for uSARA to compute an image estimate.

In all solid line curves, the compression factors $N_m N_{pb}/(Q(Q - 1)/2)$ of the modulated ROP compared to the classical scheme are implicitly available and vary from 0% to 100%, 10%, and 1% for $Q^2B/N \approx 1, 10$, and 100, respectively. It is observed that both the SNR and log SNR increase with the number $N_m N_{pb}$ of modulated ROPs and are upper bounded by the performances of the classical scheme because the Bernoulli modulation and separated ROP operators MD can only lose part of the information contained in the visibilities $GF\sigma$. Both the SNR and log SNR curves are higher for higher compression factors, showing that the compressive scheme has more interest when the number of visibilities $Q(Q - 1)/2$ is orders of magnitude above the image size N . In particular, the reconstruction using $(N_{pb}, N_m) = (80, 800)$ reaches the same SNR and log SNR than the classical scheme from an amount of modulated ROPs which is only 1% of the number of visibilities. Moreover, the quality using $(N_{pb}, N_m) = (80, 800)$ is enhanced compared to the reconstruction with the classical scheme with $Q^2B \approx N$, *i.e.*, with the same data size, which shows that the compressive scheme conserves more information about the visibilities than just dropping some visibilities to reduce the data size.

Fig. 4.14 displays the reconstructed images associated to the curves in Fig. 4.13. The first column shows the image reconstructed with the classical scheme and for three different integration times, as explained around Fig. 4.12. It is observed that the reconstruction qualities are similar, which makes sense as the three associated uv -coverages are similar and look like Fig. 4.12(b). The second and third columns respectively show the reconstructed images with the modulated ROP scheme using the smallest and highest number of modulated ROPs,

i.e., $(N_{pb}, N_m) = (10, 100)$ and $(N_{pb}, N_m) = (80, 800)$, respectively.

While the top center reconstruction completely failed, the bottom right image confirms that the quality of the reconstruction is similar to the reconstruction with the classical scheme, shown in the bottom left image.

The reconstruction SNRs are similar in all three images of the bottom row, but a too small number of modulated ROPs fails to reconstruct the faint emission, i.e., the very low values in the groundtruth image, which explains the drop in log SNR observed in Fig. 4.13(b).

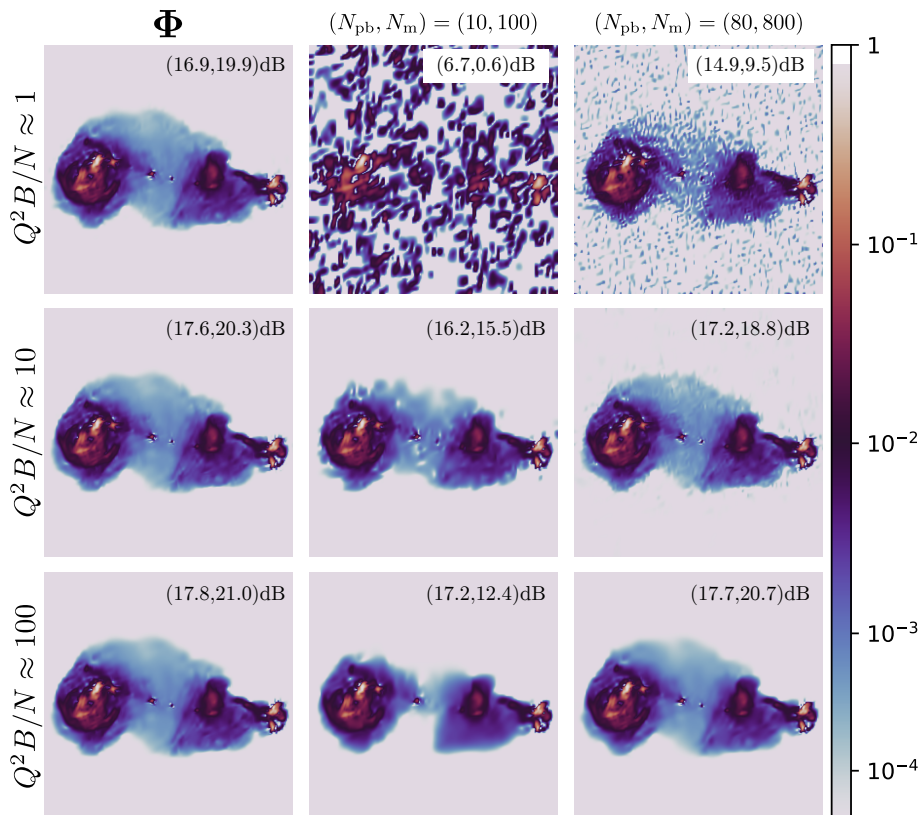


Fig. 4.14 Reconstructed images (in logarithmic scale) corresponding to the curves of Fig. 4.13. The SNRs and log SNRs are shown in the top right corner of each reconstructed image.

4 | Compressive Radio-Interferometry

4.7 Discussion

What has been done

In this chapter, we built on the contributions of Chap. 3 to propose the first computationally efficient *compressive imaging* technique for RI. The novelty of the proposition was to show that random beamforming is tantamount to applying ROPs of the covariance matrix, and that these ROPs can be efficiently combined over time by Bernoulli modulations. Compared to Chap. 3, we showed with Fig. 4.4 that the rotation of the Earth provides a denser Fourier coverage of the image.

We provided recovery guarantees and observed the derived sample complexities under numerical conditions. The success of this compressive imaging approach was validated by extensive reconstruction analyses in a super-realistic numerical setting.

About Calibration

In practical imaging systems, the antenna gains, or also the projection of their position onto the plane perpendicular to the pointing direction is not accurately known. A *calibration step* consists in estimating these unknown parameters by imaging a known image σ and fitting the parameters to the observed data. As announced in Sec. 4.3.1, we avoided discussing the calibrations aspects in the plain text because they were out of the scope of this chapter. However, we point out that, because the ROP models (4.29), (4.30), and (4.35) explained in Sec. 4.3.3 are **linear** and **independent** transformations of the measurements, they remain compatible with the latest calibration methods [SW14; Dab+21b].

Preprocessing calibration: The bilateral ROP model (3.22) for a single batch writes as

$$\bar{y} = \text{diag}(AWFD_\sigma F^* W^* A^*),$$

where the operator W models the effect of the antennas. For a known signal σ^* and associated ROP vector \bar{y}^* , a *preprocessing* calibration phase may be performed to estimate W by iteratively solving a minimization problem of the form

$$\widetilde{W}^{(k+1)} = \arg \min_W \frac{1}{2} \|\bar{y}^* - \text{diag}(AW^{(k)}FD_{\sigma^*}F^* W^* A^*)\|_2^2, \quad (4.65)$$

and the addition of the ROP operator A does not make the minimization problem (4.65) more difficult than without ROPs. The calibration technique (4.65) is well-known as an *Alternating Direction Implicit* (ADI) approach [SW14].

Joint calibration and imaging: The modulated (and other) ROP model is also compatible with joint calibration and imaging. Indeed, simplifying¹⁵ the idea of [Dab+21b] yields the following joint minimization problem

$$\tilde{\sigma}, \tilde{G} = \arg \min_{(\sigma, G)} \frac{1}{2} \|z - MDGF\sigma\|_2^2 + \mathcal{R}_1(\sigma) + \mathcal{R}_2(G), \quad (4.66)$$

with regularization terms \mathcal{R}_1 and \mathcal{R}_2 . Eq. (4.66) can be solved iteratively by alternating between a minimization with respect to σ by fixing G , *i.e.*,

$$\sigma^{(k+1)} = \arg \min_{\sigma} \frac{1}{2} \|z - MDG^{(k)}F\sigma\|_2^2 + \mathcal{R}_1(\sigma),$$

and the converse

$$G^{(k+1)} = \arg \min_G \frac{1}{2} \|z - MDGF\sigma^{(k+1)}\|_2^2 + \mathcal{R}_2(G), \quad (4.67)$$

The imaging problem has been covered in this chapter and can be solved with the recovery algorithms presented in Sec. 4.4. Since M and D are linear operators independent of G , the calibration problem (4.67) can be solved, with one step of the PGM (see Algo. 2.1) for instance as

$$G^{(k+1)} = \text{prox}_{\mathcal{R}_2} (D^* M^* (MDGF\sigma^{(k+1)} - z) \sigma^{(k+1)*}).$$

Remark 4.7. The compatibility of the ROP models with the current calibration techniques could not be obtained with a compression scheme that would store the dirty image by backprojecting the measurement vector as $\sigma_{\text{dirty}} = F^* G^* y$ [Vij+17]. Indeed, in such a situation, the dependence in the antenna contributions becomes quadratic and cannot be solved with linear or bi-linear techniques anymore.

While the reduced complexity of the modulated ROP forward model requires the precomputation of the composed operator MDG , which can be an issue for a joint calibration-imaging procedure, we

¹⁵[Dab+21b] actually considers a *bi-linear* formulation similar to (4.65).

4 | Compressive Radio-Interferometry

foresee future works that may consider a *parametric* compressed operator $G'_\theta := \mathbf{M}D\mathbf{G}_\theta$ and whose associated calibration phase would consist in learning the parameters θ as

$$\theta^{(k+1)} = \arg \min_{\theta} \frac{1}{2} \|z - G'_\theta F \sigma\|_2^2 + \mathcal{R}(\theta) \quad (4.68)$$

for a known image σ .

Limits and Open Questions

Polarimetry: Like in Chap. 3, we considered a *scalar theory*, *i.e.*, we imaged the intensity distribution of the sky. An open question is to extend our contributions to *polarization measurements* that indicate the distribution of the magnetic fields within the source [TMS17]. Such an extension would then sense the *Stokes parameters* distribution of the sky, and correlating the measurement vector would provide *Stokes visibilities*.

Holographic matrix: While we provided in Table 4.3 the computational cost of the classical visibility scheme $y = \Phi\sigma$ only for the forward model, it has been observed [Sul+12; Mon+23] that recovery algorithms that require only the dirty image for the reconstruction—such as the PGM—could precompute a *holographic matrix*

$$H := G^* G \in \mathbb{C}^{N \times N}. \quad (4.69)$$

The benefit of H is that it compresses the product of two big rectangular matrices $G \in \mathbb{C}^{J^2 B \times N}$, avoiding the instantaneous storage of $J^2 B$ values during the reconstruction process, hence reducing the computational cost of the recovery algorithm.

However, as discussed above, composing G and G^* can be an issue for a joint calibration-imaging scheme. We are not aware of works tackling this problem. The advantage of the parametric calibration in (4.68) is that it still contains a single application of G , while (4.69) unavoidably contains two.

Weighting the visibilities: Weighted minimization schemes only require an image-to-measurement vector forward model. For instance, the *weighted ℓ_1 -minimization* scheme idea relies on the distribution of the sparsity of the image among its decomposition levels [AH21, Chap. 12]. On the other hand, the *weighted least squares* imaging scheme in [VWS18, Sec. 4.4.1] reweights the visibility measurements with the

inverse of the noise covariance. For these two weighted schemes, we see no incompatibility with the modulated ROP model, whose noise model has been characterized in Sec. 4.3.5.

However, it seems that the *variable density* visibility distribution obtained at the output of $GF\sigma$ is better reweighted for stable and robust image recovery [KW14, Th. 3.1]. During the acquisition, the random beamforming prevents direct access to the visibility matrices $\{\mathcal{I}_{\Omega_b}\}_{b=1}^B$ hence any access to weighting. Hopefully, in the ROP view (4.40) reminded as

$$\bar{z}_{mp} = (\mathbf{D}_{\epsilon_m} \boldsymbol{\alpha}_p)^* \mathcal{I} (\mathbf{D}_{\tilde{\epsilon}_m} \boldsymbol{\beta}_p),$$

the interferometric matrix \mathcal{I} can be weighted with any matrix $\mathbf{W} \in \mathcal{H}^{QB}$ given its decomposition as a sum of rank-one matrices, *i.e.*, $\mathbf{W} = \sum_{k=1}^K \mathbf{w}_k \mathbf{w}_k^*$. Indeed, the *visibility-weighted* measurement can be written as

$$\begin{aligned} \bar{z}_{mp,\mathbf{W}} &= (\mathbf{D}_{\epsilon_m} \boldsymbol{\alpha}_p)^* (\mathbf{W} \cdot \mathcal{I}) (\mathbf{D}_{\tilde{\epsilon}_m} \boldsymbol{\beta}_p) \\ &= (\mathbf{D}_{\epsilon_m} \boldsymbol{\alpha}_p)^* \left(\sum_{k=1}^K \mathbf{w}_k \mathbf{w}_k^* \cdot \mathcal{I} \right) (\mathbf{D}_{\tilde{\epsilon}_m} \boldsymbol{\beta}_p) \\ &= \sum_{k=1}^K (\mathbf{D}_{\epsilon_m} \boldsymbol{\alpha}_p \cdot \mathbf{w}_k)^* \mathcal{I} (\mathbf{D}_{\tilde{\epsilon}_m} \boldsymbol{\beta}_p \cdot \mathbf{w}_k). \end{aligned} \quad (4.70)$$

Eq. (4.70) shows that the visibilities can still be weighted with the modulated ROP model, but at the cost of an **increased sample complexity**, multiplying the number of necessary ROPs by K . This suggests that a tradeoff between (*i*) improved image recovery by visibility weighting, and (*ii*) low-rank visibility weighting, must be found in order to still benefit from a compressive imaging scheme.

Reconstruction with AIRI and R2D2: The *Artificial Intelligence for Regularization in Imaging* (AIRI) [Ter+23; Ter+22] and *Residual-to-Residual DNN series for high-Dynamic range imaging* (R2D2) [A+23] are among the latest state-of-the-art image reconstruction algorithms for radio-astronomy. Both algorithms are compatible with the modulated ROP model.

AIRI is a *Plug-and-Play* (PnP) approach. In a nutshell, it replaces the proximal regularization operator with a denoiser \mathcal{D} in a Forward-Backward algorithm. \mathcal{D} is designed to remove i.i.d. Gaussian random noise from an image. While it can take many forms, the chosen denoiser is an SCUNet [Zha+23]. Targetting high dynamic range imaging of complex structure with diffuse and faint emission across the

4 | Compressive Radio-Interferometry

field of view, \mathcal{D} is specifically trained on a database of 2235 radio-interferometric images of size 512×512 explained in [Ter+22]. Some details about the convergence of AIRI in function of the *firm non-expansiveness* of \mathcal{D} and the heuristically set noise level for the denoiser, and its relation to the exponentiation factor of the target image, can be found in [Ter+23].

We provide in Algo 4.4 a version of AIRI that uses the modulated ROP model. It simply consists in replacing the classical forward operator GF by the modulated ROP operator $A_m := MDGF$. The variable $\xi_3 > 0$ is a relative variation convergence criterion, $L := \|A_m^* A_m\|$ is the *Lipschitz constant*, and $0 < \gamma < 2/L$ is the *stepsize*.

Algorithm 4.4 AIRI

Require: $0 < \gamma < 2/L$, denoiser \mathcal{D} , $\sigma^{(0)} \in \mathbb{R}^N$, $\xi_3 > 0$

```

1: repeat
2:   for  $k = 0, 1, \dots$  do
3:      $\sigma^{(k+1)} = \mathcal{D}(\sigma^{(k)} - \gamma A_m^*(A_m \sigma^{(k)} - z))$             $\triangleright$  PnP-FB step
4:   until  $\|\sigma^{(k+1)} - \sigma^{(k)}\|_2 / \|\sigma^{(k+1)}\|_2 < \xi_3$ 
5: return  $\sigma^{(k+1)}$ 

```

In our notation (see (4.16)), using R2D2 on the classical visibilities writes as

$$\sigma^{(k)} = \sigma^{(k-1)} + N_{\theta^{(k)}}(\mathbf{r}^{(k-1)}), \quad (4.71)$$

where:

- $\sigma^{(k)}$ is the k -th iterate of the image,
- $N_{\theta^{(k)}}$ is a *Deep Neural Network* (DNN) with learned parameters $\theta^{(k)}$, and
- $\mathbf{r}^{(k)} := \sigma_{\text{dirty}} - \kappa \Re\{\Phi^* \Phi\} \sigma^{(k-1)}$ is the *residual image* where the *dirty* image $\sigma_{\text{dirty}} := \kappa \Re\{\Phi^* v\}$ is the *normalized backprojected visibilities* and κ is a normalization factor.

R2D2 can also be used on the *modulated ROP* model by considering the forward operator $\Phi_m := MD\Phi$ that contains the ROP and Bernoulli modulations (see (4.35)). In this case the DNNs must be *trained* specifically from modulated ROP measurements with a training time of around 300 GPU*hours.

Image reconstruction with the modulated ROP scheme using AIRI and R2D2 is out of the scope of this work.

Link with compressive learning: In the end, the goal of radio-interferometric imaging is to estimate a 2-D map $\sigma^2(l)$ of the variances of complex normal random distributions $\mathbb{C}\mathcal{N}(0, \sigma^2(l))$. The proposed compressive sensing scheme has similarities with the *compressive learning* framework whose goal is to compute an estimate [Sch21, Fig. 2.1]

$$\tilde{\theta} = \arg \min_{\theta \in \Theta} \left\| \frac{1}{n} \sum_{i=1}^n \Phi(x_i) - \mathcal{A}_\Phi(\mathcal{P}_\theta) \right\|_2. \quad (4.72)$$

of the parameters θ of a random distribution \mathcal{P}_θ from a minimal number of *sketches* $\Phi(x_i)$ where Φ is the sketching function, $i \in \llbracket n \rrbracket$, and $x_1, \dots, x_n \sim_{\text{i.i.d.}} \mathcal{P}_\theta$.

In the context of this chapter, the analogy with (4.72) is that the parameters of interest are the discrete map σ and can be estimated from the following minimization problem

$$\tilde{\sigma} = \arg \min_{\sigma} \left\| \frac{1}{IB} \sum_{i=1}^I \sum_{b=1}^B \gamma_{mb} \alpha_{pb}^* x_b[i] x_b^*[i] \beta_{pb} - MDGF\sigma \right\|_2 \quad (4.73)$$

where the first term is related to the acquisition process (remember (4.38)) and the second term is related to the image reconstruction (remember the modulated ROP model (4.35)). The sketching function, depending on the signal set

$$\mathcal{X} := \bigcup_{b \in \llbracket B \rrbracket} \mathcal{X}_b, \quad \mathcal{X}_b := \{x_b[i], i \in \llbracket I \rrbracket\},$$

defined in (4.13) with $x_b[i] \sim_{\text{i.i.d.}} \mathbb{C}\mathcal{N}(0, \sigma^2(l))$, could be seen as

$$\Phi(x_b[i]) := \gamma_{mb} \alpha_{pb}^* x_b[i] x_b^*[i] \beta_{pb},$$

and the compressive learning operator \mathcal{A}_Φ , depending directly on the parameters σ of the distribution, could be interpreted as

$$\mathcal{A}_\Phi(\mathbb{C}\mathcal{N}(0, \sigma^2(l))) := MDGF\sigma.$$

4 | Compressive Radio-Interferometry

4.8 Appendix

4.8.1 Connections to MCFLI

The commonalities and differences between RI and multi-core fiber lensless imaging (MCFLI) are reported in this section. Let us first recall the expression of a single-pixel measurement in MCFLI:

$$y = \alpha^* \mathcal{I}_\Omega [wf] \alpha + n. \quad (4.74)$$

Eq. (4.74) must be compared with the ROP model for radio-interferometric measurements in (4.27).

Common features The role of the Q antennas in compressive radio-interferometry (CRI) is analogous to that of the Q cores in MCFLI. In both cases appears an *interferometric matrix* \mathcal{I}_Ω encoding Fourier samples (or *visibilities*) of a (stationary) 2-D image of interest taken precisely in the difference set $\Omega - \Omega$. The complex exponential terms (resp. $e^{\frac{i2\pi}{\lambda z} p_q^\top x}$ and $e^{\frac{i2\pi}{\lambda} p_q^\perp(t)^\top l}$) of the Fourier transforms encoded into the interferometric matrices come both from a dephasing of the electromagnetic signal due to the core/antenna location. The observed images are both vignetted— $f^\circ := wf$ and $\sigma^\circ := g^2\sigma^2$. In either applications, a *compressive imaging* procedure is considered by applying random ROPs of the interferometric matrix. The *sketching vector* α (and β for CRI) is set by choosing the complex amplitude of each core (resp. antenna).

Differences In MCFLI, we image a 2-D plane perpendicular to the distal end of the MCF. In CRI, however, we consider an image in *direction-cosine* coordinates l . The MCFLI application is completely *stationary*—there is no dependence on time t . The measured signal y is deterministic; no expectation needs to be approximated by summing many measurements over time. In CRI, the time dependence of the antenna locations can be exploited to sense many interferometric matrices, thus obtaining a denser Fourier sampling than in MCFLI. This is why we get only \mathcal{I}_Ω in MCFLI, but $\{\mathcal{I}_{\Omega_b}\}_{b=1}^B$ in CRI. In MCFLI, the SROPs are *imposed* by the sensing mechanism. In CRI, the ROPs are *pursued* in order to compress the measurement data. Thus, asymmetric ROPs are fully accessible. Furthermore, the noise models are different. In (4.74), the noise n is the thermal noise at the single-pixel detector. In (4.27), the final measurements are obtained by correlations. The thermal noise at the receivers is translated into a deterministic bias $\alpha^* \Sigma_n \beta$

that can be removed. The additive Gaussian noise sources in the visibilities comes from the statistical noise induced by the sample covariance and some other model imperfections.

4.8.2 About Beamforming

This section highlights the link between focused beamforming and the raster-scanning approach presented in Sec. 3.2.2 and presents the *adaptive beamforming* technique.

Focused Beamforming is Raster-Scanning

If constant weights are chosen as $\alpha = \mathbf{1}$ during the entire acquisition of a batch b , as clear from (4.27), the *noiseless* component of the measurement is given as

$$\bar{y}_b = \mathbf{1}^\top \mathcal{I}_{\Omega_b}[\sigma^\circ] \mathbf{1}.$$

From the definition of the *interferometric matrix* in (4.11), it can be further developed as

$$\bar{y}_b = \int_{\mathbb{R}^2} \sigma^\circ(\mathbf{l}) \left| \sum_{q=1}^Q e^{\frac{i2\pi}{\lambda} \mathbf{l}^\top \mathbf{p}_{bq}^\perp} \right|^2 d\mathbf{l}. \quad (4.75)$$

If (4.75) seems familiar, it is because we already met it in Chap. 3. Analogously to (3.9), we just rediscovered the *array factor* $\phi_{\Omega_b}(\mathbf{l}) = \sum_{q=1}^Q e^{\frac{i2\pi}{\lambda} \mathbf{p}_{bq}^\top \mathbf{l}}$ of the antenna arrangement Ω_b . For the same reasons as explained in Sec. 3.5 for the *Raster-Scanning* mode in MCFLI, y_b probes the content of σ° around the origin ($\mathbf{l} = \mathbf{0}$) if the antenna arrangement is dense enough over the support of $\hat{\sigma}^\circ$. Other directions can be focused using a *tilt vector* $\gamma(\boldsymbol{\theta}) := (\exp(-\frac{i2\pi}{\lambda} \boldsymbol{\theta}^\top \mathbf{l}))_{q=1}^Q$. The resulting sensing writes

$$\bar{y}_{b\boldsymbol{\theta}} = \gamma(\boldsymbol{\theta})^* \mathcal{I}_{\Omega_b}[\sigma^\circ] \gamma(\boldsymbol{\theta}) = \mathbf{1}^\top \mathcal{I}_{\Omega_b}[\mathcal{T}_{-\boldsymbol{\theta}} \sigma^\circ] \mathbf{1},$$

with the translation operator $\mathcal{T}_{\boldsymbol{\theta}} \varphi(\mathbf{l}) := \varphi(\mathbf{l} - \boldsymbol{\theta})$ and a *raster-scanning* of the sky can be considered by planning an RS path Θ traveling in all directions, as depicted in Fig. 3.5(top).

Adaptive Beamforming

The *spatially-varying convolution* model resulting from a beamforming/raster-scanning approach is not new. There exist smarter techniques of *adaptive beamforming* that take into account the spatially-varying Point Spread Function (PSF) of the antenna array. For instance, the *minimum variance distortionless response* technique [VWS18, Section 4.1.2] selects

4 | Compressive Radio-Interferometry

the *beamforming vector* $\gamma(\mathbf{l})$ such that, for a given direction \mathbf{l} , the response is distortionless in the target direction, and the variance out of that direction is minimized. With the knowledge of the covariance matrix \mathbf{C} , the corresponding constrained minimization problem reads

$$\gamma(\mathbf{l}) = \arg \min_{\mathbf{w}} \mathbf{w}^* \mathbf{C} \mathbf{w}, \quad \text{s.t. } \mathbf{w}^* \mathbf{a}(\mathbf{l}) = 1, \quad (4.76)$$

with the geometric delays of the antennas $a_q(\mathbf{l}) := e^{\frac{i2\pi}{\lambda} \mathbf{p}_q^\perp(t)^\top \mathbf{l}}$, $\forall q \in [Q]$. The solution to (4.76) is $\mathbf{w}(\mathbf{l}) = \frac{\mathbf{C}^{-1} \mathbf{a}(\mathbf{l})}{\mathbf{a}(\mathbf{l})^* \mathbf{C}^{-1} \mathbf{a}(\mathbf{l})}$. This type of adaptive beamforming technique could also have been implemented for MCFLI in Chap. 3.

4.8.3 Matrix form of interferometric measurements

Interferometric measurements associated to a discretized (vignetted) image find a natural matrix formulation. Indeed, writing the discrete image $\sigma = (\sigma^\circ[\mathbf{n}])_{\mathbf{n} \in [\mathbb{N}_1]^2} \in \mathbb{R}^N$ with $N = N_1^2$ and

$$\sigma^\circ[\mathbf{n}] := \sigma^\circ(\mathbf{n}\Delta) = \sigma^\circ(\mathbf{l}) \sum_{\mathbf{n} \in [\mathbb{N}]^2} \delta(\mathbf{l} - \mathbf{n}\Delta), \quad (4.77)$$

the definition of the interferometric matrix in (4.11) can be particularized to σ and to $t = (b - 1/2)MT$ to give

$$(\mathcal{I}_{\Omega_b}[\sigma])_{jk} := \Delta^2 \sum_{\mathbf{n} \in [\mathbb{N}_1]^2} \sigma^\circ[\mathbf{n}] e^{\frac{-i2\pi}{\lambda} (\mathbf{p}_{bk}^\perp - \mathbf{p}_{bj}^\perp)^\top \mathbf{n}\Delta}. \quad (4.78)$$

In order to express $\mathcal{I}_{\Omega_b}[\sigma]$ in discrete matrix form, the trick consists in inserting $\sum_{\mathbf{n}' \in [\mathbb{N}_1]^2} \delta_{\mathbf{n}\mathbf{n}'} = 1$ into (4.78) so as to get

$$(\mathcal{I}_{\Omega_b}[\sigma])_{jk} = \Delta^2 \sum_{\mathbf{n}, \mathbf{n}' \in [\mathbb{N}_1]^2} e^{\frac{-i2\pi}{\lambda} \mathbf{n}^\top \mathbf{p}_{bk}^\perp \Delta} \sigma^\circ[\mathbf{n}] \delta_{\mathbf{n}\mathbf{n}'} e^{\frac{i2\pi}{\lambda} \mathbf{n}'^\top \mathbf{p}_{bj}^\perp \Delta}. \quad (4.79)$$

Defining the matrix of complex exponentials $\Gamma_b \in \mathbb{C}^{Q \times N}$ s.t. $(\Gamma_b)_{qn} := \Delta e^{\frac{-i2\pi}{\lambda} \mathbf{n}^\top \mathbf{p}_{bq}^\perp \Delta}$ for the 2-D component \mathbf{n} associated to the flattened index n and the diagonal matrix $\mathbf{D}_\sigma \in \mathbb{R}^{N \times N}$ filled with the vectorized discrete image σ , the interferometric matrix at batch b writes

$$\mathcal{I}_{\Omega_b}[\sigma] := \Gamma_b \mathbf{D}_\sigma \Gamma_b^*. \quad (4.80)$$

While (4.80) is already a matrix formulation, it is common to write the decomposition $\Gamma_b := \mathbf{W}_b \mathbf{F}$ where $\mathbf{F} \in \mathcal{H}^N$ is the 2-D fast Fourier transform (FFT) matrix and $\mathbf{W}_b \in \mathbb{C}^{Q \times N}$ is a matrix interpolating the on-grid frequencies of the FFT to the set of antenna positions Ω_b . One finally gets

$$\mathcal{I}_{\Omega_b}[\sigma] := \mathbf{W}_b \mathbf{F} \mathbf{D}_\sigma \mathbf{F}^* \mathbf{W}_b^*. \quad (4.81)$$

4.8.4 Matrix form of the separated ROP

It is also possible to write the measurement vector with the *matrix form* of the sensing model, similarly to (ROPI), as

$$\begin{aligned}\bar{\mathbf{y}} &= \text{diag} \left(\begin{bmatrix} A_1 \mathbf{W}_1 \mathbf{F} \mathbf{D}_\sigma \mathbf{F}^* \mathbf{W}_1^* \mathbf{B}_1^* \\ \ddots \\ A_B \mathbf{W}_B \mathbf{F} \mathbf{D}_\sigma \mathbf{F}^* \mathbf{W}_B^* \mathbf{B}_B^* \end{bmatrix} \right) \\ &= \text{diag} \left(\begin{bmatrix} A_1 \mathbf{W}_1 & & \\ & \ddots & \\ & & A_B \mathbf{W}_B \end{bmatrix} \mathbf{F} \mathbf{D}_\sigma \mathbf{F}^* \begin{bmatrix} \mathbf{W}_1^* \mathbf{B}_1^* & & \\ & \ddots & \\ & & \mathbf{W}_B^* \mathbf{B}_B^* \end{bmatrix} \right) \\ &= \text{diag}(\mathbf{D}_A \mathbf{D}_W \mathbf{F} \mathbf{D}_\sigma \mathbf{F}^* \mathbf{D}_W^* \mathbf{D}_B^*),\end{aligned}\tag{4.82}$$

where $\mathbf{D}_A, \mathbf{D}_B \in \mathbb{C}^{BN_p \times BQ^2}$ and $\mathbf{D}_W \in \mathbb{C}^{BQ^2 \times BN}$ are *block-diagonal* matrices whose blocks are $\{\mathbf{A}_b\}_{b=1}^B$, $\{\mathbf{B}_b\}_{b=1}^B$, and $\{\mathbf{W}_b\}_{b=1}^B$, respectively. One advantage of this formulation is that it justifies the use of the “interferometry” terminology because it shows that the antenna elements, modeled in \mathbf{D}_W , are interfering through their two appearances and the Fourier transforms \mathbf{F} .

The matrix form will be discarded for the rest of the section, only the vector form will be considered. Indeed, from a computational point of view, the vector form will always be the fastest model. Introducing (i) the *number of neighbours* J used in the interpolation operators $\{\mathbf{W}_b\}_{b=1}^B$ to compute each continuous visibility, and (ii) the number of *activated pixels per interferometric matrix* N'_b , Table 4.5 shows the comparison of the complexities of both forms. The computations of the complexities follow the same philosophy as for Table 3.1, with the exception that each $\mathbf{W}_b^* \mathbf{A}_b^*$ (and $\mathbf{W}_b^* \mathbf{B}_b^*$) now costs $\mathcal{O}(JQN_p)$ because of the interpolation kernel of size J . For the vector form, the matrix \mathbf{DG} can be precomputed in $\mathcal{O}(N_p BJQ^2)$ operations. The remaining computational cost of the sensing model is the application of the DFT in $\mathcal{O}(N \log N)$, followed by the application of the precomputed \mathbf{DG} matrix in $\mathcal{O}(N_p BN'_b)$. For a quantitative comparison, we provide typical values: the image resolution is $N = 10^6$, there are typically $Q = 50$ antennas, $N_p = 50$ projections per batch, $B = 1000$ batches, the number of neighbors is $J = 50$, and the number of activated pixels per interferometric matrix is $N'_b = 1000$. Plugging these values into Table 4.5 gives $\approx 10^{10}$ operations for the matrix form versus $\approx 10^8$ operations for the vector form.

4 | Compressive Radio-Interferometry

Table 4.5 Complexities of the vector and matrix forms of the *separated ROPs* approach. The \star denotes a precomputed scheme.

Name	Model	Complexity \mathcal{O}	Value
matrix	$\text{diag}(\mathbf{D}_A \mathbf{D}_W F D_\sigma F^* \mathbf{D}_W^* \mathbf{D}_B^*)$	$B N_p N \log N + J Q B N_p$	10^{10}
vector	$DGFf$	$N_p Q^2 B + J Q^2 B + N \log N$ $\star N_p B N'_b + N \log N$	10^8 10^8

The diag operation performed in (4.82) indicates that projection values—computed for the matrix form—are discarded. Actually, the *separated ROPs* approach is a special case of another approach—named *dependent ROPs*—that preserves the off-diagonal terms in (4.82). With this approach, only $\sqrt{N_p}$ projections would yield N_p measurements per batch. However, these measurements would now be generated from only $2\sqrt{N_p}$ projections, making them statistically *dependent* on each other. This dependence may imply the need to compute slightly more projections to get the same amount of information about the image of interest σ . Furthermore, the dependent ROPs approach can only be modeled in a matrix form. From our conclusions made with Table 4.5, we decided to discard the dependent ROPs approach.

4.8.5 Proof of Prop. 4.2

The proof of Prop. 4.2 will follow the same reasoning as the proof of Prop. 3.3—a RIP $_{\ell_2/\ell_1}$ for SROP measurements—given in Sec. 3.7.2, except that the concentration of SROP measurements around the matrix they are projecting, namely Lem. 3.4, is now replaced by a tighter concentration for *asymmetric ROPs* given in [CCG15, Prop. 1].

Even if the asymmetric ROP scheme considered here is unbiased, the multiplicity Q of the DC component imposed us to assume a RIP $_{\ell_2/\ell_2}$ on the *nonzero only* visibility sampling in Assumption 4.5. The DC component of the image—contained in the diagonal of the interferometric matrix—is removed after its estimation.

First, let us highlight that the batched ROPs model can be formulated as ROPs of a *total interferometric matrix*, placing the interferometric matrices of each batch block-wisely along its diagonal. Indeed, defining $\alpha^* := [\alpha_1^*, \dots, \alpha_B^*]$ and

$$\mathcal{I} := \begin{bmatrix} \mathcal{I}_{\Omega_1} & & \\ & \ddots & \\ & & \mathcal{I}_{\Omega_B} \end{bmatrix}, \quad (4.83)$$

Appendix | 4.8

(4.30) can be rewritten as $\bar{\mathbf{y}} := \mathcal{A}(\mathcal{I}) = (\bar{y}_p)_{p=1}^{N_p}$ with $\bar{y}_p = \boldsymbol{\alpha}_p^* \mathcal{I} \boldsymbol{\beta}_p$. Two key observations can be made about \mathcal{I} . First $\mathcal{I} \in \mathcal{H}^{QB}$ as $\mathcal{I}_{\Omega_b} \in \mathcal{H}^Q \forall b \in \llbracket B \rrbracket$. Second,

$$\|\mathcal{I}\|_F^2 = \sum_{b=1}^B \|\mathcal{I}_{\Omega_b}\|_F^2 = \sum_{b=1}^B \|G_b F \sigma\|_2^2 = \|G F \sigma\|_2^2 = \|\Phi \sigma\|_2^2.$$

The same holds for the *hollowed* interferometric matrix:

$$\|\mathcal{I}_h\|_F^2 = \|G_0 F \sigma\|_2^2 = \|\Phi_0 \sigma\|_2^2, \quad (4.84)$$

with G_0 (resp. Φ_0) removing the DC component from G (resp. Φ), and $\bar{y}^c := \mathcal{A}^c(\mathcal{I}_h)$.

Remark 4.8. With these two observations, the proof given in Sec. 3.7.2 can be entirely reused, providing a RIP $_{\ell_2/\ell_1}$ for SROP measurements of zeromean images. The only change compared to the RIP given in Prop. 3.3 is in the sample complexity for the visibilities: $Q(Q-1)B \geq 4K \log(N, K, \delta)$.

Next, [CCG15, Prop. 1] is reminded here.

Lemma 4.2 ([CCG15] Concentration of ROP in the ℓ_1 -norm). Supposing Assumption 3.6 holds, given a matrix $\mathcal{J} \in \mathcal{H}^{QB}$, there exists universal constants $c_1, c_2, c_3 > 0$ such that with probability exceeding $1 - \exp(-c_3 N_p)$,

$$c_1 \|\mathcal{J}\|_F \leq \frac{1}{N_p} \|\mathcal{A}(\mathcal{J})\|_1 \leq c_2 \|\mathcal{J}\|_F. \quad (4.85)$$

As a simple corollary to the previous lemma, we can now establish the concentration of $\omega R \Phi_0 \sigma \in \mathbb{R}_+^M$ in the ℓ_1 -norm for an arbitrary K -sparse vector $\sigma \in \Sigma_K$.

4 | Compressive Radio-Interferometry

Corollary 4.2 (Concentration of $\mathbf{R}\Phi_0$ in the ℓ_1 -norm). *In the context of Lemma 4.2, suppose that assumptions [3.1, 3.2, 4.3, 3.4, 4.5, 3.6] are respected, with 4.5 set to sparsity $K > 0$ and distortion δ . Given $\sigma \in \Sigma_K$, and the operator $\mathbf{R}\Phi_0$ defined in (4.30) from the N_p ROP measurements and the $|\mathcal{V}_0| = Q(Q-1)B$ non-zero visibilities with*

$$Q(Q-1)B \geq 4K \text{plog}(N, K, \delta),$$

we have, with a failure probability smaller than $\exp(-c_5 N_p)$, for some $c_5 > 0$,

$$c'_1 \|\sigma\|_2 \leq \frac{1}{N_p} \|\mathbf{R}\Phi_0 \sigma\|_1 \leq c'_2 \|\sigma\|_2.$$

Proof. Given $\sigma \in \Sigma_K$ and \mathcal{J}_h the hollow version of $\mathcal{J} = \mathbf{WFD}_\sigma \mathbf{F}^* \mathbf{W}^* \in \mathcal{H}^{QB}$, let us assume that (4.85) holds on \mathcal{J}_h , an event with probability of failure smaller than $\exp(-c_3 N_p)$ with $c_3 > 0$. We first note that $\|\mathcal{J}_h\|_F = \|G_0 \mathbf{F} \sigma\|_2$ from (4.84). Second,

$$(1-\delta) \|\sigma\|_2^2 \leq \frac{N}{|\mathcal{V}_0|} \|G_0 \mathbf{F} \sigma\|_2^2 \leq (1+\delta) \|\sigma\|_2^2. \quad (4.86)$$

since from Assumption 4.5 the matrix $\Phi_0 := \sqrt{N} G_0 \mathbf{F}$ respects the $\text{RIP}_{\ell_2/\ell_2}(\Sigma_K, \delta)$ as soon as $|\mathcal{V}_0| = Q(Q-1)B \geq 4K \text{plog}(N, K, \delta)$. Therefore, since $\bar{\mathbf{y}}^c = \mathbf{R}\Phi_0 \sigma = \omega \mathcal{A}(\mathcal{J}_h)$, using (4.85) gives

$$\frac{1}{N_p} \|\mathbf{R}\Phi_0 \sigma\|_1 \geq c_1 \omega \|\mathcal{J}_h\|_F = c_1 \omega \|G_0 \mathbf{F} \sigma\|_2 \geq \omega c_1 \sqrt{1-\delta} \frac{\sqrt{|\mathcal{V}_0|}}{\sqrt{N}} \|\sigma\|_2.$$

Similarly, we get

$$\frac{1}{N_p} \|\mathbf{R}\Phi_0 \sigma\|_1 \leq c_2 \omega \sqrt{1+\delta} \frac{\sqrt{|\mathcal{V}_0|}}{\sqrt{N}} \|\sigma\|_2,$$

concluding the proof with $c'_1 := \omega c_1 \sqrt{1-\delta} \frac{\sqrt{|\mathcal{V}_0|}}{\sqrt{N}}$ and $c'_2 := c_2 \omega \sqrt{1+\delta} \frac{\sqrt{|\mathcal{V}_0|}}{\sqrt{N}}$. \square

We are now ready to prove Prop. 4.2. We will follow the standard proof strategy developed in [Bar+08]. By homogeneity of the $\text{RIP}_{\ell_2/\ell_2}$, we restrict the proof to unit vectors σ of Σ_{K_0} , i.e., $\sigma \in \Sigma_{K_0}^* := \Sigma_{K_0} \cap S_2^{N-1}$.

Given a radius $0 < \lambda < 1$, let $\mathcal{G}_\lambda \subset \Sigma_{K_0}^*$ be a λ covering of $\Sigma_{K_0}^*$, i.e., for all $\sigma \in \Sigma_{K_0}^*$, there exists a $\sigma' \in \mathcal{G}_\lambda$, with $\text{supp } \sigma' = \text{supp } \sigma$, such that $\|\sigma - \sigma'\| \leq \lambda$. Such a covering exists and its cardinality is smaller than $\binom{N}{K_0} (1 + \frac{2}{\lambda})^{K_0} \leq (\frac{3eN}{K_0\lambda})^{K_0}$ [Bar+08].

Appendix | 4.8

Invoking Cor. 4.2, we can apply the union bound to all points of the covering so that

$$\forall \sigma' \in \mathcal{G}_\lambda, c'_1 \leq \frac{1}{N_p} \|\mathbf{R}\Phi_0 \sigma'\|_1 \leq c'_2, \quad (4.87)$$

holds with failure probability smaller than

$$\left(\frac{3eN}{K_0\lambda}\right)^{K_0} \exp(-c_3 N_p) \leq \exp(K_0 \ln(\frac{3eN}{K_0\lambda}) - c_3 N_p).$$

Therefore, there exists a constant $C > 0$ such that, if $N_p \geq CK_0 \ln(\frac{3eN}{K_0\lambda})$, then (4.87) holds with probability exceeding $1 - \exp(-cN_p)$, for some $c > 0$.

Let us assume that this event holds. Then, for any $\sigma \in \Sigma_{K_0}$,

$$\begin{aligned} \frac{1}{N_p} \|\mathbf{R}\Phi_0 \sigma\|_1 &\leq \frac{1}{N_p} \|\mathbf{R}\Phi_0 \sigma'\|_1 + \frac{1}{N_p} \|\mathbf{R}\Phi_0(\sigma - \sigma')\|_1 \\ &\leq c'_2 + \frac{1}{N_p} \|\mathbf{R}\Phi_0\left(\frac{\sigma - \sigma'}{\|\sigma - \sigma'\|_2}\right)\|_1 \|\sigma - \sigma'\|_2 \\ &\leq c'_2 + \frac{1}{N_p} \|\mathbf{R}\Phi_0 \mathbf{r}\|_1 \lambda, \end{aligned}$$

with the unit vector $\mathbf{r} := \frac{\sigma - \sigma'}{\|\sigma - \sigma'\|_2}$. However, this vector \mathbf{r} is itself K_0 -sparse since σ and σ' share the same support. Therefore, applying recursively the same argument on the last term above, and using the fact that $\|\mathbf{R}\Phi_0 w\|_1$ is bounded for any unit vector w , we get $\frac{1}{N_p} \|\mathbf{R}\Phi_0 \mathbf{r}\|_1 \lambda \leq c'_2 \sum_{j \geq 1} \lambda^j = \frac{\lambda}{1-\lambda} c'_2$.

Consequently, since we also have

$$\begin{aligned} \frac{1}{N_p} \|\mathbf{R}\Phi_0 \sigma\|_1 &\geq \frac{1}{N_p} \|\mathbf{R}\Phi_0 \sigma'\|_1 - \frac{1}{N_p} \|\mathbf{R}\Phi_0(\sigma - \sigma')\|_1 \\ &\geq c'_1 - \frac{1}{N_p} \|\mathbf{R}\Phi_0 \mathbf{r}\|_1 \lambda, \end{aligned}$$

we conclude that

$$\frac{1-2\lambda}{1-\lambda} c'_1 \leq \frac{1}{N_p} \|\mathbf{R}\Phi_0 \sigma\|_1 \leq \frac{1}{1-\lambda} c'_2,$$

Picking $\lambda = 1/4$ finally shows that, under the conditions described above, $\mathbf{R}\Phi_0$ respects the RIP $_{\ell_2/\ell_1}(\Sigma_{K_0}, m_{K_0}, M_{K_0})$ with $m_{K_0} > \frac{2c'_1}{3}$, and $M_{K_0} < \frac{4c'_2}{3}$.

References

- [A+23] A. A et al. “R2D2: Deep neural network series for near real-time high-dynamic range imaging in radio astronomy”. In: *Dl* (2023). arXiv: [2309.03291](https://arxiv.org/abs/2309.03291).
- [AH21] B. Adcock and A. C. Hansen. *Compressive Imaging: Structure, Sampling, Learning*. Cambridge University Press, 2021.
- [Asa+21] K. M. B. Asad et al. “Primary beam effects of radio astronomy antennas - II. Modelling MeerKAT L-band beams”. In: *Monthly Notices of the Royal Astronomical Society* 502.2 (Jan. 2021), pp. 2970–2983. ISSN: 1365-2966. DOI: [10.1093/mnras/stab104](https://doi.org/10.1093/mnras/stab104).
- [Ate+18] M. Atemkeng et al. “Baseline-dependent sampling and windowing for radio interferometry: data compression, field-of-interest shaping, and outer field suppression”. In: *Monthly Notices of the Royal Astronomical Society* 477.4 (Mar. 2018), pp. 4511–4523. ISSN: 0035-8711. DOI: [10.1093/mnras/sty668](https://doi.org/10.1093/mnras/sty668).
- [Bar+08] R. Baraniuk et al. “A simple proof of the restricted isometry property for random matrices”. In: *Constructive Approximation* 28.3 (2008), pp. 253–263. ISSN: 01764276. DOI: [10.1007/s00365-007-9003-x](https://doi.org/10.1007/s00365-007-9003-x).
- [Bec17] A. Beck. *First-Order Methods in Optimization*. Philadelphia, PA, USA: SIAM-Society for Industrial and Applied Mathematics, 2017. ISBN: 1611974984.
- [Boo02] F. Boone. “Interferometric array design: Distributions of Fourier samples for imaging”. In: *aap* 386 (May 2002), pp. 1160–1171. DOI: [10.1051/0004-6361:20020297](https://doi.org/10.1051/0004-6361:20020297).
- [Bra+19] R. Braun et al. *Anticipated Performance of the Square Kilometre Array – Phase 1 (SKA1)*. 2019. arXiv: [1912 . 12699 \[astro-ph.IM\]](https://arxiv.org/abs/1912.12699).
- [Bri95] D. S. Briggs. “High fidelity deconvolution of moderately resolved sources”. In: *Ph. D. Thesis* (1995).

4 | References

- [CCG15] Y. Chen, Y. Chi, and A. J. Goldsmith. “Exact and stable covariance estimation from quadratic sampling via convex programming”. In: *IEEE Transactions on Information Theory* 61.7 (2015), pp. 4034–4059.
- [CGB08] T. J. Cornwell, K. Golap, and S. Bhatnagar. “The Non-coplanar Baselines Effect in Radio Interferometry: The W-Projection Algorithm”. In: *IEEE Journal of Selected Topics in Signal Processing* 2.5 (2008), pp. 647–657. DOI: [10.1109/JSTSP.2008.2005290](https://doi.org/10.1109/JSTSP.2008.2005290).
- [CMW12] R. E. Carrillo, J. D. McEwen, and Y. Wiaux. “Sparsity Averaging Reweighted Analysis (SARA): a novel algorithm for radio-interferometric imaging”. In: *Monthly Notices of the Royal Astronomical Society* 426.2 (2012), pp. 1223–1234.
- [CZ+15] T. T. Cai, A. Zhang, et al. “ROP: Matrix recovery via rank-one projections”. In: *Annals of Statistics* 43.1 (2015), pp. 102–138.
- [Dab+21a] A. Dabbech et al. “Cygnus A jointly calibrated and imaged via non-convex optimization from VLA data”. In: *Monthly Notices of the Royal Astronomical Society* 506.4 (2021), pp. 4855–4876. ISSN: 13652966. DOI: [10.1093/mnras/stab1903](https://doi.org/10.1093/mnras/stab1903). arXiv: [2102.00065](https://arxiv.org/abs/2102.00065).
- [Dab+21b] A. Dabbech et al. “Cygnus A jointly calibrated and imaged via non-convex optimization from VLA data”. In: *Monthly Notices of the Royal Astronomical Society* 506.4 (2021), pp. 4855–4876. ISSN: 13652966. DOI: [10.1093/mnras/stab1903](https://doi.org/10.1093/mnras/stab1903). arXiv: [2102.00065](https://arxiv.org/abs/2102.00065).
- [Dau92] I. Daubechies. *Ten Lectures on Wavelets*. Vol. 61. Society for Industrial and Applied Mathematics, 1992.
- [Eft+15] A. Eftekhari et al. “The restricted isometry property for random block diagonal matrices”. In: *Applied and Computational Harmonic Analysis* 38.1 (2015), pp. 1–31. ISSN: 1063-5203.
- [FC78] E. E. Fenimore and T. M. Cannon. “Coded aperture imaging with uniformly redundant arrays”. In: *Applied optics* 17.3 (1978), pp. 337–347.
- [FS03] J. A. Fessler and B. P. Sutton. “Nonuniform fast Fourier transforms using min-max interpolation”. In: *IEEE Transactions on Signal Processing* 51.2 (2003), pp. 560–574. ISSN: 1053587X. DOI: [10.1109/TSP.2002.807005](https://doi.org/10.1109/TSP.2002.807005).

- [Haa13] M. P. e. a. van Haarlem. “LOFAR: The LOw-Frequency ARray”. In: *Astronomy and Astrophysics* 556 (July 2013), A2. ISSN: 1432-0746. DOI: [10.1051/0004-6361/201220873](https://doi.org/10.1051/0004-6361/201220873).
- [Hög74] J. A. Högbom. “Aperture Synthesis with a Non-Regular Distribution of Interferometer Baselines”. In: 15 (June 1974), p. 417.
- [HS19] P. Hurley and A. J. Scholefield. “Towards Real-Time High-Resolution Interferometric Imaging with Bluebild”. In: 2019.
- [Kol+15] R. Koller et al. “High spatio-temporal resolution video with compressed sensing”. In: *Opt. Express* 23.12 (June 2015), pp. 15992–16007. DOI: [10.1364/OE.23.015992](https://doi.org/10.1364/OE.23.015992).
- [Kri+23] H. Krishnan et al. “Optimization and commissioning of the EPIC commensal radio transient imager for the long wavelength array”. In: *Monthly Notices of the Royal Astronomical Society* 520.2 (2023), pp. 1928–1937. ISSN: 13652966. DOI: [10.1093/mnras/stad263](https://doi.org/10.1093/mnras/stad263). arXiv: [2301.09662](https://arxiv.org/abs/2301.09662).
- [KW14] F. Krahmer and R. Ward. “Stable and robust sampling strategies for compressive imaging”. In: *IEEE Transactions on Image Processing* 23.2 (2014), pp. 612–622. ISSN: 10577149. arXiv: [1210.2380](https://arxiv.org/abs/1210.2380).
- [LWJ24] O. Leblanc, Y. Wiaux, and L. Jacques. *Compressive radio-interferometric sensing with random beamforming as rank-one signal covariance projections*. 2024. arXiv: [2409.15031](https://arxiv.org/abs/2409.15031) [eess.IV].
- [McC+20] D. McConnell et al. “The Rapid ASKAP Continuum Survey I: Design and first results”. In: *Publications of the Astronomical Society of Australia* 37 (2020). ISSN: 1448-6083. DOI: [10.1017/pasa.2020.41](https://doi.org/10.1017/pasa.2020.41).
- [Mon+23] N. Monnier et al. “Fast grid to grid interpolation for radio interferometric imaging”. In: *Astronomy and Computing* 45 (2023), p. 100767. ISSN: 2213-1337. DOI: <https://doi.org/10.1016/j.ascom.2023.100767>.
- [MZ93] S. G. Mallat and Z. Zhang. “Matching pursuits with time-frequency dictionaries”. In: *IEEE Transactions on Signal Processing* 41.12 (1993), pp. 3397–3415.

4 | References

- [Öça+15] O. Öcal et al. “Collaborative randomized beamforming for phased array radio interferometers”. In: *2015 IEEE International Conference on Acoustics, Speech and Signal Processing (ICASSP)*. 2015, pp. 5654–5658. DOI: [10 . 1109 / ICASSP . 2015 . 7179054](https://doi.org/10.1109/ICASSP.2015.7179054).
- [Oks13] B. Oksendal. *Stochastic differential equations: an introduction with applications*. Springer Science & Business Media, 2013.
- [PB14] N. Parikh and S. Boyd. “Proximal Algorithms”. In: *Found. Trends Optim.* 1.3 (Jan. 2014), pp. 127–239. ISSN: 2167-3888. DOI: [10 . 1561 / 2400000003](https://doi.org/10.1561/2400000003).
- [Pra+18] L. Pratley et al. “Robust sparse image reconstruction of radio interferometric observations with PURIFY”. In: *Monthly Notices of the Royal Astronomical Society* 473.1 (2018), pp. 1038–1058. ISSN: 13652966. DOI: [10 . 1093 / mnras/stx2237](https://doi.org/10.1093/mnras/stx2237). arXiv: [1610 . 02400](https://arxiv.org/abs/1610.02400).
- [RW20] A. Repetti and Y. Wiaux. “A Forward-Backward Algorithm for Reweighted Procedures: Application to Radio-Astronomical Imaging”. In: *ICASSP 2020 - 2020 IEEE International Conference on Acoustics, Speech and Signal Processing (ICASSP)*. 2020, pp. 1434–1438. DOI: [10 . 1109 / ICASSP40776 . 2020 . 9053284](https://doi.org/10.1109/ICASSP40776.2020.9053284).
- [RW21] A. Repetti and Y. Wiaux. “Variable Metric Forward-Backward Algorithm for Composite Minimization Problems”. In: *SIAM Journal on Optimization* 31.2 (2021), pp. 1215–1241. DOI: [10 . 1137 / 19M1277552](https://doi.org/10.1137/19M1277552). eprint: [https : // doi . org / 10 . 1137 / 19M1277552](https://doi.org/10.1137/19M1277552).
- [Sch21] V. Schellekens. “Extending the compressive statistical learning framework : quantization, privacy and beyond”. 2021.
- [Sul+12] I. S. Sullivan et al. “FAST HOLOGRAPHIC DECONVOLUTION: A NEW TECHNIQUE FOR PRECISION RADIO INTERFEROMETRY”. In: *The Astrophysical Journal* 759.1 (Oct. 2012), p. 17. DOI: [10 . 1088 / 0004 - 637X / 759 / 1 / 17](https://doi.org/10.1088/0004-637X/759/1/17).
- [SW14] S. Salvini and S. J. Wijnholds. “Fast gain calibration in radio astronomy using alternating direction implicit methods: Analysis and applications”. In: *Astronomy & Astrophysics* 571 (2014), A97.

- [Ter+22] M. Terris et al. “Image reconstruction algorithms in radio interferometry: From handcrafted to learned regularization denoisers”. In: *Monthly Notices of the Royal Astronomical Society* 518.1 (Sept. 2022), pp. 604–622. ISSN: 0035-8711. DOI: [10.1093/mnras/stac2672](https://doi.org/10.1093/mnras/stac2672).
- [Ter+23] M. Terris et al. *Plug-and-play imaging with model uncertainty quantification in radio astronomy*. 2023. arXiv: [2312.07137 \[eess.IV\]](https://arxiv.org/abs/2312.07137).
- [Tho+80] A. R. Thompson et al. “The Very Large Array”. In: *The Astrophysical Journal Supplement Series* 44 (1980), pp. 151–167. DOI: [10.1086/190685](https://doi.org/10.1086/190685).
- [Thy+17] N. Thyagarajan et al. “A generic and efficient E-field Parallel Imaging Correlator for next-generation radio telescopes”. In: *Monthly Notices of the Royal Astronomical Society* 467.1 (2017), pp. 715–730. ISSN: 13652966. DOI: [10.1093/mnras/stx113](https://doi.org/10.1093/mnras/stx113). arXiv: [1510.08318](https://arxiv.org/abs/1510.08318).
- [TMS17] A. R. Thompson, J. M. Moran, and G. W. Swenson. *Interferometry and Synthesis in Radio Astronomy*. Third. Springer, 2017. ISBN: 978-3-319-44430-4. DOI: [10.1007/978-3-319-44431-4](https://doi.org/10.1007/978-3-319-44431-4).
- [Tol+23] E. Tolley et al. “BIPP: An efficient HPC implementation of the Bluebild algorithm for radio astronomy”. In: 16.October (2023), pp. 1–16. arXiv: [2310.09200v1](https://arxiv.org/abs/2310.09200v1).
- [Van34] P. Van Cittert. “Refinement of the method of coherent scattered radiations, as applied to radio astronomy”. In: *Physica* 1.3 (1934), pp. 201–210.
- [Ver12] R. Vershynin. “Introduction to the non-asymptotic analysis of random matrices”. In: *Compressed Sensing: Theory and Applications*. Ed. by Y. C. Eldar and G. Kutyniok. Cambridge University Press, 2012, pp. 210–268. DOI: [10.1017/CBO9780511794308.006](https://doi.org/10.1017/CBO9780511794308.006).
- [VF08] D. E. Van Ewout Berg and M. P. Friedlander. “Probing the pareto frontier for basis pursuit solutions”. In: *SIAM Journal on Scientific Computing* 31.2 (2008), pp. 890–912. ISSN: 10648275. DOI: [10.1137/080714488](https://doi.org/10.1137/080714488).
- [Vij+17] S. Vijay Kartik et al. “A Fourier dimensionality reduction model for big data interferometric imaging”. In: *Monthly Notices of the Royal Astronomical Society* 468.2

4 | References

- (2017), pp. 2382–2400. ISSN: 13652966. DOI: [10 . 1093 / mnras/stx531](https://doi.org/10.1093/mnras/stx531). arXiv: [1609 . 02097](https://arxiv.org/abs/1609.02097).
- [VWS18] A. J. van der Veen, S. J. Wijnholds, and A. M. Sardarabadi. “Signal processing for radio astronomy”. In: *Handbook of Signal Processing Systems* (2018), pp. 311–360. DOI: [10 . 1007/978-3-319-91734-4_9](https://doi.org/10.1007/978-3-319-91734-4_9).
- [Wag+08] A. Wagadarikar et al. “Single disperser design for coded aperture snapshot spectral imaging”. In: *Applied optics* 47.10 (2008), B44–B51.
- [Wia+09a] Y. Wiaux et al. “Spread spectrum for imaging techniques in radio interferometry”. In: *Monthly Notices of the Royal Astronomical Society* 400.2 (2009), pp. 1029–1038. ISSN: 13652966. DOI: [10 . 1111 / j . 1365 - 2966 . 2009 . 15519 . x](https://doi.org/10.1111/j.1365-2966.2009.15519.x). arXiv: [0907 . 0944](https://arxiv.org/abs/0907.0944).
- [Wia+09b] Y. Wiaux et al. “Compressed sensing imaging techniques for radio interferometry”. In: *Monthly Notices of the Royal Astronomical Society* 395.3 (2009), pp. 1733–1742.
- [WWS18] S. J. Wijnholds, A. G. Willis, and S. Salvini. “Baseline-dependent averaging in radio interferometry”. In: *Monthly Notices of the Royal Astronomical Society* 476.2 (2018), pp. 2029–2039. ISSN: 13652966. DOI: [10 . 1093 / MNRAS / STY360](https://doi.org/10.1093/MNRAS/STY360). arXiv: [1802 . 09321](https://arxiv.org/abs/1802.09321).
- [Zer38] F. Zernike. “The concept of degree of coherence and its application to optical problems”. In: *Physica* 5.8 (1938), pp. 785–795.
- [Zha+23] K. Zhang et al. “Practical Blind Image Denoising via Swin-Conv-UNet and Data Synthesis”. In: *Machine Intelligence Research* 20.6 (Sept. 2023), pp. 822–836. ISSN: 2731-5398. DOI: [10 . 1007 / s11633 - 023 - 1466 - 0](https://doi.org/10.1007/s11633-023-1466-0).

5

Diffraction Through Inhomogeneous Media

SERVING as an introduction to the *diffraction tomography* context covered in Chap. 6, this chapter reviews the various ways to model the diffraction of light through an inhomogeneous medium, *i.e.*, a 3-D volume with a spatially-varying refractive index. Directly boiling down from the stationary *Helmholtz equation*, the *Lippmann-Schwinger* model is imposed as the chosen discrete model. Long story short, the model writes

$$\mathbf{u} = \mathbf{u}_i + \mathbf{G}\mathbf{D}_f\mathbf{u}, \quad (5.1)$$

where \mathbf{u}_i is the illuminating light field, \mathbf{G} is an operator modeling the physics of light scattering, f (placed along the diagonal of \mathbf{D}_f) informs on the spatially-varying refractive index in the medium, and \mathbf{u} is the diffracted field we aim to compute.

The few approximations behind this equation, the numerical challenges resulting from the discretization of a continuous model, and the optimization algorithms in charge of solving for \mathbf{u} , are progressively described with an emphasis on the options discarded on the way. The main achievements of this chapter are to (*i*) settle an accurate and efficient model for diffraction used later in Chap. 6, and (*ii*) gather (and possibly federate) different approximation schemes usually scattered in the literature under different names and approaches. This will push the current limitations in 3-D diffraction tomographic imaging.

The codes developed in the context of this chapter can be found at <https://github.com/olivierleblanc/cols>.

5 | Diffraction Through Inhomogeneous Media

5.1 Introduction

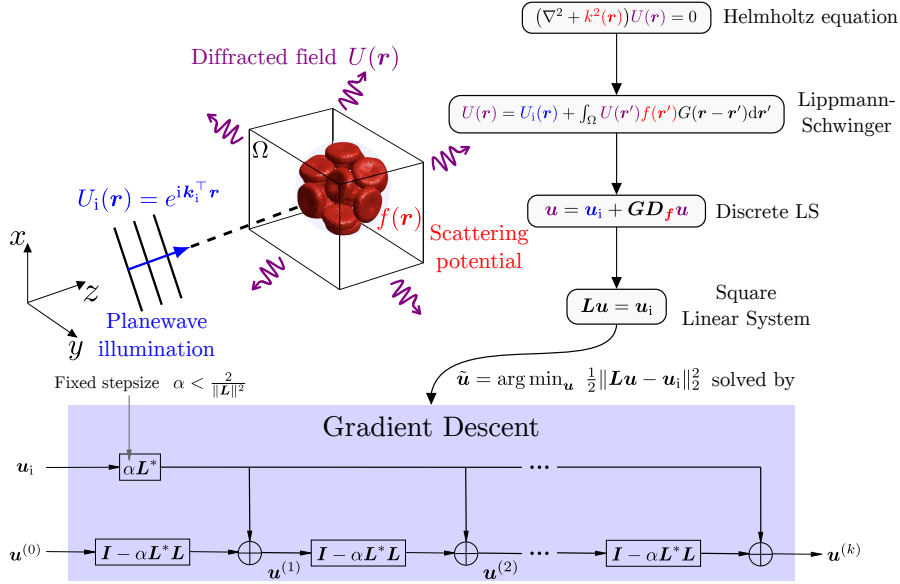


Fig. 5.1 Overview of the storyline of this chapter. Starting from the scalar Helmholtz equation, a square linear system is obtained from the discrete Lippmann-Schwinger equation. This linear system, with the forward operator $L := \mathbf{I} - GD_f$ encapsulating the scattering potential f , is solved by the fixed-step Gradient Descent method.

The goal of this chapter is to understand Fig. 5.1.

5.1.1 Motivation

Accurately modeling light interaction is at the heart of the computational imaging field. Because constructing efficient discrete models that accurately represent the physics of data acquisition is a challenging task, there is usually a lag between the community of physicists who develop these methods and the community of applied mathematicians who rarely develop them but use them to solve inverse problems. Most CI papers only briefly recall what discrete model they start from, hiding the imperfections under the hood.

The basic¹ propagation of light through an inhomogeneous medium may read as an easy problem solved long ago. However, it is still challenging nowadays because of the influence of the whole volume in its

¹i.e., without electric charge, current density, nonlinear optical effects or fluorescence, for instance.

globality on the diffraction effects. There was a need to restart from the basics of electromagnetism theory—the *Maxwell's equations*—and understand exactly what is the origin of the latest discrete model used for diffraction tomographic imaging (covered in Chap. 6).

5.1.2 Related Work

A couple of the works related to the challenges tackled in this chapter are gathered in this introductory section.

Lippmann-Schwinger for Diffraction Theory

Historically, the Lippmann-Schwinger (LS) equation that accurately models the diffraction of electromagnetic waves, has been approximated for the sake of numerical implementation in recovery procedures. In its continuous formulation, LS finds natural approximations by the Born and Rytov series [CS98; Bor+99] valid under weak-scattering conditions, *i.e.*, for small variations of the RI in the imaged semi-transparent volume. In the context of diffraction tomography, the First-Born (FB) approximation gives a linear model that can be conveniently solved as an inverse problem. It is theoretically supported the *Fourier diffraction theorem* [Kir+21; Fau+21; KS01], characterizing the Fourier covering attained by the tomographic conditions. Furthermore, its computational complexity is limited by Fourier transforms and the 4-D transfer function is easy to calibrate in an experimental setup [Lin+18]. For strongly scattering samples multiple-scattering methods such as the Beam Propagation Method (BPM) [Kam+16b; Pha+18] and Split-Step Non Paraxial (SSNP) [SA04; ZWT22] method have demonstrated higher fidelity. Still, they compute the diffracted field slice by slice by computing the illumination of each slice as the diffraction through the previous slice. This means that no reflection is taken into account for the light path.

Recently, [Pha+20] demonstrated an efficient numerical implementation of LS, dealing with the singularity of the Green kernel associated with the Helmholtz operator. This paved the way for reliable computation of the light diffracted in any direction by strongly scattering samples. The discrete LS model is also known in the literature as the *discrete-dipole approximation* [Cha22; DF94]. Solving the discrete LS model with an iterative gradient method [Liu+18] is equivalent to the *recursive Born* approach [Kam+16a].

5 | Diffraction Through Inhomogeneous Media

Optimization Aspects

Solving the discrete LS equation requires inverting a square linear system of the form $L\mathbf{u} = \mathbf{u}^i$. The *Neumann series* [GOW20], aiming to iteratively approach the inverse operator L^{-1} , can be stabilized with the adjoint operator L^* and an appropriate stepsize ensuring stability. The stabilized Neumann series is equivalent to the *Gradient Descent* method with fixed stepsize, and also shares commonalities with the *Picard iteration* [BD17]. Once the emphasis is made on first-order optimization methods [Bec17] to solve the linear system, many variants can be considered, ranging from *Adaptive Gradient Descent* methods [MM20], to *Neumann networks*²[GOW20]. Retrospectively, the Recursive Born approach [Kam+16a] can be seen as the iterations of an optimization algorithm instead of a Neumann series.

The solution of the discrete LS equation requires first-order optimization tools. This means that the convergence rate, the condition number, and all other tools to assess the convergence and stability of the optimization algorithms can be borrowed from this literature [Nes18; Bec17]. Finally, *preconditioning* techniques for the forward operator of LS have been proposed in [Yin15; CMS23].

5.1.3 Chapter Contributions

Extensive Review of the Lippmann-Schwinger Model: This chapter provides a comprehensive review of the Lippmann-Schwinger (LS) model for electromagnetic wave diffraction. It covers the historical development and theoretical foundation of the model, detailing its significance in understanding wave interactions with a spatially-varying refractive index 3-D distribution. The chapter also elaborates on the discretization techniques used to convert the continuous LS model into a solvable form. Various numerical methods for solving the discretized LS model are explored, highlighting their strengths and limitations.

Contrast-dependent convergence rate: An in-depth analysis of the convergence rate for solving the discretized Lippmann-Schwinger equation is presented. It is demonstrated that the convergence rate decreases with increasing contrast in the medium. This contrast-rate dependence is critical in explaining the challenges and failures in reconstructing high-contrast media. Theoretical insights and numerical evidence are

²A Neumann network is a particular case of a Plug-and-Play method [VBW13] where the regularization term is differentiable.

provided to elucidate the mechanisms behind this phenomenon, offering a better understanding of the limitations of current computational methods.

Development of a Python Toolbox: It is hard to value the importance of code sharing and development into a written thesis. Still, the numerical analyses accompanying this chapter have been obtained with a newly developed Python toolbox³ designed to facilitate the study and application of electromagnetic wave diffraction models. Programmed in an *object-oriented* manner, this toolbox integrates various discretization models and optimization algorithms mentioned in this chapter, providing a user-friendly interface for researchers and practitioners. The provided code has been implemented for *Pytorch* [Pas+19], making it GPU-friendly, *i.e.*, highly parallelizable. It also contains material covered in Chap. 6 such as *deep denoisers* and *implicit neural representation* architectures.

5.1.4 Notations Specific to This Chapter

This chapter introduces mathematical objects related to differential equations that were absent in Chap. 3 and Chap. 4, such as partial derivatives, cross products, gradient, curl, and divergence. Notations related to 3-D objects are also defined. Some of the notations specific to this part are briefly introduced.

The light wavefield $U(x, y, z)$ propagating in the inhomogeneous medium of interest is composed of an *incident* part U_i , whose associated variables are denoted by an index i , and a *scattered* part U_s , accompanied by an index s .

The (x, y, z) dependence of a quantity U is sometimes replaced by $\mathbf{r} := (x, y, z)$ or by (\mathbf{x}, z) with $\mathbf{x} := (x, y)$ to shorten the notation. The partial derivative of U with respect to x is denoted by $\partial_x U$. The first and second derivatives of the current density $J(\mathbf{r}, t)$ and the electric field $\mathbf{E}(\mathbf{r}, t)$ with respect to time t are written $\dot{\mathbf{J}}$ and $\ddot{\mathbf{E}}$, respectively. The “Nabla” operator is only considered in Cartesian coordinates. In 3-D it writes $\nabla := (\partial_x, \partial_y, \partial_z)$. The cross product is written \times , so for a 3-D field $\mathbf{U} = (U_x, U_y, U_z)$, Curl naturally writes $\nabla \times \mathbf{U}$. The divergence is noted as $\nabla \cdot \mathbf{U}$.

³Available at <https://github.com/olivierleblanc/cols>.

5 | Diffraction Through Inhomogeneous Media

The scattering potential $f(\mathbf{r})$ is considered enclosed in a box Ω , and its discretization \mathbf{f} is defined on a regular grid $\mathcal{G}_{(N_x, N_y, N_z)} \subset \Omega$ with N_x, N_y, N_z voxels along the axes.

Regarding the optimization part in Sec. 5.4, the optimal (in terms of convergence rate) choice of some parameter α is written as α^* .

5.2 Lippmann-Schwinger and First-Born

This section aims to trace the origin of the Lippmann-Schwinger (LS) equation in order to understand what can and cannot be modeled with it. The proposed derivations are inspired by [Bor+99, Chap. 13].

Starting from *Maxwell's equations*, the *Helmholtz equation* is first derived in Sec. 5.2.1, with all its associated simplifications. Then, in Sec. 5.2.2, the Helmholtz equation is rewritten to emphasize the diffraction of an electromagnetic wave by a diffractive object, converging to the *Lippmann-Schwinger* equation.

Next, the Born and Rytov approximations of LS are presented with their respective levels of approximation. The *Beam and Wave Propagation Method*, as well as the *Split-Step Non Paraxial* method are briefly explained. Beyond the equations, an intuitive overview of the light interaction modeled by these methods is given in Fig. 5.2.

Finally, the *Fourier diffraction theorem* is derived under the First-Born approximation, bringing out the *missing cone problem*. Everything presented in this section is well-understood by the scientific community, it will though be useful to support some arguments given in the analyses of Chap. 6.

Useful Identities

We provide three identities used for the derivations in Sec. 5.2.1 and in Sec. 5.2.3. We consider the scalar fields $u, \mu, \theta \in \mathbb{R}$ where $\theta(\mathbf{r})$ depends on the 3-D Cartesian coordinates $\mathbf{r} = (x, y, z)$ and the vector field $\mathbf{v} \in \mathbb{R}^3$.

Identity 5.1 (Product rule for the curl). $\nabla \times (uv) = u(\nabla \times \mathbf{v}) + \nabla u \times \mathbf{v}$

Identity 5.2 (Vector triple product). $\nabla \times (\nabla \times \mathbf{u}) = \nabla(\nabla \cdot \mathbf{u}) - \nabla^2 \mathbf{u}$

Identity 5.3. $\mu \nabla \left(\frac{1}{\mu} \right) = \frac{-1}{\mu} \nabla \mu = -\nabla \log(\mu)$

Identity 5.4. $\nabla^2 e^{\theta(\mathbf{r})} = \nabla \cdot [\nabla \theta(\mathbf{r}) e^{\theta(\mathbf{r})}] = e^{\theta(\mathbf{r})} [\nabla^2 \theta(\mathbf{r}) + \|\nabla \theta(\mathbf{r})\|_2^2]$.

5 | Diffraction Through Inhomogeneous Media

5.2.1 From Maxwell to Helmholtz

This section departs from the fundamental equations of electromagnetism theory—the *Maxwell's equations*⁴ [Jac98] and derive the scalar form of the *Helmholtz equation*, highlighting the assumptions made along the way. Each **new term** is highlighted in green on its first appearance.

The local form of Maxwell's equations are recalled here below.

Maxwell's equations

$$\nabla \cdot \mathbf{D} = \rho \quad (\text{Coulomb})$$

$$\nabla \cdot \mathbf{B} = 0 \quad (\text{Gauss})$$

$$\nabla \times \mathbf{E} = -\partial_t \mathbf{B} \quad (\text{Ampère})$$

$$\nabla \times \mathbf{H} = \partial_t \mathbf{D} + \mathbf{J} \quad (\text{Faraday})$$

where \mathbf{D} , \mathbf{B} , \mathbf{E} , \mathbf{H} , \mathbf{J} , and ρ are respectively the *displacement field*, *magnetic field*, *electric field*, *magnetic excitation*, *current density*, and *dielectric charge* in the medium. The space and time (resp. \mathbf{r} and t) dependencies of the involved quantities will be mostly made implicit in this section to simplify the notations.

Making slight modifications of (Ampère) and (Faraday) (highlighted in green)—without loss of generality—yields:

$$\nabla \cdot \mathbf{D} = \rho$$

$$\nabla \cdot \mathbf{B} = 0$$

$$\nabla \times \left(\frac{1}{\mu} \nabla \times \mathbf{E} \right) = -\nabla \times \left(\frac{1}{\mu} \partial_t \mathbf{B} \right) \quad (5.2)$$

$$\partial_t (\nabla \times \mathbf{H}) = \partial_t (\partial_t \mathbf{D}) + \partial_t \mathbf{J} \quad (5.3)$$

Where μ is the *magnetic permeability*. Let us make two Assumptions 5.1-5.2.

⁴It is hard to cite a single work because the Maxwell's equations have been formulated many times over time by several contributors. We therefore refer to them throughout this book [Jac98] providing detailed discussions.

Assumption 5.1 (Time-invariant linear medium). *The medium has a linear relationship between (i) the displacement and electric fields $\mathbf{D} = \epsilon\mathbf{E}$ where ϵ is the dielectric permittivity, (ii) the magnetic field and magnetic excitation $\mathbf{B} = \mu\mathbf{H}$. This implies $\nabla \times \mathbf{B} = \mu(\nabla \times \mathbf{H})$. The magnetic permeability μ and dielectric permittivity ϵ are also assumed to be time-invariant, i.e.,*

$$\mu, \epsilon \perp\!\!\!\perp t, \quad (5.4)$$

hence varying only in space $\mu(\mathbf{r})$ and $\epsilon(\mathbf{r})$. “ $\perp\!\!\!\perp$ ” denotes the independence.

Assumption 5.2 ($\mathbf{B} \in \mathcal{C}^2(\mathbb{R})$). *The magnetic field \mathbf{B} is \mathcal{C}^2 -smooth (i.e., \mathbf{B} has continuous second-order partial derivatives). From the Schwarz's theorem, it implies that the time derivative ∂_t and curl \times commute as*

$$\partial_t(\nabla \times \mathbf{B}) = \nabla \times (\partial_t \mathbf{B}) \quad (5.5)$$

Injecting Assumption 5.1 in both (5.2) and (5.3), and Assumption 5.2 in (5.3) gives

$$\begin{aligned} \nabla \cdot \mathbf{D} &= \rho \\ \nabla \cdot \mathbf{B} &= 0 \\ \nabla \times \left(\frac{1}{\mu} \nabla \times \mathbf{E} \right) + \nabla \times (\partial_t \mathbf{H}) &= 0 \end{aligned} \quad (5.6)$$

$$\nabla \times (\partial_t \mathbf{H}) = \epsilon \partial_t^2 \mathbf{E} + \partial_t \mathbf{J} \quad (5.7)$$

By denoting $\ddot{\mathbf{E}} := \partial_t^2 \mathbf{E}$, $\dot{\mathbf{J}} := \partial_t \mathbf{J}$, and combining (5.6) and (5.7), a single equation with only the electric field and current density can be obtained as

$$\nabla \times \left(\frac{1}{\mu} \nabla \times \mathbf{E} \right) + \epsilon \ddot{\mathbf{E}} + \dot{\mathbf{J}} = 0. \quad (5.8)$$

The *product rule for the curl* Id. 5.1 is used to transform (5.8) as

$$\frac{1}{\mu} (\nabla \times \nabla \times \mathbf{E}) + \nabla \left(\frac{1}{\mu} \right) \times (\nabla \times \mathbf{E}) + \epsilon \ddot{\mathbf{E}} + \dot{\mathbf{J}} = 0,$$

then the *vector triple product* Id. 5.2 modifies the first term as

$$\frac{1}{\mu} (\nabla(\nabla \cdot \mathbf{E}) - \nabla^2 \mathbf{E}) + \nabla \left(\frac{1}{\mu} \right) \times (\nabla \times \mathbf{E}) + \epsilon \ddot{\mathbf{E}} + \dot{\mathbf{J}} = 0 \quad (5.9)$$

Multiplying each term in (5.9) by $(-\mu)$ and applying Id. 5.3 yields

$$-\nabla(\nabla \cdot \mathbf{E}) + \nabla^2 \mathbf{E} + \nabla \log(\mu) \times (\nabla \times \mathbf{E}) - \mu \epsilon \ddot{\mathbf{E}} - \mu \dot{\mathbf{J}} = 0 \quad (5.10)$$

5 | Diffraction Through Inhomogeneous Media

A parenthesis is made in order to modify the first term in (5.10). From (Coulomb) and Assumption 5.1, we first get

$$\nabla \cdot \mathbf{D} = \nabla \cdot (\epsilon \mathbf{E}) = \epsilon \nabla \cdot \mathbf{E} + \mathbf{E} \cdot \nabla \epsilon = \rho. \quad (5.11)$$

Then, (5.11) can be used to modify the first term of (5.10) as

$$\nabla (\nabla \cdot \mathbf{E}) = \nabla \left(\frac{\rho}{\epsilon} - \frac{1}{\epsilon} \mathbf{E} \cdot \nabla \epsilon \right) = \nabla \left(\frac{\rho}{\epsilon} \right) - \nabla (\mathbf{E} \cdot \nabla (\log(\epsilon))) \quad (5.12)$$

Injecting (5.12) into (5.10) and rearranging the terms gives

$$\nabla^2 \mathbf{E} - \mu \epsilon \ddot{\mathbf{E}} + \nabla \log(\mu) \times (\nabla \times \mathbf{E}) - \nabla \left(\frac{\rho}{\epsilon} \right) + \nabla (\mathbf{E} \cdot \nabla (\log(\epsilon))) - \mu \dot{\mathbf{J}} = 0 \quad (5.13)$$

Let us consider a medium without time-varying current density with Assumption 5.3.

Assumption 5.3. In (Faraday), one assumes a medium devoid of current density variation in time ($\dot{\mathbf{J}} = \mathbf{0}$).

The remaining terms are

$$\nabla^2 \mathbf{E} - \mu \epsilon \ddot{\mathbf{E}} + \nabla \log(\mu) \times (\nabla \times \mathbf{E}) - \nabla \left(\frac{\rho}{\epsilon} \right) + \nabla (\mathbf{E} \cdot \nabla (\log(\epsilon))) = 0 \quad (5.14)$$

Eq. (5.14) is starting to look like the target *Helmholtz equation*: it is a single equation involving only the *electric field* \mathbf{E} , the *electric charge* ρ , and the medium properties μ and ϵ . The next assumption consists in imposing a single light frequency f —and consequently a single *pulsation* ω —into the model in order to avoid too much disorder. It also allows to ignore the dependence of the medium properties on the frequency of the light. From this, let us propose an ansatz⁵ making a separation of space \mathbf{r} and time t variables for the electric field, and further assuming that the time-dependence only takes the form of a complex exponential $e^{-i\omega t}$. This is formalized in Assumption 5.4.

Assumption 5.4 (Ansatz for unique lightwave frequency).
 $E(\mathbf{r}, t) = E(\mathbf{r}) e^{-i\omega t} \implies \ddot{\mathbf{E}}(\mathbf{r}, t) = -\omega^2 \mathbf{E}(\mathbf{r}, t)$

⁵A German term frequently used in mathematics and physics to refer to an educated guess about the form of a solution to a problem.

Assumption 5.4 can be exploited to rewrite (5.14) as

$$\nabla^2 \mathbf{E} + \omega^2 \mu \epsilon \mathbf{E} + \nabla \log(\mu) \times (\nabla \times \mathbf{E}) - \nabla \left(\frac{\rho}{\epsilon} \right) + \nabla (\mathbf{E} \cdot \nabla (\log(\epsilon))) = 0 \quad (5.15)$$

Assumption 5.4 somehow allows us to hide the time-dependence of the electric field. The time-dependent term $e^{-i\omega t}$ in (5.15) can be factorized and we are left with a *stationary* equation, only varying in space.

The *speed of light* c only depends on the magnetic permeability μ_0 and dielectric permittivity ϵ_0 of vacuum as $c := \frac{1}{\sqrt{\epsilon_0 \mu_0}}$. Decomposing each into its value in vacuum “times” *relative value* as $\mu := \mu_0 \mu_r$ and $\epsilon := \epsilon_0 \epsilon_r$, one has $\omega^2 \epsilon \mu = \omega^2 \epsilon_0 \mu_0 \epsilon_r \mu_r = \left(\frac{\omega}{c}\right)^2 \epsilon_r \mu_r = k^2 \epsilon_r \mu_r$ with the *wavenumber* in vacuum $k := \omega/c$. Finally, introducing the *refractive index* $n := \sqrt{\epsilon_r \mu_r}$, the second term in (5.15) can be rewritten as

$$\nabla^2 \mathbf{E} + k^2 n^2 \mathbf{E} + \nabla \log(\mu) \times (\nabla \times \mathbf{E}) - \nabla \left(\frac{\rho}{\epsilon} \right) + \nabla (\mathbf{E} \cdot \nabla (\log(\epsilon))) = 0 \quad (5.16)$$

Three last assumptions are used to simplify (5.16) down to the Helmholtz equation.

Assumption 5.5 (No electric charge). *There is no electric charge in the medium: $\rho = 0$.*

Assumption 5.6 (Non magnetic). *The medium is non-magnetic everywhere: $\mu = \mu_0 \perp\!\!\!\perp \mathbf{r}, \mu_r = 1$.*

Assumption 5.7 (Slow-variation of $\epsilon(\mathbf{r})$). *The dielectric permittivity $\epsilon(\mathbf{r})$ varies so slowly with respect to the position \mathbf{r} that it is effectively constant over distances of the order of the wavelength $\lambda := \frac{\omega}{c}$. Equivalently:*

$$\nabla (\mathbf{E} \cdot \nabla (\log(\epsilon))) \ll \nabla^2 \mathbf{E}. \quad (5.17)$$

Considering Assumptions 5.5, 5.6 and 5.7 finally provides the vectorial **Wave** equation.

$$\nabla^2 \mathbf{E} + k^2 n^2 \mathbf{E} = 0. \quad (\text{Wave})$$

The inhomogeneous **Wave** equation, also known as the inhomogeneous *Helmholtz equation*, is stationary—meaning the operators only act on the space-dependence of \mathbf{E} . Removing the time component of $\mathbf{E}(\mathbf{r}, t) :=$

5 | Diffraction Through Inhomogeneous Media

$E'(\mathbf{r})e^{-i\omega t}$ also gives $\nabla^2 E'(\mathbf{r}) + k^2 n(\mathbf{r})^2 E'(\mathbf{r}) = 0$. Thanks to Assumption 5.7, the three Cartesian components of $\mathbf{E}' := (E'_x, E'_y, E'_z)$ are *decoupled*. This means any component U (either E'_x , E'_y , or E'_z) of \mathbf{E}' satisfies the Helmholtz equation defined as

Inhomogeneous scalar Helmholtz equation

$$(\nabla^2 + k^2 n(\mathbf{r})^2 \mathbf{I}) U(\mathbf{r}) = 0. \quad (\text{Helmholtz})$$

We can find several variants of the Helmholtz equation, where we can recast

$$k^2 n(\mathbf{r})^2 = k(\mathbf{r})^2 = k_m^2 \left(\frac{n(\mathbf{r})}{n_m} \right)^2 \quad (5.18)$$

with $k(\mathbf{r}) := k_m \frac{n(\mathbf{r})}{n_m}$ and $k_m := kn_m$, where k_m (resp. n_m) is the wavenumber (resp. refractive index) in some presupposed *background medium m*. Throughout the derivations made in this section, it has been shown that the Helmholtz equation is only valid under Assumptions 5.1-5.7.

5.2.2 From Helmholtz to Lippmann-Schwinger

The *Lippmann-Schwinger equation* (LS) describes the electric wavefield issued from the diffraction of an incident field by a scattering potential. Re-starting from the Helmholtz equation, LS is derived in this section. The following derivations are inspired by [MSG16; SPU17; Tai94].

The *incident wavefield* is defined as the solution of (Helmholtz) when there is no variation of the refractive index within the background medium, *i.e.*,

$$(\nabla^2 + k_m^2 \mathbf{I}) U_i(\mathbf{r}) = 0. \quad (5.19)$$

Eq. (5.19) is also named the *homogeneous* solution of (Helmholtz). In analogy to the terminology used in the quantum theory of potential scattering, we can define the scattering potential (with respect to the background medium m) as

Definition 5.2.1 (Scattering potential).

$$f(\mathbf{r}) := k_m^2 \left[\left(\frac{n(\mathbf{r})}{n_m} \right)^2 - 1 \right]. \quad (5.20)$$

The scattering potential is dimensional; its units are m^{-2} . The adimensional *contrast* value, which will be useful in Sec. 5.4.2 and in

Chap. 6, is defined in Def. 5.2.2 as the maximum relative variation of the refractive index (with respect to the background medium m).

Definition 5.2.2 (Contrast).

$$C := \max_{\mathbf{r} \in \mathbb{R}^3} \frac{|f(\mathbf{r})|}{k_m^2} = \max_{\mathbf{r} \in \mathbb{R}^3} \left[\left(\frac{n(\mathbf{r})}{n_m} \right)^2 - 1 \right]. \quad (5.21)$$

Eq. (5.20) allows to rewrite (Helmholtz) as

$$(\nabla^2 + k_m^2 \mathbf{I})U(\mathbf{r}) = -f(\mathbf{r})U(\mathbf{r}).$$

Let us decompose $U(\mathbf{r})$ into its *homogeneous* and *particular* parts, or equivalently as the sum of the *incident field* $U_i(\mathbf{r})$ and the *scattered field* $U_s(\mathbf{r})$ as

$$U(\mathbf{r}) = U_i(\mathbf{r}) + U_s(\mathbf{r}). \quad (5.22)$$

$U_i(\mathbf{r})$ and $U_s(\mathbf{r})$ respectively satisfy

$$(\nabla^2 + k_m^2 \mathbf{I})U_i(\mathbf{r}) = 0 \quad (5.23)$$

$$(\nabla^2 + k_m^2 \mathbf{I})U_s(\mathbf{r}) = -f(\mathbf{r})U(\mathbf{r}) \quad (5.24)$$

From here we convert (5.23) into an integral equation. Let

$$G(\mathbf{r}) := \frac{e^{ik_m|\mathbf{r}|}}{4\pi|\mathbf{r}|} \quad (5.25)$$

be the Green function associated with the Helmholtz operator $\nabla_r^2 + k_m^2 \mathbf{I}$ [Tai94], i.e., a solution of

$$(\nabla_r^2 + k_m^2 \mathbf{I})G(\mathbf{r} - \mathbf{r}') = -\delta(\mathbf{r} - \mathbf{r}') \quad (5.26)$$

We can integrate (5.26) into a volume Ω s.t. $\text{supp } f \subset \Omega$ to get an expression similar to (5.24) as

$$\begin{aligned} \int_{\Omega} (\nabla_r^2 + k_m^2 \mathbf{I})G(\mathbf{r} - \mathbf{r}')f(\mathbf{r}')U(\mathbf{r}')d\mathbf{r}' &= \int_{\Omega} -\delta(\mathbf{r} - \mathbf{r}')f(\mathbf{r}')U(\mathbf{r}')d\mathbf{r}' \\ &= -f(\mathbf{r})U(\mathbf{r}), \end{aligned}$$

and by identification with (5.24) conclude that

$$U_s(\mathbf{r}) = \int_{\Omega} f(\mathbf{r}')U(\mathbf{r}')G(\mathbf{r} - \mathbf{r}')d\mathbf{r}' \quad (5.27)$$

Combining (5.22) and (5.27), we finally obtain the *Lippmann-Schwinger* equation.

5 | Diffraction Through Inhomogeneous Media

Lippmann-Schwinger equation

$$U(\mathbf{r}) = U_i(\mathbf{r}) + \int_{\Omega} f(\mathbf{r}') U(\mathbf{r}') G(\mathbf{r} - \mathbf{r}') d\mathbf{r}' \quad (\text{LS})$$

Eq. (LS) describes the *total field* $U(\mathbf{r})$ as a function of the *incident field* $U_i(\mathbf{r})$ and the *scattering potential* $f(\mathbf{r})$ defined in (5.21). This is an implicit equation, involving the solution U on both sides of the equal sign. Furthermore, the interaction between the total field U and the scattering potential f is convolutive. The knowledge of f in the entire volume Ω is necessary. Note that the value of k_m in the definition of the scattering potential f can be set to any arbitrary value.

5.2.3 The First-Born Approximation

As the implicit equation (LS) is very hard to solve, many simplifications of the Lippmann-Schwinger equation have been studied and used in the last century [Bor+99]. In this section, we explain the *Born approximation*, used in the numerical experiments of this thesis. We also mention other approximation techniques and report their details in Appendix 5.6.

The most straightforward simplification of (LS) consists in assuming that the scattered field is negligible compared to the incident field, *i.e.*, $|U_s(\mathbf{r})| \ll |U_i(\mathbf{r})|, \forall \mathbf{r} \in \Omega$. This assumption allows replacing U by U_i into the right-hand term of (LS) as

$$U_1(\mathbf{r}) = U_i(\mathbf{r}) + \int_{\Omega} f(\mathbf{r}') \textcolor{green}{U}_i(\mathbf{r}') G(\mathbf{r} - \mathbf{r}') d\mathbf{r}' \quad (\text{First-Born})$$

which is known as the *First-Born* (FB) approximation [CS98]. First-Born is easy to compute because it is linear with respect to the scattering potential $f(\mathbf{r})$. The $(n + 1)$ -order Born approximation consists in substituting the n -order approximation for U as

$$U_{n+1}(\mathbf{r}) = U_i(\mathbf{r}) + \int_{\Omega} f(\mathbf{r}') U_n(\mathbf{r}') G(\mathbf{r} - \mathbf{r}') d\mathbf{r}'. \quad (5.28)$$

Unrolling (5.28) yields a series known as the *Liouville-Neumann series* [Bor+99, Chap. 13]. The n -order Born approximation naturally implies computing n integrals, so computing more than the second-order Born approximation in continuous form has rarely been done in practice. The n -order Born approximation is expected to converge to (LS) as $n \rightarrow \infty$ under certain conditions, but these conditions are difficult to

establish. The stability conditions are studied in Sec. 5.4 for the discrete version of (LS), emphasizing that the n -th iterate of the *gradient descent* method is a kind of stabilized n -order approximation.

There exists many other approximations to the LS model that improve over the First-Born approximation. Namely, the *Rytov approximation*, *Beam Propagation Method* (BPM), *Wave Propagation Method* (WPM), and *Split-Step Non Paraxial* (SSNP) method are detaild in Appendix 5.6. The levels of approximation of these different methods are divided in three classes in Fig. 5.2. The First-Born and Rytov approximations consider only the interaction of the object with the incident illumination. The BPM, WPM, and SSNP are multi-slice models that alternate between the diffraction through a phase mask related to each slice of the RI object content, and a free-propagation in the background medium until the next slice. The LS model is the only one without approximation, because it models the infinite order of interactions between all the scattering elements of the volume.

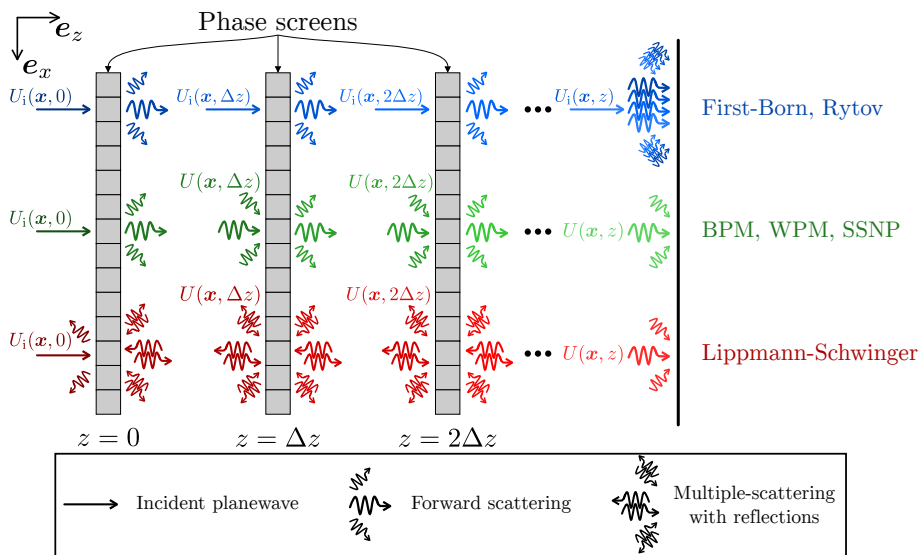


Fig. 5.2 Illustration of the three families of diffraction methods. (top) The total field computed by the First-Born and Rytov approximations is the sum of the incident field and its separated interaction with each slice of the scattering potential. The deformation of the incident field through each slice to illuminate the next slice is neglected. (middle) For BPM, WPM, and SSNP, the total field at depth z is given as the composition of the effect of each scattering slice on the incident lightwave. The models neglect the reflections. (bottom) In the Lippmann-Schwinger model, the total field at position r depends on the entire RI volume through a convolution, where each voxel plays the role of a new light source.

5 | Diffraction Through Inhomogeneous Media

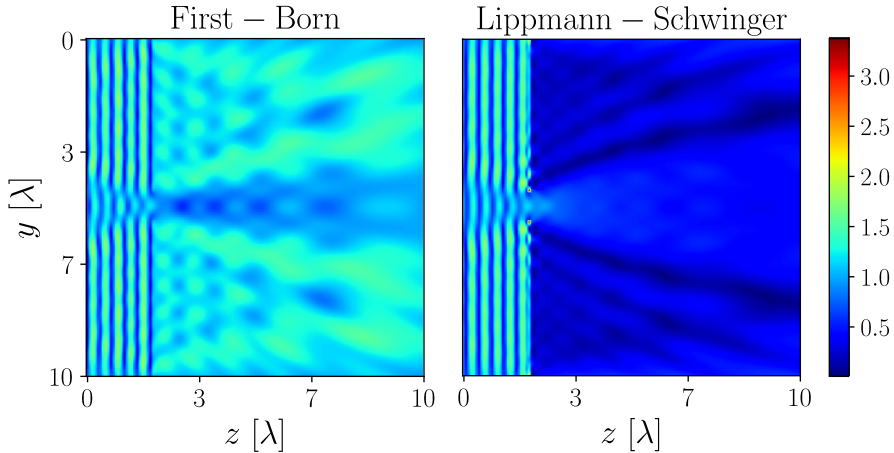


Fig. 5.3 Diffraction of an incident planewave through a slit with (left) the First-Born approximation, and (right) the LS model.

In order to provide a realistic illustration, Fig. 5.3 depicts the diffraction of an incident planewave of wavelength $\lambda = 515\text{nm}$ in vacuum propagating along the z -axis in water ($n_m = 1.333$). The centered slit mask, of width λ and contrast $C = 2$ (corresponding to a RI $n = 2.75$) has been placed at depth $z = 2\lambda$. In Fig. 5.3, one observes that LS adequately models the major reflection imposed by the mask while FB only takes into account the interaction of the incident planewave with every voxel of the scattering potential, and considers that the right-hand side of the mask behaves as a new diffracting source.

Remark 5.1. There exists a multitude of finite difference methods [Str04] that directly solve the Helmholtz equation after a discretization of the volume. For instance, the central difference method (particularized to 1-D) writes

$$\frac{u_{i+1} - 2u_i + u_{i-1}}{\Delta x^2} + k_m^2 u_i = f_i,$$

for an integer i indexing some position along the x -axis, and a spatial resolution Δx . The drawbacks of finite difference methods compared to the methods presented in this section are threefold: (i) Ensuring stability requires careful selection of grid spacing, especially for explicit methods. (ii) A large number of grid points are often required to accurately capture wave phenomena, leading to high memory and processing requirements. (iii) Implementing appropriate absorbing boundary conditions to simulate open domains can be complex and imperfect, leading to reflections that affect the solution.

This section aimed to convince the reader of the importance to work with an efficient version of the LS equation, free of the approximations considered in the other presented models. Sec. 5.3 will deal with the numerical challenges associated to its discretization.

5.2.4 Fourier Diffraction Theorem

The Fourier diffraction theorem [Kir+21; Fau+21; KS01] is fundamental to diffraction tomography. Under the First-Born approximation, it relates the Fourier transform of the measured forward scattered data to the Fourier transform of the object.

5 | Diffraction Through Inhomogeneous Media

Theorem 5.1 (Fourier diffraction theorem). Let $f(\mathbf{r}) \in \mathbb{R}$ be the scattering potential distribution at position $\mathbf{r} \in \mathbb{R}^3$, $\hat{f}(\omega, \omega_z) \in \mathbb{C}$ be its 3-D Fourier transform with $\omega \in \mathbb{R}^2$, $\omega_z \in \mathbb{R}$, and let $U_1^s(\mathbf{r}; \mathbf{k}_i) \in \mathbb{C}$ be the scattered component of the First-Born approximation under a planewave illumination $U_i(\mathbf{r}; \mathbf{k}_i) = e^{-i\mathbf{k}_i^\top \mathbf{r}}$ with wavevector $\mathbf{k}_i \in \mathbb{R}^3$. The transversal 2-D Fourier transform of the scattered component at depth z , denoted \mathcal{F}_2 , is related to the 3-D Fourier transform of the scattering potential as

$$\mathcal{F}_2\{U_1^s(\cdot, z; \mathbf{k}_i)\}[\omega] = \frac{i}{2\sqrt{\pi}} \frac{e^{i\eta(\omega)z}}{\eta(\omega)} \hat{f}(\omega + \omega_i, \eta(\omega_i) - \eta(\omega)), \quad (5.29)$$

where

$$\eta(\omega) := \sqrt{k_m^2 - \|\omega\|_2^2}. \quad (5.30)$$

The proof is given in Appendix 5.6.2. The *Fourier diffraction theorem* informs on which partial Fourier content of the scattering potential f can be accessed by the scattered field U_1^s . Let us consider a single view with incident direction $\mathbf{k}_i := k_m \mathbf{e}_z$, i.e., with $\omega_i = \mathbf{0} \Rightarrow \eta(\omega_i) = k_m$. For this single view, and a given observation depth z , (5.29) shows that by varying ω , the Fourier transform \hat{f} can be accessed only at coordinates $(\omega, k_m - \sqrt{k_m^2 - \|\omega\|_2^2})$. This defines a hemispherical surface centered on $(\mathbf{0}, k_m)$ with radius k_m and depicted in Fig. 5.29(a). The Fourier diffraction theorem is a generalization of the *Fourier slice theorem* [MSG16] only valid in classical tomography, i.e., when the illumination wavelength is negligible compared to the dimension of the scattering potential.

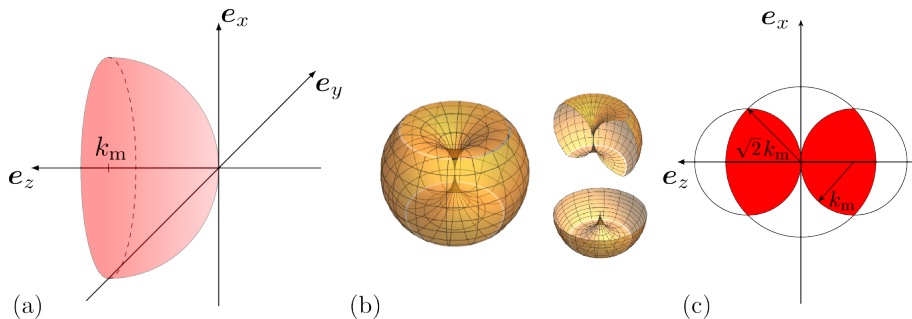


Fig. 5.4 (a) Accessible points $(\omega, k_m - \sqrt{k_m^2 - \|\omega\|_2^2})$ of \hat{f} in transmission imaging and for an incident field $U_i(\mathbf{r}) = e^{-ik_m z}$. (b) Complete revolution of the points in (a) around the e_x -axis. (c) Projection of (b) in the $e_x - e_z$ plane. Adapted from [Kir+21].

Fig. 5.4(a) shows that, under the **First-Born** approximation, the Fourier content accessed by the front-scattered field U_i^s is very limited. For image recovery purposes, multiple views are necessary. Fig. 5.4(b-c) show the Fourier coverage obtained from a complete revolution of the object (or equivalently the incident field, see Claim 5.1) around the e_x -axis. Even in this situation, the frequency content along the e_x direction remains poor. The sphere of radius $\sqrt{2}k_m$ can be accessed by further considering a complete revolution around the e_y -axis.

Claim 5.1. *Rotating the incident U_i on a fixed object is equivalent to considering a fixed incident field on a rotated object. To prove this, let us consider any arbitrary 3-D rotation matrix \mathbf{R} , and insert the rotated incident field $U_i(\mathbf{R}\mathbf{r})$ into (LS). It writes*

$$U(\mathbf{r}; \mathbf{R}) = U_i(\mathbf{R}\mathbf{r}) + \int_{\Omega} f(\mathbf{r}') U(\mathbf{r}') G(\mathbf{r} - \mathbf{r}') d\mathbf{r}'.$$

Applying the change of variable $\tilde{\mathbf{r}} := \mathbf{R}\mathbf{r}$ yields

$$\begin{aligned} U(\mathbf{R}^\top \tilde{\mathbf{r}}; \mathbf{R}) &= U_i(\tilde{\mathbf{r}}) + \int_{\Omega} f(\mathbf{r}') U(\mathbf{r}') G(\mathbf{R}^\top \tilde{\mathbf{r}} - \mathbf{r}') d\mathbf{r}' \\ &= U_i(\tilde{\mathbf{r}}) + \int_{\Omega} f(\mathbf{R}^\top \tilde{\mathbf{r}}') U(\mathbf{R}^\top \tilde{\mathbf{r}}') G(\mathbf{R}^\top \tilde{\mathbf{r}} - \mathbf{R}^\top \tilde{\mathbf{r}}') d(\mathbf{R}^\top \tilde{\mathbf{r}}') \\ &= U_i(\tilde{\mathbf{r}}) + \int_{\Omega} f(\mathbf{R}^\top \tilde{\mathbf{r}}') U(\mathbf{R}^\top \tilde{\mathbf{r}}') G(\tilde{\mathbf{r}} - \tilde{\mathbf{r}}') d\tilde{\mathbf{r}}', \end{aligned} \quad (5.31)$$

where the last two terms were changed by knowing that \mathbf{R} preserves the distances. Eq. (5.31) shows the equivalence between incident field rotation and object rotation in the opposite sense.

In general, the imaging conditions restrict the set of possible angles from which to illuminate the object. The lack of Fourier information imposed by this restricted view often induces artifacts in the 3-D image estimated by an inverse problem solving. This phenomenon is well-known as the **missing cone problem** [Lim+15] depicted later in Fig. 6.5. Part of the analysis presented in Chap. 6 will be oriented towards presenting use-cases where the nonlinearity of the Lippmann-Schwinger model (LS) mitigates this missing cone problem.

5.2.5 Passive Illumination Sources

The main difference between the LS model and its **First-Born** approximation is that LS can model multiple reflections. This fact can be leveraged to our advantage by inserting known strongly scattering tiny ob-

5 | Diffraction Through Inhomogeneous Media

jects into the volume Ω in the aim to induce strong reflections that modify the effective illumination. Indeed, let us consider a modified RI object

$$\tilde{f}(\mathbf{r}) := f(\mathbf{r}) + \sum_{q=1}^Q c_q \delta(\mathbf{r} - \mathbf{p}_q), \quad (5.32)$$

where f is the RI object that we aim to image by diffraction tomography, and $\sum_{q=1}^Q c_q \delta(\mathbf{r} - \mathbf{p}_q)$ is a sum of Q ponctual sources with respective scattering potential c_q and position $\mathbf{p}_q \in \mathbb{R}^3$. Injecting (5.32) into (LS) gives

$$U(\mathbf{r}) = U_i(\mathbf{r}) + \sum_{q=1}^Q c_q U(\mathbf{p}_q) G(\mathbf{r} - \mathbf{p}_q) + \int_{\Omega} f(\mathbf{r}') U(\mathbf{r}') G(\mathbf{r} - \mathbf{r}') d\mathbf{r}'. \quad (5.33)$$

By identification with (LS), it appears that (5.33) now has an equivalent illumination

$$\tilde{U}_i(\mathbf{r}) := U_i(\mathbf{r}) + \sum_{q=1}^Q c_q U(\mathbf{p}_q) G(\mathbf{r} - \mathbf{p}_q). \quad (5.34)$$

Obviously, the equivalent incident field in (5.34) requires the total field at the position of the passive sources $U(\mathbf{p}_q)$ as it interacts with the object to be imaged. But if the passive sources are sufficiently far away from the object, the equivalent illumination can be approximated as

$$\tilde{U}_i(\mathbf{r}) \approx U_i(\mathbf{r}) + \sum_{q=1}^Q c_q \textcolor{green}{U}_i(\mathbf{p}_q) G(\mathbf{r} - \mathbf{p}_q). \quad (5.35)$$

Remark 5.2. This view in (5.34) could not be obtained with the (First-Born) model. In that case the diffracted field would have been written

$$U(\mathbf{r}) = U_i(\mathbf{r}) + \sum_{q=1}^Q c_q U_i(\mathbf{p}_q) G(\mathbf{r} - \mathbf{p}_q) + \int_{\Omega} f(\mathbf{r}') U_i(\mathbf{r}') G(\mathbf{r} - \mathbf{r}') d\mathbf{r}',$$

and one observes that the passive sources have no influence on the field illuminating f in the last term, which remains $U_i(\mathbf{r})$.

With the definition of the Green's function given in (5.25), if the passive sources are sufficiently far away from f , their contribution can be approximated as planewaves coming from their position. Eq. (5.33)

shows that the passive sources give access to illumination angles possibly unreachable in the tomographic imaging conditions. The insertion of these strongly scattering objects mitigates the *missing cone problem* [Lim+15] illustrated later in Fig. 6.5(b). This technique is standard in *ultrasound imaging* [Hua+14], *seismic imaging* [Wan+20], and *radar* [LH07].

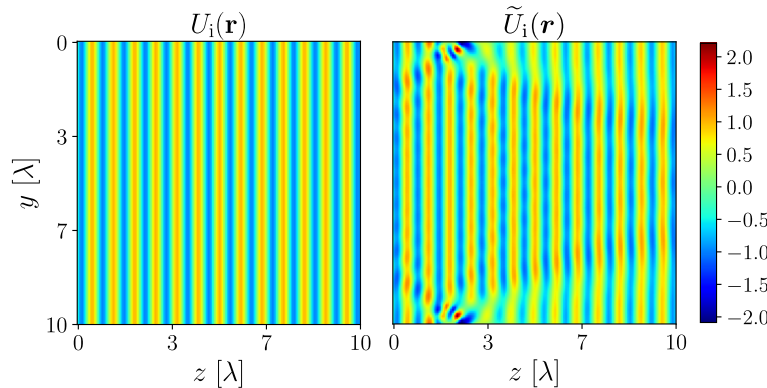


Fig. 5.5 Field scattered by passive sources. (left) Incident field $U_i(\mathbf{r}) = e^{ik_m z}$ (right) Equivalent incident field $\tilde{U}_i(\mathbf{r})$ resulting from the diffraction of U_i through two passive sources of contrast $C = 2$ respectively located at $(5\lambda, \frac{5}{32}\lambda, \frac{125}{64}\lambda)$ and $(5\lambda, \frac{125}{64}\lambda, \frac{315}{32}\lambda)$. Both are shown in the plane $x = 5\lambda$.

Fig. 5.5 illustrates the approximate equivalent incident illumination $\tilde{U}_i(\mathbf{r})$ obtained using (5.35) by placing two passive sources on the sides of the domain Ω , with contrast value $C = 2$ (corresponding to a RI $n = 2.75$). The incident planewave has wavelength in vacuum $\lambda = 515\text{nm}$ and propagates along the z -axis in water ($n_m = 1.333$). It can be seen in Fig. 5.5(right) that the passive sources induce new (almost) planewave illuminations coming from their locations. This results in an illumination with a larger illumination angle of the volume Ω than in their absence, as seen in Fig. 5.5(left).

5 | Diffraction Through Inhomogeneous Media

5.3 Discrete Model

A discrete version of the Lippmann-Schwinger equation ([LS](#)) is derived in this section, accompanied by an efficient implementation of the convolution with the Green kernel.

5.3.1 Spatial Sampling

Let us consider the *spatial sampling operator* III_3 sampling a 3-D continuous function h on a regular 3-D grid $\mathcal{G}_{(N_x, N_y, N_z)}^{(L_x, L_y, L_z)} := \{\mathbf{r}_0, \dots, \mathbf{r}_{N-1}\}$ with resolutions (N_x, N_y, N_z) along the (x, y, z) axes by using a Dirac's bed $\sum_{n=1}^N \delta(\mathbf{r} - \mathbf{r}_n)$ with $\mathbf{r}_n \in \mathcal{G}_{(N_x, N_y, N_z)}^{(L_x, L_y, L_z)}$. One has $\mathbf{r}_n := \mathbf{r}'_n \bullet \mathbf{L}$ for the spatial dimensions $\mathbf{L} := (L_x, L_y, L_z)$, and $\mathbf{r}'_l = (\frac{i}{N_x}, \frac{j}{N_y}, \frac{k}{N_z})$ for $l := i + jN_x + kN_y^2, i \in \llbracket N_x \rrbracket, j \in \llbracket N_y \rrbracket, k \in \llbracket N_z \rrbracket$.

Applying III_3 to U, U_i, U_s, f , and G and gathering the N nonzero values into vectors respectively yields $\mathbf{u}, \mathbf{u}_i, \mathbf{u}_s, \mathbf{f}$, and \mathbf{g} all belonging to \mathbb{R}^N .

First, let us realize that the continuous equation ([LS](#)) is valid at any position $\mathbf{r} \in \mathbb{R}^3$. It can thus be particularized to a position $\mathbf{r}_n \in \mathcal{G}_{(N_x, N_y, N_z)}^{(L_x, L_y, L_z)} \subset \Omega$ as

$$U(\mathbf{r}_n) = U_i(\mathbf{r}_n) + \int_{\Omega} f(\mathbf{r}') U(\mathbf{r}') G(\mathbf{r}_n - \mathbf{r}') d\mathbf{r}'. \quad (5.36)$$

Second, applying III_3 to f and U in the integral of (5.36) gives

$$\begin{aligned} U(\mathbf{r}_n) &\approx U_i(\mathbf{r}_n) + \int_{\Omega} \text{III}_3 f(\mathbf{r}') U(\mathbf{r}') G(\mathbf{r}_n - \mathbf{r}') d\mathbf{r}' \\ &= U_i(\mathbf{r}_n) + \int_{\Omega} \sum_{n'=1}^N \delta(\mathbf{r}' - \mathbf{r}_{n'}) f(\mathbf{r}') U(\mathbf{r}') G(\mathbf{r}_n - \mathbf{r}') d\mathbf{r}' \\ &= U_i(\mathbf{r}_n) + \sum_{n'=1}^N f(\mathbf{r}_{n'}) U(\mathbf{r}_{n'}) G(\mathbf{r}_n - \mathbf{r}_{n'}) \end{aligned}$$

where we used $\int_{\Omega} \delta(\mathbf{r}' - \mathbf{r}_{n'}) d\mathbf{r}' = 1$. The discrete solution $\mathbf{u} := (U(\mathbf{r}_n))_{n=1}^N$ can thus be computed as

$$\begin{bmatrix} U(\mathbf{r}_1) \\ \vdots \\ U(\mathbf{r}_N) \end{bmatrix} = \begin{bmatrix} U_i(\mathbf{r}_1) \\ \vdots \\ U_i(\mathbf{r}_N) \end{bmatrix} + \begin{bmatrix} G(\mathbf{0}) & G(\mathbf{r}_1 - \mathbf{r}_2) & \cdots & G(\mathbf{r}_1 - \mathbf{r}_N) \\ G(\mathbf{r}_2 - \mathbf{r}_1) & G(\mathbf{0}) & \cdots & G(\mathbf{r}_2 - \mathbf{r}_N) \\ \vdots & \ddots & \ddots & \vdots \\ G(\mathbf{r}_N - \mathbf{r}_1) & G(\mathbf{r}_N - \mathbf{r}_2) & \cdots & G(\mathbf{0}) \end{bmatrix} \begin{bmatrix} f(\mathbf{r}_1) U(\mathbf{r}_1) \\ \vdots \\ f(\mathbf{r}_N) U(\mathbf{r}_N) \end{bmatrix},$$

or, equivalently

Discrete Lippmann-Schwinger

$$\mathbf{u} = \mathbf{u}_i + \mathbf{G}\mathbf{D}_f\mathbf{u} \quad (\text{LSd})$$

where $\mathbf{D}_f := \text{diag}(f) \in \mathbb{R}^{N \times N}$ is a diagonal matrix filled with f , and $\mathbf{G} \in \mathbb{C}^{N \times N}$ the *circulant matrix* with $(\mathbf{G})_{jk} = G[j - k]_N$, i.e.,

$$\mathbf{G} = \mathbf{F}\mathbf{D}_{F^*g}\mathbf{F}^* = \mathbf{F}^*\mathbf{D}_{Fg}\mathbf{F} \quad (5.37)$$

with the 3-D Fourier operator \mathbf{F} . The second equality in (5.37) exploits the isotropy of the Green function G . The discrete Lippmann-Schwinger equation (LSd) is also known as the *discrete-dipole approximation*. [Cha22; DF94]. Eq. (LSd) also exists for the three vector components of the electric field \mathbf{E} combined together. In this case, a similar system involves operators of size $3N \times 3N$ and vectors of size $3N$, where the scattering potential becomes a 3×3 tensor, so \mathbf{D}_f becomes a block-diagonal matrix with blocks of size 3×3 .

In the same fashion as for LS, the discretization of the First-Born model writes

Discrete First-Born

$$\mathbf{u} = \mathbf{u}_i + \mathbf{G}\mathbf{D}_f\mathbf{u}_i \quad (\text{FBd})$$

5.3.2 Accurate and Efficient \mathbf{G}

An accurate and efficient implementation of the forward model is proposed here; exploiting the FFT for applying the forward operator \mathbf{G} , and truncating the singularity of the Green function at the origin.

The problem with computing model (LSd) for now is that it requires a discretization \hat{g} of the Fourier transform of the Green function $\hat{G}(\mathbf{u}) := 1/(k_m^2 - \|\boldsymbol{\omega}\|_2^2)$. Both $G(\mathbf{r})$ and $\hat{G}(\mathbf{u})$ have a singularity which prevents from a direct discretization. It has been shown [Pha+20] that the *truncated Green function*

$$G_t(\mathbf{r}) := \text{rect}\left(\frac{\|\mathbf{r}\|}{2L}\right)G(\mathbf{r}) \quad (5.38)$$

for $L := \sqrt{3} \max_{\mathbf{r}_1, \mathbf{r}_2 \in \Omega} \|\mathbf{r}_1 - \mathbf{r}_2\|$ can replace the exact Green function with negligible relative error for the application of the operator \mathbf{G} in

5 | Diffraction Through Inhomogeneous Media

(LSd). The Fourier transform of G_t writes

$$\hat{G}_t(\omega) := \frac{1}{\|\omega\|^2 - k_m^2} \left(1 - e^{iLk_m} \left(\cos(L\|\omega\|) + ik_m L \operatorname{sinc}(L\|\omega\|) \right) \right)$$

when $\|\omega\| \neq k_m$ and

$$\hat{G}_t(\omega) := i \left(\frac{L}{2k_m} - \frac{e^{iLk_m}}{2k_m^2} \sin(Lk_m) \right)$$

when $\|\omega\| = k_m$.

Let $v \in \mathbb{C}^N$ be any arbitrary vector and v_p be its p -times zero-padded version, from (5.37) and exploiting [Pha+20, Prop. 3.2], we have

$$Gv_p = F^* D_{Fg} F v_p = F^*(\hat{g}_t \bullet \widehat{v}_p) = F^*(\widehat{g}_t^p \bullet \widehat{v}_2) \quad (5.39)$$

where v_2 is a twofold zero-padded version of v , and \widehat{g}_t^p is the modified kernel

$$\widehat{g}_t^p[k] = \frac{8}{p^3} \sum_{s \in [\frac{p}{2}-1]^3} F^*(\widehat{g}_t[\frac{p}{2} \cdot -s])[k] e^{\frac{-i2\pi}{np} k^\top s}. \quad (5.40)$$

The last formulation in (5.39) allows to conserve a fixed memory cost bounded by a twofold zero-padding of v for any choice of the zero-padding factor $p > 4$. In the experiments presented later in this chapter, and also in Chap. 6, the application of G will be implemented as in (5.39) and with $p = 4$.

Eq. (LSd) provides us a discrete model to compute the total light-field u resulting from the diffraction of an incident field u_i through an inhomogeneous RI volume f . Sec. 5.4 will discuss how to solve it.

5.4 System Solving

The fruit of Sec. 5.3 is a discrete model ([LSD](#)) for computing the light field \mathbf{u} from the knowledge of an incident field \mathbf{u}_i and a RI volume f . Here, numerical methods are investigated to solve the subsequent linear system. The classical gradient descent method is theoretically studied to introduce the concepts of convergence rate and condition number. Others are numerically analyzed in the provided comparison results. It is numerically demonstrated that the contrast of the refractive index volume directly affects the convergence rate of the system solving. Preconditioning techniques to improve the convergence rate are mentioned.

5.4.1 Bridging Neumann Series and Gradient Descent

The discrete Lippmann-Schwinger equation ([LS](#)) is equivalently written as

$$(\mathbf{I} - \mathbf{G}\mathbf{D}_f)\mathbf{u} = \mathbf{u}_i.$$

By introducing $\mathbf{A} := \mathbf{G}\mathbf{D}_f \in \mathbb{C}^{N \times N}$, and $\mathbf{L} := \mathbf{I} - \mathbf{A} \in \mathbb{C}^{N \times N}$, it can be recast as

$$\mathbf{L}\mathbf{u} = \mathbf{u}_i. \quad (5.41)$$

Eq. (5.41) appears to be a *square linear system* that needs to be solved for \mathbf{u} . Obviously, when there is no variation in the RI, *i.e.*, $f = 0$, the solution is simply $\mathbf{u} = \mathbf{u}_i$. Compared to common inverse problems encountered in CI applications that are under-determined and ill-posed, such as those in Chap. 3, 4, 6 the system in (5.41) is most often fully determined. However, some uncertainties such as an imperfect knowledge of either f , \mathbf{u}_i , or both might be modeled as additive noise. In this case, it is good practice to solve a regularized minimization problem by injecting a prior on the expected solution \mathbf{u} . While it is not harder in terms of implementation to regularize the minimization problem, it complexifies the theoretical analysis. For the sake of simplicity in the analysis, the non-regularized minimization problem will be considered below.

The continuous version of (5.41)—either ([Helmholtz](#)) or ([LS](#))—is known to have a unique solution if the electric field satisfies the *Sommerfeld radiation condition*⁶ [[CK13](#), Th. 9.4]. Analogously, the solution of

⁶The Sommerfeld radiation condition selects only waves that radiate outward from known sources and thus vanish at infinity.

5 | Diffraction Through Inhomogeneous Media

(5.41) is unique if the inverse L^{-1} exists. Provided that $\|A\| < 1$, this inverse exists and u can be computed as

$$u = L^{-1}u_i. \quad (5.42)$$

Indeed, as $\|A\| = \sigma_{\max}(A) < 1$, $\sigma_{\min}(I-A) > 0 \Rightarrow \det(I-A) = \det(L) \neq 0$. Hence, L^{-1} exists. The inverse operator L^{-1} can be decomposed into a converging Neumann series [GOW20], transforming (5.42) as

$$u = \sum_{k=0}^{\infty} A^k u_i. \quad (\text{Neumann})$$

If $\|A\| \geq 1$, the Neumann series diverges. L^{-1} may not exist with the possible situation $\ker L := \{u \text{ s.t. } Lu = 0\} \neq \{0\}$. Yet, it is always possible to formulate the minimization problem

$$\tilde{u} = \arg \min_u \mathcal{L}(u) = \arg \min_u \frac{1}{2} \|Lu - u_i\|_2^2 \quad (5.43)$$

whose solution is not unique but a set. Indeed, if u^* is a solution of (5.43), then $u^* + \ker L$ is the set of solutions. By differentiating \mathcal{L} , the solution of (5.43) must satisfy $L^*Lu = L^*u_i$, and in the case where L^{-1} exists (hence $(L^*L)^{-1}$), one gets

$$u = L^\dagger u_i = (L^*L)^{-1}L^*u_i = \sum_{k=0}^{\infty} (I - L^*L)^k L^*u_i. \quad (5.44)$$

The solution of (5.43) explicated in (5.44) is the (left) pseudo-inverse of the linear operator L applied to u_i . For the same reasons as for the Neumann series in (Neumann), the above series converges if $\|I - L^*L\| < 1$, which is not guaranteed in general. This is why (5.43) is stabilized by adding a scaling factor α in front of (5.44). After adding a stabilization factor $\alpha < 2/\|L\|^2$ to ensure convergence, this results in a solution computed as

$$u = \sum_{k=0}^{\infty} (I - \alpha L^*L)^k \alpha L^*u_i. \quad (5.45)$$

This stabilization is formalized in Claim 5.2 which is proven in Appendix 5.6.3.

Claim 5.2. Given any linear operator \mathbf{L} , it is always possible to choose a scalar value α such that the series $\sum_{k=0}^{\infty} (\mathbf{I} - \alpha \mathbf{L}^* \mathbf{L})^k \alpha \mathbf{L}^* \mathbf{u}_i$ converges. The convergence condition is equivalent to upper bounding the stepsize α , with

$$\|\mathbf{I} - \alpha \mathbf{L}^* \mathbf{L}\| < 1 \Leftrightarrow \alpha < \frac{2}{\|\mathbf{L}\|^2}. \quad (5.46)$$

Remark 5.3. Eq. (5.45) is equivalent to applying the GD algorithm to the minimization of the cost in (5.43). The matching is clearer by recasting every iteration as

$$\begin{aligned} \mathbf{u}^{(k+1)} &= (\mathbf{I} - \alpha \mathbf{L}^* \mathbf{L}) \mathbf{u}^{(k)} + \alpha \mathbf{L}^* \mathbf{u}_i \\ &= \mathbf{u}^{(k)} - \alpha \mathbf{L}^* (\mathbf{L} \mathbf{u}^{(k)} - \mathbf{u}_i) \\ &= \mathbf{u}^{(k)} - \alpha \nabla \mathcal{L}(\mathbf{u}^{(k)}) \end{aligned} \quad (\text{GD})$$

which is stable only if the stepsize $\alpha < \frac{2}{\|\mathbf{L}\|^2}$.

Fig. 5.6 provides a geometrical intuition of the condition on the fixed stepsize $\alpha = \frac{\eta}{L^2}$ to ensure stability of the GD method for minimizing the loss function $\mathcal{L}(u) = \frac{1}{2}(Lu)^2$ with $L = 0.5$. Particularized to this 1-D example, the k -th iterate in (GD) can be recast as $u^{(k)} = (1 - \eta)^k u^{(0)}$. The constraint $|1 - \eta| < 1$ for stability is immediate.

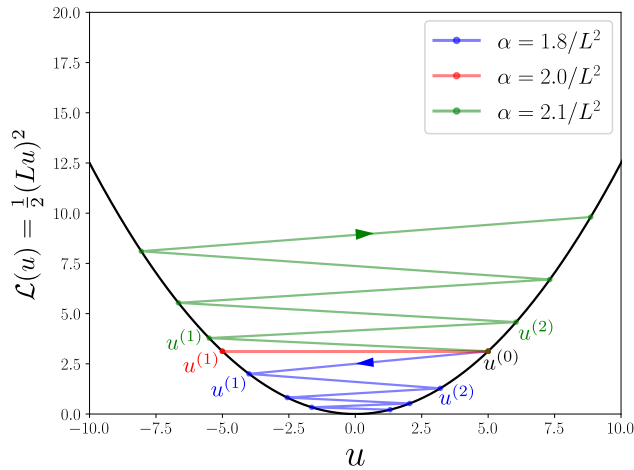


Fig. 5.6 Geometrical intuition of the fixed stepsize GD method applied to a 1-D example. With slope $L = 0.5$ and an initialization $u^{(0)} = 5$, the stepsizes $\alpha \in \{\frac{1.8}{L^2}, \frac{2}{L^2}, \frac{2.1}{L^2}\}$, respectively converge to the global minimum, oscillate, and diverge to infinity.

5 | Diffraction Through Inhomogeneous Media

Remark 5.4. The Neumann series can also be interpreted as a Picard iteration [BD17, Th. 2.8.1]. Indeed, the Picard operator P is simply defined as computing the right term of the discrete Lippmann-Schwinger equation (LSd) as

$$P(\mathbf{v}) := \mathbf{u}_i + A\mathbf{v}.$$

Applying j times P to \mathbf{u}_i corresponds to the $j+1$ first terms of the Neumann series. For $\mathbf{u}^{(0)} = \mathbf{0}$, one has $\mathbf{u}^{(1)} := P(\mathbf{u}^{(0)}) = \mathbf{u}_i$, $\mathbf{u}^{(2)} := P(\mathbf{u}^{(1)}) = \mathbf{u}_i + A\mathbf{u}_i$ and, for $j \geq 0$,

$$\mathbf{u}^{(j+1)} := P(\mathbf{u}^{(j)}) = P^{(j+1)}(\mathbf{0}) = \sum_{k=0}^j A^k \mathbf{u}_i.$$

Interestingly, the Neumann series converges to \mathbf{u} iff \mathbf{u} is a fixed point of P .

Remark 5.5. The approximation error of (FBd) directly depends the contrast of the RI object. Indeed, if $\|A\| < 1$, (Neumann) gives

$$\mathbf{u} = \mathbf{u}_i + \mathbf{G}\mathbf{D}_f\mathbf{u}_i + \underbrace{\sum_{k=2}^{\infty} A^k \mathbf{u}_i}_{e}.$$

An upper bound on the error committed by (FBd) can be obtained as

$$\begin{aligned} \|e\| &= \left\| \sum_{k=2}^{\infty} A^k \mathbf{u}_i \right\| \leq \sum_{k=2}^{\infty} \|A^k \mathbf{u}_i\| \leq \sum_{k=2}^{\infty} \|A\|^k \|\mathbf{u}_i\| \\ &\leq \sum_{k=2}^{\infty} (\|\mathbf{G}\| \|\mathbf{D}_f\|)^k \|\mathbf{u}_i\| \leq \sum_{k=2}^{\infty} (\|g\|_{\infty} \|f\|_{\infty})^k \|\mathbf{u}_i\| \\ &\leq \frac{\|g\|_{\infty}^2 \|f\|_{\infty}^2}{1 - \|g\|_{\infty} \|f\|_{\infty}} \|\mathbf{u}_i\|, \end{aligned}$$

where $\|f\|_{\infty}$ is the contrast value. This result is a discrete equivalent of the results given in [Buc+01].

5.4.2 Convergence Rate

The well-documented link between the convergence rate and the conditioning of the forward operator is explained in the context of the discrete Lippmann-Schwinger equation (LSd). We provide numerical evidence that the conditioning of the operator L is worsened for increasing

contrast values.

Using (GD) to solve the linear system (5.41), let us analyze the evolution of the loss function value $\mathcal{L}(\mathbf{u}^{(k)}) = \frac{1}{2} \|\mathbf{L}\mathbf{u}^{(k)} - \mathbf{u}_i\|_2^2$ at iteration k . The results that will be obtained below are known results for the gradient method on *strongly convex* functions [Nes18, Sec. 2.1-2.2], [Bec17]. Let us define governing parameters for the analysis of convergence.

Definition 5.4.1 (Parameters in optimization theory). *In the context of the minimization of strongly convex functions, the convergence rate is defined as*

$$c := \left(\frac{\gamma - 1}{\gamma + 1} \right)^2 = \left(\frac{m - L}{m + L} \right)^2, \quad (5.47)$$

where $\gamma := \frac{m}{L}$, $m = \sigma_r(\mathbf{L})^2$ is the strong convexity coefficient with r being the rank of \mathbf{L} , and $L = \sigma_1(\mathbf{L})^2 := \|\mathbf{L}\|^2$ is the Lipschitz constant of $\nabla \mathcal{L}$. $\sigma_1(\mathbf{L})$ and $\sigma_r(\mathbf{L})$ are respectively the first and r -th singular values of the operator \mathbf{L} .

The literature shows that the distance to the optimum \mathbf{u}^* writes

$$\|\mathbf{u}^{(k)} - \mathbf{u}^*\|_2^2 \leq c^k \|\mathbf{u}^{(0)} - \mathbf{u}^*\|_2^2, \quad (5.48)$$

and the upper bound on the function value is

$$\mathcal{L}(\mathbf{u}^{(k)}) - \mathcal{L}(\mathbf{u}^*) \leq \frac{L}{2} \|\mathbf{u}^{(k)} - \mathbf{u}^*\|_2^2 \leq \frac{c^k L}{2} \|\mathbf{u}^{(0)} - \mathbf{u}^*\|_2^2. \quad (5.49)$$

The convergence rate stated here above is called *linear*. These known results will be demonstrated for our particular case. By remembering from (5.45) that $\mathbf{u}^{(k)} = \sum_{j=0}^{k-1} (\mathbf{I} - \alpha \mathbf{L}^* \mathbf{L})^j \alpha \mathbf{L}^* \mathbf{u}_i$, and writing the SVD $\mathbf{L} :=$

5 | Diffraction Through Inhomogeneous Media

$\mathbf{U}\Sigma\mathbf{V}^*$ with the properties $\mathbf{V}^*\mathbf{V} = \mathbf{I}_r$ and $\mathbf{U}^*\mathbf{U} = \mathbf{I}_r$, one gets

$$\begin{aligned}
\mathbf{L}\mathbf{u}^{(k)} &= \sum_{j=0}^{k-1} \mathbf{U}\Sigma\mathbf{V}^*(\mathbf{I}_n - \alpha\mathbf{V}\Sigma^2\mathbf{V}^*)(\mathbf{I}_n - \alpha\mathbf{L}^*\mathbf{L})^{j-1}\alpha\mathbf{L}^*\mathbf{u}_i \\
&= \sum_{j=0}^{k-1} \mathbf{U}\Sigma(\mathbf{I}_r - \alpha\Sigma^2)\mathbf{V}^*(\mathbf{I}_n - \alpha\mathbf{L}^*\mathbf{L})^{j-1}\alpha\mathbf{L}^*\mathbf{u}_i \\
&= \sum_{j=0}^{k-1} \mathbf{U}\Sigma(\mathbf{I}_r - \alpha\Sigma^2)^j\mathbf{V}^*\alpha\mathbf{L}^*\mathbf{u}_i \\
&= \mathbf{U}\Sigma \underbrace{\sum_{j=0}^{k-1} (\mathbf{I}_r - \alpha\Sigma^2)^j}_{(\alpha\Sigma^2)^{-1}(\mathbf{I}_r - (\mathbf{I}_r - \alpha\Sigma^2)^k)} \alpha\Sigma\mathbf{U}^*\mathbf{u}_i \\
&= \mathbf{U}\Sigma^{-1}(\mathbf{I}_r - (\mathbf{I}_r - \alpha\Sigma^2)^k)\Sigma\mathbf{U}^*\mathbf{u}_i \\
&= \mathbf{U}(\mathbf{I}_r - (\mathbf{I}_r - \alpha\Sigma^2)^k)\mathbf{U}^*\mathbf{u}_i.
\end{aligned} \tag{5.50}$$

Hence,

$$\begin{aligned}
\mathcal{L}(\mathbf{u}^{(k)}) &= \frac{1}{2} \left\| \underbrace{(\mathbf{U}\mathbf{U}^* - \mathbf{I}_n)\mathbf{u}_i}_{\perp \text{Im } \mathbf{U}} - \mathbf{U} \text{diag} \left(1 - \eta \left(\frac{\sigma_i}{\sigma_1} \right)^2 \right)^k \mathbf{U}^* \mathbf{u}_i \right\|_2^2 \\
&= \frac{1}{2} \|(\mathbf{U}\mathbf{U}^* - \mathbf{I}_n)\mathbf{u}_i\|_2^2 + \frac{1}{2} \left\| \mathbf{U} \text{diag} \left(1 - \eta \left(\frac{\sigma_i}{\sigma_1} \right)^2 \right)^k \mathbf{U}^* \mathbf{u}_i \right\|_2^2 \\
&= \frac{1}{2} \|(\mathbf{U}\mathbf{U}^* - \mathbf{I}_n)\mathbf{u}_i\|_2^2 + \frac{1}{2} \left\| \text{diag} \left(1 - \eta \left(\frac{\sigma_i}{\sigma_1} \right)^2 \right)^k \mathbf{U}^* \mathbf{u}_i \right\|_2^2 \\
&\leq \frac{1}{2} \|(\mathbf{U}\mathbf{U}^* - \mathbf{I}_n)\mathbf{u}_i\|_2^2 + \frac{1}{2} \max_{i \in \llbracket r \rrbracket} \left| 1 - \eta \left(\frac{\sigma_i}{\sigma_1} \right)^2 \right|^{2k} \|\mathbf{U}^* \mathbf{u}_i\|_2^2
\end{aligned} \tag{5.51}$$

The *stepsize factor* has been defined as $\eta := \alpha\|\mathbf{L}\|^2$. The third line is obtained from the second line by using the identity $\|\mathbf{U}\mathbf{M}\|_2^2 = \langle \mathbf{U}\mathbf{M}, \mathbf{U}\mathbf{M} \rangle = \langle \mathbf{U}^*\mathbf{U}\mathbf{M}, \mathbf{M} \rangle = \langle \mathbf{M}, \mathbf{M} \rangle = \|\mathbf{M}\|_2^2$. By convention in the SVD $\mathbf{L} = \mathbf{U}\Sigma\mathbf{V}^*$, one has $\|\mathbf{L}\| = \sigma_{\max} = \sigma_1$. By defining the optimal value of the loss function as $\mathcal{L}^* := \mathcal{L}(\mathbf{u}^*) = \frac{1}{2} \|(\mathbf{U}\mathbf{U}^* - \mathbf{I}_n)\mathbf{u}_i\|_2^2$, (5.51) can be rewritten as

$$\mathcal{L}(\mathbf{u}^{(k)}) - \mathcal{L}^* \leq \frac{1}{2} \max_{i \in \llbracket r \rrbracket} \left| 1 - \eta \left(\frac{\sigma_i}{\sigma_1} \right)^2 \right|^{2k} \|\mathbf{U}^* \mathbf{u}_i\|_2^2, \tag{5.52}$$

and identified with (5.49) by setting $c = \max_{i \in \llbracket r \rrbracket} \left| 1 - \eta \left(\frac{\sigma_i}{\sigma_1} \right)^2 \right|^2$, $\mathbf{u}^{(0)} = \mathbf{0}$, and $\|\mathbf{U}^* \mathbf{u}_i\|_2^2 \leq L \|\mathbf{u}^*\|_2^2$. \mathcal{L}^* is independent of k . Considering a **GD**

scheme with fixed stepsize $\alpha = \eta/L$, the choice of stepsize factor η that optimizes the convergence rate c must satisfy

$$\begin{aligned} \min_{\eta} \max_{i \in [r]} \left| 1 - \eta \left(\frac{\sigma_i}{\sigma_1} \right)^2 \right| &= \min_{\eta} \max \left(\max_{i \in [r]} 1 - \eta \left(\frac{\sigma_i}{\sigma_1} \right)^2, \max_{i \in [r]} \eta \left(\frac{\sigma_i}{\sigma_1} \right)^2 - 1 \right) \\ &= \min_{\eta} \max \left(1 - \eta \left(\frac{\sigma_r}{\sigma_1} \right)^2, \eta - 1 \right) \end{aligned}$$

which is reached when

$$\begin{aligned} 1 - \eta^* \left(\frac{\sigma_r}{\sigma_1} \right)^2 &= \eta^* - 1 \\ \Leftrightarrow \eta^* &= \frac{2}{1 + (\sigma_r/\sigma_1)^2}. \end{aligned} \tag{5.53}$$

This gives an optimal stepsize

$$\alpha^* = \frac{2}{\sigma_1^2 + \sigma_r^2} = \frac{2}{L + m}. \tag{5.54}$$

In particular, injecting the optimal stepsize factor choice of (5.53) into the convergence rate of (5.52) yields

$$\begin{aligned} \mathcal{L}(\mathbf{u}^{(k)}) - \mathcal{L}^* &\leq \frac{1}{2} |\eta^* - 1|^{2k} \|\mathbf{U}^* \mathbf{u}_i\|_2^2 \\ &= \frac{1}{2} \left| \frac{1 - (\sigma_r/\sigma_1)^2}{1 + (\sigma_r/\sigma_1)^2} \right|^{2k} \|\mathbf{U}^* \mathbf{u}_i\|_2^2 \\ &= \frac{1}{2} \left| \frac{\kappa^2 - 1}{\kappa^2 + 1} \right|^{2k} \|\mathbf{U}^* \mathbf{u}_i\|_2^2, \end{aligned} \tag{5.55}$$

meaning that the convergence rate of the GD method is slower when $\sigma_r \ll \sigma_1$. Their ratio is defined in Def. 5.4.2

Definition 5.4.2. The condition number is given as the ratio between the two extreme singular values of \mathbf{L} , i.e.,

$$\kappa(\mathbf{L}) := \frac{\sigma_1(\mathbf{L})}{\sigma_r(\mathbf{L})} > 1. \tag{5.56}$$

While the above derivations were specific to the GD method applied to the strongly convex function \mathcal{L} , in a broader context it is still known that decreasing $\kappa(\mathbf{L})$ speeds up the convergence of minimization algorithms [Wik]. A branch of the optimization literature is devoted to the study of techniques for reducing this condition number. This technique, called *preconditioning*, is discussed in Sec. 5.4.4.

5 | Diffraction Through Inhomogeneous Media

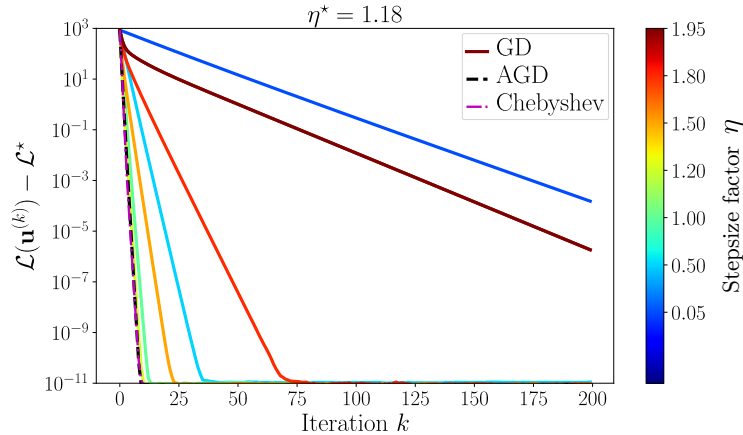


Fig. 5.7 Decay of the loss function \mathcal{L} over the iterations k and as a function of the stepsize factor η for a toy linear system $Lx = y$ with $L \in \mathbb{R}^{128 \times 128}$ of rank $r = 12$. In this experiment, the ideal choice following (5.53) was $\eta^* = 1.18$. Both the AGD and Chebyshev methods converge as fast as GD with the ideal stepsize η^* .

Let us start by confirming the convergence results and optimal stepsize derived in this section. To do so, Fig. 5.7 analyzes a toy square linear system $Lx = y$ with a randomly generated matrix $L \in \mathbb{R}^{128 \times 128}$ of rank $r = 12$. In order to obtain such L , a matrix A is first randomly generated with entries $A_{jk} \sim \mathcal{N}(0, 1)$, $\forall j, k \in \llbracket 128 \rrbracket$. Then, its SVD provides $A = U\Sigma V^*$. L is finally computed by keeping only the first r coefficients of Σ as $L := U\Sigma_r V^*$. In the experiment shown in Fig. 5.7, the knowledge of L allowed to estimate the optimal stepsize factor as $\eta^* = 1.18$. In this plot, the evolution of the loss function $\mathcal{L}(x^{(k)}) - \mathcal{L}^* = \frac{1}{2}\|Lx^{(k)} - y\|_2^2$ is shown with the y -axis in logscale.

The solid curves have been obtained by applying the **GD** method with a fixed stepsize $\alpha = \eta/\|L\|^2$, and for a set of stepsize factors $\eta \in \mathcal{S} := \{0.05, 0.5, 1.2, 1.5, 1.8, 1.95\}$. The curves nicely verify that the optimal convergence rate with **GD** is obtained for $\eta = 1.2 \in \mathcal{S}$. Then, the convergence of other choices for η depends on their distance to the optimal value η^* . For instance, the two extremes $\eta = 0.05$ and $\eta = 1.95$ exhibit the worst convergence rates.

In practice, the optimal stepsize factor η^* is unknown. If the forward operator $L \in \mathbb{R}^{N \times N}$ has a rank comparable to its dimension, *i.e.*, $r \lesssim N$, the smallest singular value σ_r is most likely negligible compared to σ_1 hence the optimal η^* tends towards 2. However, there exist several optimization techniques that improve upon the **GD** performances. In Fig. 5.7, we tested in dashed line the *Accelerated Gradient Descent* (AGD)

which is a GD algorithm with a momentum like the popular FISTA approach [BT09], and in dash-dot line the *Chebyshev* method [Man77]. It is observed that, even if η^* is unknown, both perform as good as the optimal **GD** version.

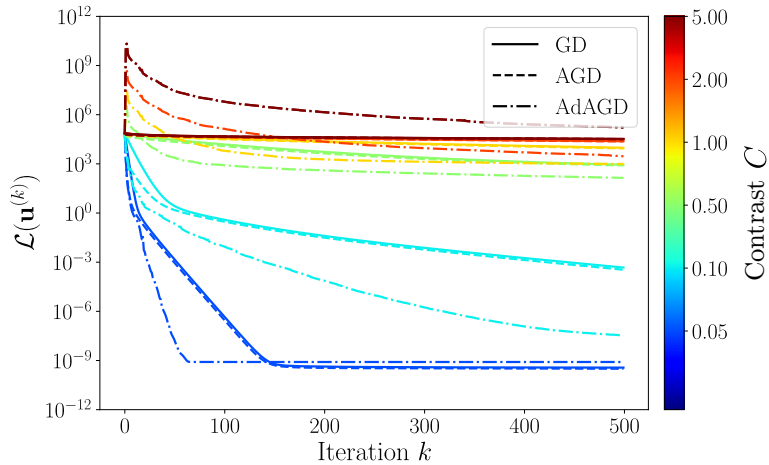


Fig. 5.8 Convergence of GD, AGD and AdAGD for solving (LSD).

Fig. 5.8 shows the evolution of the loss function $\mathcal{L}(\mathbf{u}^{(k)})$ for the GD, AGD [BT09], and *Adaptive AGD* (AdAGD) [MM20] methods for different contrast values C . As announced in (5.49) and demonstrated in (5.55), there is a *linear convergence rate*, i.e., an exponential decrease of the loss function \mathcal{L} with the iterations. For the minimization of a strongly convex function, accelerated gradient methods cannot beat the best convergence rate of the non-accelerated gradient method.

The convergence is slower for higher contrasts (remember Def. 5.2.2), which seems to indicate a higher condition number $\kappa(L)$. Unfortunately, there is no analytical solution to obtain the SVD of $L = \mathbf{I} - GD_f$ from the SVD of the circulant matrix $G = F^* \text{diag}(Fg)F$ (remember (5.37)) with $g \in \mathbb{C}^N$ the discretization of the Green function $g(r)$. However, for very small contrasts, $L \approx \mathbf{I}_n$ implies $\sigma_r \rightarrow \sigma_1 \Rightarrow \kappa \rightarrow 1$ and thus a faster convergence of the optimization methods. In practice, the smallest eigenvalue σ_r can be estimated with numerical methods, e.g., [MT20a, Sec. 6.4]. Preconditioning techniques aimed at reducing the condition number are discussed in Sec. 5.4.4.

5 | Diffraction Through Inhomogeneous Media

5.4.3 Estimating the Lipschitz Constant

The Lipschitz constant of the gradient of the loss function is equal to $L = \|L\|^2 = \|L^*L\| = \sigma_1(L^*L)$ ⁷. In order to estimate it, the *Power iteration method* [GV13] is applied to L^*L as

$$\tilde{v}_1^{(k+1)} = \frac{L^*L\tilde{v}_1^{(k)}}{\|L^*L\tilde{v}_1^{(k)}\|_2} \quad (5.57)$$

with $\tilde{v}_1^{(0)} \sim \mathcal{N}(\mathbf{0}, \sigma^2 \mathbf{I})$ then normalized to have a unit norm. It is clear from (5.57) that $\|\tilde{v}_1^{(k)}\|_2 = 1$. From (5.57), $\tilde{v}_1^{(k)}$ converges to the dominant eigenvector v_1 associated with the first eigenvalue σ_1 of L^*L at a rate $\left|\frac{\sigma_2}{\sigma_1}\right|^k$. One has

$$\begin{aligned} L^*L v_1 &= \sigma_1 v_1 \\ \Rightarrow v_1^* L^* L v_1 &= v_1^* \sigma_1 v_1 \\ \Rightarrow \|L v_1\|_2^2 &= \sigma_1 \|v_1\|_2^2 = \sigma_1. \end{aligned}$$

Thus, from $\tilde{v}_1^{(k)}$, the estimated dominant eigenvalue $\tilde{\sigma}_1$ can be obtained as $\tilde{\sigma}_1 = \|L\tilde{v}_1\|_2^2$ and the convergence rate of the estimate Lipschitz constant can be estimated as

$$\begin{aligned} |\tilde{\sigma}_1 - \sigma_1| &= |\|L\tilde{v}_1^{(k)}\|_2^2 - \|L v_1\|_2^2| \\ &\leq \|L(\tilde{v}_1^{(k)} - v_1)\|_2^2 \\ &\leq \|L\|^2 \|\tilde{v}_1^{(k)} - v_1\|_2^2 \\ &\leq \|L\|^2 \left|\frac{\sigma_2}{\sigma_1}\right|^k \|\tilde{v}_1^{(0)} - v_1\|_2^2 \\ &\leq \|L\|^2 \left|\frac{\sigma_2}{\sigma_1}\right|^k 4 \\ &\leq 4\|L\|^2, \end{aligned}$$

where the triangle inequality has been used for the two first line jumps, the convergence rate of the power method has been used for the fourth line, and $\|\tilde{v}_1^{(0)} - v_1\|_2 \leq 2$ as both are unitary. Equivalently, the estimate is bounded as $3/4\sigma_1 \leq \tilde{\sigma}_1 \leq 5/4\sigma_1$. As the chosen stepsize must satisfy $\alpha < \frac{2}{\sigma_1}$ to ensure stability, the worst-case situation is when the Lipschitz constant is underestimated, *i.e.*, when $\tilde{\sigma}_1 = 3/4\sigma_1$. With this worst-case

⁷This can be proven by the definition of the spectral norm and an SVD of L .

bound, the stepsize can be safely chosen as

$$\alpha < \frac{3}{2\tilde{\sigma}_1}. \quad (5.58)$$

Worth mentionning is the existence of the *Krylov subspace method* [MT20b] that improves on the power iteration method by considering linear combinations of the power method iterates to estimate the Lipschitz constant. There also exist *backtracking line search* methods that adaptively estimate the Lipschitz constant while solving the minimization problem [Nes13].

5.4.4 Preconditioning

Optimization alternatives aiming to increase the convergence rate of solving the LSd equation by preconditioning the GD method are discussed. It is shown they all follow the same target of approximating the inverse of the Hessian of the loss function, *i.e.*, $(L^* L)^{-1}$ without inverting operation.

With the quadratic loss function $\mathcal{L}(\mathbf{u}) = \frac{1}{2} \|L\mathbf{u} - \mathbf{u}_i\|_2^2$, the third-order derivatives are zero, hence the Taylor series expansion of the loss function at optimum writes exactly as

$$\mathcal{L}(\mathbf{u}^*) = \mathcal{L}(\mathbf{u}^{(k)}) + \nabla \mathcal{L}(\mathbf{u}^{(k)})(\mathbf{u}^* - \mathbf{u}^{(k)}) + \frac{1}{2} (\mathbf{u}^* - \mathbf{u}^{(k)})^* \nabla^2 \mathcal{L}(\mathbf{u}^{(k)}) (\mathbf{u}^* - \mathbf{u}^{(k)}). \quad (5.59)$$

The optimal value is defined so as to minimize the error in (5.59) in function of $\mathbf{u}^* - \mathbf{u}^{(k)}$. It is obtained as

$$\begin{aligned} \mathbf{u}^* &= \mathbf{u}^{(k)} - (\nabla^2 \mathcal{L}(\mathbf{u}^{(k)}))^{-1} \nabla \mathcal{L}(\mathbf{u}^{(k)}) \\ &= \mathbf{u}^{(k)} - (L^* L)^{-1} L^* (L\mathbf{u}^{(k)} - \mathbf{u}_i) \\ &= (L^* L)^{-1} L^* \mathbf{u}_i. \end{aligned} \quad (\text{Newton})$$

Eq. (Newton) can be seen as an iterative method that converges in one shot. The final result in (Newton) is obviously the pseudo-inverse solution written in (5.44), showing that the GD is trying to approximate the solution by completely removing the inverse Hessian $(L^* L)^{-1}$ and iterating with a fixed stepsize α instead. For any function, applying (Newton) is known as the *Newton method*. In general, optimization methods that involve the hessian $\nabla^2 \mathcal{L}(\mathbf{u}^{(k)})$ are called *second-order methods* [NW06].

The problem with the Newton method in this context is that it requires the inverse $(L^* L)^{-1}$ which is computationally expensive to

5 | Diffraction Through Inhomogeneous Media

obtain. *Quasi-Newton* methods try to precondition the descent direction with a *préconditionneur* P that uses only evaluations of the gradient $\nabla \mathcal{L}(\mathbf{u}^{(k)})$ (in this case, simply L and L^*), BFGS [NW06] is a popular example of such. In the [Newton](#) method viewpoint, the preconditioning can be seen as

$$\mathbf{u}^* = \mathbf{u}^{(k)} - PL^*(L\mathbf{u}^{(k)} - \mathbf{u}_i).$$

In the viewpoint of the linear system (5.41), the (invertible) preconditioner, noted Q , is inserted as

$$QL\mathbf{u} = Q\mathbf{u}_i. \quad (5.60)$$

The idea of (5.60) consists in choosing Q such that QL is sparse and easy to invert [Yin15; CMS23; LY18]. So that,

$$\mathbf{u} = (QL)^{-1}Q\mathbf{u}_i.$$

Despite their clear interest, the numerical implementation of these preconditioning methods is left for future work. This means that the numerical results presented in Chap. 6 are all obtained with the [GD](#) method (and accelerated variants) and the Lipschitz constant estimation method explained in Sec. 5.4.3.

5.5 Discussion

What has been done

This chapter proposed a comprehensive review of a discrete method for modeling the diffraction of electromagnetic waves through an inhomogeneous medium. Starting from the foundational assumptions that lead from Maxwell's equations to the inhomogeneous Helmholtz equation, the continuous Lippmann-Schwinger equation was first obtained by isolating the scattering potential in the model. The different approximations to this model were explained and discussed. Then, an efficient discretization method was presented. Finally, first-order optimization methods were used to solve the subsequent square linear system to compute the diffracted field from the knowledge of the incident illumination and the diffracting RI distribution in the discrete Lippmann-Schwinger equation.

Limits and Open Questions

For the sake of simplicity, this chapter has covered the **scalar** theory of diffraction, ignoring polarization effects, and also ignoring the possible anisotropy of the dielectric permittivity of the medium. An interesting direction would be to extend this framework to **vectorial 3-D diffractive imaging** [Ma+18, App. A]. More generally, the gradual removal of the simplifying assumptions behind the **Wave** equation, and shown in Sec. 5.2.1, to develop a very general numerical model of electromagnetic diffraction is an attractive goal.

Among the mathematical objects that will be introduced in Chap. 6 are the *Implicit Neural Representations* (INR). Such deep neural network architectures can be trained to satisfy known partial differential equations like the (**Wave**) equation. In such situation, they are usually called *Physics-Informed Neural Networks* (PINN). A clear advantage of PINN is their ability to provide a continuous representation of the object of interest. An open question is to determine **how PINNs compare to the various discrete models** covered in this chapter.

In the aim to improve the convergence rate of first-order optimization method to invert the discrete LS equation, future works will **implement the preconditioning** techniques raised in Sec. 5.4.4 accompanied with comparative numerical experiments. The limitations highlighted in this chapter were mainly in the speed of the system solving rather

5 | Diffraction Through Inhomogeneous Media

than in truly physical limitations. We look forward for a **deeper study of the physical mechanisms** occurring for very high contrast values, *i.e.*, high variation of dielectric permittivity, and breaking the validity of our assumptions.

5.6 Appendix

In this appendix, we detail a few other approximations to the LS model than the First-Born approximation.

5.6.1 Other Approximations to LS

Rytov Approximation

The following derivations are inspired by [MSG16]. In order to derive the Rytov approximation, the variables φ and φ_i are introduced *s.t.*

$$\begin{aligned} U(\mathbf{r}) &:= e^{\varphi(\mathbf{r})} \\ U_i(\mathbf{r}) &:= e^{\varphi_i(\mathbf{r})} \\ \varphi(\mathbf{r}) &:= \varphi_i(\mathbf{r}) + \varphi_s(\mathbf{r}). \end{aligned} \quad (5.61)$$

Note that U_s is now computed as

$$U_s(\mathbf{r}) = U(\mathbf{r}) - U_i(\mathbf{r}) = e^{\varphi_i(\mathbf{r})}[e^{\varphi_s(\mathbf{r})} - 1]. \quad (5.62)$$

The goal is to obtain a differential equation as a function of the phase $\varphi_s(\mathbf{r})$ only. First, (5.23) and (5.24) can be recast as

$$\begin{aligned} (\nabla^2 + k_m^2)e^{\varphi_i(\mathbf{r})} &= 0 \\ (\nabla^2 + k_m^2)e^{\varphi_s(\mathbf{r})} &= (\nabla^2 + k_m^2)e^{\varphi(\mathbf{r})} = -f(\mathbf{r})e^{\varphi(\mathbf{r})} \end{aligned}$$

Identity 5.4 can be used to transform the Laplacian in both equations and to yield

$$\nabla^2\varphi_i(\mathbf{r}) + \|\nabla\varphi_i\|_2^2 + k_m^2 = 0 \quad (5.63)$$

$$\nabla^2\varphi(\mathbf{r}) + \|\nabla\varphi\|_2^2 + k_m^2 = -f(\mathbf{r}). \quad (5.64)$$

Inserting (5.61) into (5.64) and also exploiting (5.63) gives

$$\nabla^2\varphi_s(\mathbf{r}) + 2\nabla\varphi_s(\mathbf{r}) \cdot \nabla\varphi_i(\mathbf{r}) + \|\nabla\varphi_s(\mathbf{r})\|_2^2 = -f(\mathbf{r}). \quad (5.65)$$

To simplify (5.65), we make the observation that

$$\nabla^2\varphi_s(\mathbf{r})U_i(\mathbf{r}) + 2\nabla\varphi_s(\mathbf{r}) \cdot \nabla\varphi_i(\mathbf{r})U_i(\mathbf{r}) = (\nabla^2 + k_m^2)U_i(\mathbf{r})\varphi_s(\mathbf{r}). \quad (5.66)$$

This is indeed verified with

$$\begin{aligned} \nabla^2(U_i(\mathbf{r})\varphi_s(\mathbf{r})) &= \nabla^2U_i(\mathbf{r})\varphi_s(\mathbf{r}) + 2\nabla U_i(\mathbf{r}) \cdot \nabla\varphi_s(\mathbf{r}) + U_i(\mathbf{r})\nabla^2\varphi_s(\mathbf{r}) \\ &= -k_m^2U_i(\mathbf{r})\varphi_s(\mathbf{r}) + 2U_i(\mathbf{r})\nabla\varphi_i(\mathbf{r}) \cdot \nabla\varphi_s(\mathbf{r}) + U_i(\mathbf{r})\nabla^2\varphi_s(\mathbf{r}). \end{aligned}$$

5 | Diffraction Through Inhomogeneous Media

Multiplying all terms in (5.65), we can substitute with (5.66) to obtain

$$(\nabla^2 + k_m^2)U_i(\mathbf{r})\varphi_s(\mathbf{r}) = -U_i(\mathbf{r})[\|\varphi_s(\mathbf{r})\|_2^2 + f(\mathbf{r})]. \quad (5.67)$$

The *Rytov approximation* consists in assuming that the phase gradient of the scattered field is small compared to the scattering potential. In other words, $\|\nabla\varphi_s(\mathbf{r})\|_2^2 \ll |f(\mathbf{r})|$. Re-leveraging the Green function G , this local equation (5.67) can be integrated in Ω as

$$\begin{aligned} \int_{\Omega} (\nabla^2 + k_m^2)U_i(\mathbf{r}')\varphi_s(\mathbf{r}')G(\mathbf{r} - \mathbf{r}')d\mathbf{r}' &= \int_{\Omega} -U_i(\mathbf{r}')f(\mathbf{r}')G(\mathbf{r} - \mathbf{r}')d\mathbf{r}' \\ &- \int_{\Omega} U_i(\mathbf{r})\varphi_s(\mathbf{r})\delta(\mathbf{r} - \mathbf{r}')d\mathbf{r}' = - \int_{\Omega} U_i(\mathbf{r}')f(\mathbf{r}')G(\mathbf{r} - \mathbf{r}')d\mathbf{r}', \end{aligned}$$

to finally give

$$\varphi_s(\mathbf{r}) = \frac{\int_{\Omega} f(\mathbf{r}')U_i(\mathbf{r}')G(\mathbf{r} - \mathbf{r}')d\mathbf{r}'}{U_i(\mathbf{r})}. \quad (\text{Rytov})$$

Comparing (Rytov) with (First-Born), it appears that the scattered field of the Rytov approximation $U_R(\mathbf{r})$ can be computed from the scattered field of the First-Born approximation $U_B(\mathbf{r}) := U_1(\mathbf{r}) - U_i(\mathbf{r})$ and vice-versa by using (5.62). It writes

$$U_R(\mathbf{r}) = U_i(\mathbf{r}) \left[\exp \left(\frac{U_B(\mathbf{r})}{U_i(\mathbf{r})} \right) - 1 \right]. \quad (5.68)$$

The *Rytov approximation* is known to represent a better approximation than First-Born [MSG16], and it is obtained as easily as the First-Born approximation thanks to (5.68). In contrast to First-Born, where the total phase change $\varphi(\mathbf{r})$ must be smaller than 2π , Rytov only requires that the phase change induced along a path is smaller than the variation of refractive index along this path scaled by the used wavelength λ [kak0101]. This condition remains valid for thicker samples than First-Born.

Beam Propagation Method

The *Beam Propagation Method* (BPM) [Kam+16b; Pha+18] obtains the wavefield in space $U(\mathbf{r})$ by alternating evaluation of diffraction and refraction steps. By decomposing U into a complex envelope a and a carrier paraxial planewave as $U(\mathbf{r}) := a(\mathbf{r})e^{ik_m z}$, the *Helmholtz* equation can be particularized to $a(\mathbf{r})$ [Kam+16b, App. A]. After a *slowly varying*

Appendix | 5.6

envelope approximation $\left| \frac{\partial^2 a}{\partial z^2} \right| \ll |k_m \frac{\partial a}{\partial z}|$, and a small perturbation approximation $(\Delta n(\mathbf{r}))^2 \ll 1$ with the variation in RI $\Delta n(\mathbf{r}) := n(\mathbf{r}) - n_m$, this gives the *paraxial Helmholtz equation*

$$\frac{\partial}{\partial z} a(\mathbf{r}) = \left(\frac{i}{2k_m} \nabla_{\perp}^2 + ik_m \Delta n(\mathbf{r}) \right) a(\mathbf{r}), \quad (5.69)$$

with $\nabla_{\perp}^2 := \frac{\partial^2}{\partial x^2} + \frac{\partial^2}{\partial y^2}$. On the right hand side of (5.69), the first term relates to a free-space propagation of the envelope a , and the second term relates to the application of a phase screen. The resulting discrete model is an iterative method writing as

$$a(\mathbf{x}, z + \Delta z) = e^{ik\Delta n(\mathbf{r})\Delta z} \mathcal{F}_2^{-1} \{ \mathcal{F}_2 \{ a(\cdot, z) \} K \} \quad (\text{BPM})$$

with a distance $\Delta z := L_z / N_z$ between consecutive phase screens and the paraxial free-space propagation kernel $K(\omega) := \exp \left(\frac{-i\|\omega\|^2 \Delta z}{k_m + \sqrt{k_m^2 - \|\omega\|^2}} \right)$. The initial condition in (BPM) is $a(\mathbf{x}, 0) := U_i(\mathbf{x}, 0)$. The Beam Propagation Method is also known as *Phase Screen Method* for atmospheric turbulence modeling [Fla94].

Wave Propagation Method

There also exists the *Multi-Slice Wave Propagation Method* (WPM) which divides the RI volume into slices of thickness Δz and propagates the light field slice-by-slice [MXP17]. The main difference with BPM is that it does not make the paraxial approximation. The total field is computed iteratively as

$$U(\mathbf{x}, z + \Delta z) = \mathcal{F}_2^{-1} \{ \mathcal{F}_2 \{ U(\cdot, z) \} H(\mathbf{r}, \cdot) \} \quad (\text{WPM})$$

with the *Angular Spectrum* propagation kernel $H(\mathbf{r}, \omega) := \exp(i\Delta z \sqrt{k^2 n^2(\mathbf{r}) \|\omega\|^2})$ which contains the RI information at the slice of depth z .

Split-Step Non Paraxial Method

The *Split-Step Non Paraxial* (SSNP) method computes the total field slice-by-slice like BPM and WPM. In SSNP, the *Helmholtz* equation is recast as an augmented first-order differential equation as

$$\partial_z \Phi(\mathbf{r}) = H(\mathbf{r}) \Phi(\mathbf{r}), \quad (5.70)$$

5 | Diffraction Through Inhomogeneous Media

where

$$\Phi(\mathbf{r}) = \begin{bmatrix} U(\mathbf{r}) \\ \partial_z U(\mathbf{r}) \end{bmatrix}, \quad \mathbf{H}(\mathbf{r}) = \begin{bmatrix} 0 & 1 \\ -\nabla_{\perp}^2 - k^2 n^2(\mathbf{r}) & 0 \end{bmatrix}.$$

The SSNP operator is decoupled as $\mathbf{H}(\mathbf{r}) = \mathbf{H}_1 + \mathbf{H}_2(\mathbf{r})$, with (i) the diffraction operator \mathbf{H}_1 describing the diffraction in the homogeneous background medium, and (ii) the scattering operator $\mathbf{H}_2(\mathbf{r})$ based on the distribution of the scattering potential. They write as

$$\mathbf{H}_1 = \begin{bmatrix} 0 & 1 \\ -\nabla_{\perp}^2 - k^2 n_m^2 & 0 \end{bmatrix}, \quad \mathbf{H}_2(\mathbf{r}) = \begin{bmatrix} 0 & 0 \\ k^2(n_m^2 - n^2(\mathbf{r})) & 0 \end{bmatrix}.$$

Like for BPM and WPM, the sample volume is discretized into a series of z -slices. In order to compute the field propagating a small distance Δz between two adjacent slices, (5.70) is approximated as a first-order homogeneous linear system of differential equations with constant coefficients. Separating the 3-D components as $\mathbf{r} := (\mathbf{x}, z)$, the solution is approximated as

$$\Phi(\mathbf{x}, z + \Delta z) \approx \exp(\mathbf{H}(\mathbf{x}, z)\Delta z)\Phi(\mathbf{x}, z) \approx \mathbf{P}\mathbf{Q}(\mathbf{x}, z)\Phi(\mathbf{x}, z) \quad (\text{SSNP})$$

where $\Phi(\mathbf{x}, z)$ represents the 2D field at the axial position z , and

$$\mathbf{P} = \exp(\mathbf{H}_1\Delta z), \quad \mathbf{Q}(\mathbf{x}, z) = \exp(\mathbf{H}_2(\mathbf{x}, z)\Delta z).$$

Eq. (SSNP) is an approximation in the sense that we assume that $\Phi(\mathbf{r})$ and $\mathbf{H}(\mathbf{r})$ are constant in the interval $[z, z + \Delta z]$. Moreover, since \mathbf{H}_1 and $\mathbf{H}_2(\mathbf{r})$ do not commute, the decoupling only holds approximately when Δz is small, *i.e.*,

$$\exp(\mathbf{H}(\mathbf{x}, z)\Delta z) = \exp(\mathbf{H}_1\Delta z)\exp(\mathbf{H}_2(\mathbf{x}, z)\Delta z) + \mathcal{O}([\mathbf{H}_1, \mathbf{H}_2(\mathbf{x}, z)](\Delta z)^2).$$

5.6.2 Proof of the Fourier Diffraction Theorem

This section provides a simple proof of Th. 5.1.

Proof. Inserting the expression of the incident planewave $U_i(\mathbf{r}; \mathbf{k}_i) = e^{-ik_i^\top \mathbf{r}}$ as well as the expression of the Green function G defined in (5.25) into the scattered component $U_1^s(\mathbf{r}; \mathbf{k}_i)$ of (First-Born) yields

$$U_1^s(\mathbf{r}; \mathbf{k}_i) = \int_{\Omega} f(\mathbf{r}') \frac{e^{ik_m |\mathbf{r} - \mathbf{r}'|}}{4\pi |\mathbf{r} - \mathbf{r}'|} e^{-ik_i^\top \mathbf{r}'} d\mathbf{r}'. \quad (5.71)$$

Appendix | 5.6

First, the 3-D components are separated as $\mathbf{r} := (\mathbf{x}, z)$, $\mathbf{r}' := (\mathbf{x}', z')$, and $\mathbf{k}_i := (\boldsymbol{\omega}_i, \eta(\boldsymbol{\omega}_i))$ with

$$\eta(\boldsymbol{\omega}) := \sqrt{k_m^2 - \|\boldsymbol{\omega}\|_2^2}, \quad (5.72)$$

By separating the coordinates into XY and Z components, extending the integration over \mathbb{R}^3 without consequence, and considering the *Weyl decomposition* [Bor+99] of the Green function into a superposition of planewaves (highlighted in green), (5.71) modifies as

$$U_1^s(\mathbf{r}; \mathbf{k}_i) = \int_{\mathbb{R}^2} \int_{\mathbb{R}} f(\mathbf{x}', z') e^{-i\boldsymbol{\omega}_i^\top \mathbf{x}'} e^{-i\eta(\boldsymbol{\omega}_i)z'} \frac{i}{8\pi^2} \int_{\mathbb{R}^2} e^{i\boldsymbol{\omega}^\top (\mathbf{x}-\mathbf{x}')} \frac{e^{-i\eta(\boldsymbol{\omega})|z-z'|}}{\eta(\boldsymbol{\omega})} \textcolor{green}{d\boldsymbol{\omega}} d\mathbf{x}' dz'. \quad (5.73)$$

Many Fourier transforms in (5.73) are progressively explicited as

$$\begin{aligned} U_1^s(\mathbf{r}; \mathbf{k}_i) &= \frac{i}{4\pi} \int_{\mathbb{R}^2} \int_{\mathbb{R}} \frac{1}{2\pi} \int_{\mathbb{R}^2} f(\mathbf{x}', z') e^{-i\boldsymbol{\omega}_i^\top \mathbf{x}'} e^{i\boldsymbol{\omega}^\top (\mathbf{x}-\mathbf{x}')} d\mathbf{x}' e^{-i\eta(\boldsymbol{\omega}_i)z'} \frac{e^{-i\eta(\boldsymbol{\omega})|z-z'|}}{\eta(\boldsymbol{\omega})} dz' d\boldsymbol{\omega} \\ &= \frac{i}{2\sqrt{\pi}} \int_{\mathbb{R}^2} \frac{1}{\sqrt{2\pi}} \int_{\mathbb{R}} \mathcal{F}_2\{f(\cdot, z')\}[\boldsymbol{\omega} + \boldsymbol{\omega}_i] e^{-i\eta(\boldsymbol{\omega}_i)z'} \frac{e^{-i\eta(\boldsymbol{\omega})|z-z'|}}{\eta(\boldsymbol{\omega})} e^{i\boldsymbol{\omega}^\top \mathbf{x}} dz' d\boldsymbol{\omega} \\ &= \frac{i}{2\sqrt{\pi}} \int_{\mathbb{R}^2} \frac{e^{i\eta(\boldsymbol{\omega})z}}{\eta(\boldsymbol{\omega})} \hat{f}(\boldsymbol{\omega} + \boldsymbol{\omega}_i, \eta(\boldsymbol{\omega}_i) - \eta(\boldsymbol{\omega})) e^{i\boldsymbol{\omega}^\top \mathbf{x}} d\boldsymbol{\omega}, \end{aligned} \quad (5.74)$$

with $\hat{f} := \mathcal{F}_3 f$ and where we particularized to *transmission imaging* (i.e., $z > 0 > z'$) to get the last line. Passing the 2-D Fourier transform on the left side of the equality by multiplying both sides by $\frac{1}{2\pi} \int_{\mathbb{R}^2} e^{-i\tilde{\boldsymbol{\omega}}^\top \mathbf{x}} d\mathbf{x}$ gives the *Fourier diffraction theorem*, which concludes the proof. \square

5.6.3 Proof of Claim 5.2

Proof. (\Leftarrow) Given $\alpha > 0$, for all $\mathbf{u} := \alpha \mathbf{L}^* \mathbf{u}_i \notin \ker \mathbf{L}$ we have

$$|\mathbf{u}^* (\mathbf{I} - \alpha \mathbf{L}^* \mathbf{L}) \mathbf{u}| = \|\mathbf{u}\|^2 \left| 1 - \alpha \frac{\|\mathbf{L}\mathbf{u}\|^2}{\|\mathbf{u}\|^2} \right|. \quad (5.75)$$

If $\alpha \|\mathbf{L}\|^2 < 2$, then, by definition of the operator norm, $\alpha \frac{\|\mathbf{L}\mathbf{u}\|^2}{\|\mathbf{u}\|^2} < 2$, hence

$$1 - \alpha \frac{\|\mathbf{L}\mathbf{u}\|^2}{\|\mathbf{u}\|^2} > -1. \quad (5.76)$$

Furthermore, $\mathbf{u} \notin \ker \mathbf{L} \Rightarrow \|\mathbf{L}\mathbf{u}\| \neq 0$. Hence

$$\alpha \frac{\|\mathbf{L}\mathbf{u}\|^2}{\|\mathbf{u}\|^2} > 0 \Rightarrow 1 - \alpha \frac{\|\mathbf{L}\mathbf{u}\|^2}{\|\mathbf{u}\|^2} < 1. \quad (5.77)$$

5 | Diffraction Through Inhomogeneous Media

Combining (5.76) and (5.77) gives

$$\left| 1 - \alpha \frac{\|\mathbf{L}\mathbf{u}\|^2}{\|\mathbf{u}\|^2} \right| < 1,$$

which, when inserted into (5.75), shows that

$$\|\mathbf{I} - \alpha \mathbf{L}^* \mathbf{L}\| := \sup_{\mathbf{u}} \frac{|\mathbf{u}^* (\mathbf{I} - \alpha \mathbf{L}^* \mathbf{L}) \mathbf{u}|}{\|\mathbf{u}\|^2} < 1.$$

□

Proof. (\Rightarrow)

$$\|\mathbf{I} - \alpha \mathbf{L}^* \mathbf{L}\| = \sup_{\mathbf{u}} \left| 1 - \alpha \frac{\|\mathbf{L}\mathbf{u}\|^2}{\|\mathbf{u}\|^2} \right| < 1$$

Breaking the absolute value yields two inequality conditions

$$\sup_{\mathbf{u}} 1 - \alpha \frac{\|\mathbf{L}\mathbf{u}\|^2}{\|\mathbf{u}\|^2} < 1, \quad \text{and} \quad \inf_{\mathbf{u}} 1 - \alpha \frac{\|\mathbf{L}\mathbf{u}\|^2}{\|\mathbf{u}\|^2} > -1. \quad (5.78)$$

Focusing on the right part of (5.78), one has

$$\sup_{\mathbf{u}} \alpha \frac{\|\mathbf{L}\mathbf{u}\|^2}{\|\mathbf{u}\|^2} = \alpha \|\mathbf{L}\|^2 < 2$$

which concludes the proof. □

References

- [BD17] W. E. Boyce and R. C. DiPrima. *Elementary Differential Equations and Boundary Value Problems, Textbook and Student Solutions Manual Set.* 11th. John Wiley & Sons, 2017. ISBN: 9781119443766.
- [Bec17] A. Beck. *First-Order Methods in Optimization*. Philadelphia, PA, USA: SIAM-Society for Industrial and Applied Mathematics, 2017. ISBN: 1611974984.
- [Bor+99] M. Born et al. *Principles of Optics: Electromagnetic Theory of Propagation, Interference and Diffraction of Light*. 7th ed. Cambridge University Press, 1999. DOI: [10.1017/CBO9781139644181](https://doi.org/10.1017/CBO9781139644181).
- [BT09] A. Beck and M. Teboulle. “A Fast Iterative Shrinkage-Thresholding Algorithm for Linear Inverse Problems”. In: *SIAM Journal on Imaging Sciences* 2.1 (2009), pp. 183–202.
- [Buc+01] O. M. Bucci et al. “Degree of nonlinearity and a new solution procedure in scalar two-dimensional inverse scattering problems”. In: *J. Opt. Soc. Am. A* 18.8 (Aug. 2001), pp. 1832–1843. DOI: [10.1364/JOSAA.18.001832](https://doi.org/10.1364/JOSAA.18.001832).
- [Cha22] P. C. Chaumet. “The Discrete Dipole Approximation: A Review”. In: *Mathematics* 10.17 (2022). ISSN: 2227-7390. DOI: [10.3390/math10173049](https://doi.org/10.3390/math10173049).
- [CK13] D. Colton and R. Kress. *Inverse Acoustic and Electromagnetic Scattering Theory*. 3rd. Vol. 93. Applied Mathematical Sciences. Springer, 2013. ISBN: 978-1-4614-4941-6. DOI: [10.1007/978-1-4614-4942-3](https://doi.org/10.1007/978-1-4614-4942-3).
- [CMS23] P. C. Chaumet, G. Maire, and A. Sentenac. “Accelerating the discrete dipole approximation by initializing with a scalar solution and using a circulant preconditioning”. In: *Journal of Quantitative Spectroscopy and Radiative Transfer* 298 (2023), p. 108505. DOI: [10.1016/j.jqsrt.2023.108505](https://doi.org/10.1016/j.jqsrt.2023.108505).

5 | References

- [CS98] B. Chen and J. J. Stamnes. "Validity of diffraction tomography based on the first Born and the first Rytov approximations". In: *Appl. Opt.* 37.14 (May 1998), pp. 2996–3006. DOI: [10.1364/AO.37.002996](https://doi.org/10.1364/AO.37.002996).
- [DF94] B. T. Draine and P. J. Flatau. "Discrete-Dipole Approximation For Scattering Calculations". In: *Journal of the Optical Society of America A* 11.4 (Apr. 1994), pp. 1491–1499. DOI: [10.1364/JOSAA.11.001491](https://doi.org/10.1364/JOSAA.11.001491).
- [Fau+21] F. Faucher et al. "Diffraction Tomography, Fourier Reconstruction, and Full Waveform Inversion". 31 pages, 21 figures. Oct. 2021.
- [Fla94] S. M. Flatté. "Multiple phase-screen calculation of the temporal behavior of stochastic waves". In: *Waves in Random Media* 4.3 (1994), pp. 227–244.
- [GOW20] D. Gilton, G. Ongie, and R. Willett. "Neumann Networks for Linear Inverse Problems in Imaging". In: *IEEE Transactions on Computational Imaging* 6 (2020), pp. 328–343. DOI: [10.1109/TCI.2019.2948732](https://doi.org/10.1109/TCI.2019.2948732).
- [GV13] G. H. Golub and C. F. Van Loan. *Matrix Computations*. 4th. Johns Hopkins University Press, 2013.
- [Hua+14] L. Huang et al. "Breast ultrasound waveform tomography: Using both transmission and reflection data, and numerical virtual point sources". In: *Medical Imaging 2014: Ultrasonic Imaging and Tomography*. Vol. 9040. Spie. 2014, pp. 187–198.
- [Jac98] J. D. Jackson. *Classical Electrodynamics*. 3rd. John Wiley & Sons, 1998.
- [Kam+16a] U. S. Kamilov et al. "A Recursive Born Approach to Non-linear Inverse Scattering". In: *IEEE Signal Processing Letters* 23.8 (2016), pp. 1052–1056. ISSN: 10709908. DOI: [10.1109/LSP.2016.2579647](https://doi.org/10.1109/LSP.2016.2579647). arXiv: [1603.03768](https://arxiv.org/abs/1603.03768).
- [Kam+16b] U. S. Kamilov et al. "Optical Tomographic Image Reconstruction Based on Beam Propagation and Sparse Regularization". In: *IEEE Transactions on Computational Imaging* 2.1 (2016), pp. 59–70. DOI: [10.1109/TCI.2016.2519261](https://doi.org/10.1109/TCI.2016.2519261).
- [Kir+21] C. Kirisits et al. "Fourier reconstruction for diffraction tomography of an object rotated into arbitrary orientations". In: *Inverse Problems* 37.11 (Oct. 2021), p. 115002. DOI: [10.1088/1361-6420/ac2749](https://doi.org/10.1088/1361-6420/ac2749).

- [KS01] A. C. Kak and M. Slaney. *Principles of computerized tomographic imaging*. Reprint of 1988 IEEE Press edition. Bellingham, WA: Society of Photo-Optical Instrumentation Engineers (SPIE), 2001.
- [LH07] L. Liu and K. He. "Wave interferometry applied to bore-hole radar: Virtual multioffset reflection profiling". In: *IEEE transactions on geoscience and remote sensing* 45.8 (2007), pp. 2554–2559.
- [Lim+15] J. Lim et al. "Comparative study of iterative reconstruction algorithms for missing cone problems in optical diffraction tomography". In: *Opt. Express* 23.13 (June 2015), pp. 16933–16948. DOI: [10.1364/OE.23.016933](https://doi.org/10.1364/OE.23.016933).
- [Lin+18] R. Ling et al. "High-throughput intensity diffraction tomography with a computational microscope". In: *Biomed. Opt. Express* 9.5 (May 2018), pp. 2130–2141. DOI: [10.1364/BOE.9.002130](https://doi.org/10.1364/BOE.9.002130).
- [Liu+18] H.-Y. Liu et al. "SEAGLE: Sparsity-Driven Image Reconstruction Under Multiple Scattering". In: *IEEE Transactions on Computational Imaging* 4.1 (2018), pp. 73–86. DOI: [10.1109/TCI.2017.2764461](https://doi.org/10.1109/TCI.2017.2764461).
- [LY18] F. Liu and L. Ying. "Sparsify and Sweep: An Efficient Preconditioner for the Lippmann-Schwinger Equation". In: *SIAM Journal on Scientific Computing* 40.2 (2018), B379–B404. DOI: [10.1137/17M1132057](https://doi.org/10.1137/17M1132057).
- [Ma+18] Y. Ma et al. "Accelerated Image Reconstruction for Non-linear Diffractive Imaging". In: *2018 IEEE International Conference on Acoustics, Speech and Signal Processing (ICASSP)*. 2018, pp. 6473–6477. DOI: [10.1109/ICASSP.2018.8462400](https://doi.org/10.1109/ICASSP.2018.8462400).
- [Man77] T. A. Manteuffel. "The Tchebyshev iteration for non-symmetric linear systems". In: *Numerische Mathematik* 28 (1977), pp. 307–327.
- [MM20] Y. Malitsky and K. Mishchenko. "Adaptive Gradient Descent without Descent". In: *Proceedings of the 37th International Conference on Machine Learning*. Ed. by H. D. III and A. Singh. Vol. 119. Proceedings of Machine Learning Research. PMLR, July 2020, pp. 6702–6712.
- [MSG16] P. Müller, M. Schürmann, and J. Guck. *The Theory of Diffraction Tomography*. 2016. arXiv: [1507.00466 \[q-bio.QM\]](https://arxiv.org/abs/1507.00466).

5 | References

- [MT20a] P. G. Martinsson and J. A. Tropp. “Randomized numerical linear algebra: Foundations and algorithms”. In: *Acta Numerica* 29 (2020), pp. 403–572. ISSN: 14740508. DOI: [10.1017/S0962492920000021](https://doi.org/10.1017/S0962492920000021).
- [MT20b] P.-G. Martinsson and J. A. Tropp. “Randomized Numerical Linear Algebra: Foundations & Algorithms”. In: *arXiv preprint arXiv:2002.01387* (2020). Accessed: 2024-06-15.
- [MXP17] X. Ma, W. Xiao, and F. Pan. “Optical tomographic reconstruction based on multi-slice wave propagation method”. In: *Opt. Express* 25.19 (Sept. 2017), pp. 22595–22607. DOI: [10.1364/OE.25.022595](https://doi.org/10.1364/OE.25.022595).
- [Nes13] Y. Nesterov. “Gradient methods for minimizing composite functions”. In: *Mathematical programming* 140.1 (2013), pp. 125–161.
- [Nes18] Y. Nesterov. *Lectures on convex optimization*. Second. Louvain-la-Neuve: Springer Publishing Company, Incorporated, 2018. DOI: [10.1007/978-3-319-91578-4](https://doi.org/10.1007/978-3-319-91578-4).
- [NW06] J. Nocedal and S. Wright. *Numerical Optimization*. 2nd. Springer, 2006. ISBN: 978-0387303031.
- [Pas+19] A. Paszke et al. “PyTorch: An Imperative Style, High-Performance Deep Learning Library”. In: *Advances in Neural Information Processing Systems* 32. Ed. by H. Wallach et al. Curran Associates, Inc., 2019, pp. 8024–8035.
- [Pha+18] T.-a. Pham et al. “Phaseless diffraction tomography with regularized beam propagation”. In: Apr. 2018, pp. 1268–1271. DOI: [10.1109/ISBI.2018.8363802](https://doi.org/10.1109/ISBI.2018.8363802).
- [Pha+20] T.-a. Pham et al. “Three-Dimensional Optical Diffraction Tomography With Lippmann-Schwinger Model”. In: *IEEE Transactions on Computational Imaging* 6 (2020), pp. 727–738. DOI: [10.1109/TCI.2020.2969070](https://doi.org/10.1109/TCI.2020.2969070).
- [SA04] A. Sharma and A. Agrawal. “New method for nonparaxial beam propagation”. In: *J. Opt. Soc. Am. A* 21.6 (June 2004), pp. 1082–1087. DOI: [10.1364/JOSAA.21.001082](https://doi.org/10.1364/JOSAA.21.001082).
- [SPU17] E. Soubies, T.-A. Pham, and M. Unser. “Efficient inversion of multiple-scattering model for optical diffraction tomography”. In: *Opt. Express* 25.18 (Sept. 2017), pp. 21786–21800. DOI: [10.1364/OE.25.021786](https://doi.org/10.1364/OE.25.021786).

- [Str04] J. C. Strikwerda. *Finite Difference Schemes and Partial Differential Equations*. 2nd. Society for Industrial and Applied Mathematics. SIAM, 2004. ISBN: 9780898715675.
- [Tai94] C.-T. Tai. *Dyadic Green Functions in Electromagnetic Theory*. IEEE Press Series on Electromagnetic Waves, 1994.
- [VBW13] S. V. Venkatakrishnan, C. A. Bouman, and B. Wohlberg. “Plug-and-Play Priors for Model Based Reconstruction”. In: *Proceedings of IEEE Global Conference on Signal and Information Processing (GlobalSIP)*. Austin, TX, USA, Dec. 2013, pp. 945–948. DOI: [10.1109/GlobalSIP.2013.6737048](https://doi.org/10.1109/GlobalSIP.2013.6737048).
- [Wan+20] H. Wang et al. “Regularized elastic passive equivalent source inversion with full-waveform inversion: Application to a field monitoring microseismic data set”. In: *Geophysics* 85.6 (2020), KS207–KS219.
- [Wik] Wikipedia. *Condition number*.
- [Yin15] L. Ying. “Sparsifying Preconditioner for the Lippmann–Schwinger Equation”. In: *Multiscale Modeling & Simulation* 13.2 (2015), pp. 644–660. DOI: [10.1137/140985147](https://doi.org/10.1137/140985147).
- [ZWT22] J. Zhu, H. Wang, and L. Tian. “High-fidelity intensity diffraction tomography with a non-paraxial multiple-scattering model”. In: *Opt. Express* 30.18 (Aug. 2022), pp. 32808–32821. DOI: [10.1364/OE.469503](https://doi.org/10.1364/OE.469503).

6

Diffraction Tomography with Implicit Neural Representations

THREE-DIMENSIONAL *refractive index* distribution imaging by *diffraction tomography* is studied in this chapter. The nonlinear sensing model derived in Chap. 5, which uses the discrete *Lippmann-Schwinger* equation, is combined with an *Implicit Neural Representation* (INR)¹ in order to propose a recovery procedure that is *accurate, modular, and leverages automatic differentiation* for the iterative error minimization involved. The main achievement of this chapter is to discuss the pros and cons of the “INR + discrete nonlinear sensing model” combination through several numerical experiments.

The codes developed in the context of this chapter can be found at <https://github.com/olivierleblanc/cols>.

6.1 Introduction

The goal of this chapter is to understand Fig. 6.1. The real physics of diffraction tomography (upper left) is approximated by a *sensing model* (lower left) that uses the (LSD) model derived in Chap. 5. Multiple views of the field diffracted by the scattering potential volume are collected by consecutive rotations. The candidate discrete volume is generated by querying an INR on a regular grid. By associating a loss

¹A neural network architecture specifically designed for continuous object representation.

6 | Diffraction Tomography with Implicit Neural Representations

function—consisting of a data-fidelity term and a regularization of the volume—to the INR, its weights are updated iteratively via the popular Adam algorithm in the aim to minimize this loss function, and consequently to reconstruct a continuous representation of the RI distribution.

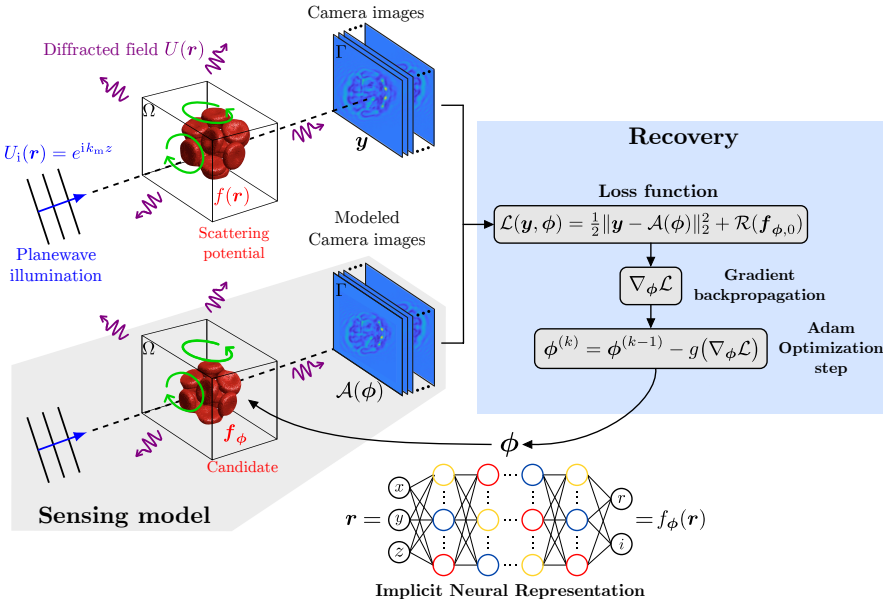


Fig. 6.1 Illustration of the diffraction tomography context. A planewave U_i illuminates a scattering potential f , and the diffracted field U is recorded by a camera. Multiple views are accumulated by rotating the object, yielding a measurement vector y . The volume is reconstructed through its continuous representation by an INR. A candidate discrete volume f_ϕ is generated from queries of the INR $f_\phi(r)$ at the locations of a 3-D regular grid G . Candidate camera measurements $\mathcal{A}(\phi)$ are computed from the (LSD) sensing model. The weights ϕ of the INR are updated iteratively to minimize a loss function \mathcal{L} . The Adam algorithm, used for the weights update by the means of a specific function g of the loss gradient $\nabla \mathcal{L}$, is described later in Algo. 6.2.

6.1.1 Motivation

Diffraction Tomography

Diffraction tomography is an advanced imaging technique used to reconstruct the internal structure of an object by analyzing how waves, such as X-rays, sound waves, or electromagnetic waves, scatter as they pass through it. Unlike conventional tomography [KS01], which assumes straight-line propagation of waves, diffraction tomography accounts for the wave-like nature of the signals, incorporating phenomena such as diffraction and interference. This method involves collect-

ing data from multiple angles and using mathematical algorithms to solve the inverse problem of reconstructing the object's properties. By leveraging the wave interactions with the internal features of the object, diffraction tomography provides higher resolution images and greater detail, making it particularly valuable in fields such as medical imaging, materials science, and nondestructive testing.

There are dozens of applications to diffraction tomography. In **medical imaging**, it is particularly useful in optical coherence tomography for detailed visualization of biological tissues, aiding in the diagnosis of retinal diseases and other conditions [Reb+15; Ela+18]. In **materials science**, diffraction tomography is employed to examine the internal structure of composite materials and detect defects or inhomogeneities at a microscopic level, ensuring material integrity and quality [MI07; MSW12]. Furthermore, in the field of **nondestructive testing**, it is used to inspect the internal features of critical components such as aerospace parts, identifying flaws or damages without causing damage to the objects being analyzed [PRG16; Ham+07]. These applications highlight the versatility and precision of diffraction tomography in capturing intricate internal details across various domains.

Implicit Neural Representations

An *Implicit Neural Representation* (INR) is a neural network that can **encode continuous spatial data** by nonlinear combinations of continuous functions, allowing a compact and flexible representation of complex structures and enabling applications such as high-resolution image reconstruction, 3-D shape modeling, and efficient signal processing.

The recent advent of INRs has opened new avenues in the field of diffraction tomography, offering a promising **alternative to traditional voxel-based imaging techniques**. This approach allows the precise reconstruction of complex structures **with fewer parameters**, effectively capturing fine details and smooth variations within the object. INRs naturally handle continuous rotations of the object. Furthermore, INRs are particularly well-designed to solve partial differential equations, like the Helmholtz equation. They hence easily integrate the wave-based physics of diffraction, facilitating more accurate modeling of wave propagation and scattering phenomena.

INRs are not black-box deep learning techniques used to solve

6 | Diffraction Tomography with Implicit Neural Representations

inverse problems; rather, they are sophisticated tools only used for signal representation. The use of INR in this chapter does not rely on the typical supervised learning paradigm whose training requires groundtruth input-output pairs—rarely available in emerging applications like diffraction tomography. Instead, INRs can be **trained in a self-supervised manner** by first representing the RI object, then choosing any sensing model to compute candidate observations, and finally optimizing the network to construct a RI distribution that fits the data.

Nonlinear Inverse Problem

In electromagnetic wave diffraction, the diffracted field can be interpreted as a polynomial function of the RI distribution with an infinity of orders with progressively decreasing influence. This means that recovering the RI distribution from a subset of the diffracted field represents a highly *nonlinear inverse problem*. Interestingly, as shown in Chap. 5 with (5.45), the degree of nonlinearity is inversely related to the diffraction power of the object. This diffraction context thus provides a nice realistic example of an inverse problem with a tunable degree of nonlinearity.

There are many results for characterizing the amount of information acquired by a linear sensing model. In diffraction tomography, the closest theoretical result is the *Fourier diffraction theorem*—directly relating the Fourier transform of a 2-D slice of the diffracted field to the Fourier transform of the RI distribution. In the case of a nonlinear sensing model, there are very few analysis characterizing the acquired information. Hopefully, in this fuzzy inverse problem context, the direction to image recovery can be driven by both the first-order approximation which is the Fourier diffraction theorem, and the physical intuition of light propagation. The intended benefit of considering a complicated nonlinear inverse problem is to overcome the current limitations of linearized sensing models to recover high contrast objects.

6.1.2 Related Work

We mention several works closely related to the scientific questions tackled in this chapter.

Diffraction Tomography

In 1969, [Wol69] proposed a ground-breaking idea for 3-D *Optical Diffraction Tomography* (ODT) based on the First-Born approximation. Since then, many contributions tried to improve the recovery performance, with algebraic reconstruction techniques [KS01], the Rytov approximation [Dev81], and more recently multi-slice methods like BPM [Kam+16b] and SSNP [Lim+19], and finally the convolutional Lippmann-Schwinger model [SPU17; Pha+20; Liu+18; Kam+16a; Ma+18], *a.k.a.* recursive Born. Orthogonal to these works exploiting the physics of diffraction to recover the image, ODT with a CNN decoder was proposed in [SXK18].

Unlike traditional ODT, which employs interferometry to capture complex-valued light fields, *Intensity Diffraction Tomography* (IDT) measures only the squared amplitude of the scattered light, as in conventional digital cameras. The cost of this simplification of the optical hardware implementation is a more ill-posed inverse problem to solve, with a phase retrieval challenge now added to the diffraction tomography problem. The inherent flexibility of IDT has led to the development of various illumination techniques, including those that integrate object scanning [GW02; JG15], angled [Lin+18] and multiplexed [TW15; MT19] illumination, or pupil engineering [Ngu+17].

Like for ODT, image recovery has been demonstrated in IDT under the First-Born approximation [Liu+22; Lin+18; Wu+19], using multi-slice methods such as BPM [Pha+18], and SSNP [ZWT22], and multi-layer Born [Che+20a].

Implicit Neural Representation

While [Pha+20] and [Che+20a] represent the closest works to our approach in terms of forward acquisition modeling, both of them, as well as the other works mentioned above, required an explicit recovery algorithm involving the computation of gradients with respect to the object voxels. [Kam+15] proposed to reconstruct the discrete volume with BPM by iteratively updating the voxels using the backpropagated computations of their gradients; an idea that leads to INRs and *automatic differentiation*. [ZH20] explored a spatial representation of the volume with a 3D CNN in a deep image prior fashion. This was another way to get a discrete representation of the object.

In the context of view synthesis, [Mil+20] paved the way for *Im-*

6 | Diffraction Tomography with Implicit Neural Representations

plicit Neural Representations, showing that plugging a *positional encoding* layer (which maps input coordinates to spatial frequencies) in front of a classical *Multi-Layer Perceptron* with ReLU activations provides a deep architecture capable of learning efficiently to provide a continuous representation of a scene. This architecture is now known to belong to the class of *Fourier Feature Networks* (FFN). *SInusoidal REpresentation Networks* (SIREN) came out in the same period with similar continuous representation performances. The expressiveness of FFNs and SIREN in the Fourier domain has been theoretically understood later with [Yuc+22; Tan+20]. There exists hundreds of declinations of INR architectures, passing by adaptive coordinate networks [Mar+21], hash encoding [Mül+22], or positional encoding with Radial Basis Functions [ZBG24].

The combination of INR with the concept of *Physics-Informed Neural Networks* (PINN) [RPK19]—an INR directly trained on a differential equation like Helmholtz—seems to be a promising way to avoid the need to discretize the volume to inject it in a discrete sensing model. Using PINNs to solve the inhomogeneous Helmholtz equation is challenging because the loss function depends precisely on the sought RI distribution. We report a proposition to tackle this challenge in 2-D given in [Che+20b]. However, the use of PINNs is out of the scope of this thesis.

The goal here is to study the interaction between an INR and the discrete Lippmann-Schwinger forward sensing model for diffraction tomography rather than to provide state-of-the-art reconstructions performances. Hence, only the classical FFN and SIREN architectures will be analyzed here with a very small parameterization compared to the upper cited works.

Nonlinear Inverse Problem

The discrete Lippmann-Schwinger model used for this diffraction tomography problem yields a nonlinear inverse problem more complicated than well-studied problems as *one-bit CS* [BB08] or *phase retrieval* [She+14]. There seems to exist some interesting literature in the direction of *Volterra series* [TD00; BOC03]; path unexplored in this thesis.

6.1.3 Chapter Contributions

Combining Lippmann-Schwinger and INRs: This work demonstrates the first combination of using the discrete Lippmann-Schwinger equation to model light diffraction with an implicit neural representation. The reconstruction follows an *error backpropagation* rule similar to [Liu+18], but that is applied to the weights of the INR, instead of the voxels of a discrete volume. Furthermore, the *automatic differentiation* process avoids the need to iteratively compute a Jacobian matrix to solve the inverse problem as in [SPU17, Sec. 2.2.1], thus also paving the way for nonlinear *intensity diffraction tomography* (not covered in this chapter).

The continuous representation with an INR offers a straightforward way to handle rotations compared to voxel-wise representations that require another interpolation technique to handle the rotations, like bilinear [JG15] or bicubic. For the rotations, we stress an equivalence between incident field and object rotation in Claim 5.1 in order to play with object rotations, and keep an incident field aligned with the boundaries of the object bounding box, similarly to [MJR23].

Numerical comparison between First-Born and Lippmann-Schwinger: numerical image reconstruction experiments provided in Sec. 6.5.2 compare the Lippmann-Schwinger and First-Born models. In particular, contrast profiles and SNR curves are given in Fig. 6.9 and Fig. 6.10, respectively. Through different slices of the reconstructed object, it is shown that the First-Born model fails to represent the inner content of refracting elements like beads.

The provided analyses have all been obtained with a *Tesla A100* GPU² provided by the supercomputing facilities of UCLouvain (CISM) and the Consortium des Equipements de Calcul Intensif en Fédération Wallonie Bruxelles (CECI) funded by FRS-FNRS, Belgium.

6.1.4 Notations Specific to This Chapter

The RI volume $f(\mathbf{r})$ will be considered enclosed in a box Ω with physical dimensions L_x , L_y , L_z along the X , Y , Z -axes, respectively. The position $\mathbf{r} \in \Omega$ is associated with normalized coordinates $\mathbf{r}' = (x', y', z') := (\frac{x}{L}, \frac{y}{L}, \frac{z}{L}) \in [0, 1]^3$, for $L := \max(L_x, L_y, L_z)$, given as input to an INR. The discrete volume f is defined on a regular grid $\mathcal{G}_{(N_x, N_y, N_z)} \subset \Omega$ with N_x , N_y , N_z voxels along the axes. The correspond-

²<https://www.nvidia.com/en-us/data-center/a100/>

6 | Diffraction Tomography with Implicit Neural Representations

ing voxel resolutions are written $\Delta x := L_x/N_x$, $\Delta y := L_y/N_y$, $\Delta z := L_z/N_z$. The normalized version of the volume is defined on the unitary grid $\mathcal{G}'_{(N_x, N_y, N_z)} \subset [0, 1]^3$.

6.2 Preliminaries

A brief explanation of *automatic differentiation* and *neural network weight optimization* is given below.

Automatic Differentiation

Deep neural network architectures are used in this chapter to provide a continuous representation of the RI volume of interest. The success of “deep nets” is due to the principle of *Automatic Differentiation* (AD) and *backpropagation*, briefly explained here.

In most cases, it is possible to break the numerical computations into a composition of elementary operations, and to create a graph representing their interdependencies. From this graph, the partial derivative of some quantity—generally an error term—with respect to the intermediate variables can be propagated step-by-step based on the *chain-rule*.

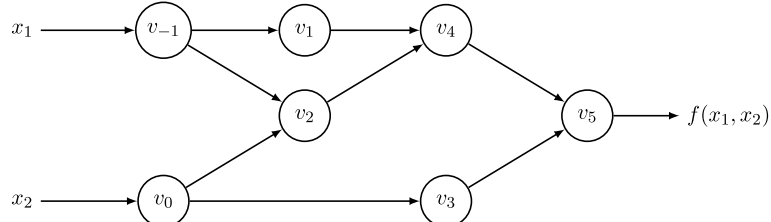


Fig. 6.2 Computational graph of the example $f(x_1, x_2) = \log(x_1) + x_1 x_2 - \sin(x_2)$ given in [Bay+18].

To illustrate AD, let us borrow the example $f(x_1, x_2) = \log(x_1) + x_1 x_2 - \sin(x_2)$ from the excellent review [Bay+18]. The computational graph for $f(x_1, x_2)$ is given in Fig. 6.2, with the value of the variables $\{v_i\}_{i=-1}^5$ given in Table 6.1. AD in reverse accumulation mode propagates derivatives backward from a given output. This is done by complementing each intermediate variable v_i with an adjoint

$$\bar{v}_i := \frac{\partial y_j}{\partial v_i},$$

which represents the sensitivity of a considered output y_j with respect to changes in v_i .

Table 6.1 Reverse mode AD example, with $y = f(x_1, x_2) = \log(x_1) + x_1 x_2 - \sin(x_2)$ evaluated at $(x_1, x_2) = (2, 5)$. After the forward evaluation of the primals on the left, the adjoint operations on the right are evaluated in reverse. Note that both $\frac{\partial y}{\partial x_1}$ and $\frac{\partial y}{\partial x_2}$ are computed in the same reverse pass, starting from the adjoint $\bar{v}_5 = \bar{y} = \frac{\partial y}{\partial y} = 1$.

Forward Primal Trace	Reverse Adjoint (Derivative) Trace
$v_{-1} = x_1 = 2$	$\bar{x}_1 = \bar{v}_{-1} = 5.5$
$v_0 = x_2 = 5$	$\bar{x}_2 = \bar{v}_0 = 1.716$
$v_1 = \ln v_{-1} = \ln 2$	$\bar{v}_{-1} = \bar{v}_{-1} + \bar{v}_1 \frac{\partial v_1}{\partial v_{-1}} = \bar{v}_{-1} + \bar{v}_1/v_{-1} = 5.5$
$v_2 = v_{-1} \times v_0 = 2 \times 5$	$\bar{v}_0 = \bar{v}_0 + \bar{v}_2 \frac{\partial v_2}{\partial v_0} = \bar{v}_0 + \bar{v}_2 \times v_{-1} = 1.716$
$v_3 = \sin v_0 = \sin 5$	$\bar{v}_{-1} = \bar{v}_2 \frac{\partial v_2}{\partial v_{-1}} = \bar{v}_2 \times v_0 = 5$
$v_4 = v_1 + v_2 = 0.693 + 10$	$\bar{v}_0 = \bar{v}_3 \frac{\partial v_3}{\partial v_0} = \bar{v}_3 \times \cos v_0 = -0.284$
$v_5 = v_4 - v_3 = 10.693 + 0.959$	$\bar{v}_2 = \bar{v}_4 \frac{\partial v_4}{\partial v_2} = \bar{v}_4 \times 1 = 1$
$y = v_5 = 11.652$	$\bar{v}_1 = \bar{v}_4 \frac{\partial v_4}{\partial v_1} = \bar{v}_4 \times 1 = 1$
	$\bar{v}_3 = \bar{v}_5 \frac{\partial v_5}{\partial v_3} = \bar{v}_5 \times (-1) = -1$
	$\bar{v}_4 = \bar{v}_5 \frac{\partial v_5}{\partial v_4} = \bar{v}_5 \times 1 = 1$
	$\bar{v}_5 = \bar{y} = 1$

In Table 6.1, we see the adjoint statements on the right, corresponding to each original elementary operation on the left. In simple terms, we are interested in computing the contribution $\bar{v}_i = \frac{\partial y}{\partial v_i}$ of the change in each variable v_i to the change in the output y . Taking the variable v_0 as an example, we see in Fig. 6.2 that it can only affect y by affecting v_2 and v_3 , so its contribution to a change in the value of y is given by

$$\frac{\partial y}{\partial v_0} = \frac{\partial y}{\partial v_2} \frac{\partial v_2}{\partial v_0} + \frac{\partial y}{\partial v_3} \frac{\partial v_3}{\partial v_0} \quad \text{or} \quad \bar{v}_0 = \bar{v}_2 \frac{\partial v_2}{\partial v_0} + \bar{v}_3 \frac{\partial v_3}{\partial v_0}.$$

After the forward pass on the left side, we do the backward pass of the adjoints on the right side, starting with $\bar{v}_5 = \bar{y} = \frac{\partial y}{\partial y} = 1$. In the end we get the derivatives $\frac{\partial y}{\partial x_1} = \bar{x}_1$ and $\frac{\partial y}{\partial x_2} = \bar{x}_2$ in just one reverse pass.

It is worth mentioning that, compared to numerical differentiation, partial derivatives computed with AD are exact as long as the derivative of each function involved in the computational graph has an exact expression.

Neural Network Weight Optimization

Once the sensitivity $\nabla_\phi \mathcal{L}(\phi)$ of the error \mathcal{L} with respect to all weights $\phi \in \mathbb{R}^P$ of a NN has been computed, we need to define a rule that up-

6 | Diffraction Tomography with Implicit Neural Representations

dates their value accordingly. This update is computed using optimization techniques like [GD](#) described in Sec. 5.4. We remind in Algos 6.1-[6.2](#), the *Stochastic Gradient Descent* (SGD) and *Adam* [KB14] optimizers, respectively. Both algorithms are called *stochastic* because the error is computed, during each iteration $k \in \llbracket K \rrbracket$, with respect to a random subset (*a.k.a. batch*) $\phi_{\mathcal{S}_k}$ of the training data, with $\mathcal{S}_k \subset \llbracket P \rrbracket$ and $|\mathcal{S}_k| = B$ for a batch size B . This provides a tradeoff between computing the error with respect to a sufficient amount of training data, and updating frequently the weights of the NN to enjoy a fast training procedure. In the ADAM algorithm Algo 6.2, we do not explicit the random subset selection and rather present the non-stochastic version for a simpler reading of the algorithm.

Algorithm 6.1 Stochastic Gradient Descent (SGD)

Require: α (learning rate), $\phi^{(0)}$ (init.).

- 1: **for** $k < K$ **do**
 - 2: Draw a random subset $\mathcal{S}_k \subset \llbracket P \rrbracket$ uniformly at random.
 - 3: $\phi_{\mathcal{S}_k}^{(k)} = \phi_{\mathcal{S}_k}^{(k-1)} - \alpha \nabla_{\phi_{\mathcal{S}_k}} \mathcal{L}(\phi^{(k-1)})$ ▷ Update weights.
 - 4: $\tilde{\phi} = \phi^{(K)}$
-

Algorithm 6.2 Adam

Require: α (learning rate), $\beta_1, \beta_2 \in [0, 1]$ (decay rates), $\phi^{(0)}$ (init.).

- 1: $m^{(0)} = \mathbf{0}$
 - 2: $v^{(0)} = \mathbf{0}$
 - 3: **for** $k < K$ **do**
 - 4: $g^{(k)} = \nabla_{\phi} \mathcal{L}(\phi^{(k-1)})$ ▷ Weights gradients
 - 5: $m^{(k)} = \beta_1 m^{(k-1)} + (1 - \beta_1) g^{(k)}$ ▷ biased 1st moment estimate.
 - 6: $v^{(k)} = \beta_2 v^{(k-1)} + (1 - \beta_2) (g^{(k)})^2$ ▷ biased 2nd raw moment estimate.
 - 7: $\hat{m}^{(k)} = m^{(k)} / (1 - \beta_1^k)$ ▷ bias-corrected 1st moment estimate.
 - 8: $\hat{v}^{(k)} = v^{(k)} / (1 - \beta_2^k)$ ▷ bias-corrected 2nd raw moment estimate.
 - 9: $\phi^{(k)} = \phi^{(k-1)} - \alpha \hat{m}^{(k)} / (\sqrt{\hat{v}^{(k)}} + \epsilon)$ ▷ Update weights.
 - 10: $\tilde{\phi} = \phi^{(K)}$
-

In Appendix 6.7.1, we quickly verify that Adam outperforms SGD, then use Adam for the rest of the analysis.

6.3 Implicit Neural Representations

This section introduces the concept of *Implicit Neural Representation* (INR). An INR is a neural network architecture aiming at representing complex scenes continuously. In our diffraction tomography context, the goal is to train an INR to map the input coordinates $\mathbf{r} = (x, y, z) \in \mathbb{R}^3$ to their associated scattering potential value $f(\mathbf{r}) \in \mathbb{C}$.

In this chapter, the two approaches considered are based on Fourier representation. To explain the philosophy of the approach, we recall the Fourier transform (and its inverse) of a three-dimensional continuous periodic signal $p(\mathbf{x})$:

$$\begin{aligned} P[\mathbf{k}] &= \int_0^1 p(\mathbf{x}) e^{-i2\pi \mathbf{k}^\top \mathbf{x}} d\mathbf{x} \\ p(\mathbf{x}) &= \sum_{\mathbf{k} \in \mathbb{Z}^3} P[\mathbf{k}] e^{i2\pi \mathbf{k}^\top \mathbf{x}}. \end{aligned} \quad (6.1)$$

The role of the INRs presented below is to attempt to approximate the Fourier decomposition (6.1) from nonlinear combinations of a subset of these frequencies \mathbf{k} . The use of spreaded support functions like the complex exponentials of the Fourier representation was the key to the first demonstrations of working INRs. Indeed, previous attempts to map input coordinates directly to image (in the broad sense) values using an MLP with ReLUs failed, especially in representing sharp transitions [Mil+20, Sec. 5.1].

6.3.1 Architectures

In this thesis, two architectures are used: *Fourier Features Networks*, and *SIRENs*.

Fourier Feature Networks The early *Fourier Feature Network* (FFN) technique [Mil+20] consists of a Fourier series decomposition input to a classical *MultiLayer Perceptron* (MLP) [Ros58; Tan+20] with *Rectified Linear Unit* (ReLU) activation functions. In the FFN architecture, depicted in Fig. 6.4(a), the 3-D spatial position \mathbf{r} is first mapped to the Fourier basis with a priori chosen 3-D spatial frequencies $\mathbf{K} \in \mathbb{R}^{K \times 3}$. The first layer of an FFN computes

$$\theta(\mathbf{r}) := (e^{i2\pi \mathbf{K}_i \mathbf{r}'})_{i=1}^K \quad (6.2)$$

with the normalized position $\mathbf{r}' \in [0, 1]^3$ s.t. $\mathbf{r} = L\mathbf{r}'$, and $L = \max(L_x, L_y, L_z)$ defining the physical dimensions of the RI volume. The

6 | Diffraction Tomography with Implicit Neural Representations

degrees of freedom of this layer, coined *Positional Encoding*, are associated to the choice of the initial frequencies \mathbf{K} .

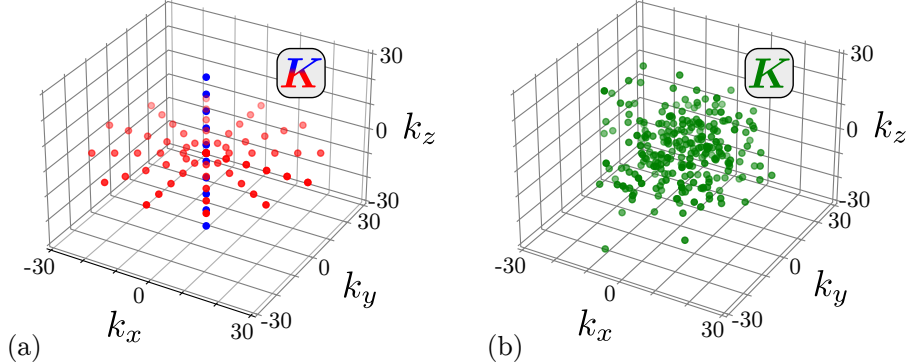


Fig. 6.3 Two positional encoding possibilities. (a) Radial arrangement in the $(k_x - k_y)$ plane and linear arrangement along the k_z -axis. (b) Random Gaussian frequencies.

In the *radial encoding* proposition of [Liu+22] shown in Fig. 6.3(a), the frequencies are chosen as $\mathbf{K} = \begin{bmatrix} \mathbf{K}_{xy} \\ \mathbf{K}_z \end{bmatrix}$ with a radial encoding in the XY-plane

$$\mathbf{K}_{xy} = (2^j (\cos(\theta_i), -\sin(\theta_i), 0))_{i \in [\![L_{xy}]\!], j \in [\![L_{rot}]\!]} \in \mathbb{R}^{L_{rot}L_{xy} \times 3}$$

(depicted in red) and a linear encoding along the Z-axis; $\mathbf{K}_z = (2^i \mathbf{e}_3^\top)_{i \in [\![L_z]\!]} \in \mathbb{R}^{L_z \times 3}$ (depicted in blue). The total number of frequencies is given as $\mathcal{K} = L_{rot}L_{xy} + L_z$ where L_{xy} is the number of frequencies linearly separated along the k_x -axis, then repeated L_{rot} times by consecutive rotations, and L_z is the number of frequencies linearly separated along the k_z -axis. Another choice, more natural, described in [Yuc+22] and depicted in Fig. 6.3(b), consists in initializing the Fourier encoding with randomly chosen frequencies $\mathbf{K}_k \stackrel{\text{i.i.d.}}{\sim} \mathcal{N}(\mathbf{0}, \sigma^2 \mathbf{I}_3)$, $k \in [\![\mathcal{K}]\!]$.

The Fourier encoding $\boldsymbol{\theta}$ of the spatial coordinates is put in a *MultiLayer Perceptron* (MLP) \mathcal{N}_ϕ —a fully-connected neural network, with Rectified Linear Unit (ReLU) neuron activations. The nonlinear modular function represented by the MLP writes

$$\mathcal{N}_\phi(\boldsymbol{\theta}) = \mathbf{W}_L(\sigma_{L-1} \circ \dots \circ \sigma_0)(\boldsymbol{\theta}) + \mathbf{b}_L, \quad (6.3)$$

with each layer l composing a linear mapping followed by the ReLU activation as

$$\sigma_l(\mathbf{x}) := \max(\mathbf{0}, \mathbf{W}_l \mathbf{x} + \mathbf{b}_l).$$

The trainable weights in (6.3) can be arranged in a vector as

$$\boldsymbol{\phi} := \text{vec}\{\mathbf{W}_L, \mathbf{b}_L, \dots, \mathbf{W}_0, \mathbf{b}_0\}, \quad (6.4)$$

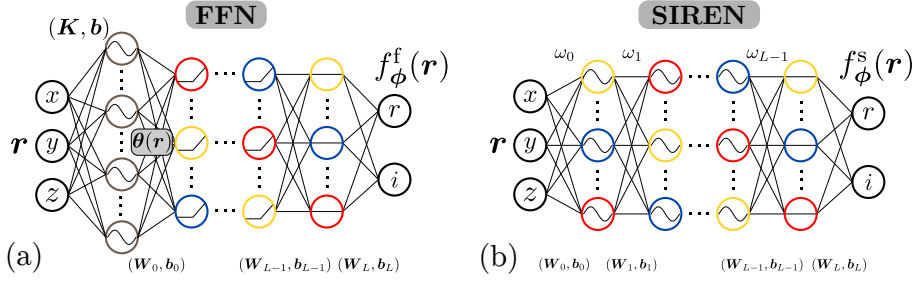


Fig. 6.4 INR architectures. (a) In the FFN, a non-trainable *Positional Encoding* layer (in gray) maps the normalized 3-D spatial position r' to spatial frequencies Ω . The Fourier samples are then fed into an MLP with ReLU activation functions. (b) A SIREN is an MLP with sinusoidal activation functions. In both (a) and (b), the final layer is only linear.

where vec concatenates the vectorizations of all elements in the set. The FFN finally composes the positional encoding and the MLP as

$$f_\phi^f(\mathbf{r}) := \mathcal{N}_\phi(\boldsymbol{\theta}(\mathbf{r})), \quad (\text{FFN})$$

with the subtlety that the network separately outputs the real and imaginary parts of $f_\phi^f(\mathbf{r})$.

SIREN *Sinusoidal Representation Networks* (SIREN) are simply MLP whose activation functions are sines, as illustrated in Fig. 6.4(b). They have been introduced in [Sit+20] for their ease in computing derivatives, and thus solving partial differential equations. The complex output of a SIREN is described as

$$f_\phi^s(\mathbf{r}) := \mathbf{W}_L(\boldsymbol{\varphi}_{L-1} \circ \boldsymbol{\varphi}_{L-2} \circ \dots \circ \boldsymbol{\varphi}_0)(\mathbf{r}') + \mathbf{b}_L, \quad (\text{SIREN})$$

with each layer l composing a linear mapping followed by a sinusoidal activation as

$$\boldsymbol{\varphi}_l(\mathbf{x}) := \sin(\omega_l(\mathbf{W}_l \mathbf{x} + \mathbf{b}_l)),$$

and a *frequency factor* ω_l tuning the frequency of the sinusoidal mapping. Like for FFN, the trainable weights ϕ are the weight matrices $\{\mathbf{W}_l\}_{l=1}^L$ and biases $\{\mathbf{b}_l\}_{l=1}^L$ hence follow definition (6.4).

Before assessing the performances of the FFN and SIREN in the context of diffraction tomography, Appendix 6.7.1 numerically studies regimes of parameters that accurately reconstruct a discrete volume. It results that the Adam algorithm exhibits a better convergence rate than SGD and that the frequency factor ω_0 and number of layers L have low influence on the reconstruction SNR. It is also seen that the SIREN

6 | Diffraction Tomography with Implicit Neural Representations

converges faster than the FFN but the FFN converges to lower error values. These observations will guide the choice of SIREN parameters used for the numerical experiments in Sec. 6.5.

6.4 Sensing Models for ODT and IDT

In this section, we rebuild two classical observation models in diffraction tomography. The starting point is the *discrete Lippmann-Schwinger* equation ([LSd](#)) that computes the electric field resulting from the diffraction of an incident illumination through an inhomogeneous medium.

The first, *Optical Diffraction Tomography* (ODT), consists in directly observing complex-valued partial information about the diffracted field \mathbf{u} obtained from ([LSd](#)). This complex-valued sensing is achieved by *holography* principles [[Kim11](#)] similar to the 8-step phase-shifting calibration explained for the MCFLI in Sec. 3.5.2. A drawback of ODT is the need for a more complicated optical setup. Indeed, cameras can only record the intensity of the light. Hence, to recover the complex field, the illuminating field must be physically separated in two parts: one directed towards the diffracting object, and another, unaltered part, directed towards the camera and interfering with the diffracted field.

The second model of diffraction tomography, *Intensity Diffraction Tomography* (IDT), consists of observing a portion of the intensity³ $|\mathbf{u}|^2$ of the diffracted field. The IDT context reflects the real acquisition process made with a digital camera, and thus requires fewer optical elements than ODT. However, IDT comes at the cost of losing the phase information. This leads to a harder inverse problem that mixes diffraction tomography and phase retrieval [[Fie82](#); [BCL02](#)].

6.4.1 From the Object Domain to the Camera

In either ODT or IDT, once the diffracted field \mathbf{u} is known in the object domain Ω , it must be mapped to the camera measurement plane Γ . In the simpler case, one assumes $\Gamma \subset \mathcal{G} \subset \Omega$ and the mapping is simply modeled as a restriction operator $\mathbf{H} \in \mathbb{R}^{M \times N}$ applied to the diffracted field \mathbf{u} .

As it is more computationally efficient to reduce the bounding box Ω as much as possible as long as $\text{supp } f \subset \Omega$, realistic acquisition scenarios have the measurement plane far away from the object's bounding box, *i.e.*, $\Gamma \not\subset \Omega$. One possibility consists in using the *Angular Spectrum* (AS) formula [[MS09](#)] to propagate \mathbf{u} up to the plane Γ . This solu-

³The absolute value is applied elementwise to the vector \mathbf{u} .

6 | Diffraction Tomography with Implicit Neural Representations

tion is especially convenient if the camera plane is parallel to the XY-plane of Ω . Otherwise, the known diffracted field $\mathbf{u} \in \Omega$ must first be interpolated to a plane parallel to Γ before using the AS method. The polyvalent solution consists in re-using (LS),

$$U(\mathbf{r}) = U_i(\mathbf{r}) + \int_{\Omega} U(\mathbf{r}') f(\mathbf{r}') G(\mathbf{r} - \mathbf{r}') d\mathbf{r}',$$

and restricting the computation of U to the discrete set of positions defining the camera plane $\Gamma = \{\mathbf{r}_1, \dots, \mathbf{r}_M\}$. In discrete form, it writes [Pha+20]

$$\mathbf{u}_{\Gamma} = \mathbf{u}_{i,\Gamma} + \tilde{\mathbf{G}} \mathbf{D}_f \mathbf{u} \quad (6.5)$$

where $\mathbf{u}_{\Gamma}, \mathbf{u}_{i,\Gamma} \in \mathbb{C}^M$ and $\tilde{\mathbf{G}} \in \mathbb{C}^{M \times N}$ models the convolution similarly to \mathbf{G} in (LSD). The mn -th entry of $\tilde{\mathbf{G}}$ writes

$$\tilde{G}_{mn} = G(\mathbf{r}_m - \mathbf{r}_n) = \frac{e^{ik_m |\mathbf{r}_m - \mathbf{r}_n|}}{4\pi |\mathbf{r}_m - \mathbf{r}_n|}$$

for $\mathbf{r}_m \in \Gamma$ and $\mathbf{r}_n \in \Omega$.

For the sake of simplicity, the AS will be considered for computing the measurement images, as illustrated in Fig. 6.5(a). In discrete form, the AS writes

$$\mathbf{u}_{\Gamma} = \mathbf{F}^* \mathbf{D}_h \mathbf{F} \mathbf{u} = \mathbf{H} \mathbf{u}, \quad (6.6)$$

where \mathbf{F} is the 2-D Fourier transform, \mathbf{h} is the AS propagation kernel [Pha+20, Eq. (16)], and \mathbf{H} is the propagation operator defined as

$$\mathbf{H} := \mathbf{F}^* \mathbf{D}_h \mathbf{F}. \quad (6.7)$$

Camera pupil In practice, the diffracted field at the measurement plane \mathbf{u}_{Γ} is recorded by a camera that has a limited aperture and may contain many optical elements to correct for some aberration effects [MCW05; Pha+20]. The effect of this aperture, or *pupil*, is modeled by a 2-D function $p(\mathbf{x})$ for $\mathbf{x} \in \mathbb{R}^2$. Consequently, the sensed quantity is actually

$$\tilde{U}_{\Gamma}(\mathbf{x}) = (p * U_{\Gamma})(\mathbf{x}) = \int_{\Gamma} p(\mathbf{x} - \mathbf{x}') U_{\Gamma}(\mathbf{x}') d\mathbf{x}'. \quad (6.8)$$

Using the convolution theorem, (6.8) can be written as

$$\tilde{U}_{\Gamma}(\mathbf{x}) = \mathcal{F}_2^{-1}\{\hat{p} \hat{U}_{\Gamma}\}[\mathbf{x}] = \int_{\Gamma} \hat{p}(\mathbf{k}) \hat{U}_{\Gamma}(\mathbf{k}) e^{i\mathbf{k}^\top \mathbf{x}} d\mathbf{k}. \quad (6.9)$$

with $\hat{p} := \mathcal{F}p$, $\hat{U} := \mathcal{F}U$. The discretization of (6.9) shows that the effect of the camera can be modeled by a linear operator $P \in \mathbb{C}^{M \times M}$ defined as

$$P := F_2^{-1} D_{Fp} F_2,$$

where $p \in \mathbb{C}^M$ is the discretized Fourier transform of the pupil function $p(x)$, generally modeled as a simple mask, and F_2 computes the 2-D FFT. For simplicity, no pupil effect is considered in this chapter.

6.4.2 Multiple Views and Object Rotation

Because of the information loss in depth, and also partially explained by the Fourier diffraction theorem (5.29) with the *missing cone problem* [Lim+15] illustrated in Fig. 6.5(b), the RI volume cannot be recovered from a single snapshot of the diffracted field. The *tomography* principle consists in illuminating the object from different angles in order to increase the acquired information.

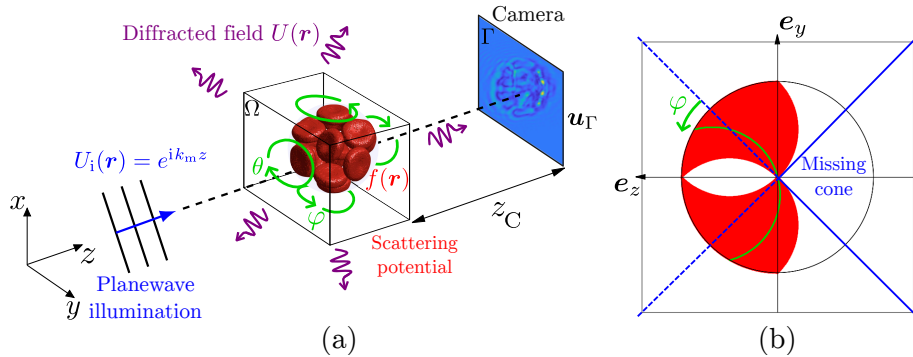


Fig. 6.5 (a) Diffraction tomography context. The illumination and camera are fixed, and the object f is rotated first by an angle ϕ around the X -axis, then by an angle θ around the Z -axis. The camera plane Γ is placed parallel to the XY -plane at a distance z_C from the object domain Ω . (b) 2-D illustration of the *missing cone problem*. If the object f is observed only by rotations $\phi \in [-45^\circ, +45^\circ]$, for instance, the Fourier diffraction theorem 5.29 predicts that the frequency sampling of f is covered by this red region, leading to a cone of unseen frequencies.

In this chapter, the different views are obtained by rotating the object f , as depicted in Fig. 6.5(a). Starting from an arbitrary orientation set at angle $\varphi = 0$ around the X -axis, and angle $\theta = 0$ around the Z -axis, the j -th rotation of f is obtained as $f(R(\theta_j, \varphi_j)r)$ with the rotation

6 | Diffraction Tomography with Implicit Neural Representations

matrix

$$\mathbf{R}(\theta_j, \varphi_j) = \mathbf{R}_Z(\theta_j)\mathbf{R}_X(\varphi_j) = \begin{pmatrix} c\theta_j & -s\theta_j & 0 \\ s\theta_j & c\theta_j & 0 \\ 0 & 0 & 1 \end{pmatrix} \begin{pmatrix} 1 & 0 & 0 \\ 0 & c\varphi_j & -s\varphi_j \\ 0 & s\varphi_j & c\varphi_j \end{pmatrix}. \quad (6.10)$$

As the diffraction model (LSD) is discrete, a discrete form of the RI volume is obtained by querying the rotated f on the 3-D regular grid $\mathcal{G}_{(N_x, N_y, N_z)}^{(L_x, L_y, L_z)}$ as

$$f_j = (f(\mathbf{R}(\theta_j, \varphi_j)\mathbf{r}))_{\mathbf{R}(\theta_j, \varphi_j)\mathbf{r} \in \mathcal{G}}. \quad (6.11)$$

Remark 6.1. *The problem with a volume with varying spatial dimensions $L_x \neq L_y \neq L_z$ is that any rotation modifies its support, as illustrated in Fig. 6.6. In order to keep a rotation-invariant support, we will simplify the analysis by recovering only cubic objects with $L_x = L_y = L_z$.*

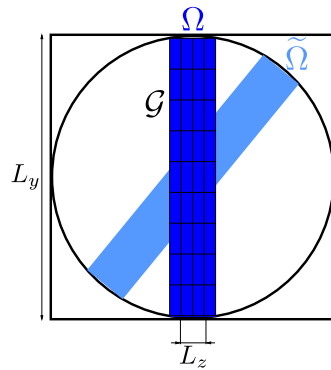


Fig. 6.6 2-D illustration of rotating an object with varying spatial dimensions. The support Ω is transformed to $\tilde{\Omega} := \{\mathbf{R}(\theta, \varphi)\mathbf{r}, \forall \mathbf{r} \in \Omega\}$ so the grid \mathcal{G} is not appropriate anymore to discretize f .

With $\mathbf{u}_j = \mathbf{L}_j^\dagger \mathbf{u}_i$ the solution of (LSD) computed using one of the optimization techniques described in Chap. 5 with $\mathbf{L}_j := \mathbf{I} - \mathbf{G}\mathbf{D}_{f_j}$, and the measurement operator \mathbf{H} defined in (6.7), the j -th camera measurement is thus obtained as

$$\mathbf{u}_{\Gamma,j} = \mathbf{H}\mathbf{u}_j = \mathbf{H}\mathbf{L}_j^\dagger \mathbf{u}_i. \quad (6.12)$$

The J images are finally collected in a measurement vector $\mathbf{u}_\Gamma \in \mathbb{C}^{MJ}$

which reads

$$\mathbf{u}_\Gamma = \begin{bmatrix} \mathbf{u}_{\Gamma,0} \\ \vdots \\ \mathbf{u}_{\Gamma,J-1} \end{bmatrix} = \begin{bmatrix} \mathbf{H}\mathbf{L}_0^\dagger \\ \vdots \\ \mathbf{H}\mathbf{L}_{J-1}^\dagger \end{bmatrix} \mathbf{u}_i. \quad (6.13)$$

In ODT, the measurement vector $\mathbf{y} \in \mathbb{C}^M$ is obtained by subtracting the incident field component of the camera measurements as

$$\mathbf{y} := \mathbf{u}_\Gamma - \mathbf{u}_{i,\Gamma} = \begin{bmatrix} \mathbf{H}(\mathbf{L}_0^\dagger - \mathbf{I}) \\ \vdots \\ \mathbf{H}(\mathbf{L}_{J-1}^\dagger - \mathbf{I}) \end{bmatrix} \mathbf{u}_i. \quad (\text{ODT})$$

In (ODT), it is the *scattered* or *background-removed* field that is observed. In IDT, the measurement vector $\mathbf{y} \in \mathbb{C}^M$ is obtained as the intensity of the complex field reaching the camera modeled in (6.13). It writes

$$\mathbf{y} = |\mathbf{u}_\Gamma|^2 \quad (\text{IDT})$$

with $\mathbf{y} \in \mathbb{R}_+^M$ (and not \mathbb{C}^M as in (ODT)).

Remark 6.2. By removing the illuminating component, there is a way to get a linear sensing model for IDT with the *First-Born* approximation. We demonstrate this in Appendix 6.7.3.

6 | Diffraction Tomography with Implicit Neural Representations

6.5 Recovery Analysis

This section covers the formulation of an inverse problem both for ODT and IDT, and provides several numerical analyses.

6.5.1 Inverse Problem Formulation

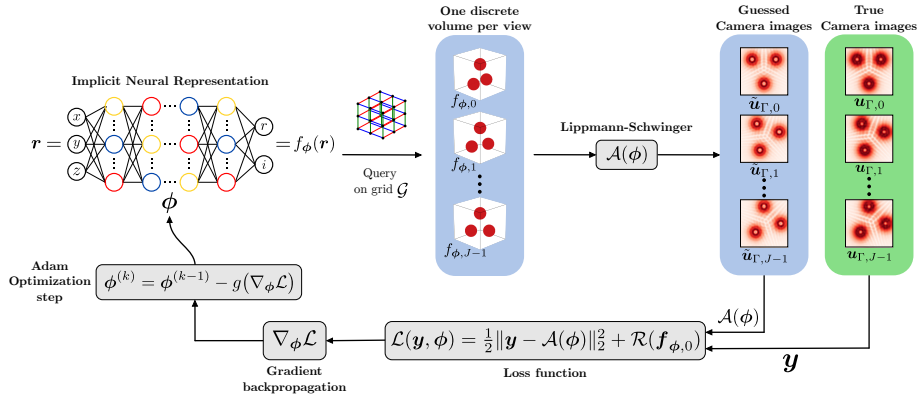


Fig. 6.7 Schematic of the recovery procedure. The INR is queried on J rotations of the 3-D regular grid to generate discrete volumes $\{f_{\phi,j}\}_{j=1}^J$. The associated observations $\mathcal{A}(\phi)$ modeled using Lippmann-Schwinger are compared with the true observation vector y into a loss function $\mathcal{L}(y, \phi)$. The weights of the INR are updated using Adam (with g a function of the loss gradient explained in Algo. 6.2) based on the backpropagated loss gradient $\nabla_\phi \mathcal{L}$. This procedure is repeated iteratively until convergence of the INR weights.

A schematic of the recovery procedure is given in Fig. 6.7. In order to solve the diffraction tomography problem, a continuous representation of the scattering potential as $f_\phi(r)$ is obtained by the intermediate of the weights of the INR computed as

$$\tilde{\phi} = \arg \min_{\phi} \mathcal{L}(y, \phi), \quad \mathcal{L}(y, \phi) := \frac{1}{2} \|y - \mathcal{A}(\phi)\|_2^2 + \mathcal{R}(f_{\phi,0}), \quad (6.14)$$

where

- y is the measurement vector associated to the images captured by the camera.
- $\mathcal{A}(\phi)$ maps the weights ϕ of the INR to the measurements y either in the **ODT** or the **IDT** model. It models all the physics of the acquisition; passing by **(LSd)** to compute the diffracted field, up to the propagation to the camera plane Γ using (6.6).

- $\mathcal{R}(f_{\phi,0})$ is a *regularization* term computed on the first orientation of the discretized volume $f_{\phi,0} := (f_{\phi}(\mathbf{r}))_{\mathbf{r} \in \mathcal{G}}$. In the results shown in Sec. 6.5.2, we do not add a regularization term ($\mathcal{R}(f_{\phi,0}) = 0$).

Similarly to (6.11), the j -th rotation of the discretized RI volume is obtained by querying the INR on a 3-D regular grid \mathcal{G} as

$$f_{\phi,j} = (f_{\phi}(\mathbf{R}(\theta_j, \varphi_j)\mathbf{r}))_{\mathbf{r} \in \mathcal{G}}. \quad (6.15)$$

The gradients $\nabla_{\phi}\mathcal{L}$ of the loss function with respect to the INR parameters are computed by automatic differentiation (described in the Preliminaries section 6.2) and updated with the Adam algorithm 6.2.

Computational cost For the diffraction tomography context, the *memory load* of the gradients computations limits the resolution $N = N_x N_y N_z$ that can be used for the discrete Lippmann-Schwinger model computing the measurement vector \mathbf{y} . Indeed, as shown in Fig. 6.8 and compatible with [SPU17, Fig. 2], the memory load is directly proportional to NJ which is the total number of queries of the INR. This dependence is intuitive because the evaluation of the loss function depends on the content of these voxels (see Fig. 6.7), and the gradient of the error must then be propagated from these voxels back to the INR parameters. The best transverse resolution (N_x, N_y) can be reached by computing only one orientation per epoch during the inverse problem solving, and setting a smaller⁴ axial resolution N_z .

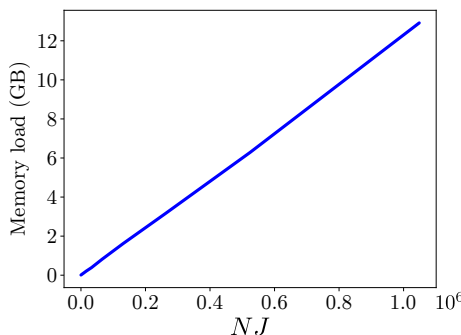


Fig. 6.8 Memory load in GB computed on a Tesla A100 GPU, as a function of the number of generated voxels NJ where N is the total number of voxels per volume, and J is the number of rotations of the object, as depicted in Fig. 6.7.

⁴The depth of the RI object is generally smaller than its width in this application [Liu+22].

6 | Diffraction Tomography with Implicit Neural Representations

Remark 6.3. As explained in Sec. 5.4.3, the stepsize α used in the gradient descent algorithm solving (LSd) is chosen in function of the estimated Lipschitz constant. Having the stepsize a function of the INR parameters induces a huge increase of the memory load. In practice, for the sake of memory savings, the gradient of the loss function is not computed with respect to this stepsize, considered as a constant value.

6.5.2 Results

For the numerical results presented in this section, Table 6.2 reports the parameters used for each figure. The background medium is water with RI $n_m = 1.333$, and the illuminating field will always be a planewave of wavelength in vacuum $\lambda = 515\text{nm}$ propagating along the Z-axis, i.e., $U_i(\mathbf{r}) = e^{ik_m e_z}$. In ODT, the camera is placed slightly at a distance $z_C = \Delta z$ behind the volume, with $\Delta z := L_z / N_z$. The (LSd) model is solved by a varying-stepsize AGD method with a maximum number of iterations $K = 400$.

The following experiments are conducted only with SIRENs. The reason is twofold, (i) the time needed for the simulations behind each figure is around one day and (ii) Fig. 6.4(a) showed that SIRENs converge faster than FFNs. The initialization of the SIREN weights $\phi^{(0)}$ follows [Sit+20].

Table 6.2 Parameters used for the numerical experiments.

	Symbol	Meaning	Fig. 6.9	Fig. 6.10	Fig. 6.11
Physics	λ	Wavelength in vacuum.	515nm		
	n_m	RI of the background.	1.333		
	(L_x, L_y, L_z)	Physical dimensions.	$(12\lambda, 12\lambda, 12\lambda)$		
	(N_x, N_y, N_z)	Discrete volume resolution.	$(48, 48, 48)$		
	C	Contrast	varying	0.3	0.4
	J	Number of orientations.	24		
	–	Illumination type.			
LSd solving	φ	Illumination angle.	45°	45°	varying
	–	Diffracton tomography type.	ODT	ODT	ODT
	Z_C	z -position of the camera.	$\frac{\lambda}{4}$		
SIREN arch.	–	Solving method.	AGD		
	$\mathbf{u}^{(0)}$	Initial condition	0		
	K	Number of iterations.	400	400	varying
SIREN training	L	Number of layers.	4		
	n_l	Number of neurons at layer l .	256		
	ω_0	Initial frequency factor.	25		
	ω_l	Hidden frequency factors.	10		
	α	Learning rate.	10^{-5}		
	B	Batch size = views per epoch.	6		
	n_{epoch}	Number of epochs.	400		

6 | Diffraction Tomography with Implicit Neural Representations

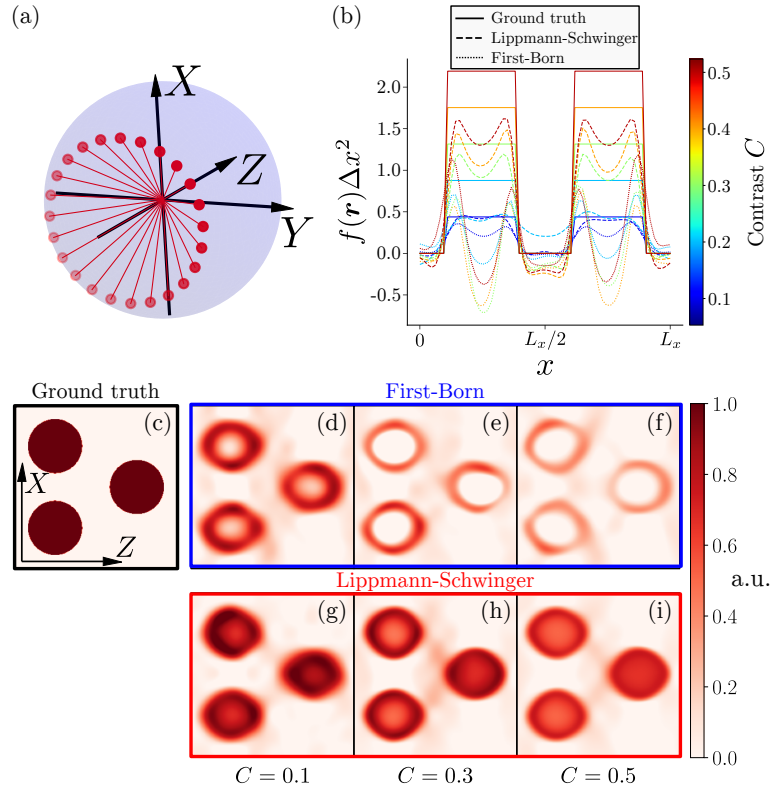


Fig. 6.9 ODT reconstructions of the three spheres shown in Fig. 6.12(a). (a) The $J = 24$ orientations of the volume, corresponding to an annulus of illuminations. (b) Adimensional scattering potential values $f(\mathbf{r})\Delta x^2$ along the X -axis for $(y', z') = (0.5, 0.25)$ in function of the contrast $C \in \{0.1, 0.2, 0.3, 0.4, 0.5\}$ using the FB and LS models; in dotted and dashed lines, respectively. (c) Ground truth in the XZ -plane at $y' = 0.5$. (d-f) Reconstruction of [First-Born](#) for $C = 0.1, 0.3, 0.5$. (g-i) Same as (d-f) for [LS](#).

Fig. 6.9 presents a comparison of the [First-Born](#) and [LS](#) performances in ODT under an annular set of views of angle 45° depicted in Fig. 6.9(a). The RI object is made of three ellipsoids living in a 3-D domain Ω of dimensions $(L_x, L_y, L_z) = (12\lambda, 12\lambda, 12\lambda)$ and whose equivalent normalized in the unit cube \mathcal{G}' are the three spheres shown in Fig. 6.12. The “true” measurement vector \mathbf{y} has been computed using [\(LSD\)](#) with $K = 3000$ iterations, aiming to be more accurate especially for high contrast values. The rest of the parameters are listed in Table 6.2.

Fig. 6.9(b) shows the profile of the adimensional scattering potential value $f(\mathbf{r})\Delta x^2$ (with $\Delta x := L_x/N_x = 128.7\text{nm}$) along the X -axis at the plane $(y', z') = (0.5, 0.25)$ for contrast values $C \in \{0.1, 0.2, 0.3, 0.4, 0.5\}$. It is seen that, even without explicit regularization term in the loss func-

tion associated to the SIREN, both FB and LS are able to identify the contours of the three ellipsoids. However, it is seen that, because of the missing-cone problem illustrated in Fig 6.5(b), FB struggles to reconstruct the inside part of the ellipsoids. This can also be seen in subplots (d-f). Thanks to the multiple-scattering effects modeled by LS, the ellipsoids are more faithfully reconstructed. It is observed that the scattering potential value is always underestimated. To explain this phenomenon, we invoke a *leakage argument* which is that the solution obtained from the minimization problem (6.14) always computes a minimum energy solution, *i.e.*, the solution minimizing the loss function and with minimal ℓ_2 -norm. This argument is supported with a proof in the simpler case of a linear system solved by [GD](#) given in Appendix 6.7.2.

Fig. 6.9(c-i) provide slices of the GT, FB and LS reconstructions. These slices are provided in an (X, Z) plane at $y' = 0.5$. Note that the resolution along the X and Z axes are not the same. The colorbars are adjusted to the range of the GT, which varies between the different choices of contrast values. It is seen that the reconstruction quality decreases when the contrast increases, both for FB and LS.

In the same setting as in Fig. 6.9 but for a fixed contrast $C = 0.3$ and varying annular illumination angle $\varphi \in \{0^\circ, 10^\circ, 20^\circ, 30^\circ, 40^\circ, 50^\circ, 60^\circ\}$, Fig. 6.10 provides another comparative view of [First-Born](#) and [LS](#).

Fig. 6.10 shows the reconstruction SNR of the volume reconstruction in function of the illumination angle φ . It is seen that, while [First-Born](#) completely fails at reconstructing the inner content of the volume no matter the illumination angle, [LS](#) has a monotonically increasing reconstruction SNR with increasing φ values.

Fig. 6.10(c-i) provide slices of the GT, FB and LS reconstructions. The subplots (d-f) (resp. (g-i)) are shown for $\varphi \in \{0^\circ, 30^\circ, 60^\circ\}$ for FB (resp. LS). These slices are provided in an (X, Z) plane at $y' = 0.5$. Note that the resolution along the X and Z axes are not the same. It is seen that, similarly to Fig. 6.9, FB does not succeed in representing the inside content of the spheres, this is the reason why the associated reconstruction SNR value is so small. While the volume cannot be reconstructed with LS for a single view ($\varphi = 0^\circ$) in Fig. 6.10(g), the reconstruction quality improves gradually in (h) then (i).

Fig. 6.11 demonstrates that the quality of the solution to [\(LSD\)](#) is critical for the ODT reconstruction. It shows that the SNR of the recon-

6 | Diffraction Tomography with Implicit Neural Representations

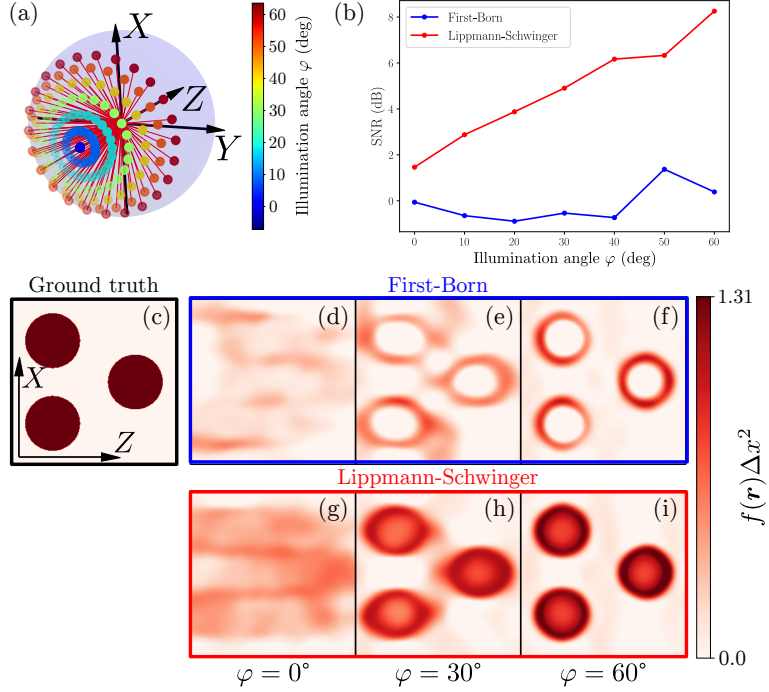


Fig. 6.10 ODT reconstructions of the three spheres shown in Fig. 6.12(a). (a) The $J = 24$ orientations of the volume given for each illumination angle $\varphi \in \{10i^\circ\}_{i=0}^6$, each corresponding to an annulus of illuminations. (b) SNR in function of the illumination angle φ for FB and LS. (c) Ground truth in the XZ-plane at $y' = 0.5$. (d-f) Reconstruction of First-Born for $\varphi = 0^\circ, 30^\circ, 60^\circ$. (g-i) Same as (d-f) for LS.

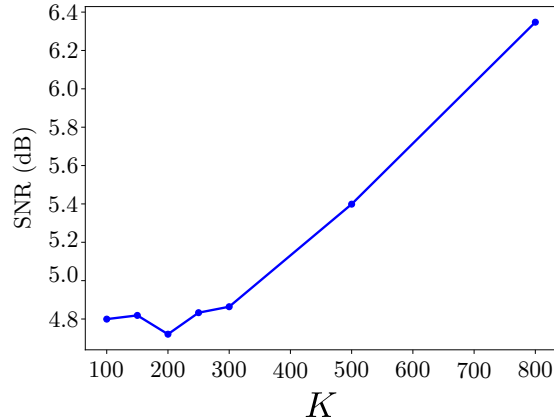


Fig. 6.11 SNR of the ODT reconstruction in function of the number iterations K used to solve (LSD), in the same ODT setting as in Fig. 6.9.

strunction increases with the number of iterations K used for the AGD method solving (LSD). The small drop in SNR occurring for $K = 200$ is due to the randomness of the initialization of the SIREN weights.

6.6 Discussion

What has been done

This chapter presented advances in the field of *diffraction tomography* by integrating the discrete *Lippmann-Schwinger equation* with *implicit neural representations* (INRs). This novel combination allows for more efficient and accurate modeling of light diffraction, using error backpropagation for INR weighting adjustments and bypassing the iterative computation of Jacobian matrices that is traditionally required. This methodological innovation not only simplifies the reconstruction process, but also supports the development of *nonlinear intensity diffraction tomography* (IDT), which provides a more accurate representation of complex refractive elements.

In addition, the continuous 3-D image representation provided by INRs improved the *handling of rotations*, eliminating the need for interpolation techniques such as bilinear or bicubic methods. This continuous approach, supported by numerical comparisons between the Lippmann-Schwinger and First-Born models, underscored the superiority of the former in representing intricate internal structures within refracting elements. By demonstrating the limitations of the First-Born model and the robustness of the Lippmann-Schwinger approach through detailed contrast profiles and SNR analyses, this work established a comprehensive and robust framework for high-fidelity image reconstruction in diffraction tomography.

Limits and Open Questions

Comparison with classical interpolation techniques: A limitation of this chapter is the introduction of an INR for diffraction tomography without benchmarking its performance against classical interpolation methods, such as linear or cubic interpolation. Beyond a straightforward numerical comparison, it would have been insightful to explore the differences in *implicit regularization* between (i) linear interpolation, which is limited to representing piecewise linear functions, and (ii) a SIREN network, known for promoting sparse Fourier representations [Yuc+22]. Such a study could provide a deeper understanding of how each approach impacts reconstruction quality and regularization behavior.

INRs are not interesting for every application: With the architectures described in Sec. 6.3, INRs are not very compatible with integral mod-

6 | Diffraction Tomography with Implicit Neural Representations

els like the Fourier subsampling models of Chap. 3-4. Indeed, an INR modeled like in (FFN) or (SIREN) is well-designed for a finite number of inferences, but computing the Fourier transform of an image $f_\phi(x)$ with $x \in \mathbb{R}^2$ at any frequency as $\int_{\mathbb{R}^2} f_\phi(x) e^{\frac{i2\pi}{\lambda z} (p_k - p_j)^\top x} dx$ like in (3.5) requires inferring the value of the INR function on the whole 2-D space which is untractable. This incompatibility was the reason why a discrete version of the Lippmann-Schwinger equation (LSD) must be considered in this chapter. INRs fit more a local view of the physics, as is the case of PINNs which are INRs trained to satisfy the local form of differential equations like the Helmholtz equation.

More extensive analysis: The Python toolbox developed for this chapter paved the way for a unified diffraction tomography framework. Due to limited research time and computational resources, many of the observed trends have not been extensively analyzed and are therefore not presented in this chapter. Among them are the SNR increase with the number of views J , the dependence on the arrangement of illumination angles and on the INR architecture (although briefly analyzed for discrete 3-D volume reconstruction in Appendix 6.7.1).

The modular organization of the code allows for easy plugging of other image representations, forward model computations, and inverse problem solving methods. We would be deeply interested in observing future numerical analyses including other INR architectures, different types of RI distributions, and also weight initialization techniques⁵.

Rotation of noncubic volumes: Supported by Fig. 6.6, we explained why it is annoying to consider rotations of an object with dimensions of different lengths. An obvious solution is to consider the object fixed and rotating the illumination. However, in this case, a camera fixed behind the object will not necessarily capture the field diffracted by a high-angle illumination, and rotating the camera plane is accompanied by other challenges not covered in this thesis.

It is not clear whether the consideration of a rotating illumination can induce aliasing effects. Still, it was observed in [MJR23] that rotating the object instead of the illumination increases the image reconstruction accuracy. One perspective of this work is to allow for any rotation of the illumination, object, and camera position.

⁵We considered the idea of initializing the weights of the INR by first reconstructing the measurements backprojected using the First-Born forward operator—out of the scope of this thesis.

Improved reconstruction with passive sources: Passive sources are highly diffracting objects that are generally placed on the sides of the optical path and reflect most of the incoming light so that they can be considered as *passive* illumination sources. We briefly discussed in Sec. 5.2.5 how the Lippmann-Schwinger equation can adequately model the presence of passive sources as if they were new sources of planewaves, and can thus mitigate the missing cone problem by increasing the illumination angle. Overall, we showed that placing passive sources at known positions is equivalent to illuminating the object with a *superposition of planewaves*.

The benefit of passive sources for the inverse problem solving is accompanied with other challenges. If the sources are not sufficiently reflective, their influence on the equivalent illumination is negligible. On the other hand, if the sources are diffracting too much, the Lippmann-Schwinger model cannot be used to compute the resulting illumination. Indeed, we showed in Sec. 5.4.2 that the conditioning of the linear system to be solved for computing the scattered field is getting worse for objects with high contrast. One solution would be to estimate the equivalent illuminating field without passing through the use of Lippmann-Schwinger, assume that the passive sources are far enough to neglect their interaction with the object to be imaged, and then forget their existence.

In the same spirit of considering more elaborate illumination, and more connected to Chap. 3-4, one might consider a **speckle illumination** of the object. Speckles are easy to produce experimentally; they have already been demonstrated under the name of *multiplexed illumination* [MT19]. Moreover, the contributions of Chap. 3-4 seem to indicate that *compressive imaging* is possible for diffraction tomography as well by the means of *random speckle illumination*.

First-Born to Lippmann-Schwinger calibration transfer: Experimental image reconstructions generally require a *calibration phase* that estimates the governing parameters of the imaging modality. Some have already been performed with the **First-Born** model for both ODT [GW02; JG15; Lin+18; MT19] and IDT [Liu+22; Lin+18; Wu+19]. In particular, the calibrated linear forward operator contains information about the *illumination angles*, the *distance to camera*, and the *pupil function* [Lin+18]. We believe that the data contained in the calibrated tensors of the FB model could be transferred to the Lippmann-Schwinger model.

6 | Diffraction Tomography with Implicit Neural Representations

Fully continuous model: A major drawback of the approach proposed in this chapter is the discretization of the volume necessary to use the discrete Lippmann-Schwinger equation. We have shown in Fig. 6.8 that querying the INR on a huge 3-D grid completely overtaxes the memory, making the approach unscalable. To circumvent this, as already mentioned in the discussion of Chap. 5, an appealing idea consists in also using a *continuous representation* for the diffracted field. In other words, the diffracted field might be computed using a PINN. If appropriately trained, the PINN would even be able to predict the scattered field in the camera plane and computing the measurements would be as simple as querying the PINN at the discrete pixel locations of the camera.

Mathematically, the total field would be represented by a PINN as $U_\gamma(\mathbf{r})$ with parameters γ . The INR for the RI object and the PINN for the total field representations might be alternately optimized by solving the minimization problem

$$\tilde{\boldsymbol{\phi}}, \tilde{\boldsymbol{\gamma}} = \arg \min_{\boldsymbol{\phi}, \boldsymbol{\gamma}} \underbrace{\lambda_1 \|\mathbf{y} - \mathbf{u}_{\boldsymbol{\gamma}, \Gamma}\|_2^2}_{\text{Data-consistency}} + \underbrace{\lambda_2 \|(\nabla^2 + k_{\boldsymbol{\phi}}^2(\mathbf{r}))U_\gamma(\mathbf{r})\|_2^2}_{\text{Helmholtz}} + \underbrace{\mathcal{R}(\boldsymbol{\phi}, \boldsymbol{\gamma})}_{\text{Regularization}} , \quad (6.16)$$

where the total field in the camera plane is $\mathbf{u}_{\boldsymbol{\gamma}, \Gamma} := (U_\gamma(\mathbf{r}))_{\mathbf{r} \in \Gamma}$, the INR for the RI object might directly model the square wavenumber $k_{\boldsymbol{\phi}}^2(\mathbf{r})$, otherwise one has $k^2(\mathbf{r}) = f(\mathbf{r}) + k_m^2$ from the definition of the *scattering potential* Def. 5.2.1. The Helmholtz equation in (6.16) would be evaluated at random sampling points of the 3-D space \mathbb{R}^3 , with a denser sampling into the object space Ω and camera space Γ .

An open question is the ill-posedness and convergence of the minimization problem (6.16). Obviously, the PINN might be pretrained with any pre-existing INR of a RI distribution.

6.7 Appendix

6.7.1 Discrete Volume Reconstruction

It is worth evaluating the performance of INRs for the simple construction of a continuous interpolation of a known discrete 3D volume before studying them in the inverse problems related to diffraction tomography. The analysis that follows is mainly prospective and experimental, and may be blind to some recent theoretical results that can characterize the performance of the FFN and SIREN representations.

Learning From Data The adaptation of the weights of the INR, called the *training* phase, is not magic. It consists in defining an error function that includes the output of the network, and then iteratively optimizing these weights to minimize this error. The reader is encouraged to read the reminder on *automatic differentiation* given in Sec. 6.2 to understand the importance of backpropagation in what follows.

In order to train an INR reconstructing a known discrete 3-D volume, let us associate a loss function that captures the reconstruction error of the INR. Let us use f_ϕ to denote either f_ϕ^f or f_ϕ^s . The error writes

$$\mathcal{L}(f, f_\phi) := \frac{1}{2}(f - f_\phi)^2. \quad (6.17)$$

The focus is made on the implicit regularization of the INR architectures and weight optimization scheme, so the loss function (6.17) does not contain any explicit regularization, as usually done when prior information about the volume to be reconstructed is available.

In the aim to save computations, it is common to update the weights of a neural network *in batches*, *i.e.*, for a set \mathcal{B} of training pairs $(\mathbf{r}, f(\mathbf{r}))$ where $f(\mathbf{r})$ is the volume to reconstruct, to infer the output of the INR as $f_\phi(\mathbf{r})$, and then to accumulate the error as

$$\mathcal{L}_{\mathcal{B}}(f, f_\phi) = \sum_{\mathbf{r} \in \mathcal{B}} \mathcal{L}(f(\mathbf{r}), f_\phi(\mathbf{r})) = \frac{1}{2} \|f_{\mathcal{B}} - f_{\phi, \mathcal{B}}\|_2^2$$

before backpropagating the error and computing one optimization step. This is the origin of the term “stochastic” used for the SGD and Adam optimizers given in Algos 6.1-6.2.

In the following experiments, the Adam optimization algorithm will be used by default after demonstrating it outperforms SGD. The initialization of the weights $\phi^{(0)}$ follows [He+15] for the FFN containing an MLP with ReLU activations and follows [Sit+20] for the SIREN.

6 | Diffraction Tomography with Implicit Neural Representations

Numerical analysis The goal of the following experiments is to capture good regimes for the FFN and SIREN. The main parameters tuned for a volume reconstruction are given in Table 6.3. The number of epochs n_{epoch} is the number of times all voxels of the discrete volume f are seen during the training phase. The number of batches per epoch is simply given by $\max(10^6, N_x N_y N_z) / B$, with a maximum of one million voxels per epoch to limit the training time for high resolution volumes.

Table 6.3 Key parameters for the architecture and training of INRs. The spatial frequencies K and the frequency factor ω_l are respectively specific to the FFN and SIREN architectures.

	Symbol	Meaning
Architecture	L	Number of layers.
	n_l	Number of hidden neurons at layer $l \in [L]$.
	K	3-D spatial frequencies of the positional encoding.
	\mathcal{K}	Number of frequencies in K .
Training	ω_l	Frequency factor at layer $l \in [L]$.
	α	Learning rate/stepsizes.
	B	Batch size.
	n_{epoch}	Number of epochs.

For both architectures, the number of trainable parameters $\|\phi\|_0$ scales like

$$\|\phi\|_0 = \left(\sum_{l=0}^{L-1} n_l(n_{l+1} + 1) \right) + n_{\text{out}}(n_{L-1} + 1),$$

where n_l is the number of neurons in the l -th hidden layer, and n_{out} is the number of outputs of the INR; $n_{\text{out}} = 2$ in this work. With the typical values $L = 5$ and $n_l = 256$ for $l \in [L]$ used in the following analyses, the number of parameters is approximately $\|\phi\|_0 \approx 3 \cdot 10^5$.

In Fig. 6.12, we compare the optimizers SGD and Adam, given in Algos 6.1-6.2, respectively. For the discrete volume made of three spheres shown in Fig. 6.12(a), SGD and Adam are used for the exact same architecture of an FFN and similarly for a SIREN. For both cases, it is seen that Adam exhibits a better convergence rate than SGD. This is in agreement, for this specific case, with the results of [KB14].

Fig. 6.13 provides two separated analyses. In Fig. 6.13(a), it is observed that both the FFN and SIREN have a lower error for small batch size B values. It can be explained by the higher number of weight optimization step updates when B is small. However, this plot hides the training time which is inversely proportional to B . So B represents a tradeoff between the error value and the training duration. In

Appendix | 6.7

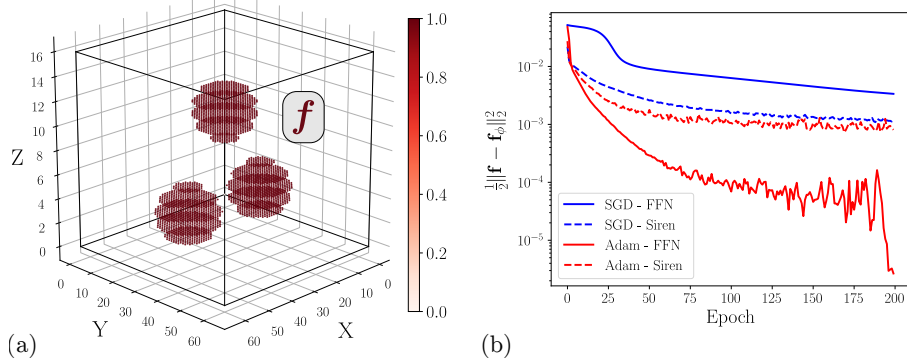


Fig. 6.12 Comparison between the SGD and Adam optimizers for the reconstruction of a discrete volume. (a) Three spheres with centers $(\frac{1}{4}, \frac{1}{2}, \frac{1}{4})$, $(\frac{3}{4}, \frac{1}{2}, \frac{1}{4})$, and $(\frac{1}{2}, \frac{1}{2}, \frac{3}{4})$ and the same radius $\frac{1}{6}$ discretized in $\mathcal{G}_{(64,64,16)}^{(1,1,1)}$. (b) Evolution of the error with the epochs for the SGD and Adam using an FFN (in solid line) with a Gaussian positional encoding containing $\mathcal{K} = 512$ frequencies, and a SIREN (in dashed line) with $\omega_0 = 15$, and $\omega_l = 5, \forall l \in [1, L]$. Both architectures used $L = 5$ layers containing $n_l = 256$ hidden neurons each and were trained with a learning rate $\alpha = 10^{-5}$ and batch size $B = 512$.

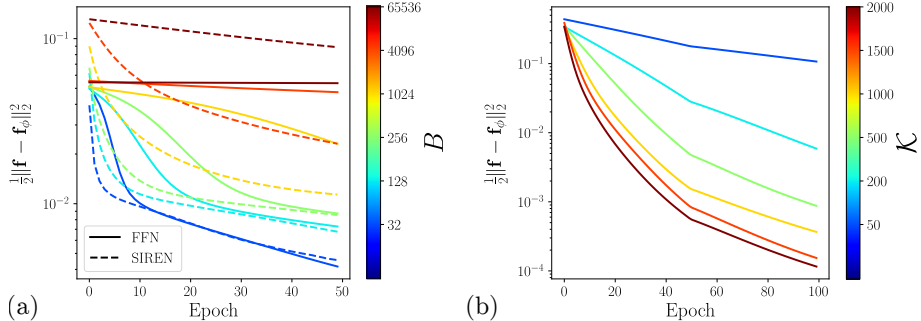


Fig. 6.13 Reconstruction error for the volume given in Fig. 6.12(a). (a) Error in function of the batch size B for an FFN (solid lines), and for a SIREN (dashed lines) using a learning rate $\alpha = 10^{-6}$. (b) Error in function of the number of frequencies \mathcal{K} for a single-layer FFN using $\alpha = 10^{-5}$ and $B = 512$.

Fig. 6.13(b), we numerically verify that increasing the number of random frequencies \mathcal{K} inside the same frequency support in an FFN, even with only the positional encoding and a linear output layer, decreases reconstruction error.

Fig. 6.14 studies the dependence of the reconstruction on the frequency support. For the FFN, the frequency factor ω_0 is defined as the radius in the frequency domain containing 99% of the frequencies drawn by the Gaussian positional encoding, *i.e.*, the frequencies are

6 | Diffraction Tomography with Implicit Neural Representations

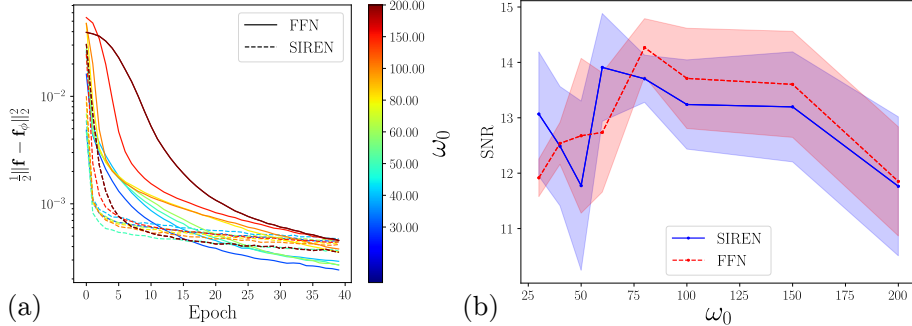


Fig. 6.14 Reconstruction of $S = 4$ volumes made of three spheres with random positions and sizes in $\mathcal{G}'_{(512, 512, 64)}$ as a function of the frequency coverage. The FFN and SIREN are composed of $L = 5$ layers, $n_l = 256$ hidden neurons $\forall l \in \llbracket L \rrbracket$ and trained with a batch size $B = 256$ and learning rate linearly progressing in $[10^{-6}, 10^{-7}]$. The hidden frequency factors of the SIREN are $\omega_l = 30$, $\forall l \in \llbracket L \rrbracket$, and there are $K = 2000$ frequencies in the Gaussian positional encoding of the FFN. 10^6 voxels ($\approx 6\%$) are seen per epoch. (a) Error in function of the epoch and frequency factor ω_0 . (b) SNR in function of ω_0 for a training with $n_{\text{epoch}} = 40$.

drawn as $\mathbf{K}_k \underset{\text{i.i.d.}}{\sim} \mathcal{N}(\mathbf{0}, (\frac{\omega_0}{3})^2 \mathbf{I}_3)$, $\forall k \in \llbracket K \rrbracket$. In Fig. 6.14(a), the curves show the average loss over the reconstruction of the $S = 4$ different volumes.

For both FFN and SIREN, there is no frequency factor value that stands out from the others in terms of reconstruction quality. Fig. 6.14(a) shows that the SIREN converges much faster than the FFN. However, the FFN eventually achieves lower error values than the SIREN for a sufficient number of epochs, which may be due to a better frequency support achieved by the FFN compared to the SIREN built with the same frequency factors $\omega_l = 30$, $\forall l \in \llbracket L \rrbracket$ in the hidden layers. This guess relies on the structured dictionary perspective of INRs given in [Yuc+22, Th. 1].

Fig. 6.15 studies the dependence of the reconstruction on the number of layers L , in a similar setting as in Fig. 6.14. It appears that the number of layers has a weak influence on the reconstruction quality. Our guess is that the sharp transitions at the spheres boundaries induce the *Gibbs phenomenon* [HH79], where an infinite number of frequencies would be necessary to properly represent these transitions.

In Fig. 6.16, we show the reconstruction of a *granulocyte* phantom created using CytoPacq [Wie+19] and already used in [Liu+22] using a SIREN architecture. Fig. 6.16(b) indicates a low SNR value. This is due to the sharp transitions occurring at the granulocytes boundaries. The SIREN having a finite frequency support (see [Yuc+22, Th. 1]), it suffers

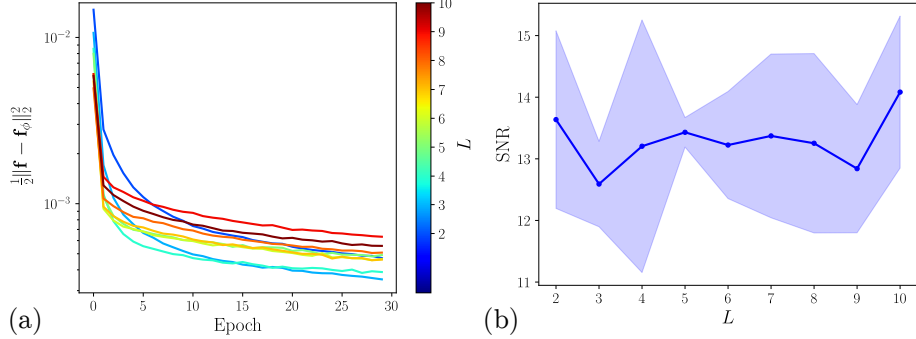


Fig. 6.15 Reconstruction as a function of the number of layers L with the same configuration as in Fig. 6.14, only for the SIREN architecture, with $\omega_0 = 75$.

from the *Gibbs phenomenon*, as seen in Fig. 6.16(a). These conclusions are also valid for the FFN architecture.

The conclusions of this section that will be useful for the experiments coming in Sec. 6.5 are:

- Ignoring the training time, a small batch size B is better.
- The positional encoding of an FFN needs a high number of frequencies.
- The frequency factor ω_0 alone is of little importance.

Based on these conclusions, the default values will be set to $B = 256$, $\mathcal{K} = 2000$, and $\omega_0 = 30$.

6.7.2 Implicit Regularization of GD

This section aims to provide a possible explanation for the underestimation of the scattering potential observed in the results presented in Sec. 6.5.2.

To do so, let us consider a simple linear system $\mathbf{L}\mathbf{u} = \mathbf{y}$ that needs to be inverted, where the matrix $\mathbf{L} \in \mathbb{C}^{n \times n}$ has a kernel dimension $n - k$, for $0 \leq k \leq n$, $\mathbf{y} \in \mathbb{C}^n$ is the observation vector, and $\mathbf{u} \in \mathbb{C}^n$ is the sought solution. The minimum energy solution

$$\min_{\mathbf{u} \in \mathbb{C}^n} \frac{1}{2} \|\mathbf{L}\mathbf{u} - \mathbf{y}\|_2^2 \quad (6.18)$$

is a set. Indeed, if \mathbf{u}^* is a solution, then $\mathbf{u}^* + \ker \mathbf{L}$ is the set of solutions. However, running the Gradient Descent (GD) algorithm on this mini-

6 | Diffraction Tomography with Implicit Neural Representations

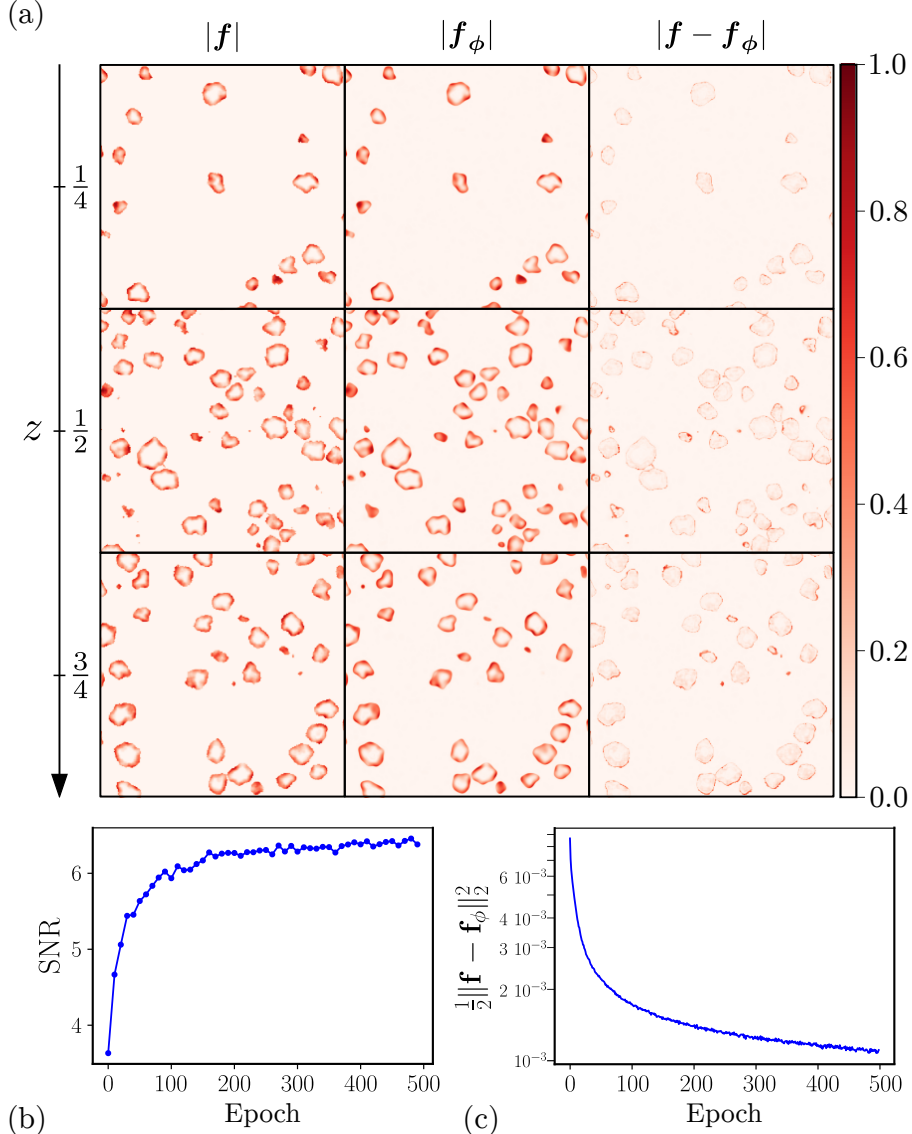


Fig. 6.16 Reconstruction f_ϕ of the cytgranulocyte phantom $f \in \mathcal{G}_{(512,512,64)}^{(1,1,1)}$ used in [Liu+22]. We use a SIREN with $L = 6$ layers, $n_l = 256$, $\forall l \in \llbracket L \rrbracket$ hidden neurons per layer, $\omega_0 = 75$, and $\omega_l = 30$, $\forall l \in \llbracket L \rrbracket$ trained over $n_{\text{epoch}} = 500$ with a learning rate α linearly progressing in $[10^{-6}, 10^{-7}]$, and a batch size $B = 256$. (a) absolute values of the GT, reconstruction, and error given for the slices at $z \in \{\frac{1}{4}, \frac{1}{2}, \frac{3}{4}\}$. (b) Evolution of the SNR with the epochs. (c) Evolution of the loss with the epochs.

mization for a stepsize $\alpha \leq \frac{2}{\|L\|^2}$ and initial condition $\mathbf{u}^{(0)} = \mathbf{0}$ provides a vector

$$\mathbf{u}^{(k+1)} = \mathbf{u}^{(k)} - \alpha L^* (L\mathbf{u}^{(k)} - \mathbf{y}) = (\mathbf{I}_n - \alpha L^* L)\mathbf{u}^{(k)} + \alpha L^* \mathbf{y}.$$

Therefore, $\mathbf{u}^{(\infty)} = \sum_{k=0}^{\infty} (\mathbf{I}_n - \alpha \mathbf{L}^* \mathbf{L})^k \alpha \mathbf{L}^* \mathbf{y}$ is not a set. Let us further analyze the obtained solution by expliciting the SVD $\mathbf{L} = \underset{\text{SVD}}{\mathbf{U}} \underset{n \times k}{\Sigma} \underset{k \times k}{\mathbf{V}} \underset{k \times n}{\mathbf{V}^*}$. As \mathbf{V} can be factorized on the left-side of the expression of $\mathbf{u}^{(\infty)}$, from the identity $\mathbf{V}^* \mathbf{V} = \mathbf{I}$, one has $\mathbf{u}^{(\infty)} = \mathbf{V} \mathbf{V}^* \mathbf{u}^{(\infty)}$. Then,

$$\begin{aligned} \underset{k \times n}{\mathbf{V}^*} (\mathbf{I}_n - \alpha \mathbf{L}^* \mathbf{L})^k &= \mathbf{V}^* (\mathbf{I}_n - \alpha \underbrace{\mathbf{L}^* \mathbf{L}}_{\mathbf{V} \Sigma^2 \mathbf{V}^*}) (\mathbf{I}_n - \alpha \mathbf{L}^* \mathbf{L})^{k-1} \\ &= (\mathbf{I}_k - \alpha \underbrace{\mathbf{V}^* \mathbf{L}^* \mathbf{L} \mathbf{V}}_{k \times k}) \mathbf{V}^* (\mathbf{I}_n - \alpha \mathbf{L}^* \mathbf{L})^{k-1} \\ &= (\mathbf{I}_k - \alpha \mathbf{V}^* \mathbf{L}^* \mathbf{L} \mathbf{V})^k \mathbf{V}^*. \end{aligned}$$

Therefore,

$$\mathbf{u}^{(\infty)} = \mathbf{V} \mathbf{V}^* \mathbf{u}^{(\infty)} = \mathbf{V} (\mathbf{V}^* \mathbf{L}^* \mathbf{L} \mathbf{V})^{-1} \mathbf{V}^* \mathbf{L}^* \mathbf{y} = \mathbf{V} (\mathbf{L} \mathbf{V})^\dagger \mathbf{y}. \quad (6.19)$$

Eq. (6.19) shows that GD enforces $\mathbf{u}_{\ker \mathbf{L}} = 0$ if started at $\mathbf{u}^{(0)} = \mathbf{0}$, as $\mathbf{V} \mathbf{V}^*$ projects on $\text{Im}(\mathbf{L})$ with \mathbf{V}^* then zeropads on $\ker(\mathbf{L})$ with \mathbf{V} . This is the *implicit regularization* effect. This effect is valid for more general cases than GD applied to a square linear system as proposed here. As minimization problems like (6.18) provide a minimum energy solution, and the true solution has generally a nonzero value in the part of the information lost by the effect of the measurement operator, this results in an underestimation.

6.7.3 Linearizing IDT

This section demonstrates how a linear forward model can still be obtained in IDT under the First-Born approximation. This linearization is not new [Wu+19].

Under the *weak scattering* assumption $\mathbf{u}_s \ll \mathbf{u}_i$, the validity of the First-Born approximation is sufficient and the IDT measurements can be linearized. Indeed, using (FBd) for the (IDT) model, the measurement vector writes

$$\begin{aligned} \mathbf{y} &= |\mathbf{H} \mathbf{u}_i + \mathbf{H} \mathbf{G} \mathbf{D}_{\mathbf{u}_i} \mathbf{f}|^2 \\ &= |\mathbf{H} \mathbf{u}_i|^2 + |\mathbf{H} \mathbf{G} \mathbf{D}_{\mathbf{u}_i} \mathbf{f}|^2 + \Re\{2 \text{diag}(\mathbf{H} \mathbf{u}_i)^* \mathbf{H} \mathbf{G} \mathbf{D}_{\mathbf{u}_i} \mathbf{f}\}. \end{aligned} \quad (6.20)$$

Removing the background intensity $|\mathbf{R} \mathbf{u}_i|^2$ from the measurements either by model estimation or by calibration, and neglecting the quadratic term $|\mathbf{R} \mathbf{G} \mathbf{D}_{\mathbf{u}_i} \mathbf{f}|^2$ because of the weak scattering assumption yields

$$\mathbf{y}' := \mathbf{y} - |\mathbf{H} \mathbf{u}_i|^2 \approx \Re\{2 \text{diag}(\mathbf{H} \mathbf{u}_i)^* \mathbf{H} \mathbf{G} \mathbf{D}_{\mathbf{u}_i} \mathbf{f}\} = \Re\{\mathbf{B} \mathbf{f}\}. \quad (6.21)$$

6 | Diffraction Tomography with Implicit Neural Representations

Eq. (6.21) is linear in f regardless of the choice of \mathbf{u}_i . By separating f into its real part $f_{\mathcal{R}}$ and imaginary part $f_{\mathcal{I}}$, it can be modeled equivalently as

$$\mathbf{y}' = \bar{\mathbf{B}}\bar{\mathbf{f}} := [\mathbf{B}_{\mathcal{R}} \quad \mathbf{B}_{\mathcal{I}}] \begin{bmatrix} f_{\mathcal{R}} \\ f_{\mathcal{I}} \end{bmatrix}. \quad (6.22)$$

Fourier Model Under Planewave Illuminations

When the incident field is a planewave $U_i(\mathbf{r}) = e^{ik_i^\top \mathbf{r}}$ with incident wavevector k_i , then, as shown in [Wol69], a *Weyl expansion* of the Green function G allows to express the linear forward model in the Fourier domain. In discrete, the forward model can be recast with FFT operators as

$$\mathbf{y}' = \mathbf{F}_2^{-1} \mathbf{T} \mathbf{F}_2 \mathbf{f}$$

where \mathbf{F}_2 takes the 2-D FFT along each transverse XY-slice of f , and $\mathbf{T} \in \mathbb{C}^{JN_x N_y \times JN_x N_y N_z}$ is a transfer function occurring in the Fourier domain that handles the camera pupil mask and the phase modulation due to the planewave illumination, and sums along the axial Z-axis. In recent experimental reconstruction results in IDT using the **First-Born** approximation [Liu+22; Lin+18], the calibration phase aimed at applying corrections to \mathbf{T} .

This model, considered in [Liu+22; Li+20; MT19], needs planewave illuminations to be valid. Eventually, the illumination can be modeled as a finite sum of planewaves which implies a transfer function of the form $\mathbf{T} = \sum_{m,m'} \mathbf{T}_{m,m'}$ where the illuminating field writes $\mathbf{u}^i = \sum_m \mathbf{u}_m^i$ with $\mathbf{u}_m^i := e^{-ik_m^\top \mathbf{r}}$.

References

- [Bay+18] A. G. Baydin et al. “Automatic Differentiation in Machine Learning: a Survey”. In: *Journal of Machine Learning Research* 18.153 (2018), pp. 1–43.
- [BB08] P. T. Boufounos and R. G. Baraniuk. “1-Bit compressive sensing”. In: *2008 42nd Annual Conference on Information Sciences and Systems*. 2008, pp. 16–21. DOI: [10.1109/CISS.2008.4558487](https://doi.org/10.1109/CISS.2008.4558487).
- [BCL02] H. H. Bauschke, P. L. Combettes, and D. R. Luke. “Phase retrieval, error reduction algorithm, and Fienup variants: a view from convex optimization”. In: *J. Opt. Soc. Am. A* 19.7 (July 2002), pp. 1334–1345. DOI: [10.1364/JOSAA.19.001334](https://doi.org/10.1364/JOSAA.19.001334).
- [BOC03] G. Bibes, R. Ouvrard, and P. Coirault. “A regularization method for nonlinear inverse problems by using a volterra model”. In: *2003 European Control Conference (ECC)*. IEEE. 2003, pp. 2068–2072.
- [Che+20a] M. Chen et al. “Multi-layer Born multiple-scattering model for 3D phase microscopy”. In: *Optica* 7.5 (May 2020), pp. 394–403. DOI: [10.1364/OPTICA.383030](https://doi.org/10.1364/OPTICA.383030).
- [Che+20b] Y. Chen et al. “Physics-Informed Neural Networks for Inverse Problems in Nano-Optics and Metamaterials”. In: *Optics Express* 28.8 (2020), pp. 11618–11633. DOI: [10.1364/OE.391036](https://doi.org/10.1364/OE.391036).
- [Dev81] A. J. Devaney. “Inverse-scattering theory within the Ryttov approximation”. In: *Opt. Lett.* 6.8 (Aug. 1981), pp. 374–376. DOI: [10.1364/OL.6.000374](https://doi.org/10.1364/OL.6.000374).
- [Ela+18] N. Eladawi et al. “Classification of retinal diseases based on OCT images”. In: *Front Biosci* 23.2 (2018), pp. 247–264.
- [Fie82] J. R. Fienup. “Phase retrieval algorithms: a comparison”. In: *Appl. Opt.* 21.15 (Aug. 1982), pp. 2758–2769. DOI: [10.1364/AO.21.002758](https://doi.org/10.1364/AO.21.002758).

6 | References

- [GW02] G. Gbur and E. Wolf. “Diffraction tomography without phase information”. In: *Opt. Lett.* 27.21 (Nov. 2002), pp. 1890–1892. DOI: [10.1364/OL.27.001890](https://doi.org/10.1364/OL.27.001890).
- [Ham+07] U. Hampel et al. “High resolution gamma ray tomography scanner for flow measurement and non-destructive testing applications”. In: *Review of scientific instruments* 78.10 (2007).
- [He+15] K. He et al. “Delving Deep into Rectifiers: Surpassing Human-Level Performance on ImageNet Classification”. In: *Proceedings of the IEEE International Conference on Computer Vision (ICCV)*. 2015, pp. 1026–1034. DOI: [10.1109/ICCV.2015.123](https://doi.org/10.1109/ICCV.2015.123).
- [HH79] E. Hewitt and R. Hewitt. “The Gibbs-Wilbraham Phenomenon: An Episode in Fourier Analysis”. In: *Archive for History of Exact Sciences* 21.2 (1979), pp. 129–160.
- [JG15] M. H. Jenkins and T. K. Gaylord. “Three-dimensional quantitative phase imaging via tomographic deconvolution phase microscopy”. In: *Appl. Opt.* 54.31 (Nov. 2015), pp. 9213–9227. DOI: [10.1364/AO.54.009213](https://doi.org/10.1364/AO.54.009213).
- [Kam+15] U. S. Kamilov et al. “Learning approach to optical tomography”. In: *Optica* 2.6 (June 2015), pp. 517–522. DOI: [10.1364/OPTICA.2.000517](https://doi.org/10.1364/OPTICA.2.000517).
- [Kam+16a] U. S. Kamilov et al. “A Recursive Born Approach to Non-linear Inverse Scattering”. In: *IEEE Signal Processing Letters* 23.8 (2016), pp. 1052–1056. ISSN: 10709908. DOI: [10.1109/LSP.2016.2579647](https://doi.org/10.1109/LSP.2016.2579647). arXiv: [1603.03768](https://arxiv.org/abs/1603.03768).
- [Kam+16b] U. S. Kamilov et al. “Optical Tomographic Image Reconstruction Based on Beam Propagation and Sparse Regularization”. In: *IEEE Transactions on Computational Imaging* 2.1 (2016), pp. 59–70. DOI: [10.1109/TCI.2016.2519261](https://doi.org/10.1109/TCI.2016.2519261).
- [KB14] D. P. Kingma and J. Ba. “Adam: A method for stochastic optimization”. In: *arXiv preprint arXiv:1412.6980* (2014).
- [Kim11] M. K. Kim. *Digital Holographic Microscopy: Principles, Techniques, and Applications*. New York: Springer, 2011. ISBN: 978-1-4419-7792-2.
- [KS01] A. C. Kak and M. Slaney. *Principles of computerized tomographic imaging*. Reprint of 1988 IEEE Press edition. Bellingham, WA: Society of Photo-Optical Instrumentation Engineers (SPIE), 2001.

- [Li+20] J. Li et al. "High-speed in vitro intensity diffraction tomography". In: 200 (2020). arXiv: [arXiv:1904.06004v3](https://arxiv.org/abs/1904.06004v3).
- [Lim+15] J. Lim et al. "Comparative study of iterative reconstruction algorithms for missing cone problems in optical diffraction tomography". In: *Opt. Express* 23.13 (June 2015), pp. 16933–16948. DOI: [10.1364/OE.23.016933](https://doi.org/10.1364/OE.23.016933).
- [Lim+19] J. Lim et al. "High-fidelity optical diffraction tomography of multiple scattering samples". In: *Light: Science & Applications* 8 (Sept. 2019). DOI: [10.1038/s41377-019-0195-1](https://doi.org/10.1038/s41377-019-0195-1).
- [Lin+18] R. Ling et al. "High-throughput intensity diffraction tomography with a computational microscope". In: *Biomed. Opt. Express* 9.5 (May 2018), pp. 2130–2141. DOI: [10.1364/BOE.9.002130](https://doi.org/10.1364/BOE.9.002130).
- [Liu+18] H.-Y. Liu et al. "SEAGLE: Sparsity-Driven Image Reconstruction Under Multiple Scattering". In: *IEEE Transactions on Computational Imaging* 4.1 (2018), pp. 73–86. DOI: [10.1109/TCI.2017.2764461](https://doi.org/10.1109/TCI.2017.2764461).
- [Liu+22] R. Liu et al. "Recovery of continuous 3D refractive index maps from discrete intensity-only measurements using neural fields". In: *Nature Machine Intelligence* 4.9 (Sept. 2022), pp. 781–791. ISSN: 2522-5839. DOI: [10.1038/s42256-022-00530-3](https://doi.org/10.1038/s42256-022-00530-3).
- [Ma+18] Y. Ma et al. "Accelerated Image Reconstruction for Non-linear Diffractive Imaging". In: *2018 IEEE International Conference on Acoustics, Speech and Signal Processing (ICASSP)*. 2018, pp. 6473–6477. DOI: [10.1109/ICASSP.2018.8462400](https://doi.org/10.1109/ICASSP.2018.8462400).
- [Mar+21] J. N. P. Martel et al. *ACORN: Adaptive Coordinate Networks for Neural Scene Representation*. 2021. arXiv: [2105.02788](https://arxiv.org/abs/2105.02788).
- [MCW05] P. Y. Maeda, P. B. Catrysse, and B. A. Wandell. "Integrating Lens Design with Digital Camera Simulation". In: *Proceedings of SPIE - The International Society for Optical Engineering*. Vol. 5678. 2005, pp. 48–58. DOI: [10.1117/12.588153](https://doi.org/10.1117/12.588153).
- [MI07] G. Möbus and B. J. Inkson. "Nanoscale tomography in materials science". In: *Materials Today* 10.12 (2007), pp. 18–25.

6 | References

- [Mil+20] B. Mildenhall et al. “NeRF: Representing Scenes as Neural Radiance Fields for View Synthesis”. In: (2020). arXiv: 2003.08934 [cs.CV].
- [MJR23] S. Moser, A. Jesacher, and M. Ritsch-Marte. “Efficient and accurate intensity diffraction tomography of multiple-scattering samples”. In: *Opt. Express* 31.11 (May 2023), pp. 18274–18289. DOI: [10.1364/OE.486296](https://doi.org/10.1364/OE.486296).
- [MS09] K. Matsushima and T. Shimobaba. “Band-limited angular spectrum method for numerical simulation of free-space propagation in far and near fields”. In: *Optics Express* 17.22 (2009), pp. 19662–19673. DOI: [10.1364/OE.17.019662](https://doi.org/10.1364/OE.17.019662).
- [MSW12] S. C. Mayo, A. W. Stevenson, and S. W. Wilkins. “In-line phase-contrast X-ray imaging and tomography for materials science”. In: *Materials* 5.5 (2012), pp. 937–965.
- [MT19] A. Matlock and L. Tian. “High-throughput, volumetric quantitative phase imaging with multiplexed intensity diffraction tomography”. In: *Biomedical Optics Express* 10.12 (2019), p. 6432. ISSN: 2156-7085. DOI: [10.1364/boe.10.006432](https://doi.org/10.1364/boe.10.006432).
- [Mül+22] T. Müller et al. “Instant neural graphics primitives with a multiresolution hash encoding”. In: *ACM Transactions on Graphics* 41.4 (July 2022), pp. 1–15. ISSN: 1557-7368. DOI: [10.1145/3528223.3530127](https://doi.org/10.1145/3528223.3530127).
- [Ngu+17] T. Nguyen et al. “Gradient light interference microscopy for 3D imaging of unlabeled specimens”. In: *Nature Communications* 8 (Dec. 2017). DOI: [10.1038/s41467-017-00190-7](https://doi.org/10.1038/s41467-017-00190-7).
- [Pha+18] T.-a. Pham et al. “Phaseless diffraction tomography with regularized beam propagation”. In: Apr. 2018, pp. 1268–1271. DOI: [10.1109/ISBI.2018.8363802](https://doi.org/10.1109/ISBI.2018.8363802).
- [Pha+20] T.-a. Pham et al. “Three-Dimensional Optical Diffraction Tomography With Lippmann-Schwinger Model”. In: *IEEE Transactions on Computational Imaging* 6 (2020), pp. 727–738. DOI: [10.1109/TCI.2020.2969070](https://doi.org/10.1109/TCI.2020.2969070).
- [PRG16] A. du Plessis, S. G. le Roux, and A. Guelpa. “Comparison of medical and industrial X-ray computed tomography for non-destructive testing”. In: *Case Studies in Non-destructive Testing and Evaluation* 6 (2016), pp. 17–25.

- [Reb+15] G. Rebollo et al. “OCT: new perspectives in neuro-ophthalmology”. In: *Saudi Journal of Ophthalmology* 29.1 (2015), pp. 9–25.
- [Ros58] F. Rosenblatt. “The perceptron: a probabilistic model for information storage and organization in the brain”. In: *Psychological review* 65.6 (1958), p. 386.
- [RPK19] M. Raissi, P. Perdikaris, and G. Karniadakis. “Physics-informed neural networks: A deep learning framework for solving forward and inverse problems involving nonlinear partial differential equations”. In: *Journal of Computational Physics* 378 (2019), pp. 686–707. ISSN: 0021-9991. DOI: <https://doi.org/10.1016/j.jcp.2018.10.045>.
- [She+14] Y. Shechtman et al. *Phase Retrieval with Application to Optical Imaging*. 2014. arXiv: [1402.7350](https://arxiv.org/abs/1402.7350).
- [Sit+20] V. Sitzmann et al. “Implicit Neural Representations with Periodic Activation Functions”. In: *arXiv*. 2020.
- [SPU17] E. Soubies, T.-A. Pham, and M. Unser. “Efficient inversion of multiple-scattering model for optical diffraction tomography”. In: *Opt. Express* 25.18 (Sept. 2017), pp. 21786–21800. DOI: [10.1364/OE.25.021786](https://doi.org/10.1364/OE.25.021786).
- [SXK18] Y. Sun, Z. Xia, and U. S. Kamilov. “Efficient and accurate inversion of multiple scattering with deep learning”. In: *Opt. Express* 26.11 (May 2018), pp. 14678–14688. DOI: [10.1364/OE.26.014678](https://doi.org/10.1364/OE.26.014678).
- [Tan+20] M. Tancik et al. “Fourier Features Let Networks Learn High Frequency Functions in Low Dimensional Domains”. In: *arXiv preprint arXiv:2006.10739* (2020).
- [TD00] G. Tsirhrintzis and A. Devaney. “Higher order (nonlinear) diffraction tomography: inversion of the Rytov series”. In: *IEEE Transactions on Information Theory* 46.5 (2000), pp. 1748–1761. DOI: [10.1109/18.857788](https://doi.org/10.1109/18.857788).
- [TW15] L. Tian and L. Waller. “3D intensity and phase imaging from light field measurements in an LED array microscope”. In: *Optica* 2.2 (Feb. 2015), pp. 104–111. DOI: [10.1364/OPTICA.2.000104](https://doi.org/10.1364/OPTICA.2.000104).
- [Wie+19] D. Wiesner et al. “CytoPacq: a web-interface for simulating multi-dimensional cell imaging”. In: *Bioinformatics* 35.21 (2019), pp. 4531–4533. DOI: [10.1093/bioinformatics/btz417](https://doi.org/10.1093/bioinformatics/btz417).

6 | References

- [Wol69] E. Wolf. "Three-dimensional structure determination of semi-transparent objects from holographic data". In: *Optics Communications* 1.4 (1969), pp. 153–156. ISSN: 0030-4018. DOI: [https://doi.org/10.1016/0030-4018\(69\)90052-2](https://doi.org/10.1016/0030-4018(69)90052-2).
- [Wu+19] Z. Wu et al. "SIMBA: Scalable Inversion in Optical Tomography Using Deep Denoising Priors". In: *IEEE Journal of Selected Topics in Signal Processing* 14 (2019), pp. 1163–1175.
- [Yuc+22] G. Yuce et al. "A Structured Dictionary Perspective on Implicit Neural Representations". In: *Proceedings of the IEEE Computer Society Conference on Computer Vision and Pattern Recognition* 2022-June (2022), pp. 19206–19216. ISSN: 10636919. DOI: [10.1109/CVPR52688.2022.01863](https://doi.org/10.1109/CVPR52688.2022.01863). arXiv: [2112.01917](https://arxiv.org/abs/2112.01917).
- [ZBG24] C. Zeng, T. Burghardt, and A. M. Gambaruto. *RBF-PINN: Non-Fourier Positional Embedding in Physics-Informed Neural Networks*. 2024. arXiv: [2402.08367](https://arxiv.org/abs/2402.08367).
- [ZH20] K. C. Zhou and R. Horstmeyer. "Diffraction tomography with a deep image prior". In: *Opt. Express* 28.9 (Apr. 2020), pp. 12872–12896. DOI: [10.1364/OE.379200](https://doi.org/10.1364/OE.379200).
- [ZWT22] J. Zhu, H. Wang, and L. Tian. "High-fidelity intensity diffraction tomography with a non-paraxial multiple-scattering model". In: *Opt. Express* 30.18 (Aug. 2022), pp. 32808–32821. DOI: [10.1364/OE.469503](https://doi.org/10.1364/OE.469503).

7

Conclusion

7.1 Summary of the Chapters

In this dissertation, as summarized in Fig. 7.1, we have extended the field of computational imaging in two main directions:

- **Compressive interferometric imaging:** compressive imaging techniques for multicore fiber lensless imaging in Chap. 3 and radio-interferometry in Chap. 4.
- **Diffraction tomography:** review of the different ways to model electromagnetic wave diffraction through inhomogeneous media in Chap. 5 and combination of an *implicit neural representation* and a nonlinear (multiple-scattering) sensing model in Chap. 6.

In this section, we summarize the contributions of each chapter in a few paragraphs below. The discussions and perspectives of each chapter are synthesized in Fig. 7.1.

Chapter 3: Multi-Core Fiber Lensless Imaging

Chapter 3 presented advancements in the field of MCFLI. Our research began by leveraging a *speckle illumination model* to underscore the interferometric nature of the MCF device. This foundational insight led to the development of a sensing model more closely aligned with the physical principles underlying MCFLI. This approach provided clear explanations for previously considered illumination modes and core arrangement designs from an interferometric perspective.

Further, we expanded the modeling of MCFLI by incorporating the physics of light propagation. This enhanced model revealed that the

7 | Conclusion

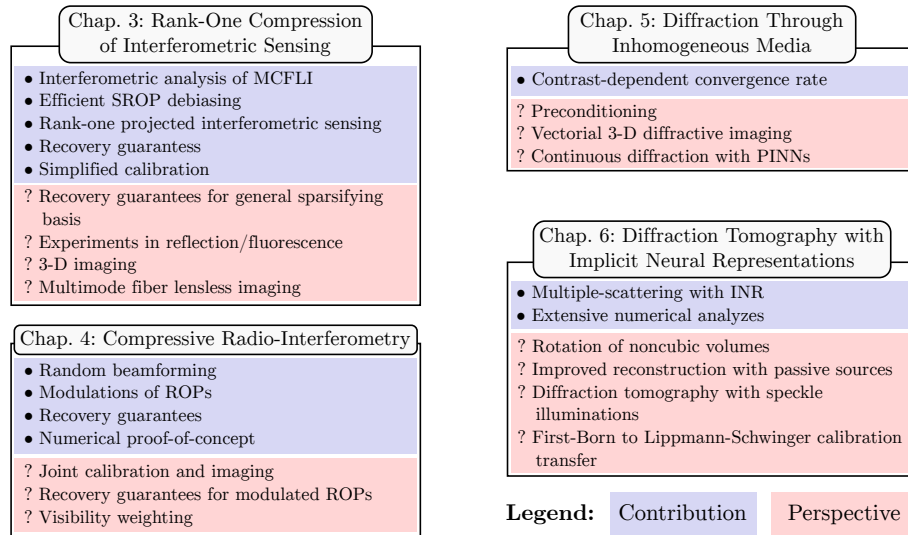


Fig. 7.1 Summary of the contributions and potential perspectives of this thesis.

accuracy of sensing a 2-D refractive index map is constrained by both the number M of applied illuminations and the number Q and arrangement of cores at the distal end of the MCF.

We provided uniform image *recovery guarantees* under realistic assumptions, which were validated through numerical phase transition diagrams. These theoretical settings were extended to more realistic image recovery in actual experimental setups. Observing the derived sample complexities in both numerical and experimental conditions confirmed the robustness and practicality of our model.

In summary, this chapter not only deepened theoretical understanding and provided practical validation for MCFLI but also emphasized the critical role of interferometric principles and light propagation physics in enhancing the design and application of multi-core fiber imaging systems.

Chapter 4: Compressive Radio-Interferometry.

In Chapter 4, we transferred and extended the contributions of Chapter 3 to another interferometric imaging modality: *Radio-Interferometry*. Initially, we re-explained the conventional imaging principle, which relied on the *covariance matrix* of the measurement vector and was intrinsically related to Fourier subsampling of the image of interest. The significant advancement presented in this chapter was the introduction of a novel approach where a random projection of the measurement vec-

tor, known as *random beamforming*, was computed before determining its covariance. This approach resulted in getting random *rank-one projections* of the covariance matrix, enabling the reuse of methodologies from Chapter 3 to achieve *compressive radio-interferometric imaging*.

The novelty of this compression scheme lay in its ability to reduce all computational costs: (i) computations during acquisition, (ii) the number of measurements, and (iii) the computation of the forward model. This efficiency was crucial for practical applications, making the technique both scalable and effective.

Similarly to the previous chapter, we provided *uniform recovery guarantees* and validated them numerically through phase transition diagrams. Additional numerical analyses were conducted in a state-of-the-art realistic simulation setting.

In summary, this chapter extended the theoretical and practical advancements in radio-interferometric imaging, offering a computationally efficient and robust framework. This work paved the way for further innovations in compressive imaging techniques, with potential applications to other interferometric imaging modalities.

Chapter 5: Diffraction Through Inhomogeneous Media

This chapter contributed to the intricate modeling of *diffraction tomography*, particularly focusing on electromagnetic wave propagation through inhomogeneous 3-D refractive index distributions. Given the complexity and vastness of the topic, this chapter primarily addressed the foundational aspects of the diffraction model.

We began by revisiting the key simplifying assumptions underlying the *Helmholtz equation* and its integral form tailored for inhomogeneous media, known as the *Lippmann-Schwinger equation*. This exact nonlinear equation was compared with other prevalent scattering models, highlighting their status as approximations. Special attention was given to the *First-Born approximation*, which, through the *Fourier Diffraction theorem*, offers a clear perspective on the information captured in tomographic imaging scenarios.

Subsequently, we focused on an efficient discretization of the Lippmann-Schwinger model. The resultant linear system was thoroughly analyzed using *first-order optimization methods*. Our numerical experiments underscored the impact of the refractive index distribution's *contrast* on the *condition number* of the linear system.

7 | Conclusion

Chapter 6: Diffraction Tomography with Implicit Neural Representations

In Chapter 6, we built upon the results of Chapter 5 to establish a comprehensive setting for diffraction tomography, incorporating *implicit neural representations* (INRs).

The first distinctive feature of this chapter is the continuous representation of the 3-D image using an INR. This approach offers several advantages: (i) it provides a reduced parameterization of the image, (ii) it facilitates the handling of continuous 3-D rotations, and (iii) it enables automatic image reconstruction through automatic differentiation and gradient backpropagation.

Another significant aspect of this chapter is the focus on nonlinear sensing models for *optical* and *intensity diffraction tomography* (resp. ODT and IDT). These nonlinear models offer a novel perspective compared to the linear approximations related to the First-Born approximation discussed previously. Through numerical simulations, we demonstrated that the nonlinearity of the sensing model, closer to reality, enhances image recovery quality.

7.2 Future Work and Comments

Bridging Chap. 3-4 with Chap. 5-6

3-D interferometric imaging Chap. 3-4 assume that the object of interest is purely 2-D which is an oversimplification in both cases. For MCFLI, assuming that (i) the 3-D fluorophore density map does not influence the 3-D speckle produced by the MCF, and that (ii) the far-field assumption still holds, which implies that the speckle is completely developed and varies with the depth only by a scaling, a single-pixel measurement is equivalent to a projection of a 2-D speckle with the projection of the 3-D map along expanding line over the depth-axis. Similarly to the context of Chap. 5-6, this corresponds to a loss of information in depth. In this case, the information in depth can only be recovered by illuminating the sample of interest from different orientations, resulting in another *tomographic imaging* context.

Conversely, any tomographic imaging scenario could be adapted to utilize speckle-based illumination, leading to a combined *interferometric and tomographic* imaging problem.

Learning techniques The use of deep learning was only introduced in Chap. 6. Notably, the neural architecture employed for the Implicit Neural Representation (INR) is designed not as a data-driven learning modality, but to deliver an efficient continuous representation of a 3D volume. While Chap. 3-4 primarily concentrated on the acquisition and imaging models inherent in the compressive imaging schemes, and Chap. 5-6 explored the innovative integration of an INR with a nonlinear sensing model, their synergy with advanced reconstruction techniques, such as *deep denoisers* [VBW13; KMW18] or those that learn the distribution of signals for specific applications, remains intact. Moreover, Sec. 4.7 elucidates that the proposed compressive model for radio-interferometry is compatible with two recent state-of-the-art reconstruction algorithms: AIRI and R2D2.

About automatic differentiation Chap. 6 introduced *automatic differentiation* (AD) and outlined in Sec. 6.1 its utility in automatically computing the gradient of a loss function with respect to the problem's parameters (*e.g.*, image pixels), thereby bypassing the tedious task of manual gradient derivation. AD extends beyond first-order derivatives, enabling the computation of second-order derivatives required for advanced optimization methods like the *Newton method* in (Newton). While AD was not explicitly necessary in Chap. 3-4 due to the ℓ_2 -norm data fidelity term in image reconstruction, which primarily required the adjoint operator, it could still have been employed. This highlights that AD is not always essential, particularly when straightforward, closed-form gradient expressions are available.

Other applications of compressive interferometric imaging

Chap. 3 and Chap. 4 presented two imaging applications which share the same conditions to yield an interferometric model: (*i*) several elements must interfere, and (*ii*) *incoherence*¹. In Chap. 3, the interferometric model was the result of a *fluorescence* phenomenon, making the sample of interest interact *incoherently* with the illumination of the MCF. In Chap. 4, it was due to the Van Cittert-Zernike theorem and the incoherence of the cosmic sources, *i.e.*, the statistical independence between the cosmic signals coming from distinct directions.

There exist other computational imaging applications with incoherent illumination such as fluorescence microscopy or X-ray and Gamma-

¹If the object interacts coherently with the illumination, this results in a phase retrieval problem [CSV13].

7 | Conclusion

ray imaging. The contributions of Chap. 3-4 could be applied to these applications as long as multiple illuminating components interfere to produce the illumination.

In a broader context, in line with Chap. 4, our compressive sensing proposition might be useful for any existing application that involve a *covariance matrix* whose entries are associated to a subsampling (not necessarily in Fourier) of the image of interest.

List of symbols and acronyms

AD	Automatic Differentiation (p. 254)
AS	Angular Spectrum (p. 261)
BPDN	Basis Pursuit DeNoise (p. 39)
BPM	Beam Propagation Method (p. 236)
CI	Computational Imaging (p. 2)
CS	Compressive Sensing (p. 47)
DFT	Discrete Fourier Transform (p. 81)
DNN	Deep Neural Network (p. 127)
FB	First-Born (p. 210)
FFN	Fourier Feature Network (p. 252)
FFT	Fast Fourier Transform (p. 6)
GT	Ground Truth (p. 102)
IDT	Intensity Diffraction Tomography (p. 251)
IP	Inverse Problem (p. 3)
LS	Lippmann-Schwinger (p. 203)
MAP	Maximum A Posteriori (p. 39)
MCFLI	MultiCore Fiber Lensless Imaging (p. 66)
MLP	MultiLayer Perceptron (p. 257)
MMF	MultiMode Fiber (p. 69)
MRI	Magnetic Resonance Imaging (p. 1)

7 | List of symbols and acronyms

NA	Numerical Aperture (p. 98)
NUFFT	NonUniform Fast Fourier Transform (p. 125)
ODT	Optical Diffraction Tomography (p. 251)
PGM	Proximal Gradient Method (p. 43)
PINN	Physics-Informed Neural Network (p. 252)
PnP	Plug-and-Play (p. 179)
PR	Phase Retrieval (p. 68)
PSF	Point-Spread Function (p. 183)
ReLU	Rectified Linear Unit (p. 257)
RI	Radio-Interferometry (p. 121)
RIP	Restricted Isometry Property (p. 50)
ROP	Rank-One Projection (p. 65)
ROPI	Rank-One Projected Interferometry (p. 81)
RS	Raster-Scanning (p. 66)
SGD	Stochastic Gradient Descent (p. 256)
SIREN	SInusoidal REpresentation Network (p. 252)
SLM	Spatial Light Modulator (p. 67)
SNR	Signal-to-Noise Ratio (p. 45)
SROP	Symmetric Rank-One Projection (p. 65)
SSNP	Split-Step Non Paraxial (p. 237)
SVD	Singular Value Decomposition (p. 30)
TV	Total-Variation (p. 38)
VCZ	Van Cittert-Zernike (p. 131)
VDS	Variable Density Sampling (p. 68)
WPM	Wave Propagation Method (p. 237)